

**BIOCOMPLEXITY RESEARCH TEAM
LABORATORY OF GENERAL BOTANY AND NATURE MANAGEMENT**

**Remote sensing of mangroves in Gazi Bay
(Kenya) with very high resolution QuickBird
satellite imagery**

-automated methods for species and assemblage identification-



By Griet Neukermans

Promoter: Prof. Dr. Nico Koedam
Co-promoters: Dr. Farid Dahdouh-Guebas and
Dr. James G. Kairo

Thesis submitted in partial fulfilment of
the requirements for the degree of
Master of Science in Ecological Marine Management
(Programme sponsored by VLIR)

June 2004



Acknowledgements

This thesis work could not have been realized without the support of several people, to whom I would like to express my gratitude.

I am very grateful to my promoter, Nico Koedam, for his guidance, trust and confidence, for putting all APNA facilities (GIS soft- and hardware, QuickBird satellite image, printer, scanner, mangrove library, copying machine, *etc.*) at my disposal and for his constructive comments on my manuscript and presentations.

I would like to thank my co-promoter, Farid Dahdouh-Guebas, for proposing this exciting thesis subject to me, for his guidance on the field and for his constructive comments on my manuscript and presentations. Also many thanks to my other co-promoter, James G. Kairo, for his support.

The heartwarming memories of my fieldtrip to Kenya in July and August 2003 (travelling scholarship sponsored by VLIR) were a source of inspiration and motivation all throughout this thesis work. The fieldwork has been an enormous enrichment both personally and educationally. It helped me understand the importance of the mangrove forest to the local people, who are in many ways dependant on its resources. *Nashukuru sana* (I am extremely grateful) to all the people in Gazi Bay, who were always very helpful in our research (giving interviews, translating, assisting on the field, guiding us through the mangrove –sometimes at the expense of their shoes-, taking us to the mangrove with their boats -at times even against the tide-...). Special thanks to family S. Ba'alawy for hosting us, to Bakari Hamisi, Mwasho and Imara for their practical help on the field.

I also received a great deal of support and assistance on the field from Helen and Anneleen, two other VUB students in Kenya.

I owe gratitude to Jonathan Chan for explaining the basic principles of remote sensing theory, to Peter Pycke for introducing me to the world of ERDAS Imagine 8.6 and to Piet Boekaerts for his appropriate warnings on the use of eCognition.

Many thanks to Jared Bosire for being kind enough to sacrifice part of his Christmas holidays in Kenya to provide me with the data needed for geometric correction and to Paul Obade for his assistance in the field and the inspiring scientific discussions.

Thanks to Nanette Daro for lending me her book “Teach yourself Kiswahili” and to Natalie Beenaerts and Anouk Verheyden for their kind help and good advice.

Thanks to Anatoly, Karolien and Diana for the inspiring scientific discussions during cosy tea-times in the lab.

Thanks to the visual image interpreters: my uncle Mark, my nephew Nicholas and my father.

Thanks to Peter De Swaef, who had to cope with my outlets of stress from time to time, for his support and for correcting my manuscript.

Special thanks to my parents and close family members who were always very supportive, who have given me the chances to study and for their confidence in my decisions.

I hope that the results of past studies on mangroves as well as my modest contribution, may have some beneficial effect on the wellbeing of the Swahili people that captured my heart.

Abstract

Mangrove degradation is occurring world-wide at a fast rate. This degradation necessitates a rational management at a local, national and global level. Satellite imagery is a valuable tool in the early detection of mangrove degradation in which floristic composition as well as areal extent are important indicators. This thesis work focuses on a tropical bay in Kenya, Gazi Bay, on which very high resolution QuickBird satellite imagery (acquired in October 2002) is available. A field mission for ground-truthing the satellite image was done in July-August 2003.

The aim of this thesis work is three fold. Firstly, to spectrally and spatially enhance the satellite image to ease visual interpretation. Different techniques were used and the most visual-interpretable images were found to be the contrast-stretched pansharpened multispectral false colour composite and the first three principal components of its principal component transformation. The former was used for visual assemblage delineation done by 3 naïve interpreters.

Secondly, to classify the mangroves of Gazi Bay at species level using unsupervised and supervised (hard and soft) per-pixel classification techniques. Incorporation of texture and normalized difference vegetation index (NDVI) measures in image classification both increased the spectral separability between the image classes, but this was not indicative for the accuracy of the classification. On the contrary, the supervised fuzzy classification of the contrast-stretched multispectral image using a 3x3 pixels convolution window appeared to be the most accurate one (based on visual image interpretation and field knowledge). The accuracy of the supervised classification (using the maximum likelihood decision rule) of the contrast-stretched multispectral image was assessed using the Point-Centred-Quarter-Method (PCQM) transect data. The overall accuracy was found to be 68%.

Thirdly, to develop automated methods for vegetation assemblage delineation, which were obtained based on fuzzy convolution techniques of an appropriate convolution window size. The automated delineation was compared with the visual delineation done by 3 naïve interpreters. Results showed that there were two possible disagreements between automated assemblages and visual assemblages: more than one automated assemblage could be included in a visual assemblage and vice versa, but overall the boundaries of the automated assemblages corresponded quite well with the visually delineated polygons. The correspondence between these delineations could however not be quantified.

We can conclude that it is possible to create a mangrove species map of adequate accuracy through supervised classification of the QuickBird satellite image and to automatically identify assemblages using fuzzy convolution techniques of an appropriate window size. Therefore QuickBird satellite imagery has proven to be a valuable tool in the early detection of mangrove degradation in which floristic composition is as important as areal extent.

Samenvatting

De vernieling van mangrovenwouden geschiedt wereldwijd aan een snel tempo. Daardoor is een rationeel beheer nodig op lokaal, nationaal en globaal vlak. Satellietbeelden zijn een waardevol instrument om de degradatie van mangroven vroegtijdig op te sporen, waarbij floristische samenstelling en bedekte oppervlakte belangrijke indicatoren zijn. In deze thesis worden de mangroven onderzocht van Gazi Bay, een tropische baai in Kenia, waarvan Quickbird satellietbeelden van zeer hoge resolutie werden gemaakt in oktober 2002. Een grondcontrole van deze satellietbeelden werd ondernomen in juli en augustus 2003.

Deze thesis heeft drie doelstellingen: ten eerste, het satellietbeeld spectraal en spatiaal te manipuleren om visuele interpretatie te vergemakkelijken. Hiervoor werden verschillende technieken gebruikt waarbij de best interpreteerbare beelden de contrast-stretched pan-gescherpte multispectrale valse kleuren composiet bleken, alsook de eerste drie principale componenten van de principale componenten transformatie van dit beeld. Eerstgenoemd beeld werd gebruikt bij een visuele assemblage delineatie door drie personen zonder kennis van de materie.

Een tweede doel is de classificatie van de verschillende soorten vegetatie in de mangroven van Gazi Bay, waarbij niet-gesuperviseerde en gesuperviseerde per-pixel classificatietechnieken werden aangewend. De toevoeging van textuur en van normalized difference vegetation index (NVDI)-metingen aan de classificatie van de beelden verhoogde in beide gevallen de spectrale separabiliteit tussen de verschillende beeldklassen, wat echter geen indicatie was voor de juistheid van de classificatie. Integendeel, de gesuperviseerde fuzzy classificatie van het contrast-stretched multispectrale beeld bij een 3x3 pixel convolutievenster leek de meest betrouwbare classificatie (gebaseerd op visuele beeldinterpretatie en kennis opgedaan bij het veldwerk). De juistheid van de gesuperviseerde classificatie (waarbij het maximum likelihood classificatiealgoritme werd gehanteerd) van het contrast-stretched multispectrale beeld werd bepaald door gebruik van Point-Centred-Quarter-Methode (PCQM) transect data. De gegevens bleken voor 68% betrouwbaar.

Een derde doelstelling is het ontwikkelen van geautomatiseerde methodes voor vegetatie assemblage delineatie, die werden verkregen op basis van fuzzy convolutietechnieken met een gepaste convolutievenstergrootte. Drie vrijwilligers zonder kennis van de materie voerden een visuele delineatie uit, waarna deze werd vergeleken met de geautomatiseerde delineatie. Dit resulteerde in twee mogelijke conflicten tussen de geautomatiseerde assemblages en de visuele assemblages: verscheidene geautomatiseerde assemblages konden vervat zijn in een visueel assemblage en vice versa, maar in het algemeen correspondeerden de grenzen van de geautomatiseerde assemblages vrij goed met die van de visueel gedelineerde polygonen. De gelijkens tussen de twee delineaties kon echter niet worden gekwantificeerd.

We kunnen besluiten dat het mogelijk is om mangrovesoorten met een aanvaardbare foutenmarge in kaart te brengen door gesuperviseerde classificatie van de QuickBird satellietbeelden en ook om identificatie van assemblages te automatiseren, dit door gebruik te maken van fuzzy convolutietechnieken met een gepaste venstergrootte.

Daardoor kunnen we stellen dat QuickBird satellietbeelden een waardevol instrument vormen in de vroege opsporing van de achteruitgang van mangroven, waarbij de floristische samenstelling een even belangrijke parameter blijkt als de bedekte oppervlakte.

Table of contents

ACKNOWLEDGEMENTS	I
ABSTRACT	III
SAMENVATTING	IV
TABLE OF CONTENTS	VI
LIST OF FIGURES	X
LIST OF TABLES	XIII
LIST OF ABBREVIATIONS	XVI
I INTRODUCTION	1
I.1 MANGROVES	1
I.1.1 ECONOMIC IMPORTANCE OF MANGROVES	2
I.1.2 THE MANGROVE - SEAGRASS BED - CORAL REEF CONTINUUM.....	3
I.2 EAST AFRICAN MANGROVE MANAGEMENT	4
I.2.1 GENERAL INTRODUCTION	4
I.2.2 THE SITUATION IN KENYA.....	7
I.3 REMOTE SENSING OF MANGROVES	9
I.3.1 GENERAL	9
I.3.2 RESEARCH BY APNA.....	9
I.4 RESEARCH OBJECTIVES	11
I.4.1 THE GAZI BAY PROJECT 2003-2004: THESIS INTERACTIONS	11
I.4.2 THIS THESIS WORK	12
II LITERATURE REVIEW	14
II.1 REMOTE SENSING	14
II.2 AIR-BORNE AND SPACE-BORNE IMAGERY (PHOTOGRAPHS AND DIGITAL IMAGERY) ..	16
II.3 DIGITAL IMAGE PROCESSING	17
II.3.1 FEATURE SPACE	18
II.4 GEOMETRIC CORRECTION	19
II.5 IMAGE ENHANCEMENT	23
II.5.1 PRINCIPAL COMPONENT TRANSFORMATION	23
II.5.2 VEGETATION INDICES	24
II.5.3 MULTIREOLUTION MERGING	25
II.6 PRINCIPLES OF PIXEL-BASED IMAGE CLASSIFICATION	26
II.7 UNSUPERVISED CLASSIFICATION	26

II.8 SUPERVISED CLASSIFICATION	27
II.8.1 SELECTION OF THE CATEGORIES OF INTEREST	28
II.8.2 SELECTION OF REPRESENTATIVE TRAINING SITES	28
II.8.3 EXTRACTION AND ANALYSIS OF THE TRAINING SITES STATISTICS	28
II.8.4 EVALUATION OF THE DEGREE OF BETWEEN-CLASS SEPARABILITY	29
II.8.4.1 Graphical representation of spectral response patterns	29
II.8.4.2 Quantitative expressions of category separation	30
II.8.4.3 Self-classification of training data sets	30
II.8.4.4 Interactive preliminary classification	30
II.8.5 SELECTION OF AN APPROPRIATE CLASSIFIER	30
II.8.6 CLASSIFICATION OF THE IMAGE	31
II.8.7 STATISTICAL EVALUATION OF THE CLASSIFIED IMAGE	31
II.9 TRADITIONAL HARD CLASSIFIERS	34
II.9.1 THE PARALLELEPIPED CLASSIFIER	34
II.9.2 THE MINIMUM DISTANCE CLASSIFIER	35
II.9.3 THE MAXIMUM LIKELIHOOD CLASSIFIER	36
II.10 CLASSIFICATION IN PRACTICE	37
II.11 TEXTURE	37
II.12 FUZZY CLASSIFICATION	39
II.13 EVOLUTION TOWARDS OBJECT-BASED ANALYSIS	40
II.14 OBJECT-BASED IMAGE ANALYSIS	41
II.15 THE FIELD SURVEY	42
II.15.1 THE REMOTE SENSING – FIELD SURVEY COMBINATION	42
II.15.2 GLOBAL POSITIONING SYSTEM (GPS)	43
II.15.3 THE POINT-CENTRED QUARTER METHOD (PCQM)	43
II.15.3.1 General description	43
II.15.3.2 PCQM in mangrove research	44
 III MATERIALS AND METHODS	 46
 III.1 DESCRIPTION OF THE STUDY SITE	 46
III.1.1 GEOGRAPHICAL	46
III.1.2 CLIMATOLOGICAL	46
III.1.3 BIOLOGICAL: MANGROVE AND SEAGRASS BEDS	46
III.1.4 HYDROLOGICAL	47
III.1.5 HISTORY OF THE MANGROVE	47
III.2 SATELLITE IMAGE	48
III.3 FIELD SURVEY	50
III.4 SATELLITE IMAGE PREPROCESSING	53
III.4.1 GEOMETRIC CORRECTION	53
III.4.2 MANGROVE SUBSET	54
III.4.3 MULTIREOLUTION MERGE	54
III.5 SPECTRAL ENHANCEMENT	54
III.5.1 COLOUR COMPOSITES	54
III.5.2 CONTRAST STRETCH THROUGH MASKING	54
III.5.3 PRINCIPAL COMPONENT TRANSFORMATION	55
III.5.4 INDICES	55
III.5.5 TEXTURE	55
III.6 UNSUPERVISED CLASSIFICATION OF THE MULTISPECTRAL IMAGES	55
III.6.1 UNSUPERVISED CLASSIFICATION OF MXS	55

III.6.2	UNSUPERVISED CLASSIFICATION OF MPXS.....	55
III.7	SUPERVISED CLASSIFICATION.....	56
III.7.1	SUPERVISED CLASSIFICATION OF MXS	56
III.7.1.1	Selection of training sites	56
III.7.1.2	Training site statistics.....	56
III.7.1.3	Evaluation of the degree of between-class separability	56
III.7.1.4	Fuzzy classification	57
III.7.1.5	Classification accuracy assessment.....	57
III.7.2	SUPERVISED CLASSIFICATION OF MPXS.....	58
III.7.2.1	Selection of training sites	58
III.7.2.2	Training sites statistics	58
III.7.2.3	Evaluation of the degree of between class separability.....	58
III.7.2.4	Fuzzy classifications	58
III.7.2.5	Classification accuracy assessment.....	59
III.8	AREA COVERED BY EACH MANGROVE SPECIES.....	59
III.9	AUTOMATED DELINEATION OF VEGETATION ASSEMBLAGES	59
III.10	VISUAL DELINEATION OF VEGETATION ASSEMBLAGES	59
III.11	AREA COVERED BY MANGROVE, SAND AND WATER.....	59
IV	RESULTS	61
IV.1	RESULTS OF THE FIELD SURVEY	61
IV.2	SATELLITE IMAGE PREPROCESSING	64
IV.2.1	GEOMETRIC CORRECTION.....	64
IV.2.2	MANGROVE SUBSET	68
IV.2.3	MULTIRESOLUTION MERGE	68
IV.3	SPECTRAL ENHANCEMENT	68
IV.3.1	NATURAL COLOUR IMAGE	68
IV.3.2	FALSE COLOUR COMPOSITE	69
IV.3.3	CONTRAST STRETCH THROUGH MASKING.....	71
IV.3.4	PRINCIPAL COMPONENTS TRANSFORMATION.....	75
IV.3.5	INDICES	78
IV.3.6	TEXTURE: VARIANCE	79
IV.4	UNSUPERVISED CLASSIFICATION OF THE MULTISPECTRAL IMAGES	81
IV.4.1	UNSUPERVISED CLASSIFICATION OF MXS	81
IV.4.2	UNSUPERVISED CLASSIFICATION OF MPXS.....	83
IV.5	SUPERVISED CLASSIFICATION.....	85
IV.5.1	SUPERVISED CLASSIFICATION OF MXS	85
IV.5.1.1	Training site selection	85
IV.5.1.2	Training site statistics.....	88
IV.5.1.3	Evaluation of the degree of between class separability	90
IV.5.1.4	Classification accuracy assessment.....	96
IV.5.1.5	Fuzzy classification.....	100
IV.5.2	SUPERVISED CLASSIFICATION OF MPXS	108
IV.5.2.1	Training site selection	108
IV.5.2.2	Training site statistics.....	108
IV.5.2.3	Evaluation of the degree of between-class separability	110
IV.5.2.4	Classification accuracy assessment.....	116
IV.5.2.5	Fuzzy classification.....	119
IV.6	AREA COVERED BY EACH MANGROVE SPECIES	122

IV.7	AUTOMATED DELINEATION OF VEGETATION ASSEMBLAGES.....	127
IV.8	VISUAL DELINEATION OF VEGETATION ASSEMBLAGES.....	132
IV.9	AREA COVERED BY MANGROVE, SAND AND WATER	135
V	DISCUSSION.....	137
V.1	VISUAL INTERPRETABILITY OF THE SATELLITE IMAGE	137
V.2	COMPARISON BETWEEN UNSUPERVISED CLASSIFICATION OF MXS AND MPXS.....	137
V.3	SEPARABILITY BETWEEN CLASSES IN SUPERVISED CLASSIFICATION.....	137
V.4	EFFECT OF INCREASING WINDOW SIZES IN FUZZY CLASSIFICATIONS.....	138
V.5	EFFECT OF THE INCORPORATION OF NDVI VALUES IN SUPERVISED CLASSIFICATION OF MULTISPECTRAL DATA	138
V.5.1	COMPARISON BETWEEN FUZZY CLASSIFICATIONS OF MXS AND MXS+NDVI USING 3X3 PIXELS CONVOLUTION WINDOW.....	139
V.5.2	COMPARISON BETWEEN FUZZY CLASSIFICATIONS OF MXS AND MXS+NDVI USING 7X7 PIXELS CONVOLUTION WINDOW.....	140
V.6	EFFECT OF THE INCORPORATION OF TEXTURE IN SUPERVISED CLASSIFICATION OF PANSHARPENED MULTISPECTRAL IMAGE.....	141
V.7	AREA COVERED BY EACH MANGROVE SPECIES.....	143
V.8	AUTOMATED STAND DELINEATION VERSUS MANUAL/VISUAL STAND DELINEATION .	143
V.9	CLASSIFICATION ACCURACY DETERMINATION	146
V.10	COMPARISON BETWEEN CLASSIFICATIONS.....	147
VI	CONCLUSION	149
VI.1	RESEARCH OBJECTIVES FULFILLED	149
VI.2	RESEARCH QUESTIONS STILL REMAINING – FUTURE WORK	149
VI.3	RECOMMENDATIONS	150
VII	RELEVANCE OF THIS THESIS IN THE FRAMEWORK OF DEVELOPMENT CO-OPERATION	149
	APPENDIX	153
	REFERENCES.....	166
	INDEX.....	177

List of Figures

Figure 1. Left: mangroves used in house construction in Gazi Bay, Kenya. Right: Woman collecting mangrove and coconut wood for fuel in Gazi Bay, Kenya (photographed by G. Neukermans, July 2003).....	6
Figure 2. Left: Mangrove stems (called pondos) used to propell boats in the mangrove mud in Gazi Bay, Kenya. Right: Fishtraps constructed from mangrove in Gazi Bay, Kenya (photographed by G. Neukermans, July 2003)	6
Figure 3. Traditional Swahili bed made of mangrove wood and rope, Gazi Bay, Kenya (photographed by A. Van Tendeloo, August 2003).....	6
Figure 4. Thesis interactions within wider research framework (post-doctoral supervisors and VLIR-IUC programme).....	11
Figure 5. Schematical representation of the steps involved in image enhancement and visual analysis.....	12
Figure 6. Schematical representation of the steps involved in image classification, classification accuracy assessment and automated assemblage delineation	13
Figure 7. The electromagnetic spectrum (Lillesand and Kiefer, 1994).....	15
Figure 8. Typical reflectance curves for soil, vegetation and water (Mather, 1999)	16
Figure 9. Feature space concept. (a) shaded pixel (5,4) image coordinates in the 7x7 pixels image, (b) DN values of the shaded pixel in each image band, (c) representation of the pixel in feature space (adapted from Tso and Mather, 2001).....	19
Figure 10. Grid of geometrically correct output pixels (full line) superimposed on grid of original distorted input pixels (dotted line) (Lillesand and Kiefer, 1994)	23
Figure 11. Basic steps in supervised classification (Adapted from Lillesand and Kiefer, 1994)	28
Figure 12. Parallelepiped decision rule (Lillesand and Kiefer, 1994)	35
Figure 13. Left: Minimum distance decision rule using the Euclidean distance measure (Lillesand and Kiefer, 1994). Right: Mahalanobis distance in feature space, resulting in ellipsoidal features space objects (ERDAS Field Guide, 2002).....	36
Figure 14. Probability density functions (left) and equiprobability contours (right) defined by maximum likelihood classifier (Lillesand and Kiefer, 1994)	37
Figure 15. (a) Map of Kenya, (b) Gazi Bay, showing the area covered by mangrove, seagrass and coral reef, rivers and tidal creeks, (c) detail of Gazi village (from Dahdouh-Guebas <i>et al.</i> , 2004a, in press)	48
Figure 16. Schematical representation of the Point-Centred-Quarter Method (PCQM of Cottam and Curtis, 1956) used to ground truth the satellite image.....	51
Figure 17. Principle of measuring tree height with a hypsometer	52
Figure 18. Location of GCPs on the panchromatic QB image indicated with green crosshairs. The names followed by (*) refer to the location of the GCP as indicated by the GPS equipment and the non-primed names show the actual location of the GCPs on the satellite image.....	66
Figure 19. Positioning of transects on a geometrically corrected classified image overlaid on the panchromatic (uncorrected) image to show the effect of the polynomial refinement of image geometric correction.....	67
Figure 20. Natural colour transformation of the PXS image: overview of region names adopted in this work.....	69
Figure 21. Overview of subsets on the PXS FCC image (B in B colour gun, G in G colour gun and NIR in R colour gun).....	71

Figure 22. Overview of subsets in MPXS FCC image (B in B colour gun, G in G colour gun, NIR in R colour gun).....	72
Figure 23. Principal component image of MPXS (PC1 in R colour gun, PC2 in G colour gun, PC3 in B colour gun).....	76
Figure 24. Comparison between different parts of assemblages on the MPXS FCC and the PCA_MPXS image (PC1 in R colour gun, PC2 in G colour gun, PC3 in B colour gun)....	78
Figure 25. NDVI image of MXS. NDVI-values range from -0.34 (black) to 0.53 (white)	79
Figure 26. Variance texture measure calculated in a 7x7 pixels window from the PAN image	80
Figure 27. Variance texture measure in a 21x21 pixels window from the PAN image	81
Figure 28. Unsupervised classification of MXS image into 15 spectral clusters (convergence threshold 95%), grouped into 8 information classes	83
Figure 29. Unsupervised classification of MPXS image into 15 spectral clusters (convergence threshold of 95%), grouped into 7 information classes.....	85
Figure 30. Training AOI's on the MPXS image. Pixels in the red polygons are training data pixels, numbers refer to the training category to which they are assigned	87
Figure 31. MXS(+NDVI) signature DN means and standard deviations in the B band.....	88
Figure 32. MXS(+NDVI) signature DN means and standard deviations in the G band.....	88
Figure 33. MXS(+NDVI) signature DN means and standard deviations in the R band.....	89
Figure 34. MXS(+NDVI) signature DN means and standard deviations in the NIR band.....	89
Figure 35. MXS(+NDVI) signature DN means and standard deviations in the NDVI (=NIR-R/NIR+R) band	89
Figure 36. Signature ellipses of 2 standard deviations from the mean (crosshair) in 2-dimensional feature space (G band values on the horizontal axis and NIR band values on the vertical axis)	92
Figure 37. Supervised classification of MXS in 15 classes	96
Figure 38. Supervised classification of MXS+NDVI in 15 classes	97
Figure 39. Fuzzy classification of MXS with 15 classes using a 3x3 pixel convolution window	101
Figure 40. Fuzzy classification of MXS with 15 classes using a 5x5 pixel convolution window	102
Figure 41. Fuzzy classification of MXS with 15 classes using a 7x7 pixel convolution window	103
Figure 42. Fuzzy classification of MXS+NDVI with 15 classes using a 3x3 pixel convolution window	104
Figure 43. Fuzzy classification of MXS+NDVI with 15 classes using a 5x5 pixel convolution window	105
Figure 44. Fuzzy classification of MXS+NDVI with 15 classes using a 7x7 pixel convolution window	106
Figure 45. MPXS(+VAR7/21) signature DN means and standard deviations in the B band ...	108
Figure 46. MPXS(+VAR7/21) signature DN means and standard deviations in the G band ...	109
Figure 47. MPXS(+VAR7/21) signature DN means and standard deviations in the R band ...	109
Figure 48. MPXS(+VAR7/21) signature DN means and standard deviations in the NIR band	109
Figure 49. MPXS(+VAR7/21) signature DN means and standard deviations in the VAR7 band	110
Figure 50. MPXS(+VAR7/21) signature DN means and standard deviations in the VAR21 band	110
Figure 51. Fuzzy 7x7 ML classification of MPXS image.....	120
Figure 52. Fuzzy 7x7 ML classification of MPXS+VAR7 image.....	121
Figure 53. Fuzzy 7x7 ML classification of MPXS+VAR21 image.....	122

Figure 54. Automated assemblages derived from the fuzzy classification of MXS using a 7x7 pixels convolution window, after elimination of continuous groups of pixels (belonging to the same image class) covering less than 50 pixels	127
Figure 55. Automated assemblages derived from the fuzzy classification of MXS+NDVI using a 7x7 pixels convolution window, after elimination of continuous groups of pixels (belonging to the same image class) covering less than 50 pixels	128
Figure 56. Contour lines derived from the fuzzy classification of MXS using a 7x7 pixel convolution window, after elimination of continuous groups of pixels (belonging to the same image class) covering less than 50 pixels	129
Figure 57. Contour lines derived from the fuzzy classification of MXS+NDVI using a 7x7 pixel convolution window, after elimination of continuous groups of pixels (belonging to the same image class) covering less than 50 pixels	130
Figure 58. Differences between the fuzzy classification (using a 7x7 pixel convolution window) of MXS and MXS+NDVI after grouping the classes per species. Changes are written as classification of species on the MXS image to classification of species on the MXS+NDVI image	131
Figure 59. Visual delineation of assemblages by interpreter 1	133
Figure 60. Visual delineation of assemblages by interpreter 2	134
Figure 61. Visual delineation of assemblages by interpreter 3	135
Figure 62. Calculation of area covered by mangrove, water and sand from an unsupervised classification with 6 classes.....	136
Figure 63. Left: woman sitting in an <i>Avicennia marina</i> tree in the ground-truthed “Amar” assemblage (or AMD training site area, see Table 17 for explanation). Right: Helen and Anneleen walking near the “Amar2” assemblage (or ALD training site area, see Table 17 for explanation) (photographed by G. Neukermans, Gazi Bay, Kenya, July-August 2003)	153
Figure 64. Left: <i>Sonneratia alba</i> natural area in front of the New Fishermen's Place (photographed by G. Neukermans, Gazi Bay, Kenya, July 2003). Right: Me and Bakari in seaward <i>Avicennia marina</i> zone (photographed by H. Defever, Gazi Bay, Kenya, August, 2003).....	153
Figure 65. Left: <i>Avicennia marina</i> shrubs. Right: <i>Ceriops tagal</i> shrubs (Photographed by A. Van Tendeloo, Gazi Bay, Kenya, July 2003).....	154

List of Tables

Table 1. Digital image processing steps (summarized in part from Lillesand and Kiefer, 1994).....	18
Table 2. Confusion matrix for classification accuracy evaluation.....	33
Table 3. Details on QuickBird image (UL: Upper left corner, UR: Upper right corner, LL: lower left corner, LR: lower right corner, source: www.digitalglobe.com).....	50
Table 4. Corner coordinates of the subset covering the whole mangrove area.....	54
Table 5. Distance table for fuzzy convolution of window size 3x3.....	57
Table 6. Distance table for fuzzy convolution of window size 5x5.....	57
Table 7. Distance table for fuzzy convolution of window size 7x7.....	57
Table 8. Regression statistics between D_{130} and height for each species.....	61
Table 9. Regression statistics between D_{130} and CD for each species.....	61
Table 10. Absolute characteristics of each ground-truthed vegetation assemblage in Gazi Bay: number of stems per 0.1 ha, mean stand height, number of species, basal area, complexity index (Cottam and Curtis, 1956) and mean crown diameter.....	62
Table 11. Relative density (DE_r), relative dominance (DO_r) and relative frequency (F_r'), importance value (IV) and rank (R) of each species in each ground-truthed vegetation assemblage in Gazi Bay (2003).....	63
Table 12. Relative density (DE_r), dominance (DO_r) and frequency (F_r'), importance value (IV) and rank (R) for all vegetation assemblages added.....	64
Table 13. UTM coordinates of ground control points (GCPs) used in the georectification of XS. Input coordinates are read from the satellite image, reference coordinates are read from the GPS recorder.....	65
Table 14. Positional accuracy of the GPS recordings at the start (S), in the middle (M) and at the end (E) of the transects.....	68
Table 15. UTM, latitude and longitude corner coordinates of subsets A-G.....	70
Table 16. MPXS FCC image description of training sites representing different assemblages. Each assemblage is described in terms of its colour, texture, structure and a crown description is given if individual crowns are discernible.....	74
Table 17. Field description of training sites representing different assemblages.....	75
Table 18. Eigenvectors, eigenvalues, percentage variance explained ($\%_p$) and cumulative percentage of variance explained (cum%) by each of the 4 principle components of the MPXS image.....	75
Table 19. PCA_MPXS image description of training sites representing assemblages. Assemblages are described in terms of their colour, texture, structure and a description of crowns is given if individual crowns are discernible.....	77
Table 20. Grouping of spectral clusters into information classes in the unsupervised classification of MXS together with their colour appearance in the MPXS image.....	82
Table 21. Grouping of spectral clusters into information classes in the unsupervised classification of MPXS together with their colour appearance in the MPXS image.....	84
Table 22. Contingency matrix for training pixel data from MXS using the ML decision rule, entries in pixel counts. User's, producer's and overall accuracy are shown.....	90
Table 23. Contingency matrix for training pixel data from MXS+NDVI using the ML decision rule, entries in pixel counts. User's, producer's and overall accuracy are shown.....	91

Table 24. Transformed divergence separability indices for the signatures extracted from the MXS image. Values lower than 1700 are shaded, average and minimum separability are shown	94
Table 25. Transformed divergence separability indices for the signatures extracted from the MXS image. Values lower than 1700 are shaded, values of separability below 1700 on MXS that increased above 1700 on MXS+NDVI are given in bold. Average and minimum separability are given	95
Table 26. Error matrix of the supervised ML classification of MXS taking into consideration all transect data as reference data	98
Table 27. Error matrix of the supervised ML classification of MXS taking into consideration only those transect data where the adult tree layer corresponds with the remotely sensed canopy	99
Table 28. Error matrix of the supervised ML classification of MXS+NDVI taking into consideration only those transect data where the adult tree layer corresponds with the remotely sensed canopy	100
Table 29. Contingency matrix for training pixel data from MPXS using the ML decision rule, entries in pixel counts. User's, producer's and overall accuracy are shown.....	110
Table 30. Contingency matrix for training pixel data from MPXS+VAR7 using the ML decision rule, entries in pixel counts. User's, producer's and overall accuracy are shown	111
Table 31. Contingency matrix for training pixel data from MPXS+VAR21 using the ML decision rule, entries in pixel counts. User's, producer's and overall accuracy are shown	112
Table 32. Transformed divergence separability indices for the signatures extracted from the MPXS image. Values lower than 1700 are shaded, average and minimum separability are shown	113
Table 33. Transformed divergence separability indices for the signatures extracted from the MPXS+VAR7 image. Values lower than 1700 are shaded, average and minimum separability are shown.....	114
Table 34. Transformed divergence separability indices for the signatures extracted from the MPXS+VAR21 image. Values lower than 1700 are shaded, decreased values of separability compared to separability values of MPXS+VAR7 are given in bold. Average and minimum separability are shown.....	115
Table 35. Error matrix of the supervised ML classification of MPXS taking into consideration only those transect data where the adult tree layer corresponds with the remotely sensed canopy	117
Table 36. Error matrix of the supervised ML classification of MPXS+VAR7 taking into consideration only those transect data where the adult tree layer corresponds with the remotely sensed canopy	118
Table 37. Error matrix of the supervised ML classification of MPXS+VAR21 taking into consideration only those transect data where the adult tree layer corresponds with the remotely sensed canopy	119
Table 38. Area covered by each class expressed as percentage of the total area covered in the supervised classifications of MXS	123
Table 39. Area covered by each class expressed as percentage of the total area covered in the supervised classifications of MXS+NDVI.....	124
Table 40. Area covered by each class expressed as a percentage of the total area covered in the supervised classifications of MPXS	126
Table 41. Differences in number of pixels and in area (km ²) between the species fuzzy classification (using a 7x7 pixel convolution window) of MXS and MXS+NDVI. Changes	

are written as classification of species on the MXS image “to” classification of species on the MXS+NDVI image. Classifications into the same species in both classifications are in bold..... 132

Table 42. Training site univariate statistics in each layer of the MXS/MXS+NDVI image (B: blue band, R: red band, G: green band, NIR: Near-infrared band and NDVI band) and covariance matrices. Min: minimum, Max: maximum, mean, SD: standard deviation and %M: SD expressed as percentage of the mean (values of %M>20 are highlighted in grey) 157

Table 43. Training site univariate statistics in each layer of the MPXS/MPXS+VAR7/MPXS+VAR21 image (B: blue band, R: red band, G: green band, NIR: Near-infrared band, VAR7: variance calculated in a 7x7 pixels window, VAR21: variance calculated in a 21x21 pixels window) and covariance matrices. Min: minimum, Max: maximum, mean, SD: standard deviation and %M: SD expressed as percentage of the mean (values of %M>20 are highlighted in grey)..... 162

List of abbreviations

General abbreviations

AOI	Area of interest
B	Blue
DN	Digital number
FCC	False Colour Composite
G	Green
GIS	Geographic information system
GPS	Global Positioning System
κ	Kappa-coefficient
KMFRI	Kenya Marine Fisheries Research Institute
ML	Maximum Likelihood
NIR	Near-infrared
OA	Overall accuracy
PA	Producer's accuracy
PCA	Principal component analysis
PC	Principal component
PCQM	Point-Centred Quarter Method
QB	QuickBird R Red
RS	Remote sensing
τ	Tau-coefficient
TS	Training site
UA	User's accuracy
VHR	Very High Resolution

Mangrove species abbreviations

<i>Amar</i>	<i>Avicennia marina</i>
<i>Bgym</i>	<i>Bruguiera gymnorrhiza</i>
<i>Ctag</i>	<i>Ceriops tagal</i>
<i>Hlit</i>	<i>Heritiera litoralis</i>
<i>Lrac</i>	<i>Lumnitzera racemosa</i>
<i>Paci</i>	<i>Pemphis acidula</i>
<i>Rmuc</i>	<i>Rhizophora mucronata</i>
<i>Salb</i>	<i>Sonneratia alba</i>
<i>Xgra</i>	<i>Xylocarpus granatus</i>
<i>Xmol</i>	<i>Xylocarpus molucensis</i>

Training site abbreviations

AGazi	<i>Amar</i> nearest to Gazi village
AML	<i>Amar</i> at the landward side with medium density compared to Agazi (highest density)
ALD	<i>Amar</i> at the landward side with low density compared to Agazi (highest density)
AS	<i>Amar</i> at the seaward side of the mangrove
BG	<i>Bgym</i> in the central mangrove area
CGazi	<i>Ctag</i> occurring nearest to Gazi village
CCM	<i>Ctag</i> in the central mangrove area
CNFP	<i>Ctag</i> at the New Fishermen's place
CNMak	<i>Ctag</i> North of Makongeni creek
CWMak	<i>Ctag</i> West of Makongeni creek
C&R	Mixed mangrove area dominated by <i>Ctag</i> and rarely interspersed with <i>Rmuc</i>
REKin	<i>Rmuc</i> East of Kinondo creek
RPlant	<i>Rmuc</i> from KMFRI <i>Rmuc</i> plantation East of Kinondo Creek
RWMak	<i>Rmuc</i> West of Makongeni Creek
SA	<i>Salb</i> South of Central mangrove area

Image abbreviations

XS	multispectral image
PAN	panchromatic image
PXS	pansharpened multispectral image
MXS	contrast-stretched multispectral image
MPXS	pansharpened contrast-stretched multispectral image
MXS+NDVI	contrast-stretched multispectral image with NDVI values as an additional layer
MPXS+VAR7	pansharpened contrast-stretched multispectral image with variance texture measure calculated in a 7x7 pixels window as an additional layer
MPXS+VAR21	pansharpened contrast-stretched multispectral image with variance texture measure calculated in a 21x21 pixels window as an additional layer

I Introduction

This thesis work is a “small brick in the wall of mangrove research” done within the Laboratory of General Botany and Nature management (in Dutch: **Algemene Plantkunde en NATuurbeheer**, APNA) at Vrije Universiteit Brussel (VUB). Different researchers of the Faculty of Sciences at the VUB investigating mangrove forests have been joined in the Mangrove Management Group, which aims to contribute scientifically to a better understanding of the mangrove ecosystem and to yield elements to improve mangrove management and conservation (<http://www.vub.ac.be/mangrove/>). This unit covers different aspects of mangrove research, such as vegetation structure and zonation, spatio-temporal dynamics and succession, regeneration and restoration of mangrove forests, propagule predation and other plant-animal interactions, air- and space-borne remote sensing of mangrove areas *etc.*

This thesis work focuses on the classification of a very high resolution satellite image (QuickBird) of a mangrove area in Gazi Bay, Kenya. Gazi Bay has been a topic of investigation at the VUB since the 1980's and for APNA in particular since 1993. Aerial photographs of the Gazi mangroves were studied at APNA since 1993 and very high resolution satellite imagery since 2002.

This introductory chapter explains what mangroves are and why we study these important, invaluable and vulnerable ecosystems. It gives an overview of mangrove management in East-Africa and Kenya in particular and of research in the field of remote sensing of mangroves.

I.1 Mangroves

Mangrove forests are intertidal forests occurring along tropical and subtropical coastlines. The mangrove trees are adapted to grow in salt water at the edge of both land and sea in lagoons, estuaries and sheltered (sub)tropical bays. Mangroves are highly productive ecosystems, serving as breeding, spawning, hatching and nursing grounds for many marine species of both lagoon and offshore origin (Tomlinson, 1986; Spalding *et al.*, 1997; Mumby *et al.* 2004).

Mangroves provide a large variety of goods and services to man, either directly (wood products such as fuel wood, building poles, fishing gear, furniture and non-wood products such as food items, medicines and tannins) or indirectly (protection of the shoreline against erosion, acting as important fishing grounds, waste-water treatment) (Tomlinson, 1986; Ewel, 1998; Dahdouh-Guebas *et al.*, 2000; Jayatissa *et al.*, 2002).

Historically human pressure on the mangrove ecosystem was limited: all but a few subsistence populations saw mangrove areas as inhospitable, unhealthy and dangerous. Few communities of people actually lived within the mangrove forest because they could only be accessed by small boats. In recent years, the pressures of increasing population, food production and industrial and urban development have led to a significant proportion of the world's mangrove forest resource being destroyed. Between 5% and nearly 85% of the original mangrove extent (which was approximately 75% of sheltered tropical coasts worldwide) in various countries, where such data are available, has been lost. Extensive losses

have occurred particularly during the second half of the 20th century (Chapman, 1976; Spalding *et al.*, 1997; Burke *et al.*, 2001). To fulfil the needs of the ever increasing population, many mangrove areas have been cleared for agricultural purposes or for the provision of fish and shrimp ponds for commercial production (Farnsworth and Ellison, 1997). Much of this reclaimed land has proved unsuitable for agriculture or aquaculture and today it lies derelict (Kairo *et al.*, 2001). Mangrove destruction also occurs as a result of reclamation for village expansion, tourism, oil spills (Duke *et al.*, 1997), freshwater diversion (Tack and Polk, 1999; Jayatissa *et al.*, 2002) and deterioration of water quality from the input of potentially toxic materials (*e.g.* heavy metals, pesticides) and nutrients to rivers and coastal waters. Mangroves have also been logged for timber, fuelwood and charcoal production, chipped for paper production and destroyed to provide land for the construction of mines, ports, tourist resorts and housing. The exploitation of mangrove forests for short term gain has usually been irreversibly destructive (Spalding *et al.*, 1997).

According to Mumby *et al.* (2004) current rates of mangrove deforestation (global loss exceeding 35%) are likely to have severe deleterious consequences for the ecosystem function, fisheries productivity and resilience of reefs. This dramatic degradation necessitates a rational management of the mangrove ecosystem on a local, regional and global level. This requires a thorough understanding of the direct and indirect impacts of man on the mangrove ecosystem. The consequences of human impact can be foreseen by knowing the ecosystem's lag time, resilience and recovery capacity (Daoudouh-Guebas, 2002). Research on the high spatio-temporal dynamism in land-use and land cover patterns includes changes in population structure of floral and faunal assemblages, in biodiversity and ecosystem functioning and in ethnobiological uses. An effective management tool for detection, description, quantification and monitoring of those changes is remote sensing, combined with geographic information systems (GIS) and fieldwork (see section I.3).

I.1.1 Economic importance of mangroves

Recent attempts to value mangrove habitat fishery linkages in Mexico, Indonesia and Thailand indicate that deforestation of mangroves is contributing to fishery decline and significant welfare losses (Ruitenbeek, 1994; Barbier and Strand, 1998; Barbier, 2001; Sathirathai and Barbier, 2001). Barbier (2003) estimated the welfare effects on coastal fisheries of mangrove conversion to shrimp aquaculture in Thailand by analysing simultaneously the impacts of shrimp farming on mangrove systems as well as the corresponding effects of mangrove loss on habitat-fishery linkages. It was concluded that although large in absolute terms, the economic losses to coastal fisheries in Thailand from mangrove deforestation are very small (\$1.3-\$1.6 million annually – estimated in 2003) relative to the total value of shrimp aquaculture production (\$1.4-\$1.7 billion annually – estimated in 2003). But a major general cost of shrimp farms is the considerable amount of water pollution (agro-chemical runoff and high salinity) they generate. After the five-year period of their productive life, shrimp ponds are left in a highly degraded state, rapidly transforming into waste lands and too poor in quality (acidic and compacted soils) to be used for any other productive use, such as agriculture. Additionally, without considerable investment in restoration, these areas do not regenerate into mangrove forests. Sathirathai and Barbier (2001) conducted an economic cost-benefit analysis of the returns to commercial shrimp farming in southern Thailand, which includes accounting for the external costs of water pollution and rehabilitating the mangrove forest as well as the full economic costs of conventional inputs. The results indicate that excluding the costs of mangrove restoration, the

discounted economic returns to commercial shrimp farming range from \$194 to \$209 per ha (estimated in 2001). If the costs of regenerating the mangrove forest are included, then the economic returns to shrimp farming are actually negative. In comparison, the net present value of local timber and non-timber harvests from the mangrove forest by a small coastal community is estimated to be around \$632-\$823 per ha (in 2001). The economic losses in habitat-fishery linkages from mangrove deforestation is estimated to be \$253 per ha (Barbier, 2003). Based on his calculations he concludes that in the long run (>20 years) the economic value of the habitat-fishery linkage is 10 times higher than the economic returns to shrimp farming.

I.1.2 The mangrove - seagrass bed - coral reef continuum

Mangrove forests occur at the land-sea interface. Seaward, in the infra-littoral zone, seagrass beds may lie along side the mangrove. Coral reefs are located seawards and rank among the most biologically productive and diverse of natural ecosystems. Reefs hold a significant portion of the world's fishery resources and they are very sensitive to overfishing (Salvat, 1987; Russ, 1991). Biotic and environmental ecological interlinkages within and between mangrove forests, seagrass meadows and coral reefs have been demonstrated (Hemminga *et al.*, 1994; Marguiller *et al.*, 1997).

Mangroves and coral reefs protect the coastline against erosion by stabilizing the sediment. Seagrasses and mangroves act as breeding, spawning, hatching and nursing grounds for many marine species, of both lagoon and off-shore origin. Some of these species are important from a "unique biodiversity" point of view, as they migrate between mangroves and coral reefs such as sharks or seahorses (Stafford-Deitsch, 1996), whereas others are socio-economically essential species (Baran, 1999).

The dominant ecological "services" of mangroves are the maintenance of near-shore marine habitats and the concomitant provision of food and refugia to a variety of organisms at different trophic levels (Odum and Heald, 1972). Mangroves also play a major role in maintaining water quality and shoreline stability by controlling nutrient and sediment distributions in estuarine waters (Twilley, 1988).

Mangroves and seagrass beds harbour high densities of juvenile reef fish (see reviews by Parrish 1989, Robertson and Blaber, 1992), acting as nurseries. Therefore they must also be managed in order to sustain yields, since reef fisheries are critical to millions of people world-wide (Munro, 1996). Several hypothesis have been proposed to explain the high abundance of (juvenile) fishes in mangroves and seagrass beds. The hypothesis are based on avoidance of predators, the abundance of food and the interception of fish larvae:

- ♦ The structural complexity of these biotopes provide excellent shelter against predators (Parrish, 1989; Robertson and Blaber, 1992)
- ♦ These biotopes are often located at a distance from the coral reef or from off-shore waters and are therefore less frequented by predators (Shulman, 1985; Parrish, 1989)
- ♦ The relatively turbid water of the bays and estuaries decrease the foraging efficiency of predators (Blaber and Blaber, 1980; Robertson and Blaber, 1992)
- ♦ These biotopes provide a great abundance of food for fishes (Odum and Heald, 1972; Ogden and Zieman, 1977)

- ◆ These biotopes often cover extensive areas and may intercept planktonic fish larvae more efficiently than the coral reef (Parrish, 1989).

The coupling of mangroves to coastal waters is considered to be the most important link in the sustainability of subsistence, commercial and recreational fisheries in estuaries and related near-shore marine habitats (Heywood, 1995).

Human occupation and exploitation of the coastal zone cause profound changes in the configuration and interaction of the major ecosystems of the coastal seascape. Coastal clearing and deforestation for development, construction materials, charcoal and mariculture and destruction of seagrass beds, cause increased runoff of sediments and nutrients inimical to coral reefs. Reef biodiversity is dependant on the accessibility of adjacent ecosystems for feeding areas, nursery grounds, and flows of energy and materials (Ogden, 1987, 1988). The direct human impacts that threaten reefs are nutrient loading (eutrophication), sedimentation and destruction from poor land-use practices, dredging and coral mining (Heywood, 1995).

It is relatively rare for mangroves to be the specific focus of a protected area in the way some marine protected areas focus on habitats such as coral reefs. However, a whole ecosystem approach is needed to ensure the conservation of coastal areas as many species found within mangroves spend part of their lives in seagrass beds and coral reefs (Nagelkerken *et al.*, 2002; Mumby *et al.*, 2004).

I.2 East African mangrove management

I.2.1 General introduction

As East African human populations have grown over recent decades, increasing pressure has been placed on mangrove resources. Simultaneously, mangrove research has boomed, unveiling the importance of the ecological, economic and protective role that mangroves fulfil (Taylor *et al.*, 2003). The mangrove ecosystems of Eastern Africa are well studied, but even the baseline information needed for environmental impact assessments and management plans is still not available. A major problem is that available information is often not disseminated and that research findings are only very slowly incorporated in a management framework (Kairo *et al.*, 2001). Numerous different national languages further hinder dissemination as findings are often confined to their countries of origin.

In East Africa, the major obstacles that have prevented rational uses of mangrove forests have been:

- ◆ the sectorial approach of mangrove resource management
- ◆ lack of community inputs into management efforts
- ◆ low prioritization
- ◆ the poverty status of many indigenous coastal communities
- ◆ a lack of awareness amongst decision makers about the true values of mangroves (Semesi, 1992; Kairo *et al.*, 2001)

Some of the major threats to mangrove ecosystems are listed below.

AQUACULTURE

The capacity of marine and coastal ecosystems to produce fish for human harvest is highly degraded by overfishing, destructive trawling techniques and loss of coastal nursery areas (such as mangroves). Some of the recent increase in the marine fish harvest comes from *aquaculture*, which has more than doubled in production since 1990 (Burke *et al.*, 2001). Aquaculture is an expanding industry in the East African region. The consequences of aquaculture projects for mangrove are well documented from Ecuador, Thailand, Malaysia, Vietnam, Bangladesh and India. In East Africa, where the aquaculture and mariculture operations are just beginning, there are real opportunities to develop mangrove-friendly aquaculture that may be truly sustainable (Kairo *et al.*, 2001). Mangrove degradation due to aquaculture development can be avoided through careful regulation of mangrove felling. Many small-scale, locally managed farms, of low intensity, would be economically and environmentally preferable to a few massive ventures (Taylor *et al.*, 2003).

LOGGING

Mangroves are *logged* for timber which is used locally in construction (Dahdouh-Guebas *et al.*, 2000) and for fuel (Figure 1). Mangroves are used in the construction of fish traps (Figure 2), canoes and rowing sticks (pondos) (Van Tendeloo, 2004; Figure 2) (because mangrove wood is more robust in salt water than other types of wood) and of furniture (see Figure 3), drums and serving dishes (Dahdouh-Guebas *et al.*, 2000). Most villages around mangrove forests construct the majority of buildings from felled mangroves as they are an easily accessible resource. *Rhizophora* species are especially utilized as fuel as they are of high quality, rich in tannin and burn almost smokelessly, imparting a pleasant taste to cooked food. Green *Avicennia marina* logs, however are very smoky and slow burning, so are often used by honey collectors and fishermen to keep away biting insects at night (Dahdouh-Guebas *et al.*, 2000). Cleared mangrove areas are converted in evaporation ponds (shallow brine-filled pits), from which salt can be harvested.

If mangroves are felled, offshore coastal areas, such as coral reefs, receive more sedimentation. Already the effects of excessive nutrient loads and sediment discharge can be seen as breaks forming in fringing reefs opposite river mouths (*e.g.* Mozambique coast). As the extent of mangroves, coastal wetlands, and seagrasses declines, coastal habitats are losing their pollutant-filtering capacity. On a global basis, nutrient inputs to coastal waters seem to be increasing because of population increase and agricultural intensification (Burke *et al.*, 2001).

OIL SPILLS AND OTHER SOURCES OF WATER POLLUTION

Oil is a major pollution threat in the region as there are tanker routes along the East African coast linking the Gulf to the Atlantic Ocean. Many countries lack even basic facilities for handling bilge in their ports and small oil spills are common (Taylor *et al.*, 2003). The effect of oiling can last for many years (Duke *et al.*, 1997). Although large-scale marine oil spills are declining, oil discharges from land-based sources and regular shipping operations are believed to be increasing (Burke *et al.*, 2001). Rivers, streams and mangroves are used as dumping sites for the textile, chemical, paper, sugar and oil industries within the region (Taylor *et al.*, 2003).

CLIMATE CHANGE

The effects of *climate change* will be felt across the region as patterns of rainfall, coastal weather, atmospheric pressure and evaporation adjust. Anticipated effects of climate change are increased temperatures, changes in hydrology regimes, a rise in sea level, increased magnitude and frequency of storms and increased carbon dioxide concentration. Effects of global climate change will be site specific as scenarios are dependent on sedimentation fluxes from river catchments and coastal topography or land composition. As temperatures rise mangroves may start to colonize higher latitudinal areas. A warmer climate may result in an increase in frequency and strength of tropical storms and previously sheltered areas, suitable for mangrove growth, may become exposed. Conversely, any changes in temperature, salinity, storm frequency or precipitation will have effects on flora and fauna composition within mangrove forests (Taylor *et al.*, 2003). Occasional natural hazards may contribute to the reduction in mangrove area; the El-Niño rains of 1997 in Kenya for instance caused siltation and a subsequently massive die-off of adult and young trees within a small *Rhizophora mucronata* stand in Gazi Bay (Dahdouh-Guebas *et al.*, 2004a, in press).

RIVER DIVERSIONS

River diversions deprive tropical coastal deltas of fresh water and silt and result in losses of mangrove species diversity and organic production, and alter the terrestrial and aquatic food webs that mangrove ecosystems support. Regional-scale changes in freshwater surface inflow into mangrove areas have also caused reduction in the secondary productivity of tropical estuarine ecosystems due to the degradations of habitat and water quality of estuarine ecosystems. Changes in the species composition of mangrove communities alter the quality of leaf litter and result in different rates of decomposition and an altered quality of organic matter export to the adjacent estuary (Snedaker, 1989).

1.2.2 The situation in Kenya

Mangroves are well developed in many areas along the Kenyan coast, being particularly concentrated in creeks, bays and estuaries. There are two large permanent rivers reaching the coast: the Tana and the Sabaki (Galana) river, both of which support mangroves (Spalding *et al.*, 1997). There are also a large number of seasonal rivers, and in many of these there is an associated ground water discharge which reduces salinities even when the rivers themselves are dry. To the north of the country, mangroves are well developed in the lee of several islands, notably Lamu, and on the corresponding sheltered coastlines. In the far south, offshore island and fringing reefs also provide a more protected coastline suitable for the development of mangroves (Spalding *et al.*, 1997). Estimates of total area of mangrove forest vary according to different sources. The Kenya Forestry Department lists 644 km², the World Mangrove Atlas lists 961 km² (Spalding *et al.*, 1997), and Ruwa (1993) lists 530 km² of mangrove area. The largest area of mangroves in Kenya is found in Lamu district where lush forests cover more than 300 km². The Kwale, Kilifi, Tana River and Mombasa districts all have mangrove areas. Mangroves have traditionally been exploited by the Swahili coastal people (Spalding *et al.*, 1997).

The threats to mangrove forests are both natural and human-induced. Natural threats include geomorphological dune shifts, diseases in *Sonneratia* and *Rhizophora* and siltations caused by

El-Niño phenomena (Dahdouh-Guebas *et al.*, 2004a, in press). The human-induced stresses are: over-exploitation for poles and firewood (Dahdouh-Guebas *et al.*, 2000), conversion of mangroves to pond cultures, oil pollution, dumping and dredging of waste, and poor land use upstream (Kairo and Dahdouh-Guebas, in prep.).

Mangrove wood is used primarily as timber, and poles are used to make fences, boats, huts and fish traps. Mangroves are also good sources of fuel, either firewood or charcoal, and some have medicinal properties (*e.g. Xylocarpus granatum*) (Van Tendeloo, 2004). Tannins and dyes are often extracted from mangroves and green *Avicennia marina* logs are burnt and used as repellent as the smoky fumes repel mosquitoes and other biting bugs (Dahdouh-Guebas *et al.*, 2000). *Avicennia marina* leaves are also often used as fodder for livestock (Taylor *et al.*, 2003).

The condition of mangrove forests had declined to the extent that export-quality poles to Somalia, Saudi Arabia and other countries in the Middle East (Rawlins, 1957) are no longer found in many areas of Kenya. From 1941 to 1956 there was a massive rise of 47% in mangrove exports (35451 scores at 20 poles per score). Since then deforestation has continued relatively unabated despite an official ban on mangrove exports. In 1992 the Forest Department licensed the removal of 72100 scores of poles from Lamu for domestic use. These extraction recommendations are based more on national demand than resource availability. Good quality wood is rapidly disappearing (Taylor *et al.*, 2003).

Oil pollution has also plagued Kenya in recent decades. Between 1983 and 1993 Mombasa port and surrounding waters experienced 391680 tonnes of oil pollution from spills. A new power-generating plant (Kipevu II) was started up in September 2001 in Mombasa which will likely increase oil waste entering the local marine environment (Taylor *et al.*, 2003). New threats facing mangroves in Kenya include increasing industrial pollution and prawn farming. The number of hotels in Mombasa tripled from 8 in 1971 to 25 in 1993 (Taylor *et al.*, 2003). This growing tourism industry could be a potential environmental threat. Future activities in Kenya which include damming activities upstream of the Tana River that could reduce downstream water flow and alter the current sediment balance, thus affecting coastal aquaculture and farming activities.

A ban on exporting mangroves was implemented in 1978. This ban was lifted in 1981 and reinstated in 1982. In 1996, as Kenyan policies regarding environmental resources were being developed, a proposal to lift the ban arose but the ban was not lifted until 2003. Even when a cutting ban is implemented it remains to be questioned if these regulations are followed by the local people (Van Tendeloo, 2004). Authorization for clearing and any other mangrove exploitation has to be obtained from the Kenya Forestry Department at the Ministry of Environment and Natural Resources. Furthermore all vehicles carrying mangrove poles must have a transit permit and timber statement. These regulations have made subsistence use of mangroves gradually more difficult. And to further complicate the situation, conflicting issues of indigenous rights and property ownerships make felling by local human populations even more problematic. Restricting access through changes in property rights has been shown elsewhere to increase poverty (Reddy and Chakravarty, 1999).

Land use change and soil erosion in semi-arid river basins of Kenya result in increased supply of terrigenous sediments into mangrove wetlands. This supply is usually within the range that can be tolerated by the mangrove forests and in moderate volumes is usually essential in substrate accretion which helps mangrove wetlands to keep pace with sea level rise (Wolanski

et al., 2001). However, in periods of high sediment supply, particularly those associated with extremely high river discharges, enormous volumes of terrigenous sediment are usually discharged into mangrove wetlands. Observations in mangrove wetlands of Kenya shows that this can result in the degradation of the mangrove forest wetland if sedimentation is heavy and far above the limit that can be tolerated. Heavy siltation blocks the breathing roots of mangroves and raises the elevation of wetland so that inundation during flood tide is restricted within zones fringing the tidal inlets and the main channel (Kitheka, 1998).

Because of the degraded status of most mangrove forests in Kenya, there is a strong need for a national Mangrove Management Plan. Such a plan should provide accurate annual allowable cuts, designate specific cutting areas and emphasise the need and importance of maximum utilisation and adequate control (Kairo and Dahdouh-Guebas, in prep.). Numerous recommendations have been put forward concerning the direction and steps to be taken towards a mangrove management plan and a sound forestry management scheme to enable sustainable exploitation of the mangrove resources (Kenya Forestry Master Plan 1994). However, few of these, if any, have been implemented to date (Dahdouh-Guebas *et al.*, 2000; Kairo *et al.*, 2001). It is recommended by Kairo and Dahdouh-Guebas (in prep.) that high-resolution remote sensing technology and GIS should be used to obtain reliable estimates of the area occupied by mangroves in Kenya.

I.3 Remote sensing of mangroves

I.3.1 General

Habitat maps derived using remote sensing (RS) technologies are widely being used to assess the status of coastal natural resources, as a basis for coastal planning, and for the conservation, management, monitoring and valuation of these resources (Green *et al.*, 2000). Mangrove areas, especially the interior of mangrove stands, are often difficult to access. RS allows information to be gathered from areas that would otherwise be logistically and practically very difficult to survey (Green *et al.*, 2000).

Mangrove habitat maps have been used for three general management applications: resource inventory, change detection and the selection and inventory of aquaculture sites. Green *et al.* (2000) summarize the sensors and image processing techniques which have been used for habitat mapping of mangroves. According to the authors there are five main categories of image processing techniques appropriate for mangrove mapping: visual interpretation, vegetation indices, unsupervised classification, supervised classification and principal components analysis of band ratios. The most common sensors used are Landsat TM and SPOT XS, but also aerial photography was probably extensively used since the 1920's (published accounts are scarce). The most important information derived from image processing are the location of the boundaries, areas of clearance and mangrove density. Their study reveals that only 12% of the publications includes an assessment of accuracy of the classification.

I.3.2 Research by APNA

Within the Biocomplexity Research Team of the laboratory of General Botany and Nature Management (Algemene Plantkunde en NATuurbeheer, APNA) of the VUB, both MSc., PhD

theses and articles have been written on remote sensing of mangrove areas. A brief overview of the most recent research on the topic of remote sensing is given below.

Dahdouh-Guebas (2002) reviews the importance of remote sensing and GIS in the sustainable development and management of tropical coastal ecosystems (mangroves, as well as coral reefs and sea grass beds). It shows how remote sensing technology and other scientific tools can be integrated in long-term studies, both retrospective and predictive, in order to anticipate degradation and take mitigating measures at an early stage. It is also stipulated that there is a need to integrate findings collected over longer periods in a GIS environment with the aim of prediction.

Verheyden *et al.* (2002) investigated the applicability of aerial photographs in the monitoring of mangrove vegetation dynamics in Sri Lanka (Galle, Rekawa and Pambala). Aerial photographs proved to be very useful for the creation of genus-based vegetation maps. The designed interpretation keys for individual trees (based on grey values, texture, crown form and size and the presence or absence of a shaded side) and for the generic compositions of species assemblages (based on structure, *i.e.* distribution of individual trees) showed basic differences between locations. It was therefore concluded that the interpretation keys should only be used at a specific location or in mangrove areas with similar floristic composition. Although the qualitative analysis of the photographs (dominant genera, delineation of assemblages) was very satisfactory, the quantitative (relative density) did not give good results. The identification of mangrove trees on species level could not be achieved.

Van Hiel (2002) and Pycke (2003) focussed on the possibility of mangrove assemblage identification using very high resolution (VHR) IKONOS satellite images (Chilaw Lagoon, Sri Lanka) as compared to aerial photographs. Van Hiel (2002) investigated different image combinations and spectral enhancement procedures for maximal visual interpretability and concluded that texture and structure are best derived from the pansharpened multispectral false colour composite. The latter together with the greenness, brightness and yellowness MSS Tasselled Cap bands and the first three principal component bands composite resulted in images with a high colour contrast and were found to be of great help in visually delineating “objects” with a different appearance than its surrounding. These “objects” were compared with vegetation maps of the area (based on an aerial photograph of 1994). Only three categories in the mangrove vegetation could be labelled as “genus *x* dominated assemblages”, possibly due to the large time gap between acquisition of the aerial photograph (1994) and the satellite image (January 2002). In addition, a preliminary study of automated image classification was done and the Bayesian decision rule in supervised classification was considered best, but it was noted that the lack of reliable and up-to-date ground truth data hampered the classification. It was concluded that the IKONOS satellite image (multispectral data with low spatial resolution) was a good substitute for aerial photography (higher spatial resolution panchromatic data).

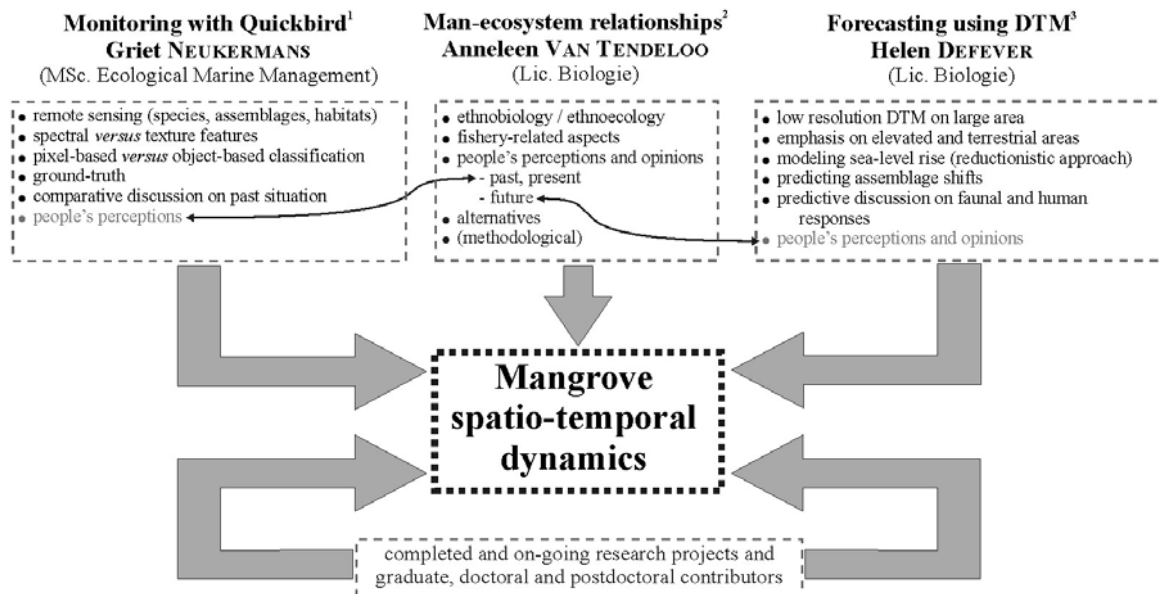
Ground truthing of the IKONOS satellite image was done in October-November 2002 and the automated analysis was further investigated by Pycke (2003). Supervised classifications using the Bayesian decision rule were performed on the pansharpened multispectral images and on the MSS Tasselled Cap images of different subsets of Chilaw Lagoon, Sri Lanka. The assemblages present on the vegetation map of 1994 could be recognized on the classified images.

Supervised classification allowed a distinction between two congeneric species (*Rhizophora apiculata* and *R. mucronata*) (Daoudou-Guebas *et al.*, 2004b, in press) and corresponded well with the visual interpretation of the enhanced satellite image. In conclusion, IKONOS imagery is a valuable tool in the early detection of mangrove degradation in which floristic composition is as important as areal extent.

I.4 Research objectives

I.4.1 The Gazi Bay project 2003-2004: thesis interactions

Thesis interactions within wider research framework (postdoctoral supervisors and VLIR-IUC programme)



AQUATIC ecology for environmental management in Kenya Project research areas and objectives :

1. To investigate the spatio-temporal change in composition and biodiversity of mangrove vegetation by means of remote sensing
2. To investigate the interactions between man, fauna, flora and environment in natural mangroves (impact of subsistence and commercial use of natural sources from mangroves by man)
3. To investigate the response of marine fauna and flora of mangroves to anthropogenic induced changes (sea-level rise)

Figure 4. Thesis interactions within wider research framework (post-doctoral supervisors and VLIR-IUC programme)

Defever (2004) investigated the possible effects of sea level rise on the mangrove ecosystem of Gazi Bay, in particular assemblage shifts, using a Digital Terrain Model (DTM). Mangrove species maps produced through supervised classification of satellite imagery (done in this thesis work) were used to relate the presence of mangrove species to inundation classes and to predict the spatial distribution of mangroves as a consequence of sea level rise.

Van Tendeloo (2004) interviewed the people of Gazi Bay and neighbouring villages to analyze their perceptions and opinions on the past, present and future of the mangrove forest of Gazi Bay and to describe the uses of the mangrove by the local people. The preference of a certain mangrove species used by the local people for various purposes can be compared to its availability using mangrove species maps.

I.4.2 This thesis work

The two main research objectives of this thesis work involve firstly, to improve the visual interpretability of the satellite image and secondly, to automate the process of vegetation assemblage delineation and species recognition. Different image enhancement techniques offered by ERDAS Imagine 8.6 Professional will be used to improve the visual interpretability of the image. Different classification approaches (per-pixel hard and soft classification) will be tested.

The research objectives of this thesis work are:

1. Spectrally and spatially enhance the satellite image to ease visual interpretability
2. Visually delineate vegetation assemblages on an enhanced satellite image
3. Ground-truth the assemblages (using PCQM)
4. Classify the satellite image at mangrove species level incorporating NDVI and texture measures
5. Automate assemblage delineation and compare with visual delineation of assemblages
6. Determine the classification accuracy using ground-truth PCQM data.

A schematical representation of the steps involved in image enhancement, visual image interpretation and assemblage delineation is shown in Figure 5. The scheme in Figure 6 represents the steps involved in image classification, classification accuracy assessment and automated assemblage delineation.

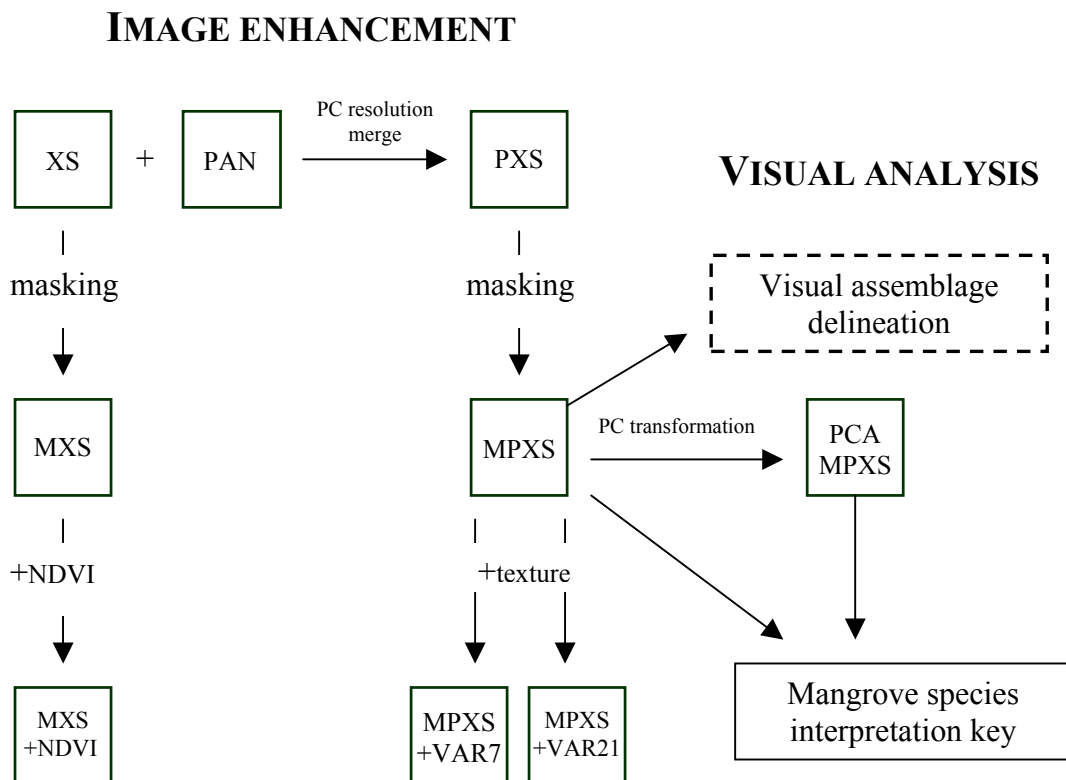


Figure 5. Schematical representation of the steps involved in image enhancement and visual analysis

IMAGE CLASSIFICATION

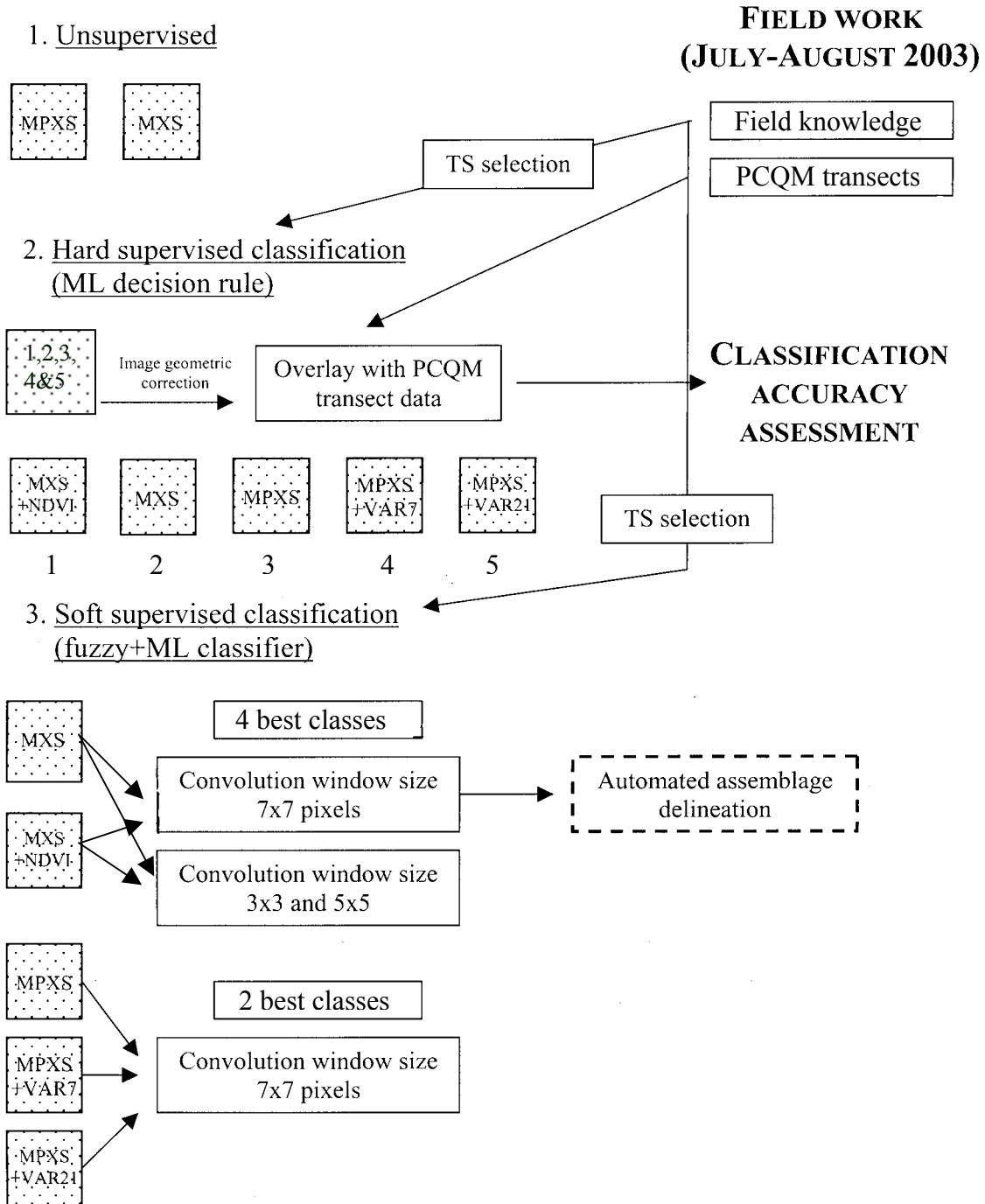


Figure 6. Schematical representation of the steps involved in image classification, classification accuracy assessment and automated assemblage delineation

II Literature review

II.1 Remote sensing

Remote sensing, according to Lillesand and Kiefer (1994), is defined as

“the science and art of obtaining information about an object, area or phenomenon through the analysis of data acquired by a device that is not in contact with the object, area or phenomenon under investigation”

Remotely sensed image data is widely used in a range of oceanographic, terrestrial, and atmospheric applications, such as land cover mapping, environmental modelling and monitoring, and the updating of geographical databases (Tso and Mather, 2001). Remote sensing makes use of sensors installed on aircraft or satellites to detect electromagnetic energy scattered from or emitted by the earth's surface. This energy is associated with a wide range of wavelengths, forming the electromagnetic spectrum (Figure 7). Wavelength is generally measured in micrometers (μm). Discrete sets of continuous wavelengths (called wavebands) have been given names such as the microwave band, the infrared band, and the visible band (Tso and Mather, 2001). Optical remote sensing systems (such as Landsat TM and MSS, SPOT HRV, NOAA AVHRR, IKONOS and QuickBird) acquire data in the visible portion of the electromagnetic spectrum and rely on the reflected sunlight as a source of radiation. An increasing amount of valuable environmental and resource information is obtained from radar (radio detection and ranging) images. This imagery is acquired by sensors operating in the microwave portion of the spectrum (1mm to 1m) and is unimpaired by atmospheric effects such as light, rain, dust and clouds. The backscattered radar signal is sensitive to the dielectric (amount of water, soil volume, plant canopy) and geometric properties (size, shape, orientation and volume) of the observed object. Examples of such sensors are ERS (European Remote Sensing Satellite), RADARSAT, ENVISAT and JERS (Japanese Earth Resources Satellite) SAR (Synthetic Aperture Radar).

In this research the object under investigation is a mangrove forest, the remote sensing device is the QuickBird satellite and the remotely collected data are data on variations in electromagnetic energy distributions.

Image interpretation is the process where remotely collected data are analysed to obtain information about the object, area or phenomenon. Sensors are used to record variations in the way earth surface features reflect and emit electromagnetic energy in different regions of the electromagnetic spectrum (Figure 7).

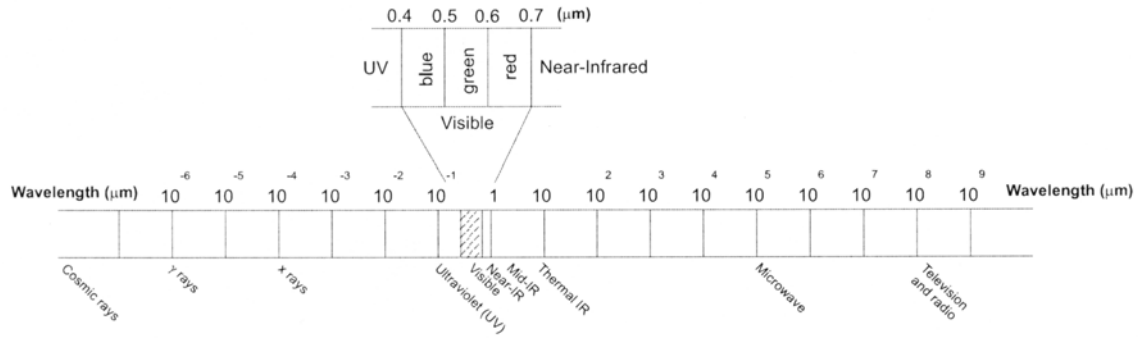


Figure 7. The electromagnetic spectrum (Lillesand and Kiefer, 1994)

When electromagnetic energy, coming from the sun, is incident on any given earth surface feature, various fractions of energy are either reflected, absorbed and/or transmitted. The proportions of energy reflected, absorbed and transmitted will vary for different earth features at different wavelengths, depending on their material type and condition. These differences permit us to distinguish different features in an image. Average reflectance curves for healthy green vegetation, dry bare soil and clear lake water for example are very distinct (Figure 8). The fact that actively growing vegetation appears green is caused by the slight reflectance peak between 0.5 and 0.6 μm (Mather, 1999). The valley in the spectrum around 0.65 μm for healthy green vegetation is due to absorption by chlorophyll pigments (Lillesand and Kiefer, 1994). As we go from the visible to the near-infrared portion of the spectrum at about 0.75 μm , the reflectance of healthy vegetation increases dramatically (this is the so called “red edge”). Plant reflectance in the range 0.75 μm to 1.35 μm results primarily from the internal structure of plant leaves (Lillesand and Kiefer, 1994; Mather, 1999). Because this structure is highly variable between plant species, reflectance measurements in this range often permit us to discriminate between species, even if they look the same in the visible wavelengths. Between 1.35 μm and 2.5 μm internal leaf structure has some effect, but the reflectance is largely controlled by leaf-tissue water content, which is the cause of the minima recorded near 1.45 μm and 1.95 μm (Mather, 1999). As the plant ages, the level of reflectance in the near-infrared region (0.75-1.35 μm) declines first, with reflectance in the visible part of the spectrum not being affected significantly. It is important to note that the near infrared reflectance increases with the number of layers of leaves in canopy. The factors that influence soil reflectance act over less specific spectral bands. These factors can be moisture content (presence of moisture will decrease its reflectance), soil texture (proportion of sand, silt and clay), surface roughness, organic matter content, *etc.* (Lillesand and Kiefer, 1994). The most distinctive characteristic of the water spectral reflectance curve is the total energy absorption at near-infrared wavelengths.

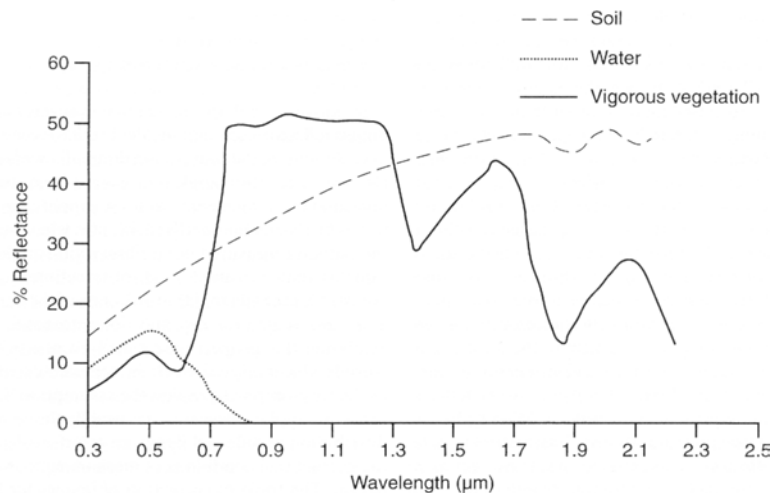


Figure 8. Typical reflectance curves for soil, vegetation and water (Mather, 1999)

II.2 Air-borne and space-borne imagery (photographs and digital imagery)

The first vegetation maps made with the help of remote sensing were based on visual interpretation of aerial photographs. The basic mapping scenario involves delineation of homogeneous patches, or stands of vegetation, for which labels are provided concerning the properties of the vegetation within the polygon. Typical vegetation properties include the overall life form of the vegetation, dominant species, height and density of the vegetation, and the presence and nature of understory vegetation. Vegetation properties can be inferred from the tone, colour, shape, texture, pattern, site, context and association observed in the aerial photograph (Estes *et al.*, 1983; Verheyden, 1997; Verheyden *et al.*, 2002) based on the knowledge of the interpreter and augmented with field visits to the area being mapped.

Photo-interpretation is easy to understand and can be performed using relatively inexpensive equipment but is both very time-consuming and suffers from the subjectivity of the interpreter, meaning that the outputs of visual interpretation will be as good or bad as the interpreter, and will vary from interpreter to interpreter (Green *et al.*, 2000). Another important point to make is that it is difficult to compare visually interpreted products (*e.g.* for the purpose of change detection) because differences may be attributable to inconsistencies in interpretation rather than real changes on the ground (Green *et al.*, 2000).

The strong reliance of air photo interpretation on the skill and experience of the interpreter is both the strength and weakness of this approach to vegetation mapping. In general, digital analysis of satellite imagery cannot match the quality of vegetation maps derived from outstanding air photo interpretation (Woodcock *et al.*, 2002). But outstanding air photo interpretation requires high expertise of the interpreter and is very time consuming (in part due to digitisation).

It is argued by Green *et al.* (2000) that a skilled interpreter can distinguish about 30 grey tones in a panchromatic image and many more different hues in a colour image. However each pixel may represent 2^{24} unique spectral signatures (3 bands at 8-bit resolution). The human eye is incapable of distinguishing this number of tones and hues. Furthermore, a colour image is displayed on a screen by projecting 3 bands through the red, green and blue guns of the

monitor. If other bands are available (*i.e.* in imagery which has more than 3 bands), they cannot be displayed and are not analysed by the interpreter whose decisions are dependant upon the bands selected. Visual interpretation therefore does not come close to utilizing the full information content of an image. This can only be achieved using statistically based digital processing: digital image classification (Green *et al.*, 2000).

Digital imagery such as satellite imagery can easily be processed by a computer, and classification can be automated using computer classification algorithms (classifiers or decision rules). While photographic systems are limited to the spectral range 0.3 μ m to 0.9 μ m in relatively wide wavelength bands, multispectral scanners (MSS), acquiring data simultaneously in several spectral bands, extend the range of sensing from 0.3 μ m to approximately 14 μ m (Lillesand and Kiefer, 1994). Furthermore, MSS systems can sense in very narrow spectral bands, including the ultraviolet, visible, near-infrared, mid-infrared and thermal spectral regions.

The advantage of aerial photographs is on the one hand their very high spatial resolution (up to 20cm) as compared to satellite images and on the other hand their availability over a much larger time range. Over the past few decades the spatial resolution of public available satellite imagery has improved and reached a level at which it challenges the spatial resolution of air-borne imagery for the first time (Dahdouh-Guebas, 2002).

IKONOS, the first commercial very high resolution (VHR) Earth Observation Satellite, launched in September 1999 by Space Imaging (US), provides both panchromatic and multispectral images with a 1m to 4m resolution. The QuickBird satellite, launched in October 2001, is at the forefront of commercial satellite imagery acquisition, with panchromatic imagery of 0.7m spatial resolution and multispectral imagery of 2.8m spatial resolution.

The high temporal resolution of space-borne imagery (revisit time of 1-3 days for QB), in contrast with air-borne imagery, marks another milestone in remote sensing technology. The main disadvantage of some of the new remote sensing technologies such as IKONOS and QuickBird are the very high prices charged that prevents the scientific community to access these data (Dahdouh-Guebas, 2002).

II.3 Digital image processing

Digital image processing involves the manipulation and interpretation of digital images with the aid of a computer, in contrast to visual interpretation, which solely makes use of the ability of the human mind to qualitatively and intuitively evaluate spatial patterns in an image and which is sensitive to subjective judgement of the analyst. The four steps involved in digital image processing as summarized from Lillesand and Kiefer (1994) are given in Table 1.

Table 1. Digital image processing steps (summarized in part from Lillesand and Kiefer, 1994)

Processing step	Aim	Example
1. Image rectification and restoration (see section II.4)	Correct disorted or degraded image data	Correction of geometric distortion, radiometric calibrations and noise removal
2. Image enhancement (see section II.5)	More effectively display or record the data	Spatial: resolution merge Spectral: PCA, false colour composites
3. Image classification (see sections II.6-II.10)	Replace or assist visual analysis with automated techniques in identifying image features	Supervised classification, unsupervised classification
4. Data merging and GIS integration	Combine image data for a given geographic area with other geographically referenced data for that area	Overlay with fieldwork data

A colour image is composed of different channels or bands. Each band is a two-dimensional array of picture elements, called pixels. The intensity of each pixel corresponds to the average brightness or radiance (converted into a digital number, DN) measured electronically over the ground area corresponding to each pixel. The DN range depends on the bit depth of the image. For an 11-bit image (e.g. IKONOS, QuickBird) the DN range is 0 to 2047. This means that 2048 (2^{11}) different values can be stored in one pixel. If an image is viewed in grey tones, 0 corresponds to black, 2047 corresponds to white, and all levels in between correspond to different shades of grey.

Most computer screens use the RGB colour system, which has three colour guns: red, green and blue. These screens use a total of 24 bits for each pixel in an image: this corresponds to 8 bits for red, green and blue, indicating a range of 256 possible intensities for each of those basic colours. Displaying a three-dimensional image can be done by displaying each of the channels in a different colour gun. Once the dimensionality of the image exceeds three, not all layers can be displayed at the same time.

II.3.1 Feature space

To be able to compare separate images pixel by pixel, the pixel grids of each image must conform to the other images in the database. *Registration* is the fitting of the coordinate system of one image to that of a second image of the same area. Now consider an image composed of n co-registered layers or bands. These layers may represent different features such as brightness values measured in different wavebands of the electromagnetic spectrum, texture, context, slope, elevation *etc.* Each pixel in the image contains a digital number (DN) in each layer representing a feature measurement. Each pixel can be referred to by its spatial row and column coordinates, but we can also think of that pixel as a vector in a n -dimensional space, where the values on the axes represent the DN values of each of the n layers (bands)

composing the image. The principle of representing a pixel in a three-layered image as a vector in feature space is illustrated in Figure 9.

Feature space is a very natural and important concept in image classification, as the classification (also called pattern recognition) process involves the subdivision of feature space into homogeneous regions separated by decision boundaries, determined by a statistical rule called decision rule or classifier. The feature vector (or pattern) for each pixel in the image to be classified will be assigned a certain class, if it meets certain statistical criteria that should be fulfilled in feature space.

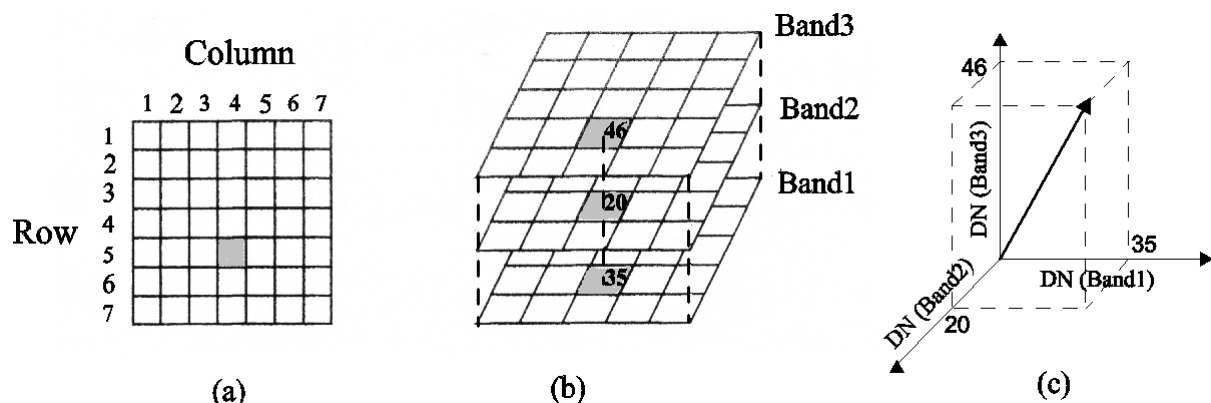


Figure 9. Feature space concept. (a) shaded pixel (5,4) image coordinates in the 7x7 pixels image, (b) DN values of the shaded pixel in each image band, (c) representation of the pixel in feature space (adapted from Tso and Mather, 2001)

II.4 Geometric correction

According to Mather (1999) geometric correction is the transformation of a remotely-sensed image so that it has the scale and projection properties of a map. Remotely sensed images contain both systematic and non-systematic geometric errors, that can be subdivided into two classes: those that can be corrected using data from platform ephemeris and knowledge of internal sensor distortion (*e.g.* scan skew, mirror-scan velocity non-linearities, panoramic distortion, spacecraft velocity, earth curvature) and those that cannot be corrected with acceptable accuracy without a sufficient number of ground control points (*e.g.* sensor system attitude and altitude) (Jensen, 1986). A *ground control point* (GCP) is a well defined and easily recognizable feature (*e.g.* intersection of roads) that can be located accurately on a map (measured in degrees of latitude and longitude or in meters easting and northing) and on the corresponding image (measured in rows and columns). The two geometric corrections most often used by earth scientists to make the remotely-sensed data truly useful are geometric rectification and geometric registration (Jensen, 1986).

Rectification is the process by which the geometry of an image area is made planimetric (Haralick *et al.*, 1973). This process almost always involves relating GCP pixel coordinates (row and column) with their map coordinate counterparts (*e.g.* easting and northing). Rectification is required when accurate area, direction and distance measurements are required (Jensen, 1986) or when information extracted from remotely-sensed images is to be integrated with map data in a geographical information system or presented to consumers in a map-like form (ERDAS Field Guide, 2002).

Image registration is the translation and rotation alignment process by which two images of like geometries and of the same set of objects are positioned coincident with respect to one another so that corresponding elements of the same ground area appear in the same place on the registered images (Haralick *et al.*, 1973). This is often done when the geometric precision obtained by the rectification process is not desired.

Georeferencing refers to the process of assigning map coordinates to image data. The image data may already be projected onto the desired plane, but not yet referenced to the proper coordinate system. Rectification involves georeferencing, since all map projection systems are associated with map coordinates. Georeferencing can be done without rectifying if there is no distortion in the image (ERDAS Field Guide, 2002).

In image rectification two basic operations must be performed:

1. *Spatial interpolation*: establishing the geometric relationship between the input pixel location (c,r) and the associated map coordinate of this same point (n,e) . This will determine the nature of the geometric coordinate transformation that must be applied to rectify or relocate every pixel in the original input image to its proper position in the rectified output image.
2. *Intensity interpolation or resampling*: determining the pixel brightness values (or DNs) in the output image through interpolation from the original input image.

Let (n_i, e_i) be the map coordinates (reference/output coordinates, *e.g.* given in northing and easting) of the i^{th} GCP and let (c_i, r_i) be its image coordinates (source/input coordinates, given in row and column number). Spatial interpolation involves finding a method to transform (n, e) to (c, r) and vice versa. This is mathematically stated as finding a solution for the two coordinate transformation equations:

$$c = f_1(n, e)$$

$$r = f_2(n, e)$$

where f_1 and f_2 are the transformation functions (Lillesand and Kiefer, 1994). The GCP values for these equations are submitted to a least-squares regression analysis to determine coefficients for the two coordinate transformation equations. The values found are put in a transformation matrix. The size of the matrix depends upon the order of transformation. Consider for example the case where the input coordinates can be expressed as a first order polynomial function of the output coordinates:

$$c = a_0 + a_1n + a_2e$$

$$r = b_0 + b_1n + b_2e$$

In this case the transformation matrix consists of 6 unknown parameters a_0, a_1, a_2, b_0, b_1 and b_2 . The goal in calculating the coefficients of the transformation matrix is to derive the polynomial equations for which there is the least possible amount of error when they are used to transform the reference coordinates of the GCPs into the source coordinates (Lillesand and Kiefer, 1994).

A first order polynomial function can accomplish scaling, rotation, shearing and reflection but not warping. A higher order polynomial can be used to correct non-linear distortions (also known as rubber sheeting). The polynomial method does not correct for relief distortions and is therefore only applicable to relatively flat areas (ERDAS Field Guide, 2002). In mathematical terms we need to take a minimal sample of n GCPs where n is the number of coefficients in the polynomial expression. For a first order polynomial, n is 3. For a second order polynomial, n is 6 *etc.* In general, the minimum number of points required to perform a transformation of order t equals

$$\frac{(t+1)(t+2)}{2}$$

(ERDAS Field Guide, 2002). These sizes are necessary purely and simply to ensure that it is possible to evaluate the equations defining the unknown coefficients. It is important to note that the statistical requirement, which is concerned with the reliability of the results, sets a much higher standard. Most conventional statistics texts suggest that a sample size of at least 30 is required to achieve reliable estimates, but experience suggests that 10-15 GCPs will give acceptable results for a first order fit and a small image area. The second aspect of sampling that should concern users is the spatial distribution of ground control points. GCPs should be evenly spread, as far as possible, over the image area. The accuracy with which GCPs are measured is also very important (Mather, 1999). Before applying the rectification to the entire set of data, it is important to determine how well the coefficients derived from the least-squares regression of the initial GCPs accounts for the geometric distortion in the input image (Jensen, 1986). The method used most often involves computation of the root mean square (RMS) error for each of the GCPs. RMS error (expressed as a distance in the units of the source coordinate system) is the difference between the desired output coordinate for a GCP and the actual output coordinate for the same point, when the point is transformed with the geometric transformation (ERDAS Field Guide, 2002). ERDAS Imagine calculates the X residual (distance between the source and retransformed coordinates in X direction) R_{x_i} , the Y residual (distance between the source and retransformed coordinates in Y direction) R_{y_i} and the RMS error R_i for each GCP with the following formulas:

$$R_{x_i} = x_r - x_i \qquad R_{y_i} = y_r - y_i \qquad R_i = \sqrt{R_{x_i}^2 + R_{y_i}^2}$$

where x_r and y_r are the retransformed coordinates and x_i and y_i are the input coordinates. R_i represents a measure of the accuracy of the corresponding GCP in the image (Jensen, 1986). Total RMS error (T), the X RMS error (R_x), the Y RMS error (R_y) are calculated from these values with the following formulae:

$$R_x = \sqrt{\frac{1}{n} \sum_{i=1}^n R_{x_i}^2} \qquad R_y = \sqrt{\frac{1}{n} \sum_{i=1}^n R_{y_i}^2} \qquad T = \sqrt{R_x^2 + R_y^2}$$

A normalized value representing each point's RMS error in relation to the total RMS error is the error contribution C_i of each point and is calculated from

$$C_i = \frac{R_i}{T}$$

Normally, the user specifies a certain amount of acceptable total RMS error (T). If an evaluation of T reveals that a given set of GCPs exceeds this threshold, it is common practice to delete from the analysis the GCP with the greatest amount of individual error, recompute the regression coefficients and recompute T until T is less than the threshold specified or until too few points remain to perform a least-squares regression (Jensen, 1986). Although it may seem sensible to eliminate GCPs that have high residual values, Morad *et al.* (1996) show that this is not necessarily the case. Instead of eliminating GCPs one should seek for the causes for the error, which may be the result of erroneous or inaccurate measurement.

The transformation equations (given above) specify how to determine the source coordinates from the reference coordinates, instead of determining the reference coordinates from the source coordinates (as it would be intuitively). First an output matrix of “empty” map cells is defined and then each cell is filled in with the DN(s) of the corresponding pixel(s) in the original image. After producing the transformation function (using least-squares method), the resampling or intensity interpolation process is used to determine the pixel values to fill into the output matrix (map coordinates) from the original image matrix (column, row coordinates). First the coordinates of each pixel centre in the output matrix (e,n) are transformed to determine their corresponding location in the original matrix (c,r). If c and r are integers it would be possible to take the pixel value at (c,r) and transfer it to the corrected image. However, c and r are most likely not integers and this implies that the corrected pixel centre lies between the columns and rows of the uncorrected image, so that a method of interpolation is needed to estimate the pixel value at (c,r). Thus, secondly, the intensity value (DN) eventually assigned to a cell in the output matrix is determined on the basis of the pixel values that surround its transformed position in the original input matrix (Mather, 1999). A number of different resampling schemes can be used to assign the appropriate DN to an output cell or pixel. Three methods are in common use:

1. *Nearest neighbour*: takes the DN of the input (source) pixel that is closest to the computed (c,r) coordinates (pixel a in Figure 10). This method has the advantage of being computationally fast and simple and avoids having to alter the original input pixel values (Lillesand and Kiefer, 1994). A disadvantage is that it tends to produce a rather blocky effect as some pixel values are repeated (Mather, 1999).
2. *Bilinear interpolation*: takes a distance-weighted average of the DNs of the four nearest pixels (pixels a and b in Figure 10). This method is simply the two-dimensional equivalent to linear interpolation and results in a smoother output image because it is essentially an averaging process. Thus sharp boundaries may be blurred in the output image. The computational time requirements are greater than those of the nearest-neighbour method.
3. *Cubic convolution*: based on the fitting of two third-degree polynomials to the region surrounding the point (c,r). The 16 nearest pixel values in the input image are used to estimate the value at (c,r) (pixels a, b and c in Figure 10). This method gives the most naturally looking image, without the blockiness of the nearest-neighbour or the over-smoothing of the bilinear method (Mather, 1999). The most important disadvantage is the considerably higher computational cost.

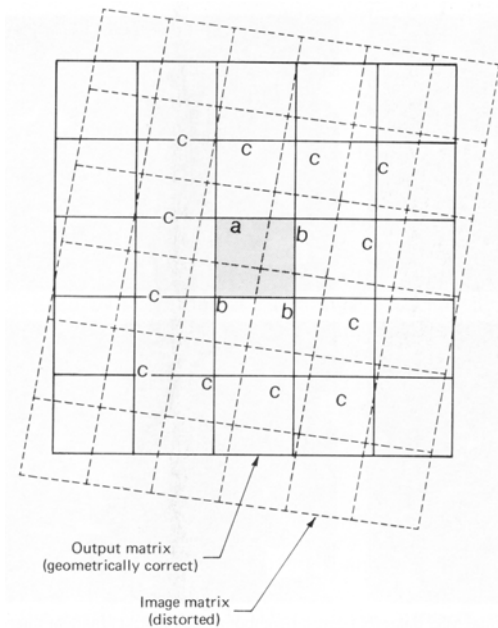


Figure 10. Grid of geometrically correct output pixels (full line) superimposed on grid of original distorted input pixels (dotted line) (Lillesand and Kiefer, 1994)

Although some of the interpolation algorithms are highly reliable, some spectral integrity of the data can be lost during rectification. Consequently, an unrectified image is more spectrally correct than a rectified image. Some analysts recommend classification before rectification, since the classification is then based on the original data values (ERDAS Field Guide, 2002).

In ERDAS Imagine Nearest Neighbour resampling is the only option for resampling thematic files. Images can be rectified on the display or on the disk. Display rectification (also termed calibration) is temporary, but disk rectification is permanent, because a new file is created.

II.5 Image enhancement

II.5.1 Principal component transformation

The transformation of the raw remote sensing data using Principal Component Analysis (PCA) can result in new images that are often better interpretable than the original data (Kaneko, 1978; Byrne *et al.*, 1980). PCA can also be used to reduce the dimensionality of the data, which is a problem frequently encountered in the analysis of multispectral image data. Multiband visible/near-infrared images of vegetated areas will show negative correlations between the near-infrared and visible red bands and positive correlations among the visible bands because the spectral characteristics of vegetation are such that as the vigour or greenness of the vegetation increases the red reflectance diminishes and the near-infrared reflectance increases (Mather, 1999).

To perform PCA, we apply a linear transformation to a correlated set of multispectral data. The application of this transformation to the correlated remotely sensed data will result in an uncorrelated multispectral data set that has certain ordered variance properties. The data along the first principal component (PC) have a greater variance or dynamic range than the data

along the second principal component *etc.* Because successive components are chosen to be orthogonal to all previous ones, the data they contain are uncorrelated (Jensen, 1986).

Let n be the number of bands, M the multi-band image mean and X the individual pixel value vector. The coefficients for the principal component transformation are computed from the original spectral covariance matrix, which is of dimension $n \times n$:

$$C = \frac{\sum_{j=1}^m (X_j - M)(X_j - M)^T}{m - 1},$$

where m is the number of pixels and T denotes the transpose function.

The calculation of the eigenvectors and eigenvalues of the covariance matrix is achieved by solving the equation

$$(C - \lambda_i I)A_i = 0$$

where $A_i = (a_1, a_2, \dots, a_n)^T$ is the eigenvector corresponding to the eigenvalue λ_i and I is the identity matrix.

The eigenvalues are in fact the variances of the principal components, which determine the percent of total variance explained by each of the principal components, $\%_p$, using the equation:

$$\%_p = \frac{\lambda_p}{\sum_{i=1}^n \lambda_i} \times 100$$

The eigenvectors determine the orientation and the length of the PC axis in the n -dimensional space.

II.5.2 Vegetation indices

One of the most common indices used in studies of vegetation status is the Simple Ratio (SR; Jordan, 1969): the ratio of the near-infrared to the equivalent red band value for each pixel location. This ratio exploits the fact that vigorous vegetation strongly scatters solar radiation in the near-infrared (0.7–1.0 μ m) because of the air-water interfaces between intercellular spaces and cell walls which cause multiple refraction (Jensen, 1983), and absorbs radiation in the red waveband (0.6–0.7 μ m) due to the presence of chlorophyll and other absorbing pigments in leaves. The resulting image gives a visual impression of variation in biomass and in green leaf area index as well as the state of health of plants (Mather, 1999). The SR is found to be a sensitive indicator of the presence and condition of green vegetation (Lillesand and Kiefer, 1994).

The normalized difference vegetation index (NDVI; Rouse *et al.*, 1973) is defined in terms of the reflectance in near-infrared (ρ_{NIR}) and red (ρ_R) bands as:

$$NDVI = \frac{\rho_{NIR} - \rho_R}{\rho_{NIR} + \rho_R}$$

The NDVI is not affected by the absolute pixel values in the near-infrared and red bands in contrast to the SR index. The NDVI is preferred to the SR index because the NDVI helps compensate for changing illumination conditions, surface slope, aspect, and other extraneous factors (Lillesand and Kiefer, 1994).

McDonald *et al.* (1998) investigated the coniferous forest information content of some selected spectral vegetation indices using reflectance models. Besides their sensitivity to biophysical parameters of vegetation (such as leaf-area index, biomass and photosynthetic activity), these vegetation indices are also sensitive to changes in soil reflectance and to atmospheric effects. Many indices have been developed to minimize each of these effects. To minimize sensitivities to changes in soil reflectance the perpendicular vegetation index (PVI) and the (transformed) soil adjusted vegetation index ((T)SAVI) were developed. The global environment monitoring index (GEMI) and the atmospherically resistant vegetation index (ARVI) were designed to minimize the effect of the atmosphere on the measurement of biophysical parameters. Relevant conclusions are listed below:

- ♦ the SR and NDVI are strongly influenced by soil reflectance
- ♦ increases in atmospheric turbidity importantly lowers the SR and NDVI values
- ♦ SR and NDVI values increase with increasing crown cover and the increase is not linear, but rather sigmoidal
- ♦ indices should be selected according to the site under investigation since no single index performs well over all degrees of crown coverage
- ♦ at high crown covers (>50%) SR and NDVI were the most sensitive indices to changes in crown cover
- ♦ for multitemporal studies, where variation in atmospheric parameters is to be expected, the use of SR and NDVI is not recommended unless atmospheric correction can be accurately performed.

II.5.3 Multiresolution merging

Multiresolution merging is a technique to combine the high spatial resolution of panchromatic data with the high spectral resolution of multispectral data. When such a merging is performed it is important that the operation maintains as much of the original spectral information as possible while maximizing the amount of spatial information from the high resolution data.

Different methods can be used to merge high spatial and high spectral resolution images. We will briefly discuss the principal component resolution merge, the Brovey transform and the multiplicative merge method, offered by ERDAS Imagine software. Other transformations such as the RGB-HIS-RGB transformation, can also be used.

In the (forward-reverse) principal component (PC) resolution merge method a PC transformation is applied to the multispectral images. The first PC is assumed to represent overall scene luminance. The high spatial resolution image is remapped onto the first PC so that it has the same numerical data range and so that its histogram shape is preserved. The first PC is replaced by these data, before the reverse transformation is performed (Chavez *et al.*, 1991). The PC merging method requires that the first PC contains only overall scene luminance and that all interband variation is contained in the other PCs (ERDAS Field Guide, 2002).

The result of the multiplicative merging technique is an increased presence of the intensity component. For some applications this can be desirable: urban or suburban studies, city planning, and utilities routing, because these applications often want roads and cultural features (which tend toward high reflection) to be pronounced in the image (ERDAS Field Guide, 2002).

The Brovey transform was developed to visually increase contrast in the low and high ends of an image histogram. Consequently, the Brovey transform should not be used if preserving the original scene radiometry is important (ERDAS Field Guide, 2002). In addition, only 3 bands at a time should be merged from the input multispectral scene.

II.6 Principles of pixel-based image classification

The objective of image classification is to replace visual analysis of the image data, which is a very time-consuming and subjective task, with quantitative techniques for automating the identification of features in a scene (Lillesand and Kiefer, 1994). Pixel-based image classification involves the analysis of multispectral image data and the application of statistically based decision rules for determining the land cover identity of each pixel in an image. These decision rules can be based on the spectral characteristics of the data (spectral pattern recognition), or on geometric shapes, sizes and patterns present in the image data (spatial pattern recognition). According to Jensen (1986), multispectral classification is a method that transforms data into information by automatically categorizing all pixels in an image into land cover classes or themes. There are two types of multispectral pattern recognition: unsupervised and supervised classification. These will be discussed in sections II.7 and II.8, respectively.

II.7 Unsupervised classification

Unsupervised classification is also called clustering because it is based on the natural groupings of pixels in the image data when they are plotted in feature space (ERDAS Field Guide, 2002). The analyst determines the land cover classes of these clusters *a posteriori* by comparing the classified image data to ground reference data. The main difference between supervised and unsupervised classification approaches is that unsupervised methods do not require the user to select training data sets to characterize the targets or to train the classifier. Instead the user specifies only the number of clusters to be generated, and the classifier automatically constructs the clusters by minimizing some predefined error function.

The natural groupings of pixels in feature space (clusters) can be determined with the ISODATA algorithm (Iterative Self Organising Data Analysis Technique) of Ball and Hall (1967), which has been widely used for this purpose. ISODATA (also called migrating means clustering algorithm) is the most generally used method of unsupervised pattern recognition. This algorithm is implemented by recursively migrating a set of cluster means using a “closest distance to mean” approach until the locations of the cluster means are unchanged, or until the change from one iteration to the next is less than some predefined threshold. The user of the ISODATA algorithm must estimate the initial number of clusters, say n , present in the data. The algorithm initially determines the location of n cluster means within the feature space, either by generating random feature vectors, or by selecting n pixels at random from the available data, or by using a predefined set of feature vectors. Each pixel is then associated with its nearest (Euclidean distance or Mahalanobis distance) cluster centre. In the next iteration, the location of each cluster mean is recalculated based on the set of pixels allocated to that centre. The process is repeated until the change between iterations becomes less than a user-specified threshold or when a maximum number of iterations has been reached (Tso and Mather, 2001).

II.8 Supervised classification

In a supervised classification, the image analyst uses *a priori* knowledge of the terrain that can be obtained through analysis of aerial photographs, land cover maps, ground truthing and personal experience. The user selects representative, homogeneous areas for each land cover class. These areas are called training sites because they are used to “train” the classifier for eventual land cover mapping of all the other pixels in the image. The training sites are used to compile a numerical “interpretation key” through the calculation of multivariate statistical parameters (mean, standard deviation, covariance matrix, correlation matrix, *etc.*). A decision rule compares the spectral characteristics of each pixel in the image with the statistical parameters of each class and assigns it to the class “it most closely resembles”.

The seven steps in performing a supervised classification are listed beneath (Jensen, 1986):

1. Selection of the categories of interest
2. Selection of representative (and homogeneous) training sites
3. Extraction and analysis of the statistics from the training sites
4. Evaluation of the degree of between-class separability
5. Selection of an appropriate decision rule
6. Classification of the image
7. Statistical evaluation of the classification output

These different steps are schematically represented in Figure 11 and will be discussed in more detail in the following sections.

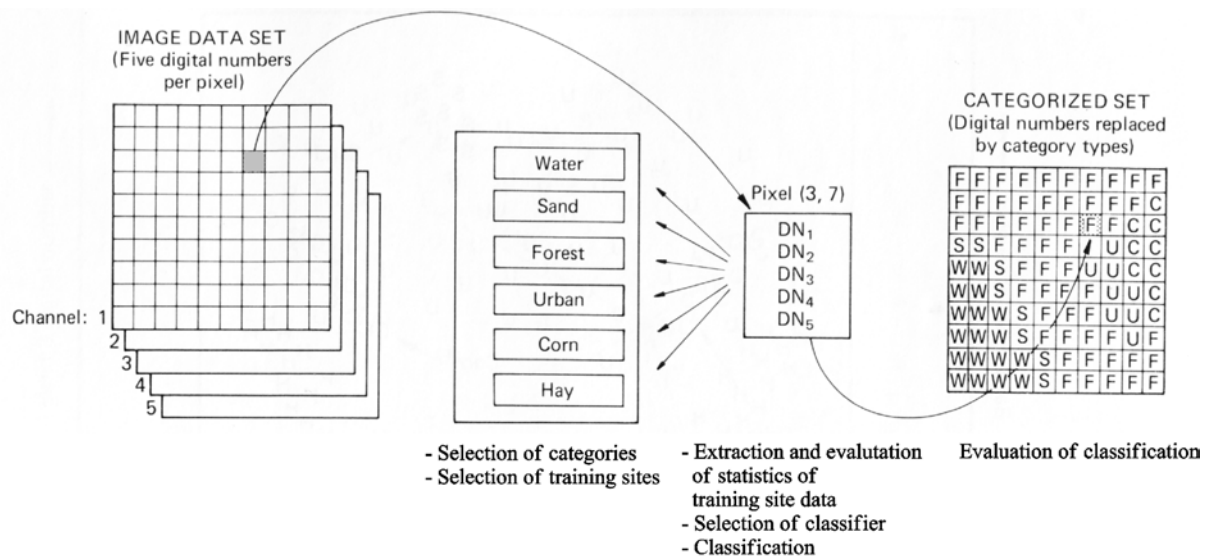


Figure 11. Basic steps in supervised classification (Adapted from Lillesand and Kiefer, 1994)

II.8.1 Selection of the categories of interest

The categories of interest must be carefully selected to successfully perform digital image classification. It is important to realize that the information classes (defined by man, such as “corn” or “hay”) will nearly never be represented by spectrally distinct spectral classes.

II.8.2 Selection of representative training sites

This is probably the most crucial and delicate step in the classification of digital imagery. It requires close interaction between the image analyst and the image data whereby the analyst uses his thorough knowledge of the area to which the data apply. The analyst selects sites within the image (training sites) that are representative for the land cover classes of interest (selected in the first step) and that should be as homogeneous as possible.

Tso and Mather (2001) point out that sample size is important in terms of the accuracy with which estimates of statistical parameters describing the different information classes are obtained. According to Jensen (1986) the general rule is that if training data are being extracted from n bands, the minimum number of pixels in a training class should be $n+1$, allowing the inverse of the covariance matrix to be calculated, which is important in some classification algorithms (such as Maximum Likelihood classifier), but that ideally more than $10n$ pixels of training data should be collected for each class. While Mather (1999) suggests that the number of training data pixels per class should be at least $30n$, based on the notion that in univariate statistics, a sample size of 30 is considered “large”.

II.8.3 Extraction and analysis of the training sites statistics

Once the training sites (TS) have been chosen, the software system is used to develop a statistical characterization of the reflectance for each information class represented by these TS. These statistical characterisations of TS are also called *signatures*.

Statistical parameters as mean, standard deviation, variance, minimum and maximum values and covariance matrix, are calculated from the training data pixels for each class. Let n be the number of image bands. The covariance matrix C_j for class j is

$$C_j = \begin{pmatrix} \text{COV}_{j11} & \text{COV}_{j12} & \cdots & \text{COV}_{j1n} \\ \text{COV}_{j21} & \text{COV}_{j22} & \cdots & \text{COV}_{j2n} \\ \vdots & \vdots & \ddots & \vdots \\ \text{COV}_{jn1} & \text{COV}_{jn2} & \cdots & \text{COV}_{jnn} \end{pmatrix}$$

where COV_{jkl} is the covariance of class j between bands k and l :

$$\text{COV}_{jkl} = \frac{m \sum_{i=1}^m DN_{ik} DN_{il} - \sum_{i=1}^m DN_{ik} \sum_{i=1}^m DN_{il}}{m(m-1)}$$

and where m is the number of training pixels in class j and DN_{ik} is the digital number (or brightness value) in band k of the i^{th} pixel in class j .

The fact that efficient estimation of statistical parameters requires a representative sample of sufficient size is well known. Consequently, as the number of parameters rises, then, for a fixed sample size, the efficiency of the estimation decreases, which implies that the confidence limits for each estimate become wider. The effectiveness of the classifier will therefore begin to decrease once a certain number of dimensions is reached. This is known as the Hughes effect (Hughes, 1968).

Training site statistics for each class can be analyzed and compared in several ways, as described in the following paragraphs.

II.8.4 Evaluation of the degree of between-class separability

II.8.4.1 GRAPHICAL REPRESENTATION OF SPECTRAL RESPONSE PATTERNS

Spectral response patterns can be graphically represented by means of a histogram. A histogram is a graph where the frequencies of occurrence of each of the digital numbers (DNs) within the image are plotted. For an 8-bit image, the DN values range from 0-255. Histogram output is particularly important when a ML classifier is used, since it provides a visual check on the normality of the spectral response distributions. If the histogram has a bimodal distribution (two distinct peaks) it is probably the result of bad training site selection, and splitting of the signature should be considered. Plotting the histograms of different classes in one graph also allows to check the level of overlap between classes.

Another means of graphical representation of spectral response patterns is by plotting ellipses in a two-dimensional feature space. This can only be done correctly if the training data pixels are normally distributed in the feature space bands. The parameters necessary for plotting these ellipses are the mean and standard deviations of the training pixels in each class in a two-dimensional feature space (two bands).

II.8.4.2 QUANTITATIVE EXPRESSIONS OF CATEGORY SEPARATION

A measure of the statistical separation between class response patterns can be computed for all pairs of classes and can be presented in the form of a matrix. One statistical parameter commonly used for this purpose is divergence, a covariance weighted distance between class means (Lillesand and Kiefer, 1994).

The formula for computing divergence between two signatures of classes l and k is:

$$D_{kl} = \frac{1}{2} \text{tr}(C_k - C_l)(C_k^{-1} - C_l^{-1}) + \frac{1}{2} \text{tr}(C_k^{-1} - C_l^{-1})(m_k - m_l)(m_k - m_l)^T,$$

where C_k is the covariance matrix of class k , m_k is the mean vector of class k , tr is the trace function (*i.e.* the sum of the diagonal elements in a matrix) and T is the transpose function (ERDAS Field Guide, 2002).

Another distance measure is transformed divergence:

$$TD_{kl} = 2000 \times \left[1 - \exp\left(\frac{-D_{kl}}{8}\right) \right]$$

which gives an exponentially decreasing weight to increasing distances between classes. The scale of the transformed divergence can range from 0 to 2000. As a general rule, if the result of transformed divergence TD_{ij} , is greater than 1900, the separation between classes i and j is good, between 1700 and 1900, separation is fairly good, and below 1700, separation is poor (Jensen, 1986). It is important to keep in mind that these distance measures will only give reliable results if the training pixel data for each class are normally distributed in each band.

II.8.4.3 SELF-CLASSIFICATION OF TRAINING DATA SETS

A classification of only the training set pixels is made, to determine what percentage of the training pixels is actually classified as expected. These percentages are presented in a contingency matrix. The structure of this matrix is analogous to the structure of the confusion or error matrix in classification accuracy assessment discussed in section II.8.7.

II.8.4.4 INTERACTIVE PRELIMINARY CLASSIFICATION

The ERDAS Alarm tool provides a visual approximation of the pixels that would be classified with the statistics from a given training area. According to the parallelepiped decision rule, the pixels that fit the classification criteria are highlighted in the displayed image (ERDAS Field Guide, 2002).

II.8.5 Selection of an appropriate classifier

The choice of a particular decision rule or classifier depends on the nature of the input data and on the desired output (Friedman, 1980). The measurement vector for each pixel is compared to each signature, according to a decision rule or algorithm. Pixels that fit the criteria established by the decision rule, are then assigned to the class for that signature

(ERDAS Field Guide, 2002). Classifiers or decision rules are divided into several categories based on assumptions made on the training pixel data distribution (parametric or non parametric classifiers) or based on the definitiveness with which decisions are made (hard or soft classifiers).

Parametric classifiers assume that the observed measurement vectors obtained for each class in each spectral band are Gaussian in nature (*i.e.* normally distributed).

Non-parametric classifiers are independent of the statistical properties of the data. If a pixel is located within the boundary of a non-parametric signature, then this decision rule assigns the pixel to the signature's class. A nonparametric rule determines whether or not a pixel is located inside the nonparametric signature boundary (ERDAS Field Guide, 2002).

Hard classifiers make a definitive decision about the land cover class to which any pixel belongs. Examples of hard classifiers are the parallelepiped, minimum distance and maximum likelihood classifiers. These classifiers will be discussed in more detail in section II.9.

Soft classifiers, as the fuzzy classification, do not make a definitive decision about the land cover class to which each pixel belongs. Rather, they develop statements of the degree to which each pixel belongs to each of the land cover classes being considered. For example, a soft classifier might indicate that a certain pixel belongs to class 1 with probability 0.70, to class 2 with probability 0.24 and to class 3 with probability 0.06 (Eastman, 1999). The fuzzy classification is discussed in more detail in section II.12.

II.8.6 Classification of the image

All pixels in the image are judged by the decision rule and are assigned to the class for which they fit the criteria. The original n -dimensional image is transformed into a one-dimensional thematic map containing information on land-cover class distribution.

II.8.7 Statistical evaluation of the classified image

No classification is complete until its accuracy has been assessed. Classification accuracy is the level of agreement between labels assigned by the classifier and class allocations based on ground truth data collected by the user. Tso and Mather (2001) note that ground truth data do not necessarily represent reality, due to observation and recording errors, mislocation of ground truth data sites, differences caused by changes in land cover between the time of observation and the date of imaging, *etc.* Therefore, they argue that "ground truth data" should be called *test data* instead.

The most common tool used for the classification accuracy assessment is in terms of a *confusion matrix* (or error matrix). A confusion matrix is a square array of dimension $n \times n$, where n is the number of classes. The matrix shows the relationship between two samples of measurements taken from the area that has been classified. The first sample represents collected test data. The second sample is composed of the labels of the pixels, allocated by the classifier, that correspond to the test data points. The columns in a confusion matrix represent test data, while rows represent the labels assigned by the classifier.

Several indices of classification accuracy can be derived from the confusion matrix. The “overall” accuracy (OA) is obtained by dividing the sum of main diagonal elements of the matrix by the total number of test data pixels. In order to assess the accuracy of each class separately, the concepts of producer’s and user’s accuracy can be used. The *producer’s accuracy* (PA) for class i (C_i) is calculated by dividing the entry (i,i) by the sum of the i^{th} column and indicates the proportion of pixels in the test data set that are correctly recognized by the classifier. PA is of greatest interest to the thematician carrying out the classification, who can claim that $x\%$ of the time an area that was classified as a certain class truly belongs to that class (Green *et al.*, 2000). The *user’s accuracy* (UA) for class i is obtained by division of entry (i,i) by the sum of the i^{th} row and measures the proportion of pixels identified by the classifier as belonging to class i that agree with the test data (see Table 2). UA is arguably the more pertinent in a management context, because a user of this map will find that, each time an area labelled as a certain class on the map is visited, there is $x\%$ chance that it is actually that class (Green *et al.*, 2000). Analysts also often discuss errors of omission and errors of commission. Errors of omission are those pixels which were missed by the Producer and thus are calculated as 100% minus the Producer’s accuracy. By extension, errors of commission are the pixels wrongly assigned to a class and are calculated as 100% minus the User’s accuracy. Thus, each error of omission from one class is also an error of commission for another class (Woodcock *et al.*, 2002).

Table 2. Confusion matrix for classification accuracy evaluation

		Test data (ground truth)					RT ^a
		C ₁	C ₂	C ₃	...	C _n	
Classification data	C ₁	a ₁₁	a ₁₂	a ₁₃	...	a _{1n}	$\sum_{l=1}^n a_{1l}$
	C ₂	a ₂₁	a ₂₂	a ₂₃	...	a _{2n}	$\sum_{l=1}^n a_{2l}$
	C ₃	a ₃₁	a ₃₂	a ₃₃	...	a _{3n}	$\sum_{l=1}^n a_{3l}$
	...						
	C _n	a _{n1}	a _{n2}	a _{n3}	...	a _{nn}	$\sum_{l=1}^n a_{nl}$
CT ^b		$\sum_{l=1}^n a_{l1}$	$\sum_{l=1}^n a_{l2}$	$\sum_{l=1}^n a_{l3}$...	$\sum_{l=1}^n a_{ln}$	$\sum_{k,l=1}^n a_{kl}$

Producer's accuracy (PA) for class C_i: $a_{ii} / \sum_{l=1}^n a_{li}$

User's accuracy (UA) for class C_i: $a_{ii} / \sum_{l=1}^n a_{il}$

Overall accuracy (OA): $\sum_{j=1}^n a_{jj} / \sum_{k,l=1}^n a_{kl}$

^a Row Total. ^b Colum Total

These accuracy measurements are based either on the principal diagonal, columns or rows of the confusion matrix only, which does not use the information from the whole confusion matrix. A multivariate index called the *kappa coefficient* (κ)(Congalton *et al.*, 1983) has found favour. κ is calculated as follows:

$$\kappa = \frac{N \sum_{i=1}^r x_{ii} - \sum_{i=1}^r (RT_i \times CT_i)}{N^2 - \sum_{i=1}^r (RT_i \times CT_i)},$$

where r is the number of rows in a matrix, x_{ii} are the diagonal elements, RT_i and CT_i are the row and column totals respectively and N is the total number of observations. The kappa coefficient uses all information in the matrix in order for the chance allocation of labels to be taken into consideration. Woodcock *et al.* (2002) state that the kappa coefficient is an accuracy estimate that removes the effect of random chance on accuracy. According to Tso and Mather (2001) the kappa coefficient expresses the proportionate reduction in error generated by a classification process compared with the error of a completely random classification. The higher the value of κ , the better the classification performance (Tso and Mather, 2001). A value of zero indicates no agreement, while a value of 1 shows perfect agreement between the classifier output and the reference data (Mather, 1999). Montserud and

Leamans (1992) suggest that a value of κ of 0.75 or greater shows a “very good to excellent” classifier performance, while a value of less than 0.4 is “poor”. However, these guidelines are only valid when the assumption that the data are randomly sampled from a multinomial distribution, with a large sample size is met. κ values are often used for comparing classifications (*e.g.* classifications done using different classifiers applied to the same data set). κ will be less than the OA unless the classification is exceptionally good (*i.e.* the number of off-diagonal elements is very low) (Green *et al.*, 2000).

Ma and Redmond (1995) recommend use of the *tau coefficient* (τ) in preference to the kappa coefficient. τ is calculated as follows:

$$\tau = \frac{OA - P_r}{1 - P_r} \quad \text{where} \quad P_r = \frac{1}{N^2} \sum_{i=1}^m RT_i \times x_{ii}$$

and where m is the number of classes, N is the total number of observations, RT_i is the row total for class i and x_{ii} is the diagonal value for class i (*i.e.* number of correct assignments for class i). The main advantage of τ is that the coefficient is readily interpretable. For example, a τ of 0.8 indicates that 80% more pixels were classified correctly than would be expected by chance alone (Green *et al.*, 2000).

In addition to the error matrix, the quality of an image classification can be quantified via an image-based approach which measures the statistical separability of digital numbers that comprise each habitat class mapped (*e.g.* the difference between mean DN values for forereef, seagrass, mangrove, *etc.*). For example, several authors have examined the separability of classes using canonical variates analyses on the image data (Jupp *et al.*, 1986; Kuchler *et al.*, 1989; Ahmad and Neil, 1994). Others have used analysis of variance on the DN values that comprise each class (Luczkovich *et al.*, 1993; Franklin *et al.*, 2001). There is nothing inherently wrong in this, provided that a high separability of image classes is not assumed to be indicative of an accurate habitat map (Green *et al.*, 2000).

II.9 Traditional hard classifiers

II.9.1 The parallelepiped classifier

The parallelepiped decision rule is implemented by defining a parallelepiped-like subspace for each class. The boundaries of each parallelepiped can be defined by the minimum and maximum pixel values in each class, or by a certain number of standard deviations on either side of the mean of the training data for the given class. If the number of bands is n , these decision boundaries form an n -dimensional parallelepiped in feature space (see Figure 12). If the DNs of a candidate pixel in each pair of bands lie above the lower decision boundary value or below the higher decision boundary value of the rectangle for a class, then the pixel is assigned to that class.

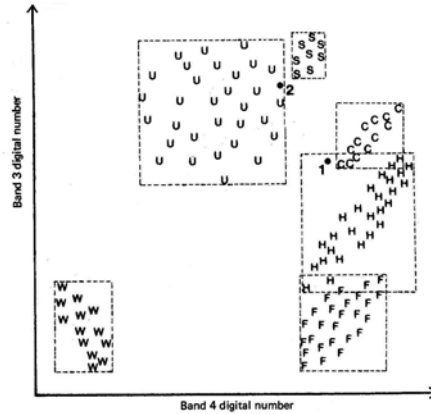


Figure 12. Parallelepiped decision rule (Lillesand and Kiefer, 1994)

The parallelepiped classification rule is easy to implement and very fast, but errors may arise, particularly when a pixel lies inside more than one parallelepiped or outside all parallelepipeds. Overlap is caused largely by category distributions exhibiting correlation or high covariance being poorly described by the rectangular decision regions.

Covariance is the tendency of spectral values to vary similarly in two bands, resulting in elongated, slanted clouds of observations in feature space. Spectral response patterns are frequently highly correlated and high covariance is often the rule rather than the exception (Lillesand and Kiefer, 1994).

II.9.2 The minimum distance classifier

The minimum distance decision rule calculates the spectral distance between the measurement vector for the candidate pixel and the mean vector for each land cover class. The distance can be either the Euclidean distance in the n -dimensional feature space:

$$D_E^2 = (X_i - m_j)^2$$

or the Mahalanobis generalized distance:

$$D_M = (X_i - m_j)^T C_j^{-1} (X_i - m_j)$$

Where T denotes the matrix transpose, C_j^{-1} is the inverse of the covariance matrix for cluster j , m_j is the class mean vector and X_i is the i^{th} candidate pixel vector (Tso and Mather, 2001). The candidate pixel is then assigned to the class with the closest mean. Figure 13 shows the minimum distance classification using the Euclidean distance measure of a pixel of unknown identity (pixel 1 and pixel 2). The class means are denoted by a “+” sign and the dashed lines represent the Euclidean distance between pixel 1 and each category mean. The Euclidean minimum distance classifier assigns pixel 1 to class C and pixel 2 to class S, in spite of the fact that the greater variability in class U suggests that class U would be a more appropriate class assignment. Pixel 2 is assigned to class U if the Mahalanobis minimum distance classifier is used.

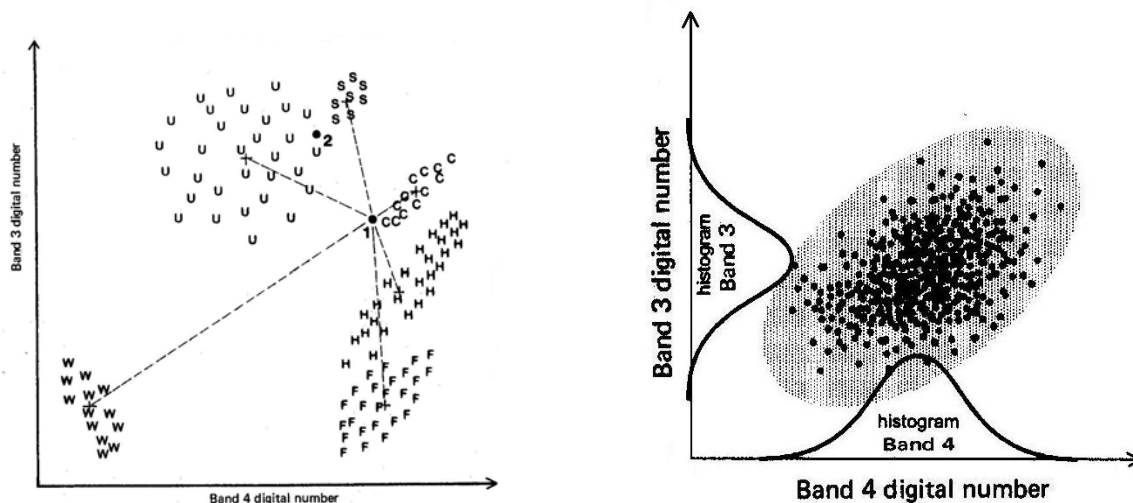


Figure 13. Left: Minimum distance decision rule using the Euclidean distance measure (Lillesand and Kiefer, 1994). Right: Mahalanobis distance in feature space, resulting in ellipsoidal features space objects (ERDAS Field Guide, 2002)

The Mahalanobis distance takes into account the shape of the frequency distribution, which is assumed to be Gaussian, for a given cluster in feature space, resulting in ellipsoidal clusters (Right in Figure 13), whereas the use of the Euclidean distance assumes equal variances and a zero correlation between the features, giving circular clusters.

II.9.3 The maximum likelihood classifier

The maximum likelihood (ML) decision rule assigns a pixel to the class for which the membership probability is the highest. The ML decision rule is based on the Bayesian probability formula, which assumes that these probabilities are equal for all classes, and that training data statistics for each class in each band are normally distributed. This decision rule assigns a measurement vector X to class j (of m possible classes), if, and only if

$$p_j > p_i \quad \forall i, j : 1 \dots m \quad i \neq j,$$

where

$$p_j = -\frac{1}{2} \ln |C_j| - \frac{1}{2} (X - m_j)^T (C_j^{-1}) (X - m_j) \quad (\text{Jensen, 1986})$$

Note that the previous equation contains the Mahalanobis distance (formula in section II.9.2), thus the geometrical shape of the cloud formed by a set of pixels belonging to a given class can be described by an ellipsoid. In the two-dimensional feature space the ML function delineates ellipsoidal equiprobability contours -, which can be viewed as decision boundaries (cfr. Figure 14).

The most important thing to keep in mind when using the ML decision rule is that it relies heavily on the normal distribution of the training data in each band.

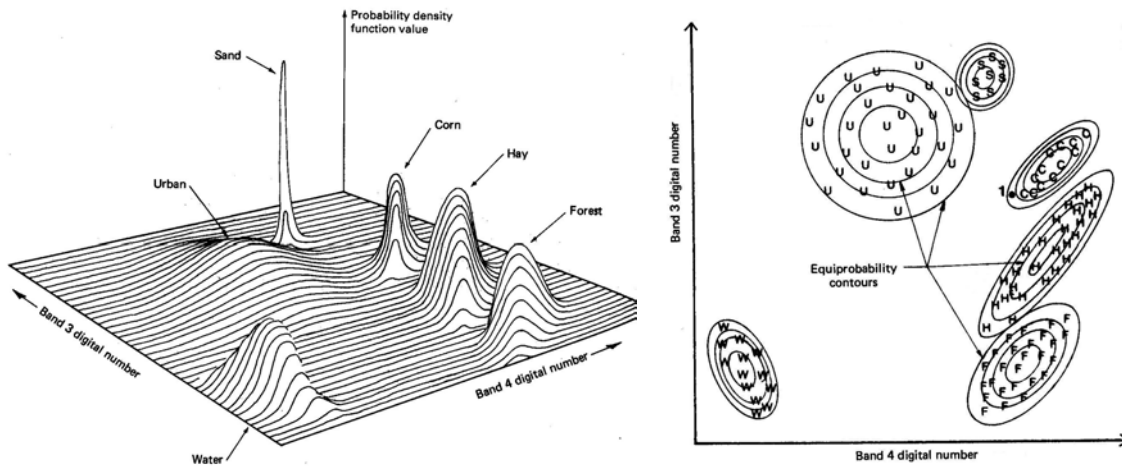


Figure 14. Probability density functions (left) and equiprobability contours (right) defined by maximum likelihood classifier (Lillesand and Kiefer, 1994)

It is generally accepted that the ML classifier is the most accurate classifier compared to the parallelepiped and minimum distance decision rule (Curran, 1985) and is therefore generally preferred.

II.10 Classification in practice

In practice visual interpretation is the first step in any classification with the image being studied in the light of existing knowledge and data. Differences between major habitats can usually be identified at a glance and closer inspection can reveal more subtle patterns in the digital data. An unsupervised classification can then be used to direct and plan a field campaign –the results of this unsupervised classification should always be studied in the light of the initial visual interpretation of the image to confirm that the classes appear sensible. Once field data have been collected these steps should serve to facilitate informed decision making during the more interactive supervised supervisions. If a habitat map produced by classification is to be used for management or monitoring it is important that it is accompanied by an assessment of its accuracy (Green *et al.*, 2000).

II.11 Texture

Tone is the grey level of a single pixel in a greyscale image. At a simple level, texture can be thought of as the variability in tone within a neighbourhood, or the pattern of spatial relationships among the grey levels of neighbouring pixels, and is usually described in terms such as “rough” or “smooth” (Mather, 1999). The observation of texture depends on two factors. One is the scale of the variation that we are willing to call “texture” –it might be local or regional. The second is the scale of observation.

The human mind integrates both spectral and spatial features in visual image interpretation. Spectral features describe variations in tone over a greyscale image, whilst spatial features reflect the spatial distribution of these tonal variations, which contain two kinds of spatial relationships: texture and context. Texture is the tonal variation focused upon the object of interest, representing the structure of the object. Context measures the broader-scale

relationship between the object being analysed and the remainder of the scene (Tso and Mather, 2001). According to Haralick *et al.* (1973) tone and texture are always present in an image, although one property can dominate the other at times, depending on the “fineness” or “roughness” of the surface of the object, and on the image resolution relative to the surface roughness of the object. If tonal variation inside a limited range is relatively small, spectral information will dominate (Tso and Mather, 2001).

According to Lillesand and Kiefer (1994) texture is the frequency of tonal change on the photographic image. Texture is produced by an aggregation of unit features that may be too small to be discerned individually on the photograph, such as tree leaves and leaf shadows. It is a product of their individual shape, size pattern, shadow and tone. It determines the overall visual “smoothness” or “coarseness” of image features.

The operational definition of texture is difficult. According to Tso and Mather (2001) the main texture recognition approaches can be categorized into four groups in terms of their different theoretical backgrounds:

1. Texture measures derived from the Fourier power spectrum via frequency domain filtering (see Jensen, 1986; Tso and Mather, 2001 for a more elaborate discussion)
2. Texture measures based on statistics that measure local properties that are thought to be related to texture (see below): histogram measures
3. Texture measures derived from the Grey-Level Co-occurrence Matrix (GLCM), which represents the distance and angular spatial relationships over an image sub-region of specified size (Haralick *et al.*, 1973)
4. Texture measurement based on the calculation of the fractal dimension of the region surrounding the pixel of interest (see Tso and Mather, 2001) and texture derived from the modelling of the image using a random field model such as the multiplicative autoregressive random (MAR) field (Frankot and Chellappa, 1987)

The most common class of texture measures is the class of histogram measures (Dekker, 2003). Well known are the mean (μ), mean Euclidean distance (m_E), variance (σ^2), skew, kurtosis, entropy (H) and energy (E). Let x_{ij} be the pixel value of pixel (i,j) in the window over which is summed, let n be the number of pixels that is summed. Let x_c represent the window’s centre pixel value and p_{ij} is the normalized pixel value. The histogram texture measures are determined as follows:

$$\mu = \frac{\sum_{i,j} x_{ij}}{n} \quad m_E = \frac{\sqrt{\sum_{i,j} (x_{ij} - x_c)^2}}{n-1} \quad \sigma^2 = \frac{\sum_{i,j} (x_{ij} - \mu)^2}{n-1}$$

$$skew = \frac{\sum_{i,j} (x_{ij} - \mu)^3}{(n-1)\sigma^3} \quad kurtosis = \frac{\sum_{i,j} (x_{ij} - \mu)^4}{(n-1)\sigma^4} \quad E = \sum_{i,j} x_{ij}^2$$

$$H = -\sum_{i,j} p_{ij} \log(p_{ij}) \quad \text{with} \quad p_{ij} = \frac{x_{ij}}{\sum_{i,j} x_{ij}}$$

II.12 Fuzzy classification

In remotely sensed imagery, information classes often overlap with each other in feature space. For those pixels lying in the overlap area of two or more classes, classification errors may occur. Townshend *et al.* (2000) point out that, a significant, but usually ignored problem with per-pixel characterization of land cover is that a substantial proportion of the signal apparently coming from the land area represented by a pixel comes from the surrounding pixels. This is caused by many factors including the optics of the instrument, the detector and the electronics, as well as atmospheric effects.

Fuzzy classification is designed to reduce classification errors of pixels that show an affinity with several information classes. This type of pixel is often described as “mixed”, and it may be more realistic to consider an approach that acknowledges this problem. Traditional or hard classification methods do not provide a good mechanism for coping with such uncertainty and imprecision (fuzziness). The fuzzy method thus takes into account that pixels cannot be definitely assigned to one and only one class, but to several classes with a certain degree of affinity. The degree of affinity of a pixel with a certain class is determined by the fuzzy membership function of that class (Tso and Mather, 2001). Fuzzy classification can also be seen as a way to include contextual information in which observations from surrounding pixels (neighbourhood information) are used to assist in the characterisation.

ERDAS Imagine can produce such fuzzy classifications, once training data pixels are presented for each class. Firstly, the user specifies the number of best classes to be calculated for each pixel in the image (*i.e.* the classes to which the pixel shows the highest affinity) and the decision rule that should be used. The outcome of the fuzzy classification is on the one hand a multi-layered classification image, containing as many layers as there are best classes to be calculated and on the other hand, a distance file in which each data file value represents the result of a spectral distance equation, depending upon the decision rule used. In a maximum likelihood classification, for example, the data file values represent the Mahalanobis distance between the measurement vector of the pixel and the mean vector of the pixel’s class.

Secondly, fuzzy convolution is applied to the multi-layered classification file and the distance file. Fuzzy convolution allows to perform a moving window convolution on a fuzzy classification with multiple output class assignments and creates a new single class output file by computing a total weighted inverse distance of all the classes in the window of pixels. Then, it assigns the centre pixel to the class with the largest total inverse distance summed over the entire set of fuzzy classification layers. Let f be the number of fuzzy classification layers (=number of best classes to be calculated) and let the convolution window be of size s (either 3, 5 or 7), then the total weighted inverse distance of that window for class k is:

$$T[k] = \sum_{i=1}^s \sum_{j=1}^s \sum_{m=1}^f \frac{w_{ij}}{D_{ijm}[k]}$$

where i and j are the row and column indices of the pixels in the convolution window, m is the fuzzy layer number, w_{ij} is the weight table for window pixel (i,j) and $D_{ijm}[k]$ is the distance file value of window pixel (i,j) for class k (ERDAS Field Guide, 2002). $T[k]$ is computed for all classes and the centre pixel is assigned to the class for which $T[k]$ is maximal.

This has the effect of creating a context-based classification to reduce the salt and pepper in the classification. Classes with a very small distance value remain unchanged while classes with higher distance values may change to a neighbouring value if there is a sufficient number of neighbouring pixels with that class value and small corresponding distance values.

II.13 Evolution towards object-based analysis

During the last ten years in the history of remote sensing, emphasis was laid on increasing the spectral and spatial resolution of the sensors. But with the development of these advanced sensors the user community faces new problems in the automated analysis of these types of data.

The high spatial resolution of the advanced sensors increases the spectral within-field variability and therefore may decrease the classification accuracy of traditional methods: per-pixel classification in a multi-dimensional feature space. Traditional multispectral algorithms only consider spectral similarities independently from their occurrence and do not make use of any spatial concepts (context, neighbourhood, texture, form...) (Blaschke *et al.*, 2000; Blaschke and Strobl, 2001; Schiewe *et al.*, 2001; Schiewe, 2002). Especially in high-resolution images it is very likely that neighbouring pixels belong to the same land-cover class as the pixel under consideration. Most image data exhibit characteristic texture which is neglected in traditional classification approaches.

While some users still argue for steadily increasing resolutions it becomes more obvious that progress in environmental applications is hampered by the quality of spectral information that can be reliably extracted from remotely sensed data. The whole conceptual framework based on a pixel as the smallest unit of consideration is limited as long as spatial neighbourhood and proximity are not considered (Blaschke *et al.*, 2000).

The concept of object-based analysis as an alternative to pixel-based analysis emerged as early as the 1970s (de Kok *et al.*, 1999), but the early models of object-based image classification faced obstacles in fusing information from multilevel analysis, validating classifications, reconciling conflicting results, attaining reasonable efficiency in processing and automating the analysis. They were also limited by hardware, software, poor resolution of images and interpretation theories. Pixel-based analysis provided reasonably satisfactory results and was much more efficient so it remained the industry standard. Instead of going towards an object-based model, enormous efforts were invested in advanced pixel-based processes to enhance per-pixel image analysis (Blaschke and Strobl, 2001). Those advanced methods, including soft or fuzzy classification methods, sub-pixel approaches and spectral unmixing methods, focus mostly on the well-known phenomenon of the mixed pixel. This term implies that the scale of observation is inappropriate and does not match the scale of variation in the landscape. By increasing spatial resolution this phenomenon does not disappear. One can observe that the percentage of pixels regarded as “real mixed pixels”, *e.g.* falling between two adjacent fields, is actually decreasing. At the same time, a new problem appears: areas which are relatively homogeneous at a 30m resolution exhibit variation at 4m resolution. Therefore, it is argued that while decreasing the importance of the mixed pixel problem, the consistency of groups of pixels become more important instead. Concepts of adjacency and context of information are becoming more important (Blaschke *et al.*, 2000).

Since the mid 1990s, hardware capabilities have increased dramatically. The availability of images from high spatial resolution satellite sensors, with increased spectral variability within map-sized objects, has increased the demand for object-oriented techniques (de Kok *et al.*, 1999).

II.14 Object-based image analysis

The human mind is until today the only “instrument” that fully exploits spatial as well as spectral information in the process of image classification. By integrating colour, structure, shape, size, form, context, neighbourhood and texture, the human mind assigns classes to objects generated as such. The human mind does not consider pixels separately, but rather homogeneous groups of pixels.

Image analysis leads to meaningful objects only when the image -prior to classification- is segmented into “homogeneous” areas. According to Schiewe (2002) segmentation is the process of completely partitioning a scene (*e.g.* a remote sensing image) into non-overlapping regions (segments) in scene space (*e.g.*, image space). There are a number of possibilities how to segment an image. Most approaches can be grouped into two classes, namely edge-based algorithms and area-based algorithms. This classification also includes fractal-based approaches aiming at detecting discontinuities as well as fractal-based or texture-based algorithms aiming at finding of homogeneous areas. The most promising recent developments are fractal approaches spearheaded by the developments of INRIA in Paris (Véhel and Mignot, 1994) and Definiens AG in Munich (Baatz and Schäpe, 2000). While images often are legitimately seen as the most information-rich data available, extraction of information frequently had to rely on human interpretation. Only now we are getting close to applying spatial thinking to image processing, paving the way to algorithmically formulate some more advanced aspects of cognition and inference (Blaschke and Strobl, 2001).

Since the release of the eCognition software in 2000, several comparative studies between classical pixel-based classifications (conducted with ERDAS Imagine) and the recently developed object-based classifications (conducted with eCognition) of IKONOS images were done in the field of urban planning (Hofmann, 2001), but also in forestry mapping (Kristof *et al.*, 2002) and environmental monitoring (Meinel *et al.*, 2001). These studies conclude that eCognition is much more efficient in classifying IKONOS data and that eCognition is more open towards integration of spatial information, which is of increasing importance in the classification of VHR satellite imagery.

To perform an object-based classification, one needs a technique to extract objects from the image and an algorithm for subsequent classification. One technique to extract objects is image segmentation, whose basic task is to merge image elements (pixels) based on homogeneity parameters or on the differentiation to neighbouring regions (heterogeneity). Thus, segmentation methods follow the two strongly correlated principles of neighbourhood and value similarity.

II.15 The field survey

II.15.1 The Remote Sensing – Field Survey combination

RS is often (erroneously) considered as an alternative to field survey. It should be seen as a technology which makes field survey more cost-effective. A solely field survey based approach to habitat mapping is shown to be extremely cost-inefficient (Green *et al.*, 2000). On the other hand, a RS approach without extensive field survey is shown to be too inaccurate. The best strategy is to combine RS and field survey because (Green *et al.*, 2000):

- ♦ RS is very good at indicating the extent of habitats and location of boundaries between habitats
- ♦ field survey identifies what the habitats are
- ♦ digital image processing then extends the survey coverage to the whole area of management interest.

Mangrove areas are often difficult to reach and equally difficult to penetrate. Thus field survey of mangroves is logistically demanding particularly where the areas are large. RS offers a very cost-effective method of extending limited field survey to map large areas of mangroves (Green *et al.*, 2000).

Every remote sensing exercise requires field surveys at some stage (*e.g.* to define habitats, calibrate remotely sensed imagery, to test the accuracy of RS outputs). The aims of field survey are threefold:

1. to identify each feature of interest
2. to locate representative areas of each feature in order to generate spectral signatures
3. to generate adequate additional data to test the quality or accuracy of the image classification

This latter consideration is extremely important for any mapping exercise. Coastal management initiatives based on a habitat map of unknown accuracy could lead to unnecessary or inappropriate action, although it is difficult to predict or generalize specific problems arising from such circumstances. Surprisingly though, accuracy assessments are fairly scarce in the context of mapping tropical coastal resources. Green *et al.* (1996) found that only a quarter of papers reviewed included an assessment of accuracy. To test a classification rigorously, further field data are required which must be independent of the field data used to classify the imagery in the first place.

There has been a tendency in RS to accept the accuracy of photo interpretation as correct without confirmation. As a result, digital classifications have often been assessed with reference to aerial photographs. While there is nothing wrong with using aerial photographs as surrogate field data, it is important to realize that the assumption that photo interpretation is without error is rarely valid and serious misclassifications can arise as a consequence (Biging and Congalton, 1989).

II.15.2 Global Positioning System (GPS)

In a remote sensing context, GPS has 2 major applications (Green *et al.*, 2000):

1. to measure the position of prominent features on an image *in situ* which can be used to provide ground control points for geometric correction
2. to assign positions to field data. These field data can then be correlated with spectral information at the same point on a geometrically corrected image. Conversely, a group of image pixels of particular interest can be surveyed in the field by using a GPS to navigate to that location.

II.15.3 The Point-Centred Quarter Method (PCQM)

II.15.3.1 GENERAL DESCRIPTION

The Point-Centred Quarter Method (PCQM) of Cottam and Curtis (1956) is a method to estimate density and biomass in a forest. Cottam and Curtis (1956) compared different methods for calculating forest density applied to three different forest communities, representing a wide range of species complexity, tree size and tree density. The methods compared are closest individual, nearest neighbour, random pairs, PCQM and quadrat methods. All these methods are based on the measurement of mean area (M) or the amount of area per tree, which is the reciprocal of the density. As such the distance between trees can lead to an accurate estimate of the mean area and the density. For detailed descriptions of the methods besides PCQM (mentioned above) see Cottam and Curtis (1956). Cottam and Curtis (1956) concluded that the PCQM gives the least variable results for distance determinations, provides more data on tree species per sampling point, and is least susceptible to subjective bias and is therefore in most respects superior to the other distance methods.

In the PCQM each sampling point is considered the centre of the four quarters (quadrants) with orientation given by the compass line of traverse. At each point, the closest tree to the point in each of the four quadrants around the point is chosen as the sample. Distances are measured from the point to each of the four trees, and their species and basal areas recorded. The average of the four distances is equal to \sqrt{M} . Computation of density and dominance with the PCQM requires the determination of the mean distance, relative density, relative dominance and basal area per tree. Diameter is closely related to stand development, and can easily be converted to basal area (the area occupied by the tree stems). Other stand characteristics such as height, crown diameter and biomass can often be predicted from the stem diameter (Cintrón and Schaeffer Novelli, 1984). Formulas used in the calculation of relative density, dominance, frequency and importance value are given below.

- ♦ *Relative density* of a species (contribution of a species to total number of stems):

$$DE_r = \frac{SD_{Species} (n^\circ stems / m^2)}{\sum_{AllSpecies} SD_{Species} (n^\circ stems / m^2)} \times 100$$

- ◆ *Relative dominance* of a species (contribution of a species to total basal area):

$$DO_r = \frac{BasalArea_{Species}}{\sum_{AllSpecies} BasalArea_{Species}} \times 100$$

- ◆ *Relative frequency* of a species (probability of occurrence of a species):

$$F_r' = \frac{FrequencyOfOccurrence(\%)}{\sum_{AllSpecies} FrequencyOfOccurrence(\%)} \times 100$$

- ◆ *Importance value* of a species (according to Curtis, 1959):

$$IV = DE_r + DO_r + F_r'$$

The IV reaches 300 in monospecific stands. These parameters together can be used to interpret the importance of the contribution of each component species to the stand in terms of density, contribution to basal area (dominance) and the probability of occurrence throughout the plot (frequency). Comparison of frequencies can only be made between plots of a similar size, because the probability of a plant occurring in a given plot is a function of plot size.

These relative measures should generally be used as a supplement to absolute values. Relative data alone are of limited value, since both densely and sparsely vegetated sites could have similar relative values if species composition is similar.

The accuracy of all absolute values (density, dominance) is dependant in part upon an accurate figure for the number of trees per ha. It follows that care should be taken to insure that the sample of distances is adequate and that the measurements are made with accuracy (Cottam and Curtis, 1956).

The accuracy of the method increases with the number of sampling points and a minimum of 20 points is recommended (Cottam and Curtis, 1956). The method has two limitations that may cause problems in some circumstances:

- ◆ an individual tree must be located in each quarter
- ◆ an individual tree must not be measured twice

Problems are most likely to be encountered in widely spaced stands.

II.15.3.2 PCQM IN MANGROVE RESEARCH

Cintrón and Schaeffer Novelli (1984) evaluated the PCQM for use in mangrove forest structure research. They argued that diameter estimation based on measurements of circumference, will not be perfectly accurate unless the tree is circular in cross-section. When the stem has an eccentric form, use of a tape will lead to error. Fortunately, serious eccentricity of form is not common in most mangrove species or stands, so for most purposes the errors resulting from stem eccentricity can be ignored.

Because of the shape and growth forms of mangrove trees, it is sometimes difficult to decide where to measure the circumference. For this reason the following standard procedures were recommended:

- ♦ When a stem forks below 130cm height along the tree stem, or sprouts from a single base close to the ground or above it, measure each branch as a separate stem
- ♦ When the stem forks at 130cm height along the tree stem or slightly above, measure the diameter at 130cm height along the tree stem or just below the swelling caused by the fork
- ♦ When the stem has prop roots or fluted lower trunk, measure the diameter above them
- ♦ When the stem has swellings, branches or abnormalities at the point of measurement, take the diameter slightly above or below the irregularity where it stops affecting normal form

Dahdouh-Guebas (2001) analysed problems that follow from the use of the PCQM in mangroves, due to the aggregation of trees, ambiguous settings for measuring the distance to sample point or the tree diameters, and over- or underestimation of structural parameters of the forest. Simulations of the PCQM on real digitised vegetation, exactly representing the situation in three mangrove forests in Kenya and Sri Lanka with different densities and aggregation levels, were done to assess the influence of sampling method (*at random* PCQM and transect PCQM) and forest complexity on the accuracy of the common PCQM-derived forest parameters.

The problems investigated were:

1. ambiguous situations for the choice of the stem closest to the sample point, which influences the density
2. exact location for the measurement of the tree diameter, which influences basal area
3. over- or under estimation of structural parameters (*e.g.* biomass and density)
4. what happens if the conditions for the use of the PCQM (see above) are not met?

The advice given by the author:

1. Make sure that each quadrat contains a tree, whatever its distance, instead of adopting a distance limit, as the latter will need to be corrected in a later phase (Verheyden, 1997)
2. If the mangrove displays different zones or patches transects should be subdivided accordingly and PCQM calculations should be made for each zone or patch separate

The comparison of the real values and values obtained after applying the PCQM indicate a deviation up to a factor 2 for density and up to a factor 6 for basal area, depending on the forest structure and on the type of PCQM approach used. There is little opportunity to follow a diameter or distance measurement by the book, but each tree should be approached separately and the researcher should adopt a “best professional consistency”. Transect PCQM yields more accurate, but less precise, values for both density and basal area than *at random* PCQM does. In forests with extreme simplicity (*e.g.* very sparse, young, low, monospecific forests) the *at random* PCQM approach generates more precise as well as more accurate results.

III Materials and methods

III.1 Description of the study site

III.1.1 Geographical

Gazi (Maftaha) Bay (4°25'S and 39°30'E) is situated in southern Kenya, approximately 47km south of Mombasa in Kwale district. It is a shallow, tropical coastal water system with mean depth often less than 5m (Kitheka, 1996). The Bay is sheltered from strong waves by the presence of the Chale peninsula to the east and a fringing coral reef to the south (see Figure 15). The total area of the Bay, excluding the area covered by mangroves, is about 10km². The mangrove forest of Gazi Bay covers about 5km². The seagrass zone which is dominated by *Thalassia* sp, is found in the central region of the Bay and covers an additional area of 7km². The Bay is open to the Indian ocean through a relatively wide (3.5km) and shallow (between 3 and 8m) entrance in the south from the Chale peninsula to the Mkurumuji estuary (Kitheka, 1996).

III.1.2 Climatological

The climate in Gazi is typical of the Kenyan coast and principally influenced by monsoon winds. Rainy seasons are a result of the location of the intertropical convergence zone (ITCZ) in the East African region. The long rains fall from April to August under the influence of the southeast monsoon winds, while the short rains fall between October and November under the influence of the northeast monsoon winds. Total annual precipitation varies between 1000 and 1600mm showing a bimodal pattern of distribution. It is normally hot and humid with an average annual air temperature of about 28°C with little seasonal variation. Air temperature in Gazi Bay varies between 24 and 39°C (data recorded by the Meteorological Department). Relative humidity is about 95% due to the close proximity to the sea (Bosire *et al.*, 2003). The rates of evaporation range between 1950 and 2200mm per year. Wind blows into the area with an easterly component and is always onshore (Eastern Africa Database and Atlas Project (EADAP), 1994).

III.1.3 Biological: mangrove and seagrass beds

The mangrove forest covers an area of about 5km². All ten East-African mangrove species have been reported in Gazi Bay: *Avicennia marina* (Forsk.) Vierh., *Bruguiera gymnorrhiza* (L.) Lam., *Ceriops tagal* (Perr.) C.B. Robinson, *Heritiera littoralis* Dryand., *Lumnitzera racemosa* Willd., *Pemphis acidula* Forst., *Rhizophora mucronata* Lam., *Sonneratia alba* Sm., *Xylocarpus granatum* Koen and *X. moluccensis* (Lamk.) Roem. (nomenclature according to Tomlinson, 1986).

The seagrass zone, dominated by *Thalassodendron ciliatum*, is found in the central region of the bay and covers an additional area of 7km² (Kitheka, 1996).

III.1.4 Hydrological

Two seasonal rivers, Mkurumuji (in the south) and Kidogoweni (in the north), provide most of the inland freshwater input into the Bay. There are two tidal creeks, Makongeni Creek (also called Kidogoweni Creek) receiving fresh water from Kidogoweni River and Kinondo Creek, lacking direct surface freshwater input. Because of the seasonality of Mkurumuji and Kidogoweni rivers, the influence of freshwater input into the mangrove depends on the amount of rainfall inland (Tack and Polk, 1999): river discharge is important during the wet season, which enhances weak stratification in the upper parts of Makongeni Creek, whereas in the dry season, well mixed homogeneous water is found in most regions of the Bay (Kitheka, 1996). The presence of a wide shallow entrance, absence of topographic controls (sills) and the orientation of the bay with respect to the dominant tidal water flow patterns result in very high water exchange rates (60-90%) between the inshore and offshore waters (Kitheka, 1996).

Salinity variations in Makongeni Creek are very wide, ranging from as low as 2 to as high as 38ppt (parts per thousand). In Kinondo Creek salinity fluctuation is low, ranging between 22 and 38ppt, where the variability in salinity may be a result of groundwater influx or surface runoff input from the surrounding deforested mangrove areas. High evapotranspiration rates cause a salinity maximum zone (38ppt) in the dry season in the upper parts of the mangrove creeks (Kitheka, 1996).

The astronomical tide is the main forcing function driving water circulation in Gazi Bay. Other factors are river discharge and onshore wind. The tides are semidiurnal with a spring tidal range of 3.2m and a neap tidal range of 1.4m, generating strong reversing currents in the deep and narrow tidal channels in the mangrove zone, but not in the seagrass beds and the coral reefs (Kitheka, 1997).

In the mangrove creeks, tidal asymmetry (with ebb currents being stronger than flood currents) is attributed to the flow-retarding effects of the dense mangrove vegetation during spring high tide when flood waters inundate most parts of the mangrove forest. The tidal asymmetry promotes the net-downstream longitudinal current which is responsible for carrying away organic detritus to the seagrass zones in the open region of Gazi Bay, possibly enhancing the export of nutrients from the mangrove zone to the seagrass beds (Kitheka, 1996).

III.1.5 History of the mangrove

The mangrove forests of Gazi have been exploited for many years especially for wood used for industrial fuel (in the calcium and brick industries in the 1970s) and building poles (Kairo, 1995; Dahdouh-Guebas *et al.*, 2000). The clear-felling due to the industrial extraction left some areas along the coastline completely denuded. Experimental reforestation (plantation trials) was initiated in Gazi Bay in 1991 (Kairo, 1995).

Gazi Bay is probably the best studied mangrove bay in Africa, with over 100 refereed publications over the last 10 years (Kairo and Dahdouh-Guebas, in prep.)

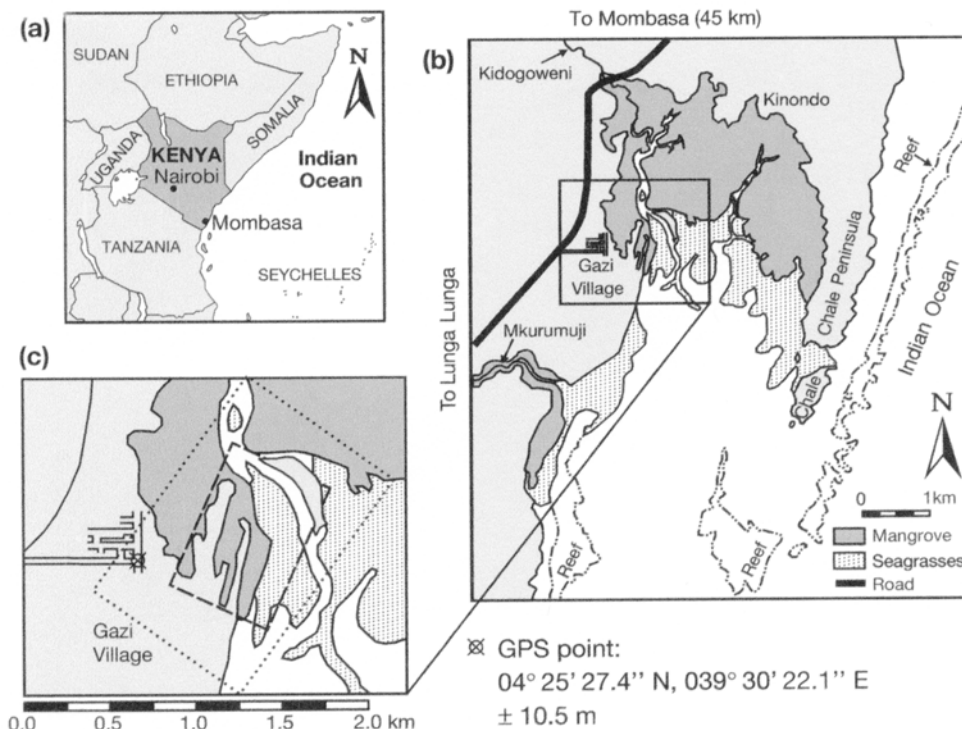


Figure 15. (a) Map of Kenya, (b) Gazi Bay, showing the area covered by mangrove, seagrass and coral reef, rivers and tidal creeks, (c) detail of Gazi village (from Dahdouh-Guebas *et al.*, 2004a, in press)

III.2 Satellite image

The QuickBird satellite, launched in October 2001, is at the forefront of commercial satellite imagery acquisition, with panchromatic imagery of sub-meter (0.7m) spatial resolution and multispectral imagery of 2.8m spatial resolution. A “Standard” DigitalGlobe QuickBird image was purchased by APNA. DigitalGlobe Standard Imagery products are radiometrically corrected, sensor corrected, geometrically corrected and mapped to a cartographic projection.

1. Radiometric corrections: relative radiometric response between detectors (removes differences in imagery due to sensitivity variations between pixels), non-responsive detector fill (fills in null values on imagery due to detectors that are no longer collecting data), and a conversion for absolute radiometry (calibrates overall detector response from known radiometric signals)
2. Sensor corrections: internal detector geometry (combines the six digital chip assemblies into a virtual array), optical distortion (corrects image distortion caused by sensor optics), scan distortion (corrects image distortion caused by slew and scan rate), any line-rate variations (corrects for variations in the panchromatic scan rate), and registration of the panchromatic and multispectral bands (all multispectral bands line up with each other, but the panchromatic and multispectral bands are not registered)
3. Geometric corrections: remove spacecraft orbit position and attitude uncertainty, Earth rotation and curvature and panoramic distortion

Standard imagery also has a coarse Digital Elevation Model (DEM) applied to it, which is used to normalize for topographic relief with respect to the reference ellipsoid. The degree of

normalization is relatively small, so while this image has terrain corrections, it is not considered orthorectified (<http://www.digitalglobe.com>).

Standard imagery products have an average absolute geo-location accuracy of 23 m CE90%, excluding any topographic displacement and off-nadir viewing angle.

Further details on the bundled panchromatic and multispectral QuickBird images are given in Table 3.

Table 3. Details on QuickBird image (UL: Upper left corner, UR: Upper right corner, LL: lower left corner, LR: lower right corner, source: www.digitalglobe.com)

Characteristic	QB image	
Bit depth	16	
Resampling option	4x4 cubic convolution	
Map projection & zone	UTM 37S	
Absolute geo-location accuracy	23 m	
Image data format	GeoTIFF 1.0	
	Panchromatic	Multispectral
Resolution (m)	0.7	2.8
Image bands (μm)	0.45-0.9	B ^a : 0.45-0.52 G ^b :0.52-0.60 R ^c :0.63-0.69 NIR ^d : 0.76-0.90
acquisition date/time	2002-10-01T07:42:41.788190	2002-10-01T07:42:42.016938
Solar azimuth (°)	87.5754	87.5752
Solar elevation (°)	67.7637	67.7646
Satellite azimuth (°)	136.0510	136.6640
Satellite elevation (°)	73.3995	73.2791
In track View angle (°)	-9.6492	-9.8475
Cross track view angle (°)	12.1852	12.1719
UL longitude (°)	39.479004	39.447901
UL latitude (°)	-4.397039	-4.397049
UR longitude (°)	39.551197	39.551188
UR latitude (°)	-4.396989	-4.396999
LL longitude (°)	39.479051	39.479060
LL latitude (°)	-4.469401	-4.469391
LR longitude (°)	39.551251	39.551241
LR latitude (°)	-4.469350	-4.469341
UL X	553145.950000	553147.000000
UL Y	9513968.450002	9513967.400002
UR X	561156.050000	561155.000000
UR Y	9513986.450002	9513967.400002
LL X	553145.950000	553147.000000
LL Y	9505969.550002	9505970.600002
LR X	561156.050000	561155.000000
LR Y	9505969.550002	9505970.600002
Row uncertainty	71.720000	72.730000
Colum uncertainty	69.740000	69.570000

^aBlue band. ^bGreen band. ^cRed band. ^dNear infra-red band

III.3 Field survey

A field mission was conducted in July-August 2003. Species assemblages were delineated visually on the panchromatic image based on grey values, structure and texture. At least one transect was done in each vegetation assemblage (vegetation class) using the Point-Centred-Quarter Method (PCQM) of Cottam and Curtis (1956) as described by Cintrón and Schaeffer

Novelli (1984) for use in mangrove forests. In each sample point (chosen at 10 or 20m intervals) four quadrants were established at 90° with respect to the navigational direction. In each quadrant the distance to the closest adult (dA) and young tree (dY) was recorded and for the adult tree the G_{130} (the girth at 130cm height along the main tree stem). Total vegetation coverage in the $5 \times 5 \text{m}^2$ ($10 \times 10 \text{m}^2$) quadrant nearest to the sampling point was estimated and juveniles were counted in the nearest $1 \times 1 \text{m}^2$ in each quadrant. Juveniles are defined as propagules (either dead or alive), seeds or (young) plants with no more than 6 leaves. The distinction between young and adult trees is that adult trees have a G_{130} of more than 8cm. Twenty transect points were taken in each assemblage. A schematical representation of the PCQM is given below. Distances were measured with an optical range-finder, which is generally presumed to give more accurate measurements than a tape. GPS locations of strategically important transect points (e.g. begin, middle and end points) were recorded with Garmin's GPS III.

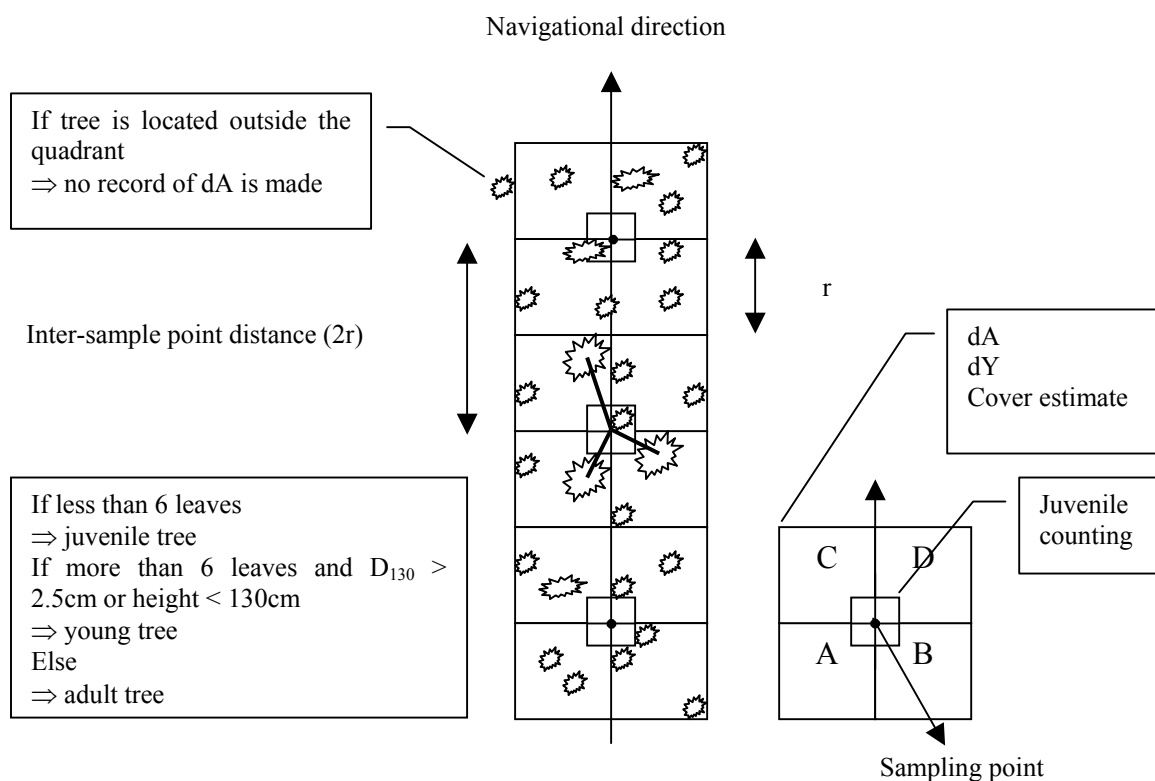


Figure 16. Schematical representation of the Point-Centred-Quarter Method (PCQM of Cottam and Curtis, 1956) used to ground truth the satellite image

Additionally, the relationship between tree height and D_{130} (term according to Brokaw and Thompson (2000), but formerly referred to as DBH, the diameter at breast height) and between crown diameter and D_{130} was experimentally determined for every species encountered in the PCQM surveys. Assuming that the horizontal cross-section of the stem is nearly circular, the D_{130} can be approximated from the G_{130} (measured with tape) with the following formula:

$$D_{130} \cong \frac{G_{130}}{\pi}$$

Tree height was determined with a hypsometer, which immediately transforms angle measurements into height measurements. The principle of measuring tree height with a hypsometer is explained in Figure 17. At a horizontal distance $d(o,t)$ from the tree, the observer measures the angle α between eye height of the observer H_o at distance $d(o,t)$ and the top leaf of the tree. Using the trigonometric relationships of right triangles, H_t' can be determined from the measurement of the angle α and $d(o,t)$:

$$H_t' = d(o,t) \times \text{tg}\alpha$$

The tree height H_t is then the sum of H_t' and H_o . The (significance of the) relationship between tree height and D_{130} and between D_{130} and crown diameter (CD) was tested with an F-test.

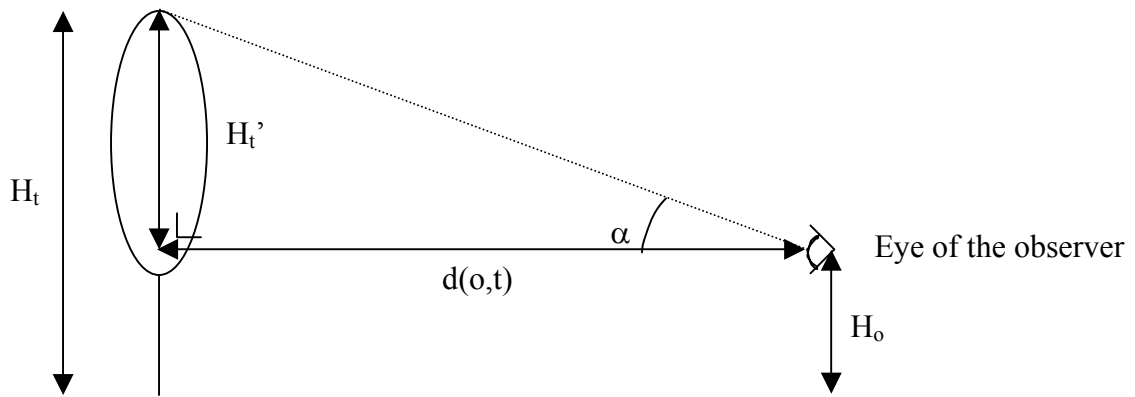


Figure 17. Principle of measuring tree height with a hypsometer

The distance to the nearest young tree (dY) and the counting of the juveniles is not of direct importance in this work, but is important for studies on vegetation structure dynamics (Dahdouh-Guebas, 2001) of the mangrove forest. Also, some forest parameters for each ground truthed assemblage were calculated using the methods described by Cintrón and Schaeffer Novelli (1984).

For each assemblage parameters s.a. absolute density, height, basal area, complexity index, (see formulas below) relative density, relative dominance, relative frequency and importance value (see formulas in section II.15.3.2) were calculated. Because the PCQM was performed with the 5 or 10m limit for tree distance from the sample point, a correction factor for the density calculation, as suggested by Verheyden (1997) was introduced (taking into account the number of empty cells). The density was computed as follows:

$$\text{density}'(m^{-2}) = \text{density}(m^{-2}) \times \frac{n^{\circ} \text{FullCells}}{n^{\circ} \text{TotalCells}}$$

The stem density per species is

$$SD_{Species} (n^{\circ} stems / 0.1ha) = \frac{n^{\circ} OccurencesOfSpecies}{\sum_{AllSpecies} n^{\circ} OccurencesOfSpecies} \times density'(m^{-2}) \times 1000$$

and the total stem density of an assemblage is

$$TSD(n^{\circ} stems / 0.1ha) = \sum_{AllSpecies} SD_{Species} (n^{\circ} stems / 0.1ha)$$

The basal area of a tree with stem diameter D_{130} is

$$BA(m^2) = \frac{\pi \times D_{130}(cm)^2}{40000}$$

We continue by taking the average of basal areas of trees of a certain species in the assemblage $m(BA_{Species})$. The basal area of a species $BA_{Species}$ in an assemblage is

$$BA_{Species} (m^2 / 0.1ha) = SD_{Species} (n^{\circ} stems / 0.1ha) \times m(BA_{Species})$$

and the total basal area of the assemblage is

$$TBA(m^2 / 0.1ha) = \sum_{AllSpecies} BA_{Species} (m^2 / 0.1ha)$$

The *complexity index* (*CI*) (Holdridge *et al.*, 1971) is calculated from

$$CI = TSD \times TBA \times n^{\circ} Species \times TreeHeight ,$$

where *TreeHeight* is the average tree height in the assemblage.

III.4 Satellite image preprocessing

III.4.1 Geometric correction

The model used in the image geometric correction was the QuickBird RPC model, based on rational polynomial coefficients (RPCs) that are generated by the data provider based on the position of the satellite at the time of image capture. These RPCs were further refined using GCPs, so as to apply polynomial corrections of the first order to the original rational function model. This corrects the remaining error and refines the mathematical solution. GPS positions for a number of easily recognizable and well spread GCPs on the satellite image were recorded by KMFRI staff members in January 2004 with Garmin's GPS III.

X and Y residuals, RMS error and error contribution were calculated for each GCP, as well as the total X and Y residual and RMS error.

III.4.2 Mangrove subset

To speed up the further processing of the image (resolution merge, spectral image enhancement and spectral classification), a subset of the original satellite image was created: the smallest possible rectangle that covered the mangrove area of interest. The UTM coordinates of the upper left corner and the lower right corner are given in Table 4.

Table 4. Corner coordinates of the subset covering the whole mangrove area

	Upper left corner	Lower right corner
X (UTM)	555664.45	559647.08
Y (UTM)	9513696.87	9509830.24

III.4.3 Multiresolution merge

The subsetting panchromatic (PAN) and multispectral (XS) images were merged using the principle component merge and the cubic convolution resampling method. The resulting pansharpened multispectral image is referred to as PXS further in this work.

III.5 Spectral enhancement

III.5.1 Colour composites

A false (or true) colour composite image results if the DN values measured by the sensor in the green portion of the spectrum are represented in the green colour gun, the blue in the blue and the near-infrared (or red) in the red colour gun.

III.5.2 Contrast stretch through masking

At first, two-dimensional feature space images of the multispectral image were made to get a first graphical view of the distribution of the image data pixels in feature space. An attempt was made to locate typical pixels for water, sand, infrastructure, mangrove vegetation, and terrestrial vegetation in feature space to evaluate the possibility of creating a non-mangrove mask through feature space masking.

Later on, a mask separating the mangrove from the non-mangrove area was made manually. An unsupervised classification of the PXS and the XS image was done using 4 classes (convergence threshold of 95% was reached after 7 iterations) to further mask out the water and sandy areas in the mangrove. This was done for both the XS and the PXS image and the resulting images will be referred to as MXS and MPXS respectively.

The assemblages corresponding to each of the TS used in supervised classification (see section IV.5.1.1) are described in terms of their tonality, texture, structure on the MPXS false

colour composite (FCC) image and if individual tree crowns are discernable a description of their shape and size is given.

III.5.3 Principal component transformation

A principal component image of the MPXS image was produced and will be referred to as PCA_MPXS. Eigenvalues and eigenvectors were calculated.

The assemblages corresponding to each of the TS used in supervised classification (see section IV.5.1.1) are described in terms of their tonality, texture, structure on the PCA_MPXS image (PC1 in R colour gun, PC2 in G colour gun, PC3 in B colour gun) and if individual tree crowns are discernable a description of their shape and size is given. The visual interpretability of PCA_MPXS was compared with the original image (MPXS).

III.5.4 Indices

The normalized difference vegetation index (NDVI) was calculated for MXS using settings predefined for the Landsat MSS sensor, so that

$$NDVI = \frac{NIR - R}{NIR + R}$$

The NDVI-layer was added to MXS as an additional layer resulting in a five-dimensional image: MXS+NDVI.

III.5.5 Texture

The variance texture measure was calculated in a 7x7 pixels window around the centre pixel and in a 21x21 pixels window from the PAN image and was added as an additional layer to the MPXS image. The resulting five-dimensional images will be referred to as MPXS+VAR7 and MPXS+VAR21.

III.6 Unsupervised classification of the multispectral images

III.6.1 Unsupervised classification of MXS

An unsupervised classification of MXS was done using the ISODATA clustering method with fifteen spectral classes. A convergence threshold of 95% was reached after 8 iterations.

III.6.2 Unsupervised classification of MPXS

An unsupervised classification of MPXS was done using the ISODATA clustering method with 15 spectral classes. The results were compared with the results for the unsupervised classification of MXS.

III.7 Supervised classification

III.7.1 Supervised classification of MXS

III.7.1.1 SELECTION OF TRAINING SITES

When selecting training sites it is important to realize that many factors influence the reflectance from vegetation canopies, some diagnostic of the vegetation types of interest in the vegetation mapping process and others unrelated. The vegetation factors known to influence the spectral reflectance of vegetation canopies include the overall life form of the vegetation, leaf properties (leaf area and leaf angle distribution and spectral reflectance properties), vegetation height or tree size, the fractional cover of vegetation, and the health and water content of leaves. In addition, the soil colour and wetness contribute to the spectral response at any given location in the image. The net effect is that the same vegetation type may have many spectral manifestations in the image, which significantly complicates the image classification process (Woodcock *et al.*, 2002).

The most homogeneous and most representative groups of pixels in each category of interest were selected by drawing training areas of interest (AOI). Those categories include the most common species encountered in the mangroves of Gazi Bay: *Avicennia marina* (Amar), *Bruguiera gymnorrhiza* (Bgym), *Ceriops tagal* (Ctag), *Rhizophora mucronata* (Rmuc) and *Sonneratia alba* (Salb).

No training sites were developed for the remaining less common mangrove species *Heritiera littoralis*, *Lumnitzera racemosa*, *Pemphis acidula*, *Xylocarpus granatum* and *X. moluccensis*, because of a lack of large enough homogeneous regions.

Training pixel data were deduced from the same training AOI's in both the MXS and the MXS+NDVI image.

Overlap between training sites and PCQM transects (test data) should be avoided, but here this was not always the case because the satellite image was only geometrically corrected in February 2004 (after the ground control points were recorded). Overlap between transect data and training sites occurs for AS and A&R&C, AS and A&R, CNFP and Ctag, AGazi and Amar, ALD and C&a, and for CNMak and Ctag2.

III.7.1.2 TRAINING SITE STATISTICS

A signature report was produced containing the mean, minimum, maximum and standard deviation of each signature in each band. Histograms were visually checked for unimodality to validate the use of the ML classifier. When large deviations (*e.g.* bimodality) were noted, signatures were refined or changed.

III.7.1.3 EVALUATION OF THE DEGREE OF BETWEEN-CLASS SEPARABILITY

Contingency matrices, transformed divergence indices and feature space ellipses were calculated to evaluate the between-class separability of the signatures for the classes generated by the training data pixels. Based on these matrices and indices, classes were merged, separated or deleted.

III.7.1.4 FUZZY CLASSIFICATION

Fuzzy classifications were computed for both the MXS image and the MXS+NDVI image.

In a first step a fuzzy classification was done, calculating the four best classes according to the ML classifier for each pixel in the image and a distance file containing the Mahalanobis distance between the feature vector of each pixel and the mean vector of the pixel's class.

Secondly, fuzzy convolution with various window sizes (3x3, 5x5 and 7x7) was performed. The values from the distance D_{ijm} file were weighted by distance from the centre pixel (values of w_{ij} in formula in section II.12). The distance tables used in the various fuzzy convolutions (3x3, 5x5 and 7x7) are given in Table 5, Table 6 and Table 7, respectively.

Table 5. Distance table for fuzzy convolution of window size 3x3

0.500	0.646	0.500
0.646	1.000	0.646
0.500	0.646	0.500

Table 6. Distance table for fuzzy convolution of window size 5x5

0.500	0.605	0.646	0.605	0.500
0.605	0.750	0.823	0.750	0.605
0.646	0.823	1.000	0.823	0.646
0.605	0.750	0.823	0.750	0.605
0.500	0.605	0.646	0.605	0.500

Table 7. Distance table for fuzzy convolution of window size 7x7

0.500	0.575	0.627	0.646	0.627	0.575	0.500
0.575	0.667	0.736	0.764	0.736	0.667	0.575
0.627	0.736	0.833	0.882	0.833	0.736	0.627
0.646	0.764	0.882	1.000	0.882	0.764	0.646
0.627	0.736	0.833	0.882	0.833	0.736	0.627
0.575	0.667	0.736	0.764	0.736	0.667	0.575
0.500	0.575	0.627	0.646	0.627	0.575	0.500

III.7.1.5 CLASSIFICATION ACCURACY ASSESSMENT

Transect PCQM data from the adult tree layer was used as it was assumed that this layer represented the remotely sensed canopy (e.g. Dahdouh-Guebas *et al.*, 2004a, in press). The 15 transects were drawn in a vector layer and an overlay analysis of these transects and the geometrically corrected classified MXS image was done. Classification accuracy (testing 1200 PCQM observations) was determined using an error matrix, calculating overall, user's and producer's accuracy and κ and τ coefficients (see section II.8.7).

In the PCQM each quadrant corresponds to a certain species (assumed to be the dominant species in that quadrant), while one quadrant covers many pixels, mostly belonging to different classes. The classification of a whole quadrant needs to be compared to the

observation on the field (a mangrove species). The class covering the largest area of the quadrant was assigned to the whole quadrant. If there was no dominance of a single class, different classes were assigned to a single quadrant with different proportionality coefficients corresponding to the area covered by each class (e.g. 0.5 Class 1 and 0.5 Class 2).

An exception to this rule is made for the class “Nil”. On the field, “Nil” corresponds to an empty quadrant, meaning that there was no mangrove tree found in an 5x5m² or 10x10m² area. Masked pixels (which correspond to water or sand) are considered empty (containing no mangrove) and form class “Nil”. A quadrant was only assigned class Nil if it was completely covered by masked pixels. If class Nil dominantly covered a quadrant, but also some other classes are present in the quadrant, the quadrant will be assigned the dominant class, other than the Nil class.

As it was often not the case that the adult tree layer represented the remotely sensed canopy, another classification accuracy assessment was done taking into consideration only those transect data where the assumption was fulfilled. The transect data used in this classification accuracy determination were Amar, Amar2, Ctag (only until the 13th PCQM point), Ctag2, Ctag3, Rmuc, Rmuc2 and Salb, amounting to 612 PCQM observations. Classification accuracies were determined for MXS and MXS+NDVI.

III.7.2 Supervised classification of MPXS

III.7.2.1 SELECTION OF TRAINING SITES

The TS selected here were essentially the same as the TS selected for the classification of the MXS image. Some small adaptations were made to exclude zero pixels in the AOIs resulting from the masking of water and sand.

III.7.2.2 TRAINING SITES STATISTICS

A signature report was produced containing the mean, minimum, maximum and standard deviation of each signature in each band. Histograms were visually checked for unimodality to validate the use of the ML classifier. When large deviations (e.g. bimodality) were noted, signatures were refined or changed.

III.7.2.3 EVALUATION OF THE DEGREE OF BETWEEN CLASS SEPARABILITY

Contingency matrices and transformed divergence indices were calculated to evaluate the between-class separability of the signatures for the classes generated by the training data pixels.

III.7.2.4 FUZZY CLASSIFICATIONS

Fuzzy classifications were calculated for the MPXS, the MPXS+VAR7 and the MPXS+VAR21 images. To save processing time, only the two best classes were calculated for each pixel. Fuzzy convolution was applied using a 7x7 window.

III.7.2.5 CLASSIFICATION ACCURACY ASSESSMENT

Classification accuracy (error matrix) was determined for the MPXS, the MPXS+VAR7 and the MPXS+VAR21 images using the transect data from those transects where the assumption that the adult tree layer in the PCQM transects represented the remotely sensed canopy was not violated (see section III.7.1.5). From the error matrices, overall, producer's and user's accuracies, κ and τ coefficients were determined.

III.8 Area covered by each mangrove species

The area covered by each of the 15 classes was calculated from the histogram values using the formula

$$area(km^2) = \frac{histvalue \times pixelsize(m)^2}{10^6}$$

The areas of the classes representing the same mangrove species were then summed to obtain an area per species.

III.9 Automated delineation of vegetation assemblages

Automated assemblages were derived from the fuzzy classifications of the MXS and MXS+NDVI images using a 7x7 pixel convolution window. Continuous groups of pixels (including the diagonal pixels) belonging to the same image class covering less than 50 pixels (= 392m²) were eliminated in the image, replacing the values of pixels in these groups with the value of nearby larger groups. Afterwards contour lines were drawn around these continuous areas. These contour line images are also put on transparency so that they can be overlaid on the classifications.

III.10 Visual delineation of vegetation assemblages

Visual delineation of vegetation assemblages was done on the MPXS FCC by three naïve volunteers (meaning that they have no experience in image interpretation). The delineation was done with pens on slides on print-outs of the FCC of the MPXS image. The delineation was then digitized in a vector layer. And this vector layer was overlaid on the fuzzy classifications of the MXS and MXS+NDVI image after elimination of continuous pixel groups of less than 50 pixels.

III.11 Area covered by mangrove, sand and water

The area covered by the mangrove vegetation of Gazi Bay, sand and water were calculated from the QB satellite image. Another mask than formerly used, more accurately delineating the mangrove from the non-mangrove, was created. An unsupervised classification of the selected area with 6 classes (3 mangrove classes, 2 water classes and 1 sand class) was done

and the area covered by each class was calculated from the histogram values of each class, as explained in section III.8.

IV Results

IV.1 Results of the field survey

In total, 15 transects of 20 sampling points each were conducted in different vegetation assemblages in the mangrove area. The number of stems per 0.1ha, stand height (SH), number of species, basal area (BA), complexity index (CI) and average crown diameter (CD) were calculated for each ground-truthed vegetation assemblage and are shown in Table 10. Statistical results of the regression analysis between D_{130} and height for each mangrove species and between D_{130} and CD are given in Table 8 and Table 9, respectively. The plots of tree height vs. D_{130} and CD vs. D_{130} and the equations obtained are given in the Appendix.

Table 8. Regression statistics between D_{130} and height for each species

Species	#obs	df	F	p	R^2	Equation
<i>Amar</i>	60	1.580	186.230	0.000000	0.7625	H = 5.3193Ln(D_{130}) - 4.7831
<i>Bgym</i>	68	1.660	3.684	0.053540	0.0553	H = 0.7579Ln(D_{130}) + 3.3425
<i>Ctag</i>	110	1.108	24.728	0.000003	0.1863	H = 1.3423Ln(D_{130}) + 1.6023
<i>Rmuc</i>	304	1.302	192.462	0.000000	0.3892	H = 1.6898Ln(D_{130}) + 2.3347
<i>Salb</i>	139	1.137	127.764	0.000000	0.4826	H = 1.6116Ln(D_{130}) + 1.6939

Table 9. Regression statistics between D_{130} and CD for each species

Species	#obs	df	F	p	R^2	Equation
<i>Amar</i>	40	1.380	69.168	0.000000	0.6454	CD = 2.8067Ln(D_{130}) + 0.1417
<i>Bgym</i>	7	1.500	17.509	0.008619	0.7779	CD = 8.1594Ln(D_{130}) - 8.5757
<i>Ctag</i>	45	1.430	24.313	0.000013	0.3612	CD = 1.0584 Ln(D_{130}) + 0.7566
<i>Rmuc</i>	207	1.205	1.205	0.000000	0.7079	CD = 1.7565Ln(D_{130}) - 0.2466
<i>Salb</i>	74	1.720	93.067	0.000000	0.5638	CD = 1.5093Ln(D_{130}) + 0.4508

Relative density (DE_r), dominance (DO_r) and frequency (F_r'), importance value (IV) and rank (R) were calculated for each species in each vegetation assemblage and are given in Table 11. The formulas are given in section III.3. Because of the great extent of vegetation assemblages *Rmuc2* and *R&B*, the distance between two sampling points on the transect line was 20m, instead of 10m. An imaginary assemblage “All” is created from all PCQM data added. Its absolute characteristics are given in Table 10 and its relative characteristics are given in Table 12.

The naming of the vegetation assemblages was done based on the values of relative dominance of each species in the vegetation assemblage. If the difference between the relative dominance of the dominant species and the relative dominance of the second dominant

species is more than 60%, the name of the assemblage is the name of the dominant species (*e.g.* Amar). If this difference is between 45% and 60%, the name of the assemblage consist of two parts: the first letter of the dominant species in capital, followed by “&” and the first letter of the second dominant species. If the difference is between 10% and 45%, the name of the assemblage consist again of multiple parts: the first letter of the dominant species in capital, followed by “&” and the first letter of the second dominant species also in capital. Maybe followed by the first letter of the third dominant species if the difference in relative dominance between the second and third dominant species is between 10 and 45%. A species with a relative dominance of less than 10% is not mentioned in the name of the assemblage. And finally, if more than 4 species have a relative dominance greater than 5%, the name of the vegetation assemblage is “Mixed”.

Table 10. Absolute characteristics of each ground-truthed vegetation assemblage in Gazi Bay: number of stems per 0.1 ha, mean stand height, number of species, basal area, complexity index (Cottam and Curtis, 1956) and mean crown diameter

Vegetation assemblage	#Stems/0.1h	SH(m) ^a	#Spp	BA(m ² /0.1ha) ^b	CI ^c	CD(m) ^d
Amar	242.70	4.80	1	0.93	1.08	2.99
Amar2	203.67	1.64	1	0.24	0.08	1.63
A&R	101.13	5.11	3	0.58	0.90	2.69
A&R&C	217.79	5.25	3	0.83	2.86	2.98
B&R	244.55	4.59	3	0.88	2.95	2.58
C&a	578.62	2.48	3	0.76	3.29	1.84
Ctag	584.39	3.38	1	1.09	2.17	2.16
Ctag2	998.25	3.43	1	1.41	4.84	2.20
Ctag3	1014.15	2.84	2	0.98	5.67	1.97
Mixed1	429.51	4.76	4	3.37	27.58	2.61
Mixed2	279.42	5.17	4	2.51	14.49	2.81
R&B	167.44	5.83	3	2.46	7.20	3.32
Rmuc	293.81	5.08	1	1.90	2.83	2.37
Rmuc2	354.07	4.93	4	1.35	9.43	2.68
Salb	67.81	4.06	2	2.36	1.30	4.09
ALL	281.38	4.22	5	1.25	7.41	2.55

^aStand height. ^bBasal area. ^cComplexity index. ^dCrown diameter

Table 11. Relative density (DE_r), relative dominance (DO_r) and relative frequency (Fr'), importance value (IV) and rank (R) of each species in each ground-truthed vegetation assemblage in Gazi Bay (2003)

Species	Vegetation class																								
	Amar					Amar2					A&R					A&R&C					B&R				
	DE _r (%)	DO _r (%)	Fr' (%)	IV	R	DE _r (%)	DO _r (%)	Fr' (%)	IV	R	DE _r (%)	DO _r (%)	Fr' (%)	IV	R	DE _r (%)	DO _r (%)	Fr' (%)	IV	R	DE _r (%)	DO _r (%)	Fr' (%)	IV	R
<i>Amar</i>	100.0	100.0	100.0	300.0	1	100.0	100.0	100.0	300.0	1	32.4	58.6	45.5	136.4	2	30.4	44.8	28.6	103.8	2	0.0	0.0	0.0	0.0	4
<i>Bgym</i>	0.0	0.0	0.0	0.0	2	0.0	0.0	0.0	0.0	2	0.0	0.0	0.0	0.0	4	0.0	0.0	0.0	0.0	4	64.9	62.4	51.5	178.9	1
<i>Ctag</i>	0.0	0.0	0.0	0.0	2	0.0	0.0	0.0	0.0	2	0.0	0.0	0.0	0.0	4	26.6	21.3	25.7	73.6	3	5.2	1.4	9.1	15.7	3
<i>Rmuc</i>	0.0	0.0	0.0	0.0	2	0.0	0.0	0.0	0.0	2	66.2	32.6	51.5	150.3	1	43.0	33.9	45.7	122.6	1	29.9	36.1	39.4	105.4	2
<i>Salb</i>	0.0	0.0	0.0	0.0	2	0.0	0.0	0.0	0.0	2	1.4	8.8	3.0	13.2	3	0.0	0.0	0.0	0.0	4	0.0	0.0	0.0	0.0	4
Species	C&a					Ctag					Ctag2					Ctag3					Mixed1				
	DE _r (%)	DO _r (%)	Fr' (%)	IV	R	DE _r (%)	DO _r (%)	Fr' (%)	IV	R	DE _r (%)	DO _r (%)	Fr' (%)	IV	R	DE _r (%)	DO _r (%)	Fr' (%)	IV	R	DE _r (%)	DO _r (%)	Fr' (%)	IV	R
	<i>Amar</i>	32.5	21.4	37.9	91.8	2	0.0	0.0	3.8	3.8	4	0.0	0.0	0.0	0.0	2	2.5	2.2	9.1	13.7	2	6.4	28.5	11.6	46.6
<i>Bgym</i>	0.0	0.0	0.0	0.0	4	0.0	0.0	11.5	11.5	2	0.0	0.0	0.0	0.0	2	0.0	0.0	0.0	0.0	3	17.9	28.7	25.6	72.2	3
<i>Ctag</i>	66.3	72.7	58.6	197.6	1	100.0	100.0	76.9	276.9	1	100.0	100.0	100.0	300.0	1	97.5	97.8	90.9	286.3	1	35.9	11.8	30.2	77.9	2
<i>Rmuc</i>	1.3	5.9	3.4	10.6	3	0.0	0.0	7.7	7.7	3	0.0	0.0	0.0	0.0	2	0.0	0.0	0.0	0.0	3	39.7	31.0	32.6	103.3	1
<i>Salb</i>	0.0	0.0	0.0	0.0	4	0.0	0.0	0.0	0.0	5	0.0	0.0	0.0	0.0	2	0.0	0.0	0.0	0.0	3	0.0	0.0	0.0	0.0	5
Species	Mixed2					R&B					Rmuc					Rmuc2					Salb				
	DE _r (%)	DO _r (%)	Fr' (%)	IV	R	DE _r (%)	DO _r (%)	Fr' (%)	IV	R	DE _r (%)	DO _r (%)	Fr' (%)	IV	R	DE _r (%)	DO _r (%)	Fr' (%)	IV	R	DE _r (%)	DO _r (%)	Fr' (%)	IV	R
	<i>Amar</i>	10.4	13.7	11.8	35.8	4	2.5	5.3	6.1	13.9	3	0.0	0.0	16.1	16.1	2	0.0	0.0	0.0	0.0	5	0.0	0.0	0.0	0.0
<i>Bgym</i>	6.5	43.8	11.8	62.1	2	16.3	41.1	33.3	90.6	2	0.0	0.0	12.9	12.9	3	5.0	6.2	10.7	22.0	3	0.0	0.0	0.0	0.0	3
<i>Ctag</i>	16.9	2.7	20.6	40.2	3	0.0	0.0	0.0	0.0	4	0.0	0.0	9.7	9.7	4	6.3	3.5	14.3	24.1	2	0.0	0.0	0.0	0.0	3
<i>Rmuc</i>	66.2	39.8	55.9	161.9	1	81.3	53.6	60.6	195.5	1	100.0	100.0	61.3	261.3	1	87.5	86.7	71.4	245.6	1	4.1	0.3	9.1	13.5	2
<i>Salb</i>	0.0	0.0	0.0	0.0	5	0.0	0.0	0.0	0.0	4	0.0	0.0	0.0	0.0	5	1.3	3.6	3.6	8.4	4	95.9	99.7	90.9	286.5	1

Table 12. Relative density (DE_r), dominance (DO_r) and frequency (Fr'), importance value (IV) and rank (R) for all vegetation assemblages added

	ALL				
	DE _r	DO _r	Fr'	IV	R
	(%)	(%)	(%)		
<i>Amar</i>	21.7	21.5	20.4	63.6	3
<i>Bgym</i>	7.5	22.1	11.6	41.2	4
<i>Ctag</i>	31.5	12.9	29.7	74.0	2
<i>Rmuc</i>	35.1	43.5	33.5	112.2	1
<i>Salb</i>	4.3	0.0	4.7	9.0	5

IV.2 Satellite image preprocessing

IV.2.1 Geometric correction

The QB satellite image is already geometrically corrected and mapped onto a cartographic projection by Digital Globe company. The coordinates of a ground control point (GCP) as read from the satellite image seemed not to correspond to the coordinates of the GCP as measured on the field with a GPS (denoted by asterisks in Figure 18). The coordinates as measured on the field were systematically located South West of the true location of the GCP on the satellite image (see Figure 18 and Table 13). Unfortunately, the accuracy of the GPS measurements was not recorded. But, based on the fact that all points were located in open sky with no hindrance of for example canopy, we can assume that the positional accuracy was between 3 and 4m at every point. The distance between the true location of the point and the GPS coordinates varied between 6 and 14m. This was an indication that the satellite image georeferencing needed further refinement.

The UTM coordinates of the GCPs used are given in Table 13 together with parameters obtained through model solution (X residual (R_{xi}), Y residual (R_{yi}), RMS error (R_i) and error contribution (C_i) for each GCP). The total RMS error (T), X RMS error (R_x) and Y RMS error (R_y) were also calculated with the formulas given in section II.4.

The positions of the PCQM transects are shown in Figure 19. If no polynomial refinement of the geometric correction would have been done, the transect begin points of Mixed2 and Rmuc2 were located in the water.

Table 13. UTM coordinates of ground control points (GCPs) used in the georectification of xs. Input coordinates are read from the satellite image, reference coordinates are read from the GPS recorder.

GCP	Input		Reference		Model			
	X (UTM)	Y (UTM)	X (UTM)	Y (UTM)	R_{xi}^a	R_{yi}^b	R_i^c	C_i^d
Ref	556157.849453	9510971.799781	556148.366008	9510964.021795	-0.767	0.586	0.965	0.881
Madrasa	556267.839825	9510882.120131	556256.624262	9510875.068046	-1.296	0.259	1.322	1.207
Coco1	556111.805000	9510465.890000	556108.454838	9510460.058132	1.443	-0.261	1.466	1.339
Coco2	556263.308972	9510368.102626	556259.008500	9510326.010000	1.226	-0.254	1.252	1.143
Salb1	557663.889497	9511186.468490	557652.336074	9511178.009047	-0.403	0.367	0.545	0.497
Salb2	557610.378556	9511221.231072	557600.557723	9511214.045262	0.174	-0.058	0.183	0.167
Salb3	557543.040700	9511188.733917	557528.864622	9511183.129983	-1.432	-0.607	1.556	1.420
MRoad	556509.816852	9513588.116003	556501.659898	9513586.102578	-0.286	-0.732	0.786	0.717
CoralDog	558045.925410	9512780.374816	558038.762090	9512774.145841	1.298	-0.040	1.298	1.185
SaltPan	557095.430219	9513404.940980	557086.919473	9513398.053046	0.044	0.739	0.740	0.676
					$R_x^e = 0.9932$			
					$R_y^f = 0.4620$			
					$T^g = 1.0954$			

^aX residual, ^bY residual, ^cRMS error and ^dError contribution per GCP. ^eX RMS error. ^fY RMS error. ^gTotal RMS error.

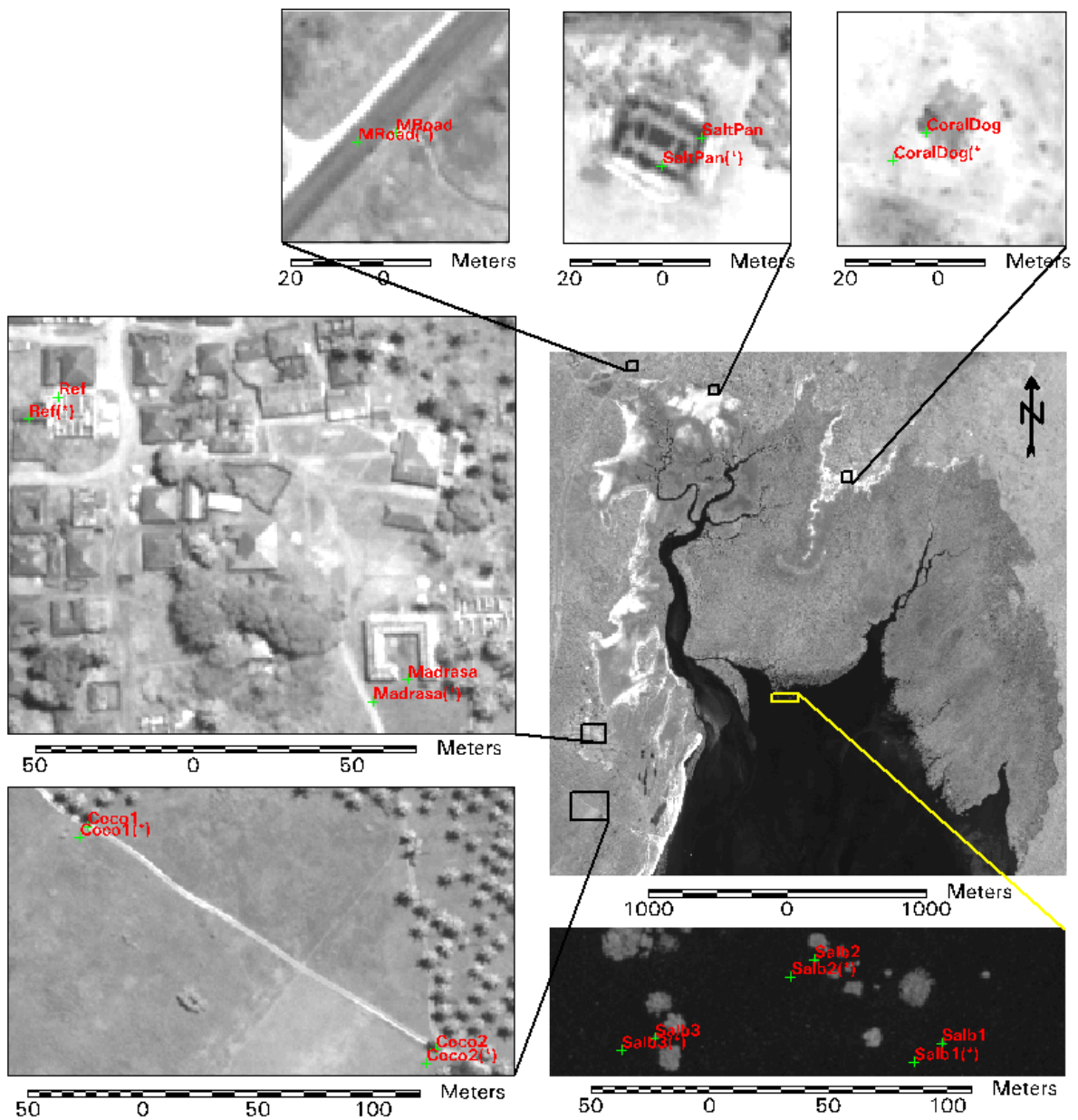


Figure 18. Location of GCPs on the panchromatic QB image indicated with green crosshairs. The names followed by (*) refer to the location of the GCP as indicated by the GPS equipment and the non-primed names show the actual location of the GCPs on the satellite image

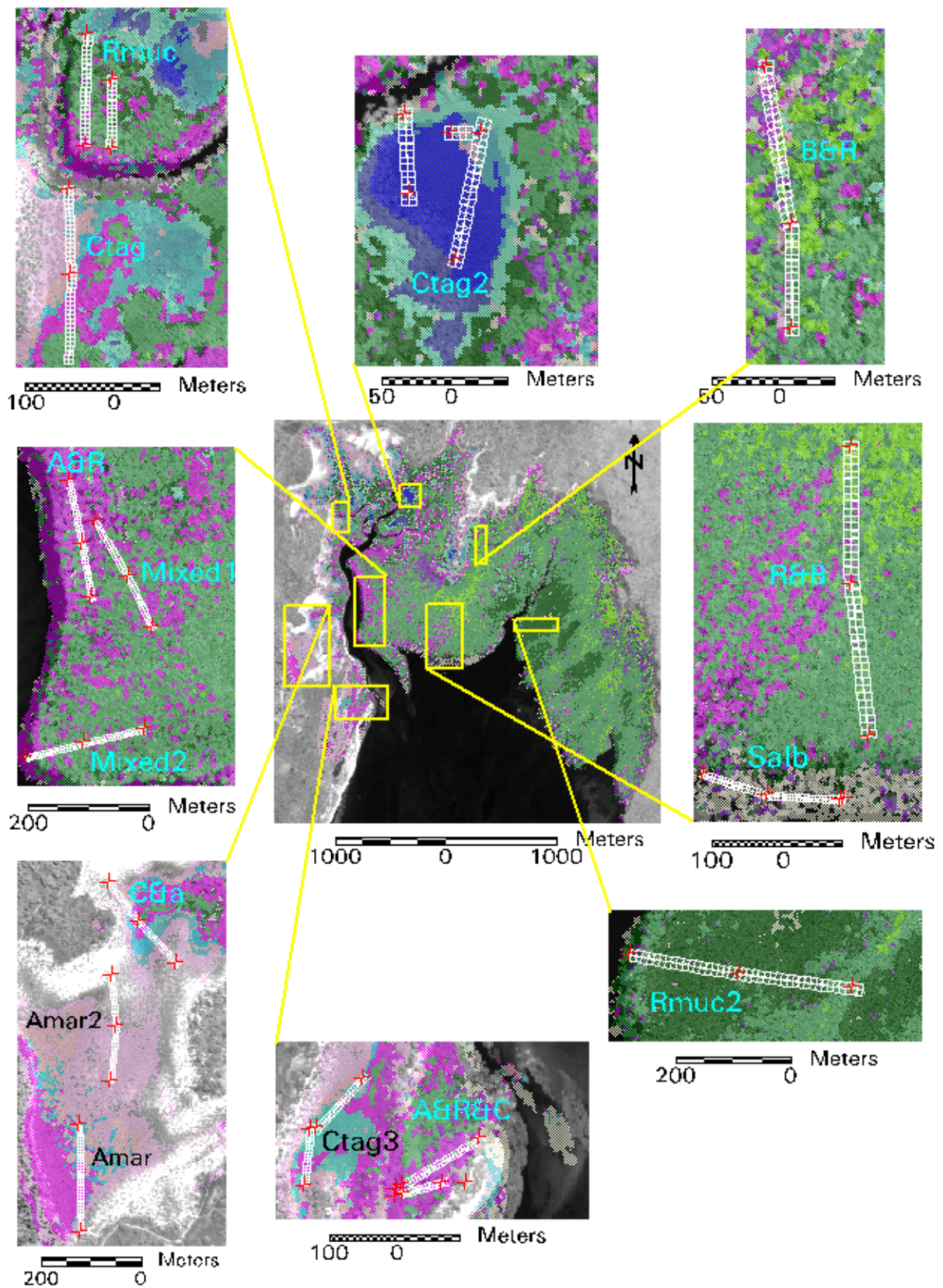


Figure 19. Positioning of transects on a geometrically corrected classified image overlaid on the panchromatic (uncorrected) image to show the effect of the polynomial refinement of image geometric correction

Table 14 shows the positional accuracy of the GPS readings at the start, in the middle and at the end of the transects. Sometimes it was not possible to do a straight transect in an assemblage because of its small size, and in those cases transects were split into pieces (e.g. A&R&C). It is clear that the height and density of the canopy influences the accuracy of the GPS measurement. At the endpoint of the Ctag transect it was even impossible to do a GPS measurement because of the dense canopy. Therefore the position of the endpoint was determined at 100m south of CtagM.

Table 14. Positional accuracy of the GPS recordings at the start (S), in the middle (M) and at the end (E) of the transects

<u>GPS point</u>	<u>Acc.^a (m)</u>						
AmarS	3.7	B&RS	7.4	Ctag2E	2.9	RmucS	8.8
AmarE	5.3	B&RM	8.8	Ctag3s	3.6	RmucE1	6.3
Amar2S	3.1	B&RE	7.2	Ctag3M	3.7	RmucS2	6.4
Amar2M	3.1	C&aS	3.2	Ctag3E	3.1	RmucE2	6.2
Amar2E	3.5	C&aM	6.5	Mixed1S	9.1	Rmuc2S	4.5
A&RS	7.8	C&aE	2.8	Mixed1M	6.2	Rmuc2M	5.3
A&RM	6.1	CtagS	2	Mixed1E	5.5	Rmuc2E	6.4
A&RE	8.3	CtagM	2.9	Mixed2S	3.9	SalbS	4.3
A&R&CS	3.7	CtagE	impossible	Mixed2M	10.3	SalbM	5.8
A&R&CE1	5	Ctag2S	4	Mixed2E	6.3	SalbE	6.5
A&R&CS2	5	Ctag2M	4.3	R&BS	6.3		
A&R&CE2	3.3	Ctag2S2	3.3	R&BM	8.3		
		Ctag2S3	3.4	R&BE	6.7		

^aAccuracy

IV.2.2 Mangrove subset

The mangrove subset is roughly equal to the central image in the FCC image in Figure 21.

IV.2.3 Multiresolution merge

A natural colour image of PXS is given in Figure 20. A FCC of the PXS image is given in Figure 21.

IV.3 Spectral enhancement

IV.3.1 Natural colour image

Some important geographical features will be referred to by their local names: Makongeni Creek, Kinondo Creek, New fishermen's place, Old fishermen's place, *Salb* plantation and

other's were given a name: *Salb* island*, Banana shaped island, Landward *Amar* zone, East Kinondo mangrove area, Central mangrove area and North Makongeni mangrove area. These features are shown on a natural colour image in Figure 20.

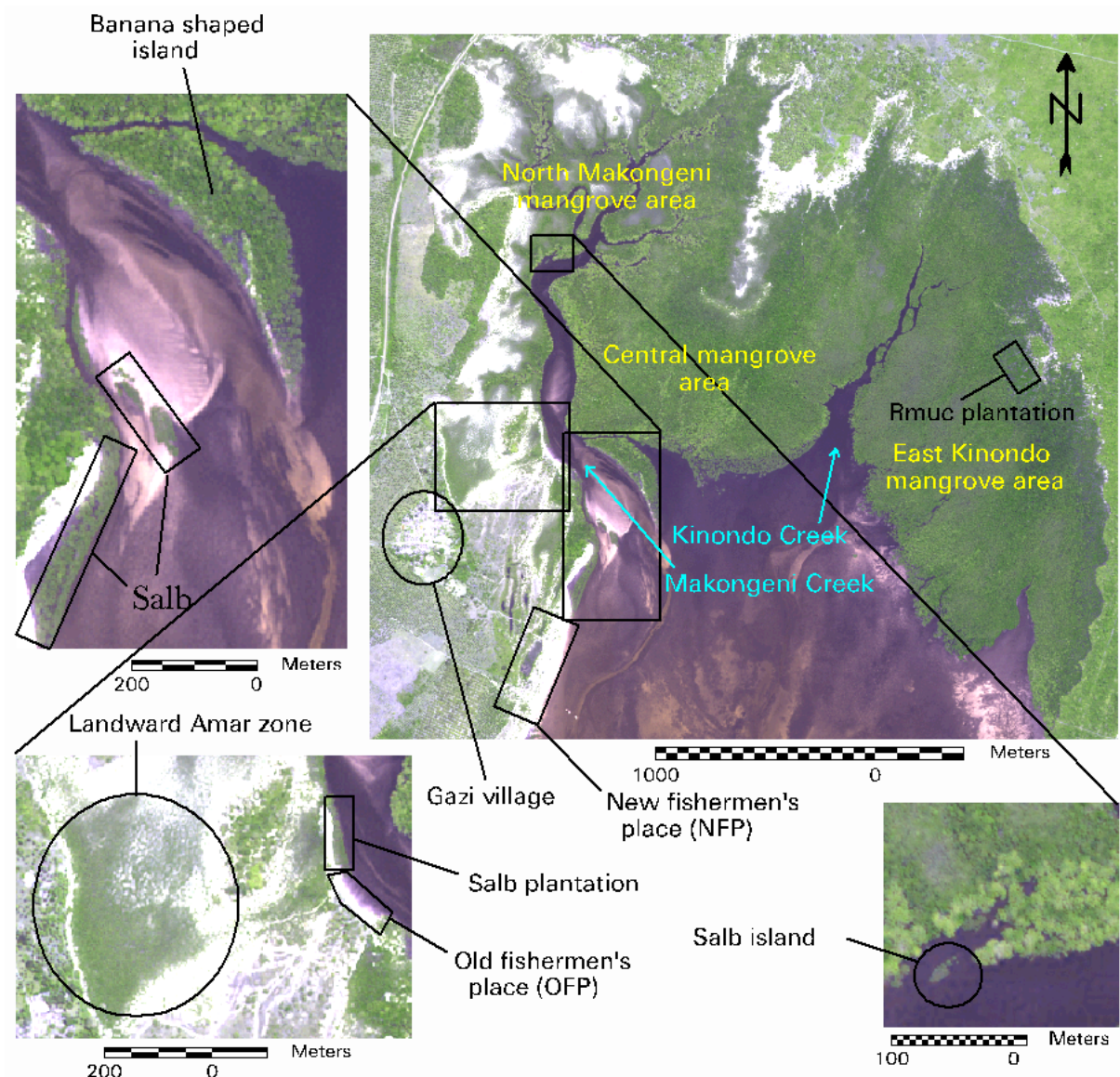


Figure 20. Natural colour transformation of the PXS image: overview of region names adopted in this work

IV.3.2 False colour composite

To ease comparison between two images resulting from a certain image processing step (spectral enhancement or image classification), 7 subsets were created and are shown on the FCC image in Figure 21. The coordinates of the upper left and lower right corner of each of those subsets are given in Table 15.

* End point of what is known as GAZI COVERED (Verneirt, 1994; De Bondt, 1995; Matthys, 1996; Dahdouh-Guebas *et al.*, 2002; Dahdouh-Guebas *et al.*, 2004c, in press)

Table 15. UTM, latitude and longitude corner coordinates of subsets A-G

	Upper left corner				Lower right corner			
	<u>X (UTM)</u>	<u>Y (UTM)</u>	<u>Latitude</u>	<u>Longitude</u>	<u>X (UTM)</u>	<u>Y (UTM)</u>	<u>Latitude</u>	<u>Longitude</u>
Subset A	556555.78	9512985.38	39 30 35.07E	04 24 21.28S	557099.57	9512334.02	39 30 52.73E	04 24 42.48S
Subset B	557091.08	9512926.48	39 30 52.44E	04 24 23.19S	557446.61	9512498.77	39 31 03.99E	04 24 37.11S
Subset C	556867.40	9512183.31	39 30 45.20E	04 24 47.40S	557231.05	9511755.73	39 30 57.01E	04 25 01.31S
Subset D	558056.64	9512413.37	39 31 23.78E	04 24 39.88S	558606.79	9511760.36	39 31 41.65E	04 25 01.13S
Subset E	556215.98	9511744.27	39 30 24.07E	04 25 01.35S	556662.68	9511223.62	39 30 38.58E	04 25 18.66S
Subset F	557517.17	9512105.35	39 31 06.29E	04 24 49.92S	557786.75	9511246.65	39 31 15.05E	04 25 17.88S
Subset G	556696.32	9511093.27	39 30 39.67E	04 25 22.90S	557057.58	9510667.86	39 30 51.41E	04 25 36.75S

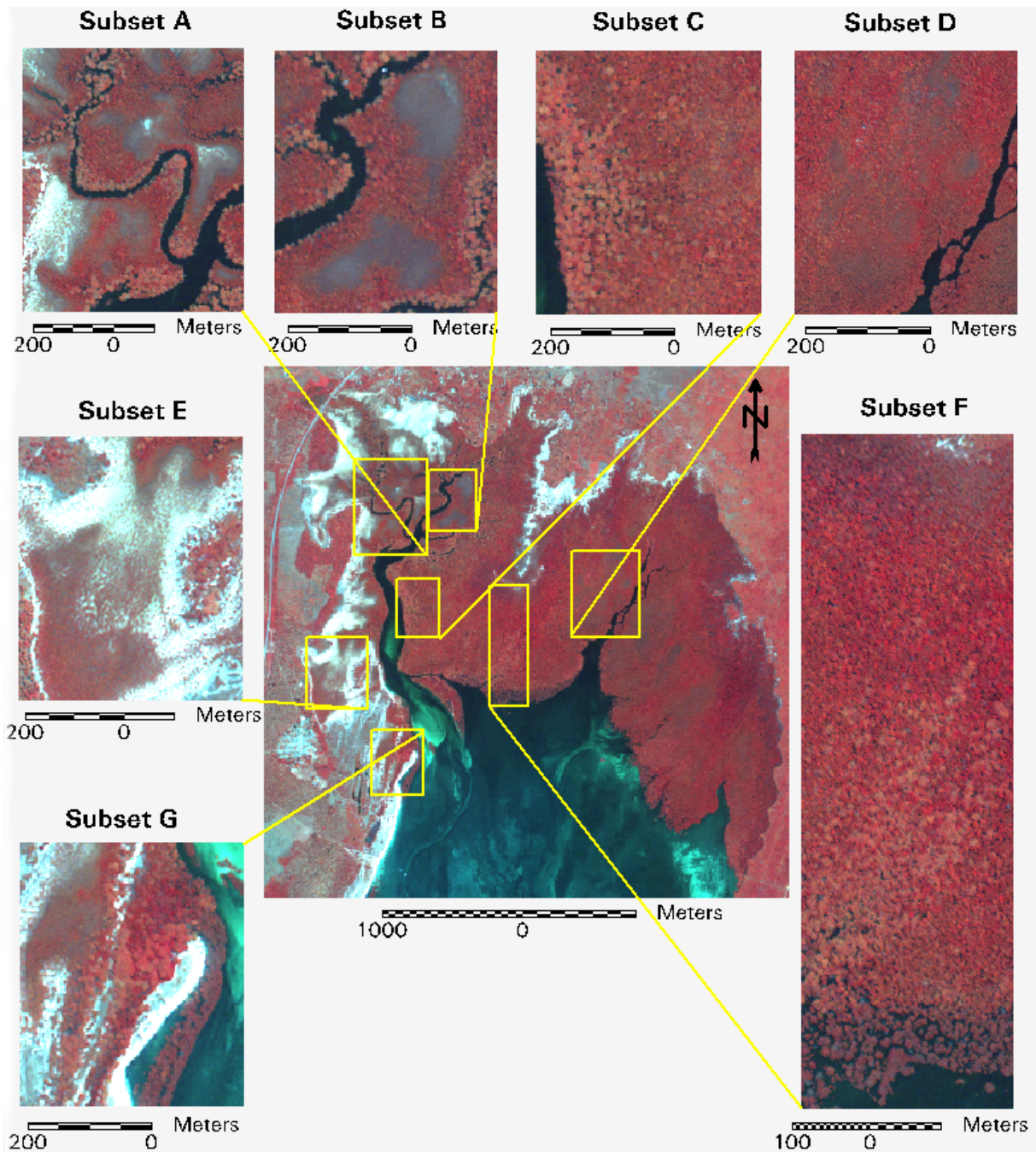


Figure 21. Overview of subsets on the PXS FCC image (B in B colour gun, G in G colour gun and NIR in R colour gun).

IV.3.3 Contrast stretch through masking

In masking through feature space, polygons are created in feature space and all the pixels that have feature space values in that polygon are masked in the original image. This means that in feature space masking it comes to exactly locating all pixels corresponding to a certain feature one wants to mask in the original image and then accurately creating polygons in feature space containing all those pixels. In our case it was impossible to locate exactly all the pixels corresponding to water and sand. A much less time consuming method was used instead (see below).

A mangrove mask separating non-mangrove from mangrove was created manually and an unsupervised classification using four classes was used to mask out water and sand. The resulting masked XS/PXS images will be referred to as MXS/MPXS, showing a very high contrast (see Figure 22).

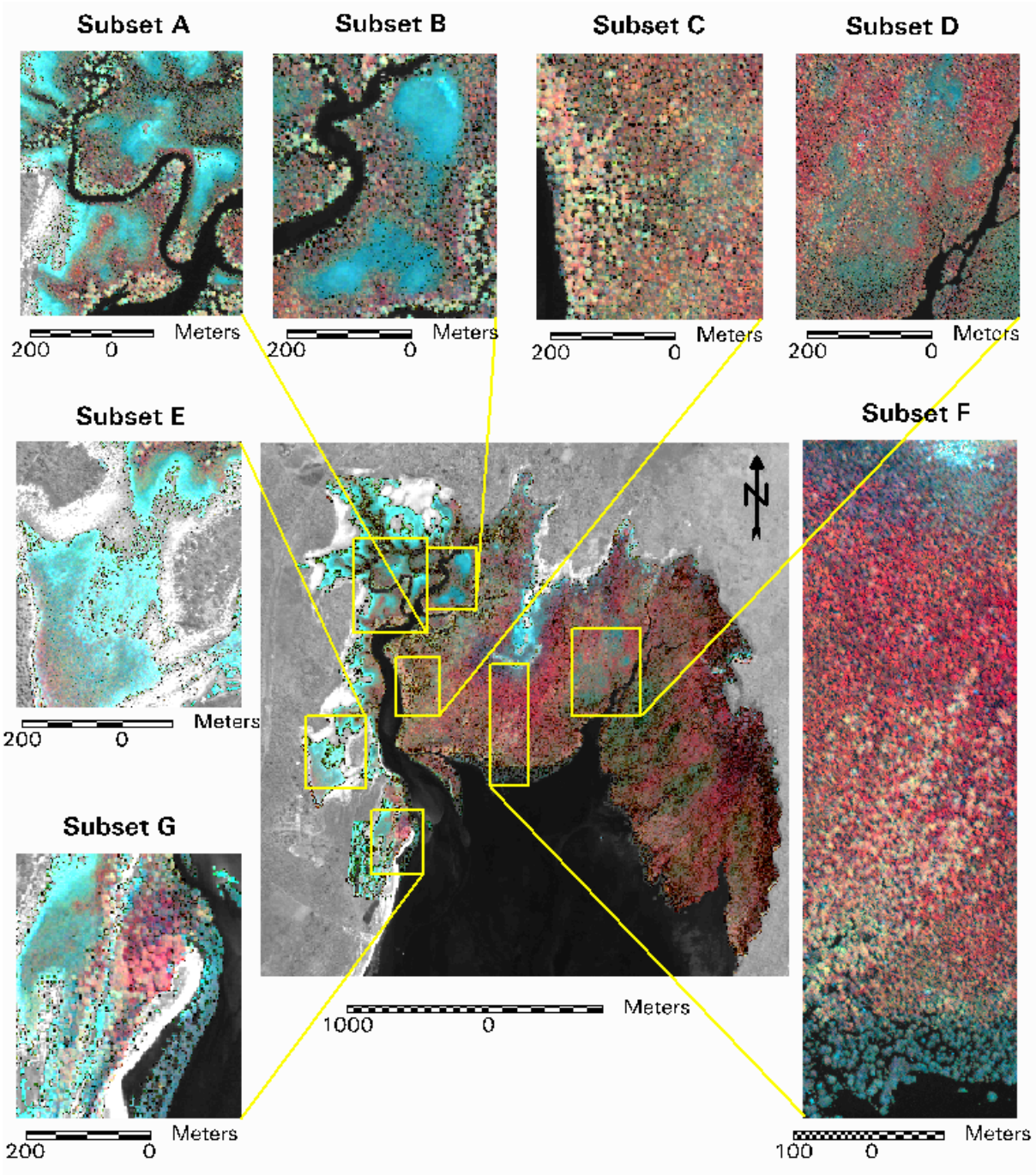


Figure 22. Overview of subsets in MPXS FCC image (B in B colour gun, G in G colour gun , NIR in R colour gun).

An MPXS image description of the training sites (TS) used in supervised classification (see IV.5.1.1) corresponding to different assemblages is given in Table 16. A field description describing the vegetation and the substrate in each assemblage is given in Table 17.

Table 16. MPXS FCC image description of training sites representing different assemblages. Each assemblage is described in terms of its colour, texture, structure and a crown description is given if individual crowns are discernible

TS ^a	MPXS FCC ^b image description			
	Colour	Texture	Structure	Description of crowns
AGazi	orange-pink	rough, irregular	crowns not discernible	
AMD	yellow-green-blue	blurry	crowns difficult to separate	
ALD	light blue-white	wrinkled foil	crowns not discernible	
AS	yellow-pink	of crown: cauliflower	crowns easily discernible	round and large crowns
BG	purple	of crown: cauliflower	crowns easily discernible	round, medium sized crowns
CGazi	green-blue	smooth, woolly, blurred	continuous canopy	
CCM	green-blue	smooth	continuous canopy	
CNFP	brown-green	woolly, blurred	continuous canopy	
CNMak	blue	smooth, blurred	continuous canopy	
CWMak	blue-yellow-green	woolly, blurred	discontinuous canopy	
C&R	dark blue	less smooth, regular	continuous canopy	
REKin	dark green	rough, irregular	discontinuous canopy	
RPlant	bright red	smooth	continuous canopy	
RWMak	brown-red	shingle	shingle	
SA	dark blue	rough	crowns not discernible except as individual trees surrounded by water	small to large sized, irregular shaped crowns

^aTraining Site. ^bFalse Colour Composite

Table 17. Field description of training sites representing different assemblages

TS ^a	Field description	
	Vegetation	Top Substratum
AGazi	Landward <i>Avicennia marina</i> closest to Gazi village	Sand
AMD	Landward <i>Avicennia marina</i> with medium dense canopy	Sand
ALD	Landward <i>Avicennia marina</i> with low density canopy	Sand
AS	Seaward <i>Avicennia marina</i> (NFP ^b , highest density canopy)	Dark mud (a lot of leaf litter present)
BG	<i>Bruguiera gymnorrhiza</i>	Unknown
CGazi	<i>Ceriops tagal</i> closest to Gazi village	Sand
CCM	<i>Ceriops tagal</i> in Central mangrove area	Unknown
CNFP	<i>Ceriops tagal</i> at NFP ^b	Sand
CNMak	<i>Ceriops tagal</i> North of Makongeni river	Dark mud
CWMak	<i>Ceriops tagal</i> West of Makongeni river	Dark mud
C&R	<i>Ceriops tagal</i> interspaced with <i>Rhizophora mucronata</i>	Dark mud
REKin	<i>Rhizophora mucronata</i> in East Kinondo region	Dark mud
RPlant	<i>Rhizophora mucronata</i> at KMFRI ^c plantation	Dark mud and coral stones
RWMak	<i>Rhizophora mucronata</i> West of Makongeni river	Unknown
SA	<i>Sonneratia alba</i> South of Central Mangrove	Dark mud

^aTraining Site. ^bNew Fishermen's Place. ^cKenya Marine and Fisheries Research Institute

IV.3.4 Principal components transformation

The Principal components transformation of MPXS will be referred to as PCA_MPXS. The eigenvalues and eigenvectors, the percentage of variance explained (%p) and the cumulative percentage of variance explained (cum%) are given in Table 18. Four principal components were calculated, the three first principal components gave the best display combination (PC1 in R colour gun, PC2 in G colour gun, PC3 in B colour gun), which is shown in Figure 23.

Table 18. Eigenvectors, eigenvalues, percentage variance explained (%p) and cumulative percentage of variance explained (cum%) by each of the 4 principle components of the MPXS image

PC	Eigenvector	eigenvalue	%p	cum%
PC1	(0.067;0.226;0.118;0.965)	2912.076	58.334	58.334
PC2	(-0.285;-0.613;-0.694;0.248)	1999.460	40.053	98.387
PC3	(-0.144;-0.692;0.702;0.087)	66.056	1.323	99.711
PC4	(0.945;-0.307;-0.110;0.020)	14.446	0.289	100.000

A PCA_MPXS image description of the TS used in supervised classification (see IV.5.1.1) corresponding to different assemblages is given in Table 19.

Table 19. PCA_MPXS image description of training sites representing assemblages. Assemblages are described in terms of their colour, texture, structure and a description of crowns is given if individual crowns are discernible

TS ^a	PCA_MPXS image description (PC1 in R colour gun, PC2 in G colour gun, PC3 in B colour gun)			
	Colour	Texture	Structure	Description of crowns
AGazi	orange-purple	rough, irregular	crowns not discernible	
AMD	dark purple-red	very rough	crowns discernible	
ALD	light purple-red	very rough	crowns discernible	
AS	oker orange-yellow	of crown: cauliflower	crowns easily discernible	round and large crowns
BG	yellow-blue	of crown: cauliflower	crowns easily discernible	round, medium sized crowns
CGazi	red brown	granular	continuous canopy	
CCM	purple-blue	blurred to granular	continuous canopy	
CNFP	purple-brown	granular	discontinuous canopy	
CNMak	dark blue	granular	discontinuous canopy	
CWMak	purple-red	granular	discontinuous canopy	
C&R	dark blue	irrugulary spaced dots on a blue background	crowns discernible	round, small crowns
REKin	blue	rough, irregular	discontinuous canopy	
RPlant	bright yellow-green	smooth	continuous canopy	
RWMak	green-yellow	irregular	irregular	
SA	blue-green	rough	crowns not discernible except as individual trees surrounded by water	small-large sized, irregularly shaped crowns

^aTraining Site

Certain areas on the satellite image corresponding to TS used in supervised classification further in this work (see section IV.5) are compared on the MPXS FCC image and on the PCA_MPXS image in Figure 24. For CNFP more texture was apparent on the pca image than on the original image, especially at the edges of the area, where there is high reflectance. Crowns were detectable on the pca image but not on the original image for AMD and C&R. For RWMak and BG texture was more pronounced in the mpxs image. For AS, both images were of comparable visual quality. A tremendous difference in visual quality between both images is clear for ALD; while nearly all texture is gone in the MPXS image, the texture is very rough on the pca image. In general, areas of low crown cover and thus higher reflectance are badly displayed on MPXS (because reflectance is high in all bands, thus the white appearance) and more textural and structural details can be seen on PCA_MPXS.

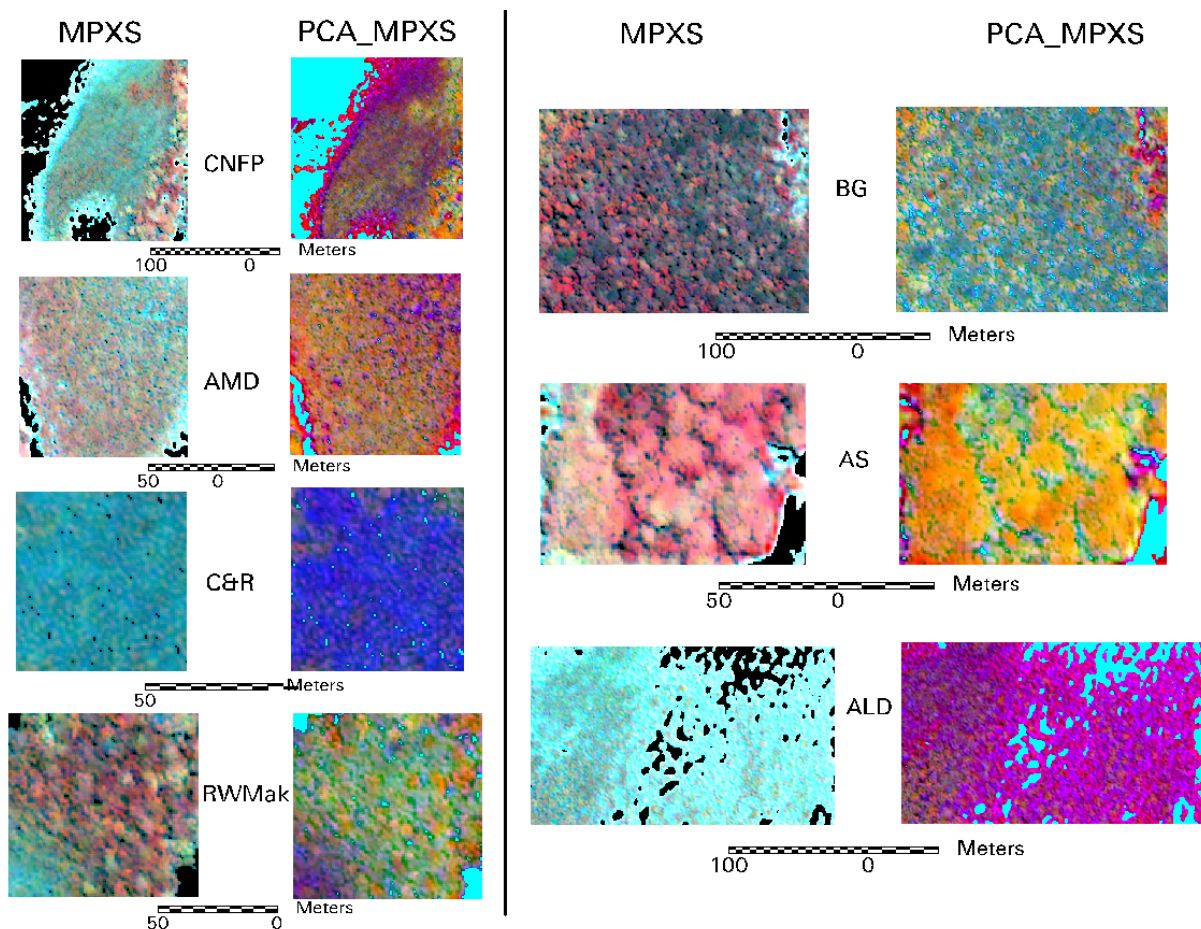


Figure 24. Comparison between different parts of assemblages on the MPXS FCC and the PCA_MPXS image (PC1 in R colour gun, PC2 in G colour gun, PC3 in B colour gun)

IV.3.5 Indices

The NDVI values were calculated for the MXS image and these values were added to the multispectral image as an additional layer, resulting in a five dimensional multispectral image: MXS+NDVI.

The NDVI image is shown in Figure 25. NDVI-values range from -0.34 (black) to 0.53 (white).

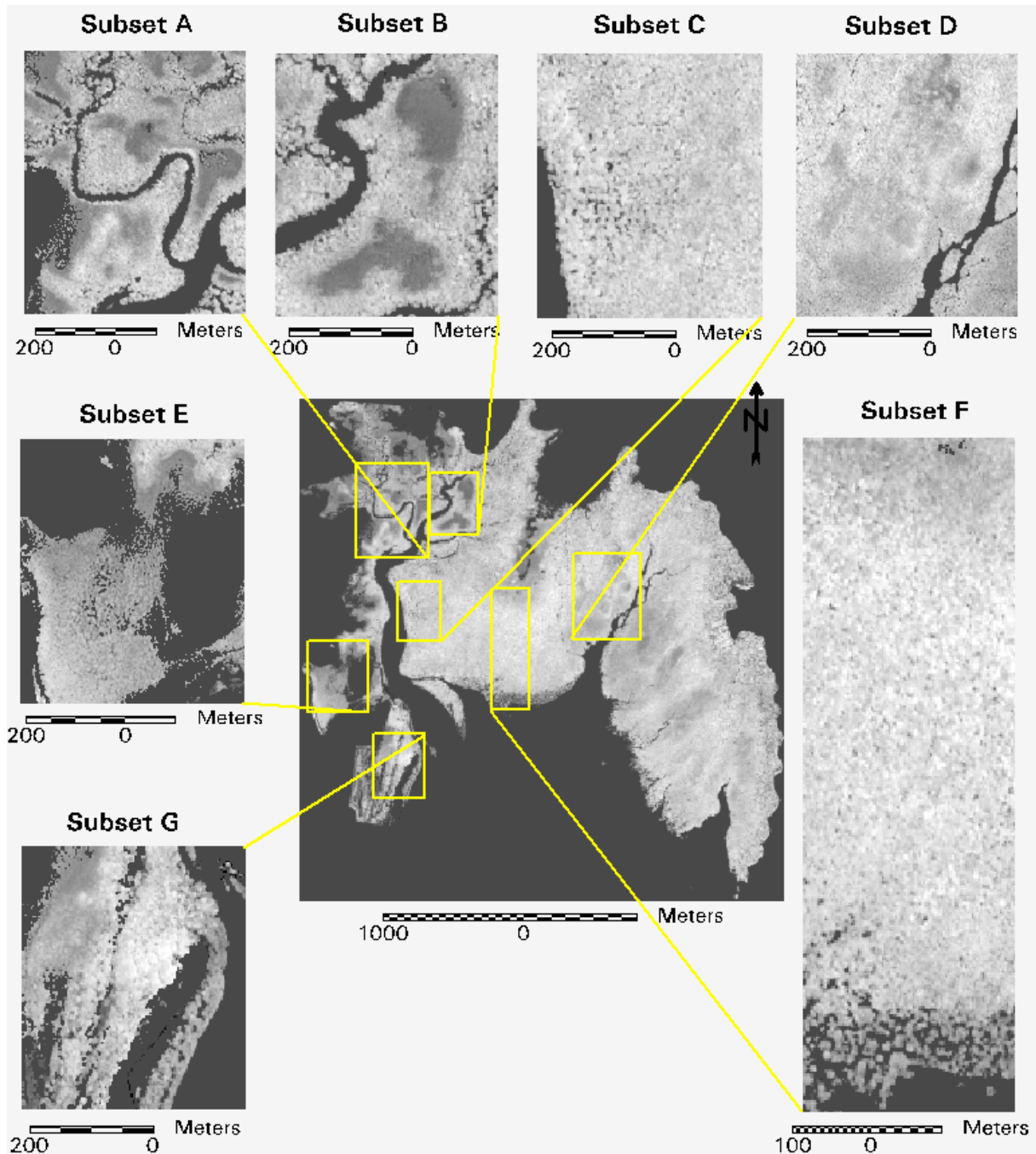


Figure 25. NDVI image of MXS. NDVI-values range from -0.34 (black) to 0.53 (white)

IV.3.6 Texture: variance

The variance texture measure was calculated in a 7×7 pixels window around the centre pixel (see Figure 26) and in a 21×21 pixels window (see Figure 27) from the PAN image and was added as an additional layer to the MPXS image. The resulting image will be referred to as MPXS+VAR7 and MPXS+VAR21.

Variance values calculated in a 7x7 window (Figure 26) range from 15.90 (black) to 28520.14 (white) and values calculated in a 21x21 window (Figure 27) range from 39.86 (black) to 58974.05 (white).

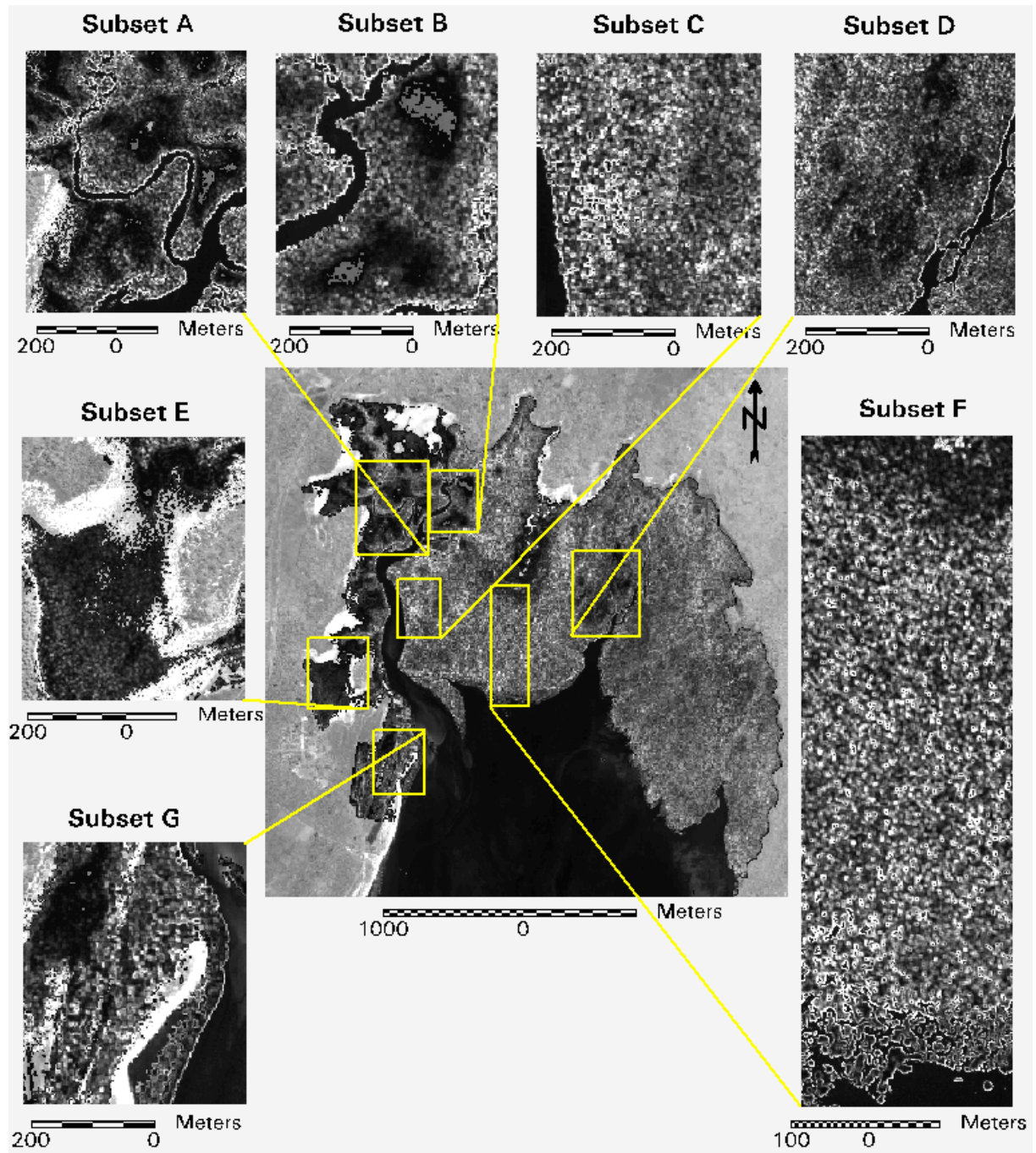


Figure 26. Variance texture measure calculated in a 7x7 pixels window from the PAN image

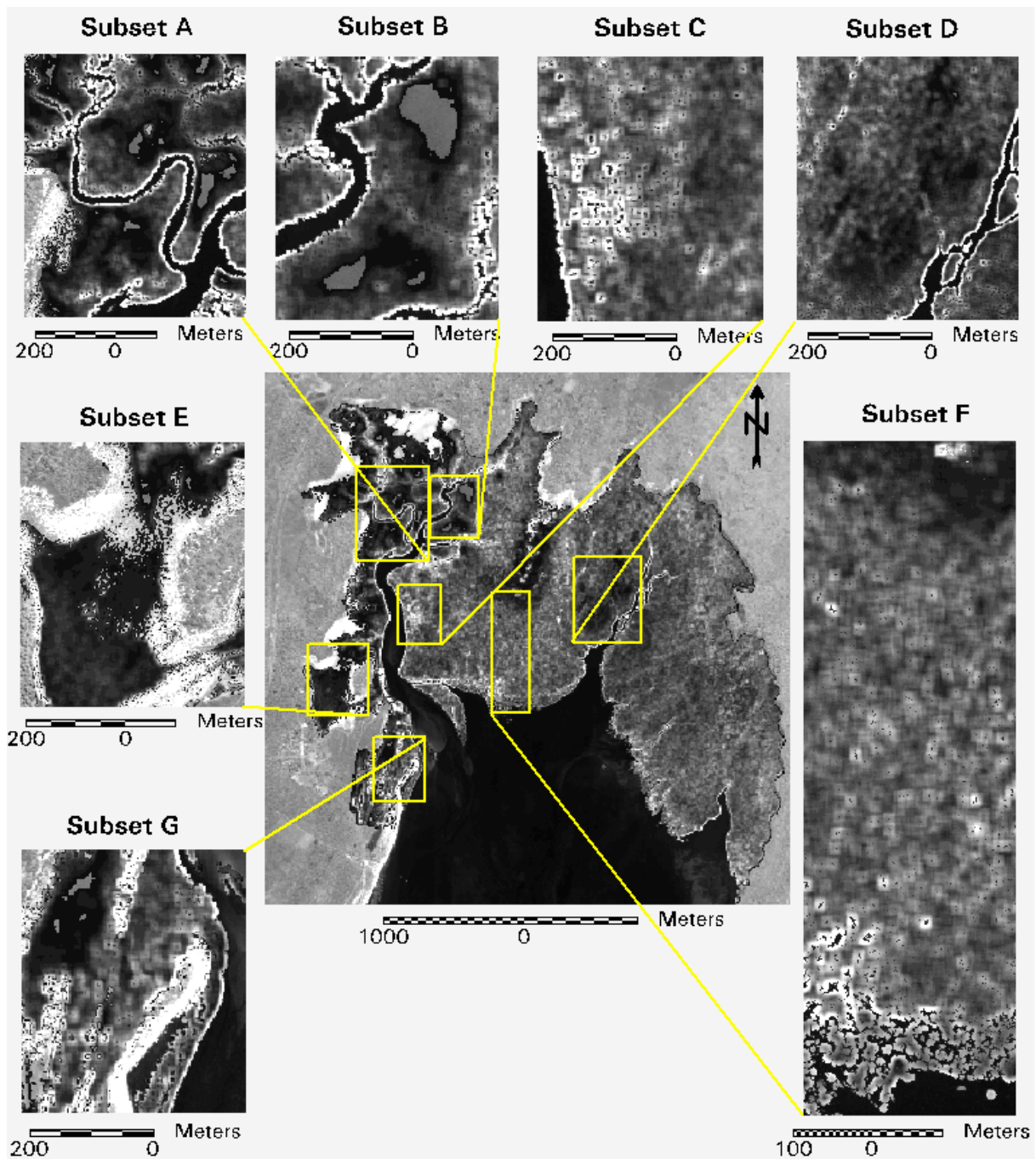


Figure 27. Variance texture measure in a 21x21 pixels window from the PAN image

IV.4 Unsupervised classification of the multispectral images

IV.4.1 Unsupervised classification of MXS

An unsupervised classification of the MXS image in 15 clusters was done. Those clusters were regrouped after close inspection into 8 resulting information classes. Clusters 1 and 2 correspond to different parts of *Salb* crowns, dark blue areas in the masked XS image such as *Ctag* (subset B), dark spots East of Kinondo river and dark purple *Bgym* crowns. The lighter *Bgym* crowns are represented by cluster 4. Clusters 3 and 7 represent sparsely vegetated areas,

while the pixels with a more orange appearance are grouped in cluster 5. This cluster corresponds well to the least dense landward *Amar* zone and the landward *Ctag* zone. Clusters 6, 8 and 9 were grouped together representing parts of *Salb*, *Rmuc* and *Bgym* crowns and to pixels with a very green appearance in the area East of Kinondo river. Cluster 10, 12 and 14 correspond to different levels of reddishness in *Amar* crowns going from the yellow to the orange-red respectively. The pixels with the most red appearance are grouped together in clusters 11 and 13. Cluster 15 corresponds well to very dense seaward *Amar* crowns.

Table 20. Grouping of spectral clusters into information classes in the unsupervised classification of MXS together with their colour appearance in the MPXS image

Spectral cluster	Colour appearance in MPXS	Information class
1 & 2	Dark blue to dark purple	<i>Salb, Ctag, Bgym</i>
3 & 7	Very light blue	High reflectance
4	Light purple	<i>Bgym</i>
5	Light blue with orange-green	Landward <i>Amar</i> , Landward <i>Ctag</i>
6, 8 & 9	Dark blue to green	<i>Bgym, Rmuc</i> and <i>Salb</i>
10, 12 & 14	Yellow to orange-red	<i>Amar</i>
11 & 13	Bright red	<i>Rmuc</i>
15	Orange-red	Seaward <i>Amar</i>

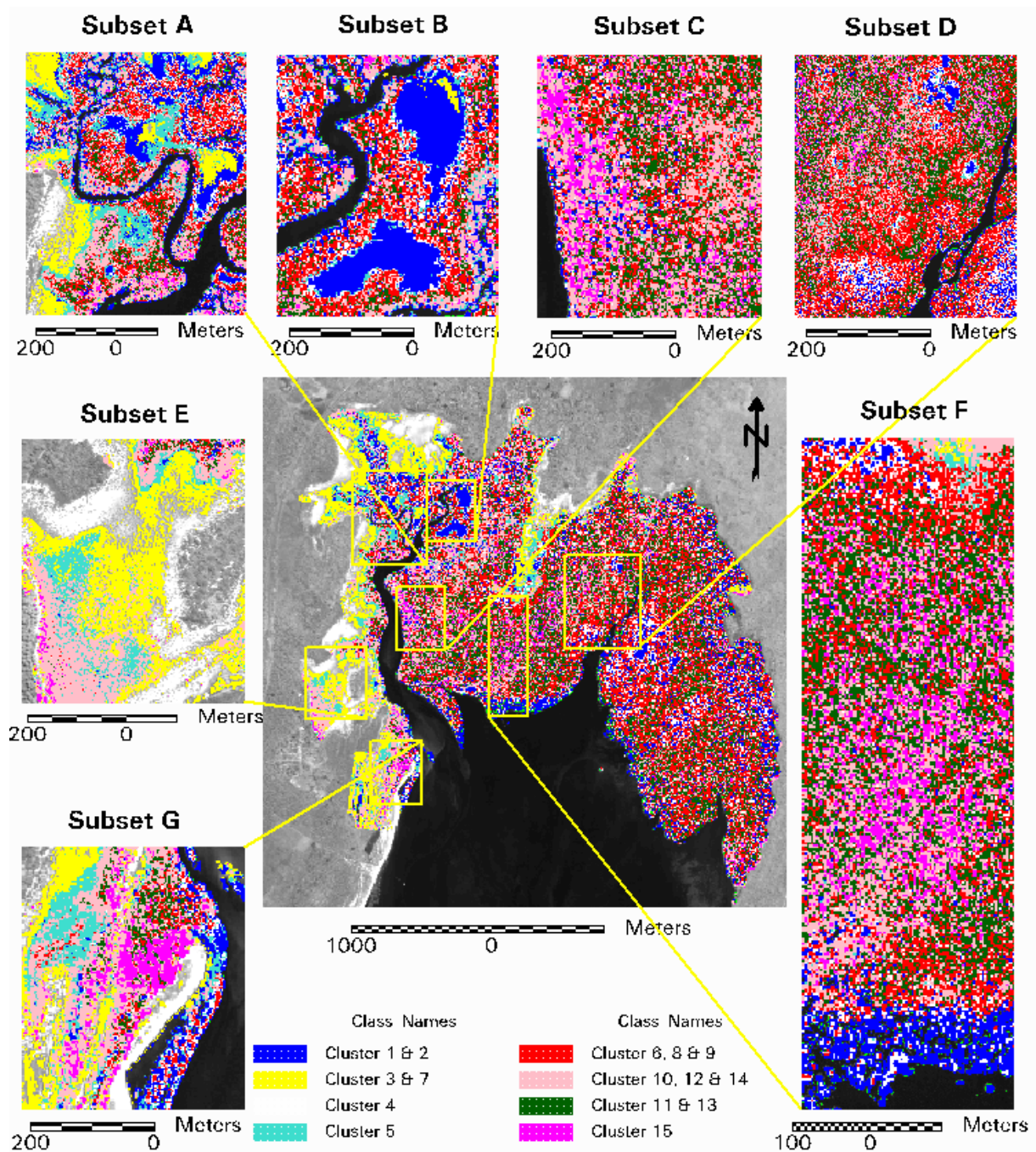


Figure 28. Unsupervised classification of MXS image into 15 spectral clusters (convergence threshold 95%), grouped into 8 information classes

IV.4.2 Unsupervised classification of MPXS

Clusters 1, 3, 4 and 7 were grouped together because they largely correspond to different parts of *Salb* crowns. Clusters 1 (and 3) correspond to pixels in *Salb* crowns with the most dark blue (less dark blue) appearance, but also to parts of *Bgym* crowns and parts in the dark green (green) of East Kinondo mangrove area. Most pixels of *Salb* (*Bgym*) crowns and pixels in the dark green areas of East Kinondo mangrove area belong to cluster 4 (cluster 7). Nearly all the pixels in the landward *Ctag* area belong to cluster 2. Cluster 5 contains pixels with a green-yellow appearance, especially present near the edges of the mangrove, and also some parts of

the landward *Amar* and *Ctag* zones. Pixels in the image with a bright red to dark orange appearance are grouped in clusters 6, 9, 11 and 12. Orange to yellow pixels are grouped in clusters 8 and 10 and correspond to parts of landward *Amar* and *Ctag* zones but also some pixels in seaward *Amar* crowns along Makongeni creek. Clusters 13 and 14 represent most of the pixels in dense seaward *Amar* crowns. Cluster 15 represents areas of high reflection.

Table 21. Grouping of spectral clusters into information classes in the unsupervised classification of MPXS together with their colour appearance in the MPXS image

Spectral clusters	Colour appearance in MPXS	Information class
1, 3, 4 & 7	Blue	<i>Salb</i> and <i>Bgym</i>
2	Dark blue	<i>Ctag</i>
5	Green-yellow	Landward <i>Amar</i> , landward <i>Ctag</i>
6, 9, 11 & 12	Bright red to dark orange	<i>Rmuc</i> , seaward <i>Amar</i>
8 & 10	Orange to yellow	Landward and seaward <i>Amar</i> , landward <i>Ctag</i>
13 & 14	Orange-red	Dense seaward <i>Amar</i>
15	Light blue	High reflectance

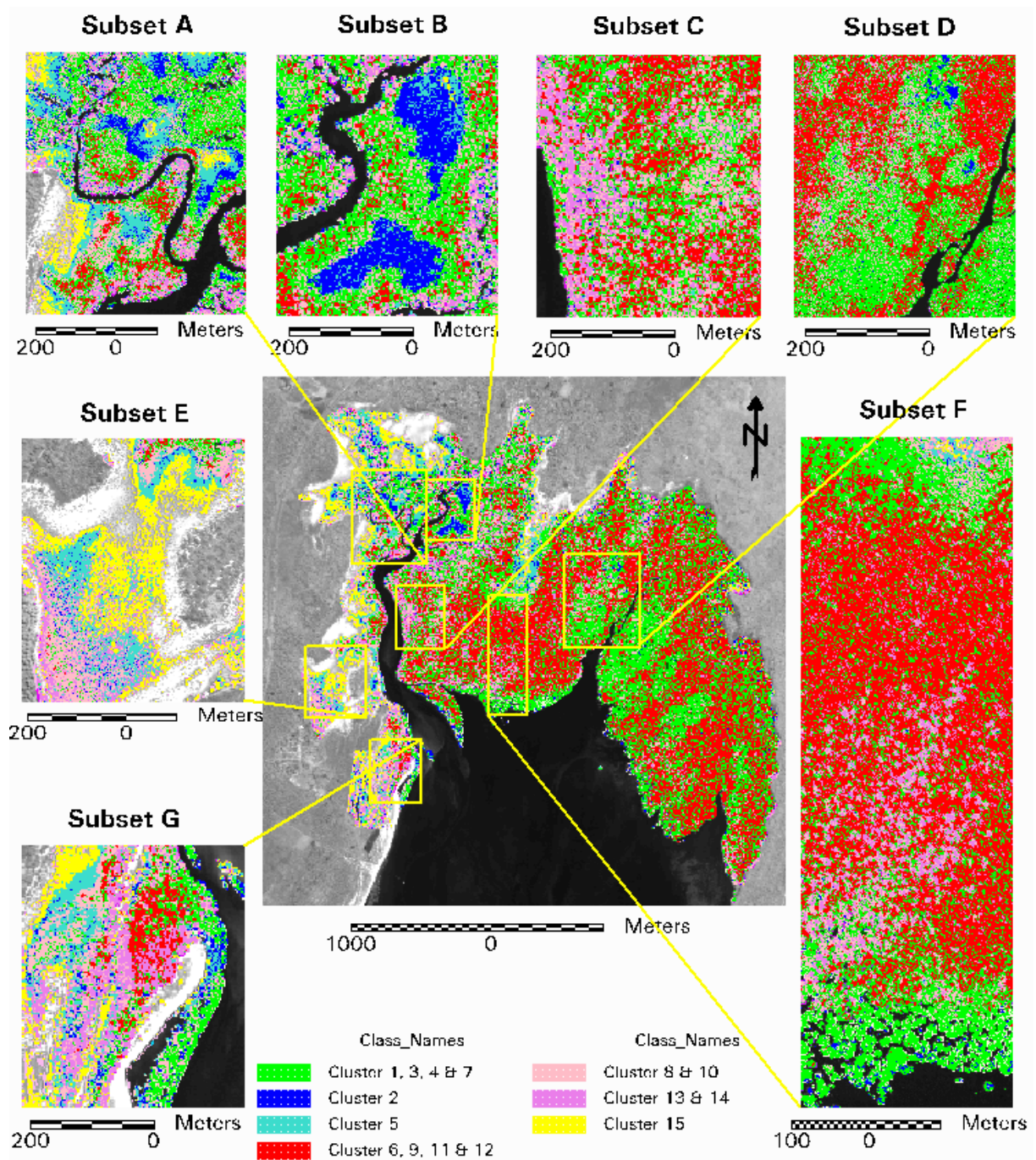


Figure 29. Unsupervised classification of MPXS image into 15 spectral clusters (convergence threshold of 95%), grouped into 7 information classes

IV.5 Supervised classification

IV.5.1 Supervised classification of MXS

IV.5.1.1 TRAINING SITE SELECTION

The most homogeneous and most representative pixels in each category of interest were selected and are shown in Figure 30. These categories include the most common species

encountered in the mangroves of Gazi Bay: *Avicennia marina* (*Amar*), *Bruguiera gymnorrhiza* (*Bgym*), *Ceriops tagal* (*Ctag*), *Rhizophora mucronata* (*Rmuc*) and *Sonneratia alba* (*Salb*).

For *Amar* a distinction was made between the trees occurring near the seaward side (AS) – having a much denser canopy and mostly a *Rmuc* understory- and the landward side of the mangrove. At the landward side AGazi, AMD and ALD TS were chosen corresponding to decreasing levels of density and height, respectively (AGazi: *Amar* closest to Gazi village), AMD: *Amar* Medium Dense, ALD: *Amar* Low Density). For *Ctag* a distinction was made between the trees occurring at the edge of the mangrove (CGazi, CNFP) and the trees occurring more seaward (CCM, CNMak, CWMak). An additional signature for a mixed occurrence of *Ctag* and *Rmuc* was developed (C&R). One TS for *Rmuc* was selected from KMFRI's *Rmuc* plantation near Kinondo village (RPlant), another set of training pixels for *Rmuc* were selected at different locations along Makongeni river (RWMak) and another set was selected in the East Kinondo mangrove area (REKin). TS for *Sonneratia alba* (SA) and *Bruguiera gymnorrhiza* (BG) were also selected.

Descriptions of tonality (colour), texture (internal structure in one crown, if distinguishable or, in the case of non-distinguishable crowns, the appearance of several close crowns), and structure as visually detected from the MPXS image together with a field description (substrate and vegetation) for these TS are given in Table 16 and Table 17.

No TS were developed for the remaining less common mangrove species *Heritiera littoralis*, *Lumnitzera racemosa*, *Pemphis acidula*, *Xylocarpus granatum* and *X. moluccensis* (nomenclature according to Tomlinson, 1986). An attempt was made to create a signature for *Lumnitzera racemosa* because it frequently occurs in strips near the pools encountered between the village and the New fishermen's place, but the strips were too small to create representative TS from.

IV.5.1.2 TRAINING SITE STATISTICS

Fifteen signatures were created from the TS. In each case the number of training data pixels was larger than 30 times the number of layers* (4 for MXS and 5 for MXS+NDVI) used in classification; the minimum number of pixels was 169 for CCM. Univariate statistical parameters such as minimum, maximum, mean and standard deviation were measured for each signature in each image layer and the covariance matrix for each signature was calculated. Results of these statistical parameter calculations are given in the appendix. The same TS were used to develop signatures for MXS and MXS+NDVI. Signature means and standard deviations in each band are plotted in Figure 31-Figure 35.

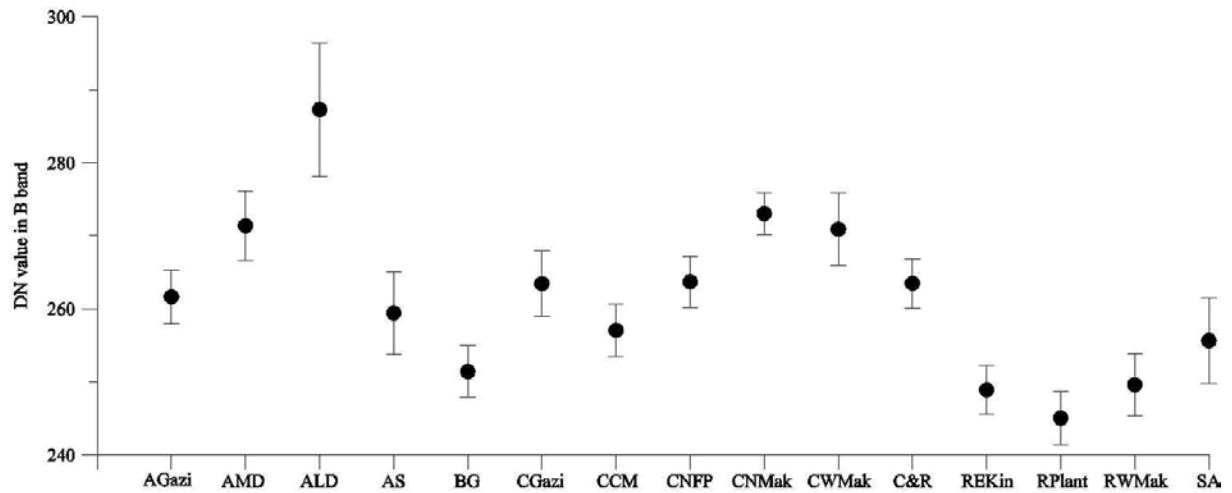


Figure 31. MXS(+NDVI) signature DN means and standard deviations in the B band

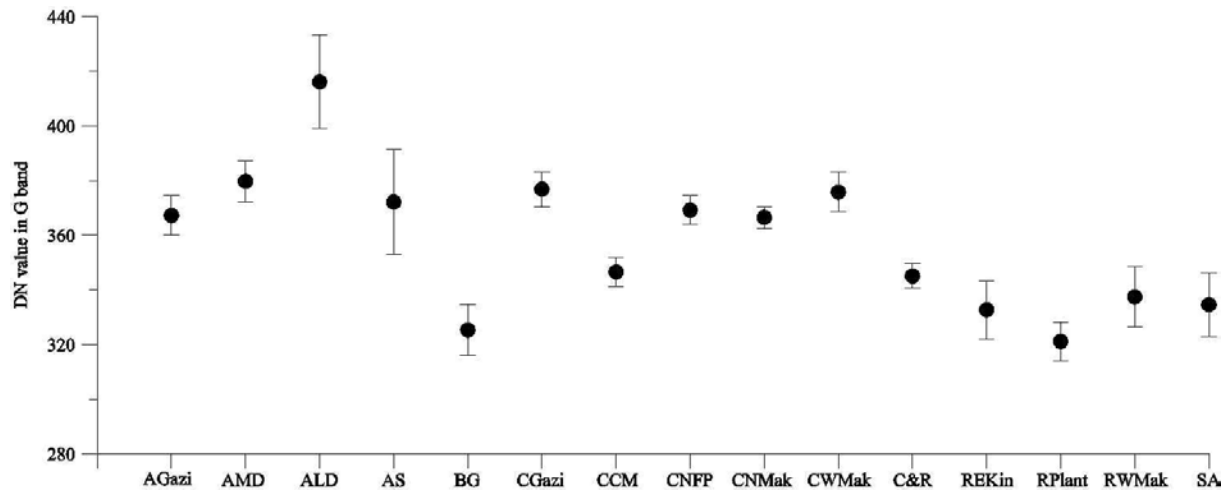


Figure 32. MXS(+NDVI) signature DN means and standard deviations in the G band

* As recommended by Mather (1999), see section II.8.2.

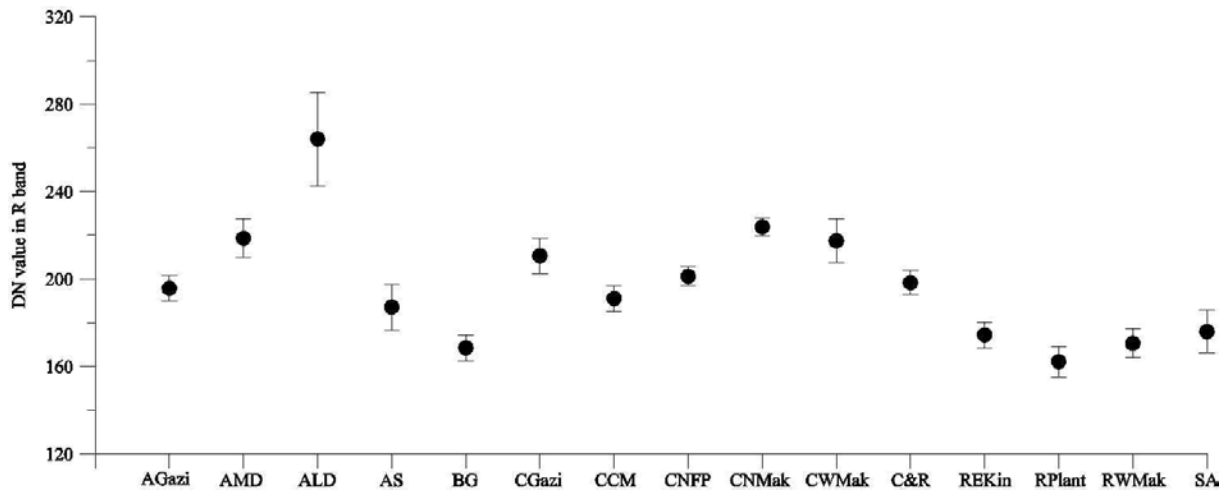


Figure 33. MXS(+NDVI) signature DN means and standard deviations in the R band

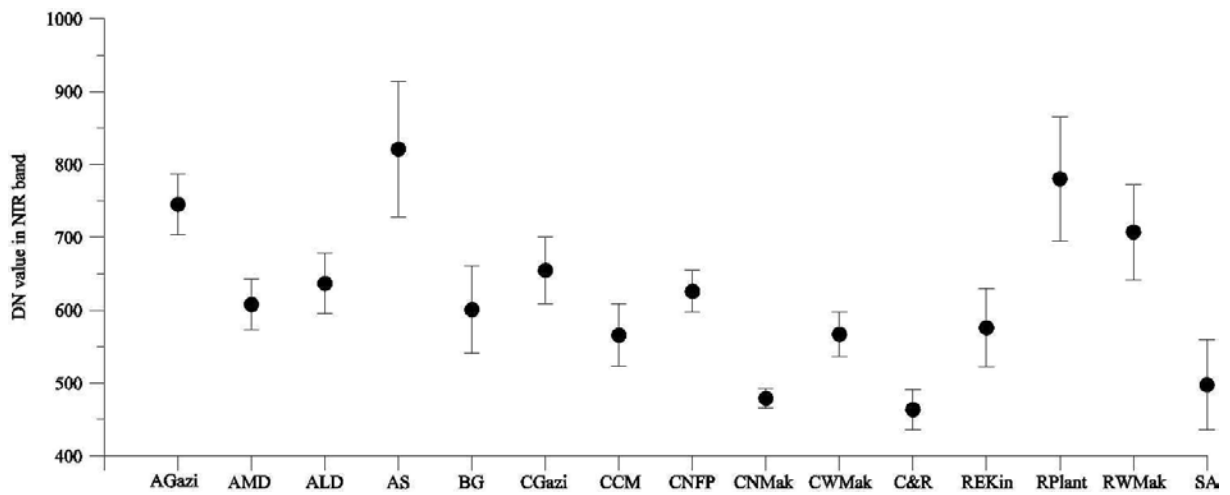


Figure 34. MXS(+NDVI) signature DN means and standard deviations in the NIR band

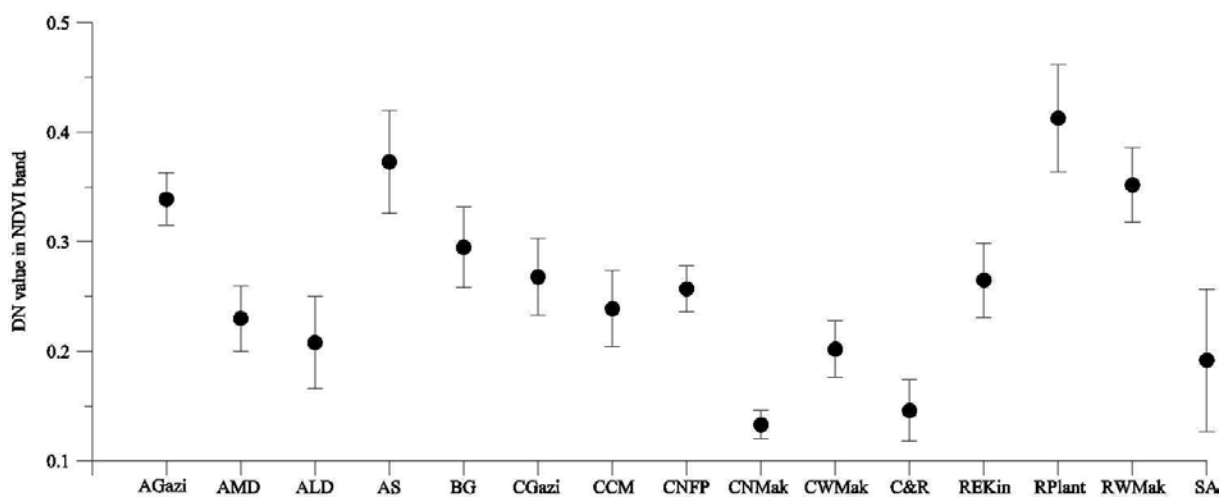


Figure 35. MXS(+NDVI) signature DN means and standard deviations in the NDVI (=NIR-R/NIR+R) band

IV.5.1.3 EVALUATION OF THE DEGREE OF BETWEEN CLASS SEPARABILITY

Contingency matrices were calculated for all 15 signatures. Results for training pixel data extracted from the MXS and MXS+NDVI image are shown in Table 22 and Table 23, respectively. The overall accuracy for training pixel classification in the MXS image is 83% and 81% for the MXS+NDVI image.

Table 22. Contingency matrix for training pixel data from MXS using the ML decision rule, entries in pixel counts. User's, producer's and overall accuracy are shown

		Reference data															RT ^d	UA ^e
		AGazi	AMD	ALD	AS	BG	CGazi	CCM	CNFP	CNMak	CWMak	C&R	REkin	RPlant	RWMak	SA		
Classified data	AGazi	772	2	0	174	9	8	1	9	0	0	0	3	14	0	992	0.78	
	AMD	4	244	8	1	0	16	0	12	0	58	0	1	0	0	344	0.71	
	ALD	2	6	1	0	2	0	0	0	2	0	0	0	0	0	1363	0.99	
	AS		1	0	2384	4	0	0	0	0	0	0	9		45	2479	0.96	
	BG	1	0	0		956	0	1	0	0	0	0	86	12	78	1212	0.79	
	CGazi	30	44	12	7	0	121	0	22	0	13	0	1	0	0	250	0.48	
	CCM	5	0	0	7	5		143	6	0	5	13		4	2	3	284	0.50
	CNFP	20	27		14	0	13	1	281		32	0	5	0	1	0	394	0.71
	CNMak	0	0	0	0	0	0		0	553	1	1	0		0	0	555	1.00
	CWMak	1	75	2	3		14	0	7	3	297		1	0	0	2	406	0.73
	C&R	0		0	2	0	0	10		2	0	446	1	0	0		473	0.94
	REkin	1	0	0	47	70		10	0	0	0	6		2	33	33	1542	0.87
	RPlant	0	0	0		22	0	0	0	0		0	6	384	54	0	521	0.74
	RWMak		0	0	244	59	0	0	0	0	0	0	54	14	480	1	855	0.56
	SA	0	0	0	26	41	0	3	0	0	0	11	57	1	6	354	499	0.71
CT ^a	873	399	1372	3001	1166	174	169	337	558	408	478	1651	423	713	447			
PA ^b	0.88	0.61	0.98	0.79	0.82	0.70	0.85	0.83	0.99	0.73	0.93	0.81	0.91	0.67	0.79			
OA ^c	0.83																	

^aColumn Total. ^bProducer's Accuracy. ^cOverall Accuracy. ^dRow Total. ^eUser's Accuracy

Table 23. Contingency matrix for training pixel data from MXS+NDVI using the ML decision rule, entries in pixel counts. User's, producer's and overall accuracy are shown

		Reference data														RT ^d UA ^e			
		AGazi	AMD	ALD	AS	BG	CGazi	CCM	CNFP	CNMak	CWMak	C&R	REkin	RPlant	RWMak			SA	
Classified data	AGazi	808		3	304	13	11	1	8			0	0	5	1	23		1181	0.68
	AMD	3	231	10	0	0		0	9	0	52	0		2	0	0		326	0.71
	ALD	2	4	1339		0	2	0	0	0		0	0	0	0	0		1348	0.99
	AS		0	0	2200	0	0	0		0	0	0	0	0	1			2245	0.98
	BG	1	0	0	25		0	0	0	0	0	0	85	11	71	52		1179	0.79
	CGazi	15	30	11	7	0	103	0	11	0	10	0	1	0	0	0		188	0.55
	CCM	2	0		5		0		3		3	12	101	5	0	7		287	0.49
	CNFP	26	37	0	20	0	20		291	0	28	0	10	1	1	0		437	0.67
	CNMak	0	0	0	0	0	0		0	549	4	1	0		0	0		554	0.99
	CWMak	1	93	9		0	19	1	15	6	310		3	0	0	1		466	0.67
	C&R	0		0	2	0	0	11		3	0	451	1	0		14		482	0.94
	REkin	0	0	0	45	74	0	11	0	0	0	5	1311	2	37	43		1528	0.86
	RPlant	0	0	0	51	15	0	0	0		0	0	1	375	45	0		487	0.77
	RWMak		0	0	312	80	0		0	0	0	0	73		501	0		991	0.51
	SA	0	0	0	24		0	1	0	0	0		58	1	3	330		466	0.71
CT ^a	873	399	1372	3001	1166	174	169	337	558	408	478	1649	423	711	447				
PA ^b	0.93	0.58	0.98	0.73	0.80	0.59	0.83	0.86	0.98	0.76	0.94	0.80	0.89	0.70	0.74				
OA ^c	0.81																		

^aColumn Total. ^bProducer's Accuracy. ^cOverall Accuracy. ^dRow Total. ^eUser's Accuracy

Ellipses of concentration were calculated using the mean and standard deviation of the signatures. In Figure 36, these ellipses are displayed in two-dimensional feature space (G band values on the X-axis and NIR band values on the Y-axis) and are based on the range of 2 standard deviations from the mean. Bright colours indicate a high density of pixels in the original image (MXS). Ellipses of concentration in feature space allow us to visualize the amount of overlap between signatures in one pair of bands.

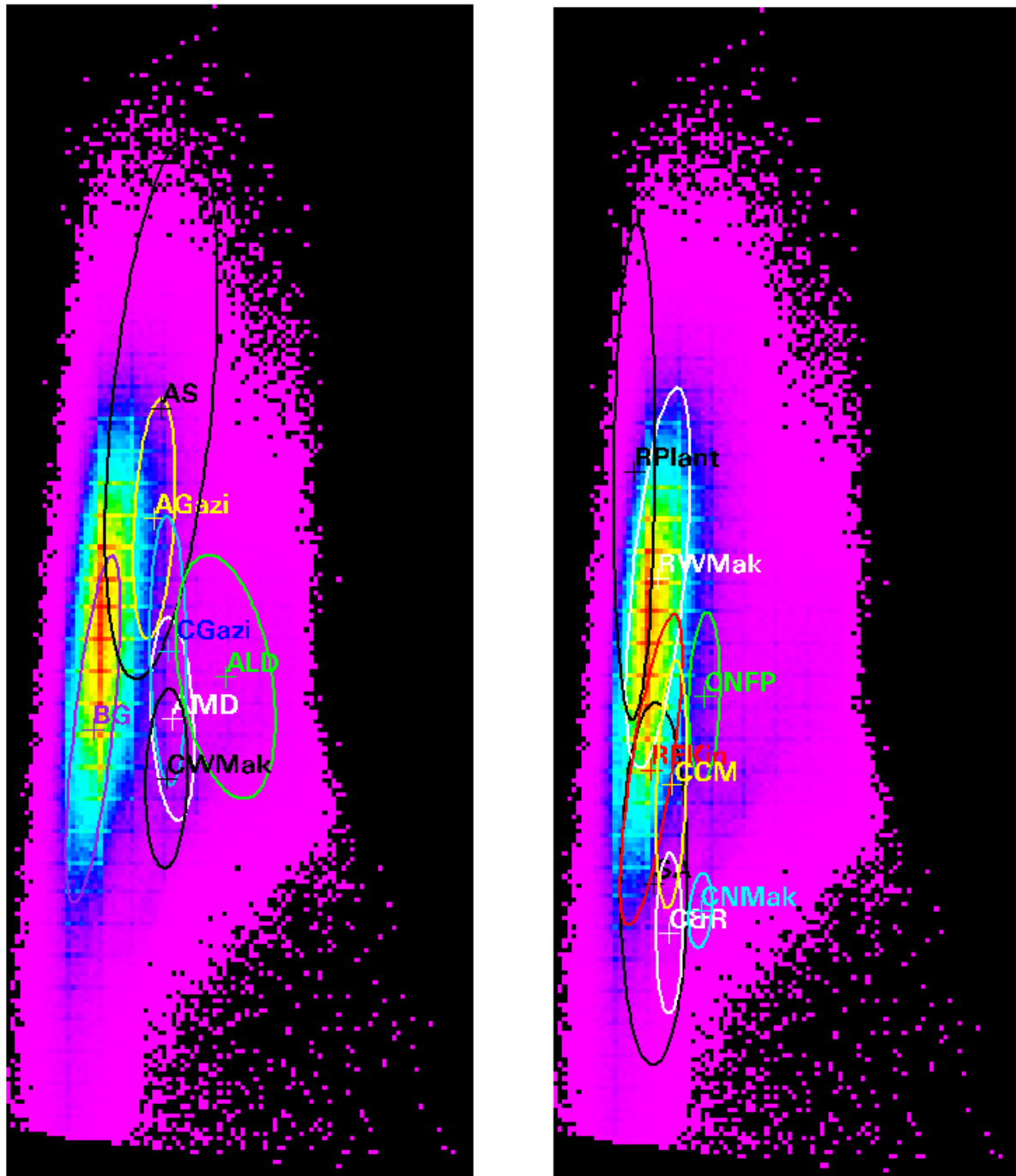


Figure 36. Signature ellipses of 2 standard deviations from the mean (crosshair) in 2-dimensional feature space (G band values on the horizontal axis and NIR band values on the vertical axis)

Transformed divergence indices were calculated using all bands in the images MXS and MXS+NDVI. These indices are a measure for separability between any pair of signatures. A separability listing is a report of the computed divergence for every class pair. According to Jensen (1986) separation is poor if the transformed divergence index between two signatures is below 1700. Values lower than 1700 are therefore highlighted in the separability listings in Table 24 and Table 25.

All separability indices increased through the addition of the NDVI layer. The highest increase was 736.75 between AMD and CWMak, followed by 686.31 between CGazi and

CWMak. The separability increased from poor (<1700) to good (>1900) in the following pairs of signatures: AGazi and AS, AGazi and CGazi, BG and SA, CGazi and CWMak, CCM and C&R, CNFP and CWMak, REKin and RWMak.

This can also be seen on Figure 31 - Figure 35 (*e.g.* the overlap between the signatures BG and SA is high in all bands, except in the NDVI band, where the signatures are clearly separated).

Table 24. Transformed divergence separability indices for the signatures extracted from the MXS image. Values lower than 1700 are shaded, average and minimum separability are shown

	AGazi	AMD	ALD	AS	BG	CGazi	CCM	CNFP	CNMak	CWMak	C&R	REkin	RPlant	RWMak	SA
AGazi	0.00	1871.17	1999.92	1477.74	1969.09	1530.96	1951.92	1703.55	2000.00	1987.46	2000.00	1948.13	1995.83	1819.17	1951.92
AMD	1871.17	0.00	1962.60	1992.56	1999.95	777.41	1985.55	1522.71	1999.92		1999.95	1999.60	1999.92	1998.78	1998.46
ALD	1999.92	1962.60	0.00	1999.93	2000.00	1989.78	2000.00	2000.00	2000.00	1938.74	2000.00	2000.00	2000.00	2000.00	1999.99
AS	1477.74	1992.56	1999.93	0.00	1899.26	1926.22	1992.60	1988.34	2000.00	1999.82	2000.00	1875.78	1984.94	1305.93	1955.11
BG	1969.09	1999.95	2000.00	1899.26	0.00	1999.87	1953.71	1999.48	2000.00	1999.94	1999.21	1343.53	1834.73	1170.06	
CGazi	1530.96	777.41	1989.78	1926.22	1999.87	0.00	1978.64	1273.02	2000.00	1308.41	1999.97	1997.62	1999.99	1994.81	1999.00
CCM	1951.92	1985.55	2000.00	1992.60	1953.71	1978.64	0.00	1837.60	1999.98	1952.37	1619.65		1998.40	1923.81	1878.85
CNFP	1703.55	1522.71	2000.00	1988.34	1999.48	1273.02	1837.60	0.00	2000.00	1605.00	1998.66	1992.08	1999.99	1995.55	1996.28
CNMak	2000.00	1999.92	2000.00	2000.00	2000.00	2000.00	1999.98	2000.00	0.00	1992.88	1992.36	2000.00	2000.00	2000.00	2000.00
CWMak	1987.46	686.81	1938.74	1999.82	1999.94	1308.41	1952.37		1992.88	0.00	1997.75	1998.97	2000.00	1999.80	1973.27
C&R	2000.00	1999.95	2000.00	2000.00	1999.21	1999.97	1619.65	1998.66	1992.36	1997.75	0.00	1985.13	2000.00	1999.96	1875.48
REkin	1948.13	1999.60	2000.00	1875.78	1343.53	1997.62	1649.03	1992.08	2000.00	1998.97	1985.13	0.00	1975.26	1466.67	
RPlant	1995.83	1999.92	2000.00	1984.94	1834.73	1999.99	1998.40	1999.99	2000.00	2000.00	2000.00	1975.26	0.00	1479.24	1909.28
RWMak	1819.17	1998.78	2000.00	1305.93		1994.81	1923.81	1995.55	2000.00	1999.80	1999.96	1466.67		0.00	1973.27
SA	1951.92	1998.46	1999.99	1955.11	1461.24	1999.00	1878.85	1996.28	2000.00	1973.27	1875.48	1496.80	1909.28	1973.27	0.00

Average separability: 1874.90
Minimum separability: 686.81

Table 25. Transformed divergence separability indices for the signatures extracted from the MXS image. Values lower than 1700 are shaded, values of separability below 1700 on MXS that increased above 1700 on MXS+NDVI are given in bold. Average and minimum separability are given

	AGazi	AMD	ALD	AS	BG	CGazi	CCM	CNFP	CNMak	CWMak	C&R	REkin	RPlant	RWMak	SA
AGazi	0.00	2000.00	1999.99	1970.34	1999.58	1949.01	2000.00	2000.00	2000.00	2000.00	2000.00	2000.00	1998.86	1872.03	2000.00
AMD	2000.00	0.00	1981.87	2000.00	1999.97	1161.56	1993.07	1625.69	2000.00		2000.00	1999.76	2000.00	2000.00	2000.00
ALD	1999.99	1981.87	0.00	2000.00	2000.00	1990.66	2000.00	2000.00	2000.00	1990.52	2000.00	2000.00	2000.00	2000.00	2000.00
AS	1970.34	2000.00	2000.00	0.00	1999.14	2000.00	2000.00	2000.00	2000.00	2000.00	2000.00	2000.00	1986.74	1561.56	2000.00
BG	1999.58	1999.97	2000.00	1999.14	0.00	1999.94	1976.10	1999.89	2000.00	2000.00	2000.00	1417.61	1998.35	1715.28	1966.47
CGazi	1949.01	1161.56	1990.66	2000.00	1999.94	0.00	1996.51	1581.75	2000.00	1994.72	2000.00	1998.68	2000.00	1998.34	2000.00
CCM	2000.00	1993.07	2000.00	2000.00	1976.10	1996.51	0.00	1993.52	2000.00	1959.74	1972.03	1710.16	2000.00	2000.00	1996.24
CNFP	2000.00	1625.69	2000.00	2000.00	1999.89	1581.75	1993.52	0.00	2000.00	1981.81	2000.00	1999.15	2000.00	2000.00	2000.00
CNMak	2000.00	2000.00	2000.00	2000.00	2000.00	2000.00	2000.00	2000.00	0.00	2000.00	1999.73	2000.00	2000.00	2000.00	2000.00
CWMak	2000.00	1423.56	1990.52	2000.00	2000.00	1994.72	1959.74	1981.81	2000.00	0.00	1999.99	1999.55	2000.00	2000.00	2000.00
C&R	2000.00	2000.00	2000.00	2000.00	2000.00	2000.00	1972.03	2000.00	1999.73	1999.99	0.00	1999.54	2000.00	2000.00	1923.09
REkin	2000.00	1999.76	2000.00	2000.00	1417.61	1998.68	1710.16	1999.15	2000.00	1999.55	1999.54	0.00	2000.00	1967.11	1898.37
RPlant	1998.86	2000.00	2000.00	1986.74	1998.35	2000.00	2000.00	2000.00	2000.00	2000.00	2000.00	2000.00	0.00	1632.72	2000.00
RWMak	1872.03	2000.00	2000.00	1561.56	1715.28	1998.34	2000.00	2000.00	2000.00	2000.00	2000.00	1967.11	1632.72	0.00	2000.00
SA	2000.00	2000.00	2000.00	2000.00	1966.47	2000.00	1996.24	2000.00	2000.00	2000.00	1923.09	1898.37	2000.00	2000.00	0.00
Average separability:				1954.10											
Minimum separability:				1161.56											

IV.5.1.4 CLASSIFICATION ACCURACY ASSESSMENT

The classified MXS and MXS+NDVI images are shown in Figure 37 and Figure 38. An error matrix was produced for each ground-truthed assemblage. The error matrix obtained by adding all transect data together (1200 PCQM observations) is shown in Table 26. Counts for different classes representing the same mangrove species are added together to form a species class, which are highlighted in the error matrix. PA, UA and OA and κ and τ coefficients were determined using the formulas given in section II.8.7.

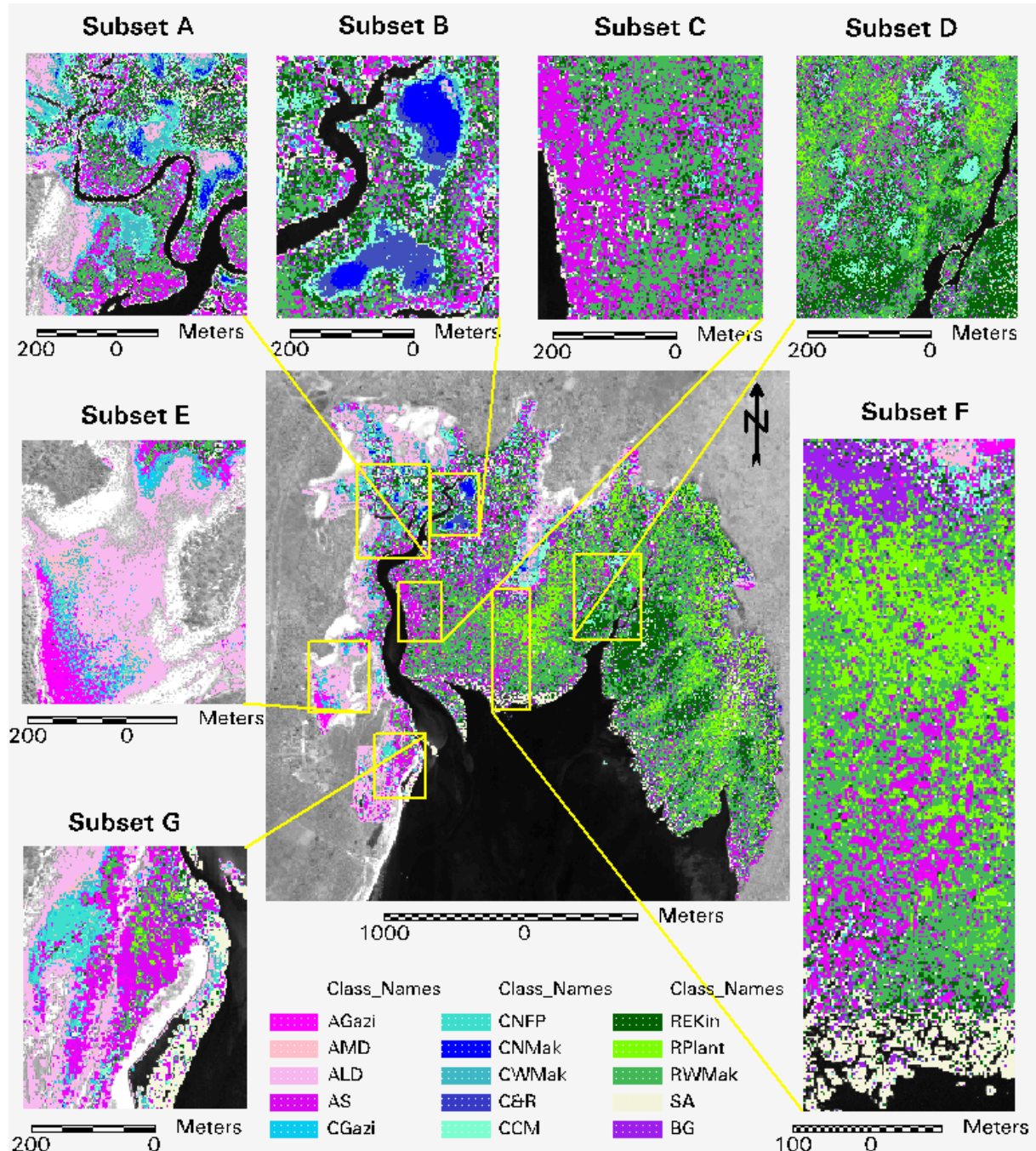


Figure 37. Supervised classification of MXS in 15 classes

Table 26. Error matrix of the supervised ML classification of MXS taking into consideration all transect data as reference data

		Reference data						RT ^d	UA ^e
		<i>Amar</i>	<i>Bgym</i>	<i>Ctag</i>	<i>Rmuc</i>	<i>Salb</i>	Nil		
Classified data	AGazi	49.50	0.00	23.83	12.83	0.00	0.00	86.16	
	AMD	5.50	0.00	20.50	0.00	0.00	0.00	26.00	
	ALD	86.50	0.00	52.50	0.00	0.00	0.00	139.00	
	AS	52.18	8.83	21.50	96.40	1.00	7.00	186.91	
	<i>Amar</i>	193.68	8.83		109.23		7.00	438.07	0.442
	BG (<i>Bgym</i>)	0.00	10.98		16.06		1.83	31.70	0.346
	CGazi	13.00	0.00	20.83	1.75	0.00	0.00	35.58	
	CCM	0.00	1.66	8.00	3.91	0.00	0.00	13.57	
	CNFP	7.00	1.00	49.00	1.00	0.00	0.00	58.00	
	CNMak	0.00	0.83	63.00	1.25	0.00	0.00	65.08	
	CWMak	1.83	2.00	14.00	1.33	0.00	0.00	19.16	
	C&R	0.00	0.00	10.00	0.00	0.00	0.00	10.00	
	<i>Ctag</i>		5.49	164.83		0.00		201.39	0.818
	REkin	0.66	4.66	7.00	80.07	2.50	0.83	95.72	
	RPlant	2.00	23.66	0.83	34.65	0.00	0.00	61.14	
	RWMak	8.00	34.50	52.16	136.82	0.00	2.00	233.48	
	<i>Rmuc</i>		62.82		251.54	2.50		390.34	0.644
	SA (<i>Salb</i>)	4.83		0.00	12.81	47.50	27.33	96.37	0.493
	Nil		0.00	11.00	0.00	0.00	2.00	42.00	0.048
	CT ^a		260.00	92.02	355.98	398.88	52.00	40.99	
PA ^b		0.745	0.119	0.463	0.631	0.913	0.049		
OA^c		0.559	κ		0.417	τ		0.377	

aColumn Total. bProducer's accuracy. cOverall accuracy. dRow Total. eUser's accuracy.

Table 27 and Table 28 represent the error matrix from the classification of MXS and MXS+NDVI obtained when only those transect data where the adult tree layer represents the remotely sensed canopy (see materials and methods) are included as reference data (612 PCQM observations).

Through the removal of reference data where the adult tree layer did not represent the remotely sensed canopy in the classification of MXS, the OA increased from 55.9% to 67.8%. The kappa coefficient increased from 0.417 to 0.571 and the tau coefficient increased from 0.377 to 0.465.

If we look at the error matrix for MXS (calculated without unsuitable test data), we find that the UA's of *Ctag* and *Rmuc* are quite high, being 84.5% and 90.3%, respectively. This means that 84.5% (90.3%) of all pixels classified as *Ctag* (*Rmuc*) is actually *Ctag* (*Rmuc*) on the field. The PA of *Salb* is the highest: 90.3%. This means that *Salb* pixels (parts of *Salb* crowns) are classified as *Salb* in 90.3% of the cases. The PA's of *Amar* and *Rmuc* are also acceptable, being 75.0% and 72.4%, respectively.

Through the addition of an NDVI layer in the classification process, the accuracy measures only slightly increased: the OA increased from 67.8% to 68.2%, κ increased slightly from 57.1% to 57.7% and τ remained 46.5%. This means that in these classifications 46.5% more pixels are classified correctly than would be expected from chance alone. Both UA and PA of class *Bgym* are zero and the UA and PA of Nil are below 10%.

Table 27. Error matrix of the supervised ML classification of MXS taking into consideration only those transect data where the adult tree layer corresponds with the remotely sensed canopy

		Reference data						RT ^d	UA ^e
		<i>Amar</i>	<i>Bgym</i>	<i>Ctag</i>	<i>Rmuc</i>	<i>Salb</i>	Nil		
Classified data	AGazi	46.50	0.00	11.50	9.33	0.00	0.00	67.33	
	AMD	5.50	0.00	20.50	0.00	0.00	0.00	26.00	
	ALD	69.50	0.00	40.00	0.00	0.00	0.00	109.50	
	AS	0.00	0.00	0.00	14.91	0.00	0.00	14.91	
	<i>Amar</i>		0.00		24.24	0.00	0.00	217.74	
	BG (<i>Bgym</i>)	0.00	0.00	0.00	8.58	1.00	0.33	9.91	
	CGazi	13.00	0.00	5.50	0.00	0.00	0.00	18.50	
	CCM	0.00	0.00	6.00	1.25	0.00	0.00	7.25	
	CNFP	7.00	0.00	43.50	1.00	0.00	0.00	51.50	
	CNMak	0.00	0.00	63.00	0.00	0.00	0.00	63.00	
	CWMak	1.50	0.00	10.00	1.66	0.00	0.00	13.16	
	C&R	0.00	0.00	10.00	0.00	0.00	0.00	10.00	
	<i>Ctag</i>	21.50	0.00	138.00	3.91	0.00	0.00	163.41	0.845
	REkin	0.00	3.00	2.00	75.49	2.50	0.33	83.32	
	RPlant	0.00	0.00	0.00	1.00	0.00	0.00	1.00	
	RWMak	0.00	1.00	3.00	33.58	0.00	0.00	37.58	
	<i>Rmuc</i>	0.00	4.00	5.00		2.50	0.33	121.90	0.903
	SA (<i>Salb</i>)	0.00	0.00	0.00	5.16	43.50		76.99	0.565
		19.00	0.00	0.00	0.00	1.00	2.00	22.00	0.091
CT ^a		162.00	4.00	215.00	151.96	48.00	30.99		611.950
PA ^b		0.750	0.000	0.642	0.724	0.906	0.065		
OA^c		0.678		κ	0.571		τ		0.465

aColumn Total. bProducer's accuracy. cOverall accuracy. dRow Total. eUser's accuracy.

Table 28. Error matrix of the supervised ML classification of MXS+NDVI taking into consideration only those transect data where the adult tree layer corresponds with the remotely sensed canopy

		Reference data					RT ^d	UA ^e	
		<i>Amar</i>	<i>Bgym</i>	<i>Ctag</i>	<i>Rmuc</i>	<i>Salb</i>			Nil
Classified data	AGazi	43.00	0.00	15.83	7.83	0.00	0.00	66.66	
	AMD	9.50	0.00	18.00	0.00	0.00	0.00	27.50	
	ALD	71.00	0.00	31.50	0.00	0.00	0.00	102.50	
	AS	0.00	0.00	1.50	5.50	0.00	0.00	7.00	
	<i>Amar</i>	123.50	0.00	66.83	13.33		0.00	203.66	0.606
	BG (<i>Bgym</i>)	0.00	0.00	0.00		4.50	0.00	12.66	0.000
	CGazi	11.00	0.00	3.00	2.00	0.00	0.00	16.00	
	CCM	0.00	0.00	5.83	1.50	2.00	0.00	9.33	
	CNFP	5.50	0.00	2.00	0.00	0.00	0.00	7.50	
	CNMak	0.00	0.00	104.33	0.00	0.00	0.00	104.33	
	CWMak	0.00	0.00	16.50	0.00	0.00	0.00	16.50	
	C&R	0.00	0.00	7.00	0.00	0.00	0.00	7.00	
	<i>Ctag</i>	16.50	0.00	138.66	3.50		0.00	160.66	0.863
	REkin	0.00	3.50	4.00	71.50	4.50	2.00	85.50	
	RPlant	0.00	0.00	0.00	0.00	0.00	0.00	0.00	
	RWMak	0.00	0.50	1.75	51.41	0.00	0.00	53.66	
	<i>Rmuc</i>	0.00	4.00	5.75	122.91	4.50	2.00	139.16	0.883
	SA (<i>Salb</i>)	0.00	0.00	3.75	4.08	30.00	27.00	64.83	0.463
		22.00		0.00		7.00	2.00	31.00	0.065
	CT ^a	162.00	4.00	214.99	151.98	48.00	31.00		611.970
PA ^b	0.762	0.000	0.645	0.809	0.625	0.065			
OA^c	0.682		κ	0.577		τ		0.465	

aColumn Total. bProducer's accuracy. cOverall accuracy. dRow Total. eUser's accuracy.

IV.5.1.5 FUZZY CLASSIFICATION

Fuzzy classifications using the four best classes of the MXS and the MXS+NDVI images were calculated and fuzzy convolution was performed using various window sizes: 3x3, 5x5 and 7x7 pixels. Such fuzzy classifications of MXS are shown in Figure 39, Figure 40 and Figure 41 respectively. Fuzzy classifications of MXS+NDVI are shown in Figure 42, Figure 43 and Figure 44, respectively.

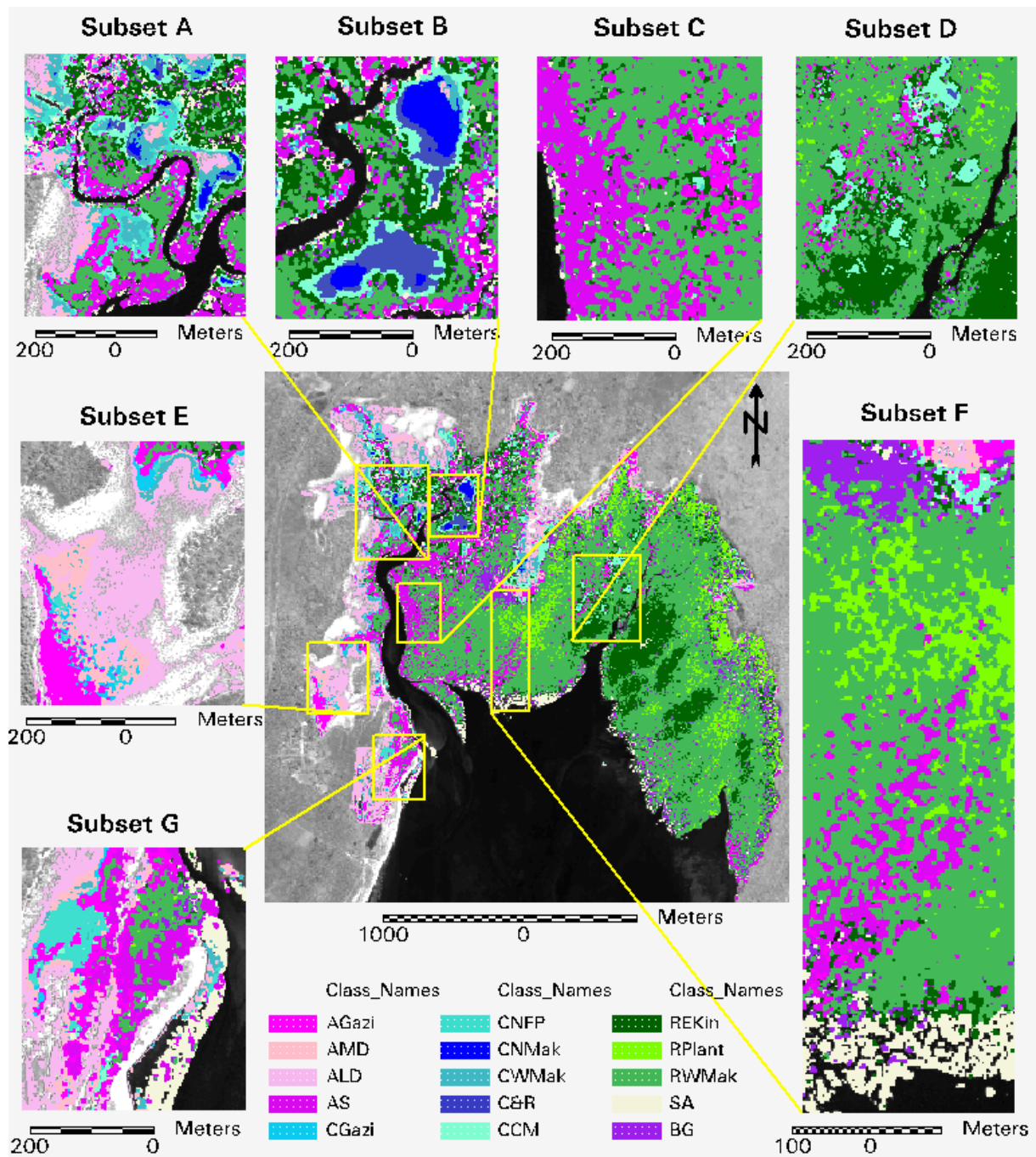


Figure 39. Fuzzy classification of MXS with 15 classes using a 3x3 pixel convolution window

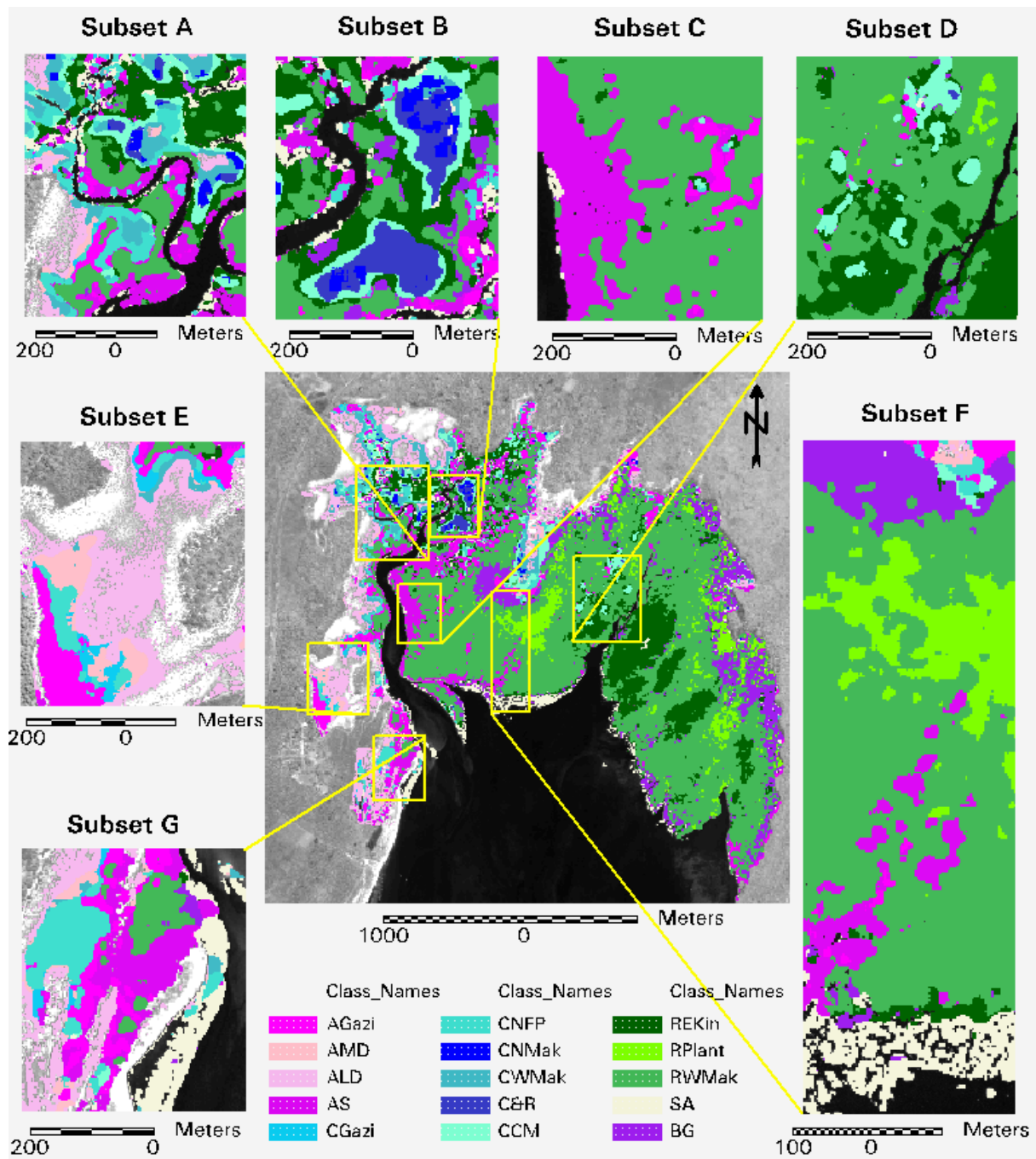


Figure 44. Fuzzy classification of MXS+NDVI with 15 classes using a 7x7 pixel convolution window

In what follows a comparison between the ML classification of MXS and its fuzzy classifications with convolution window sizes 3, 5 and 7 is done.

SUBSET A

Many pixels are classified as SA (especially at the edges of the creek), but these wrongly classified pixels are converted into other classes through fuzzy classification. The *Salb* island is classified correctly in all classifications.

SUBSET B

In the non-fuzzy classification some pixels in the Southern *Ctag* area were classified as SA and CCM, but these were transformed into C&R in the fuzzy3 classification (and subsequently also in the fuzzy5 and fuzzy7 classifications). The zone surrounding the *Ctag* areas is very heterogeneously classified in MXS image: a mixture of SA, AS and BG which were transformed into RWMak and REKin in the fuzzy images. There is still some BG left though in the fuzzy7 image.

SUBSET C

The seaward *Amar* zone is classified as a mixture of (in order of importance) AS, SA, CGazi, REKin, RWMak, CWMak, and BG in the non-fuzzy classification. In the fuzzy3 classification most of the *Ctag* is filtered out and in the fuzzy 5 also the SA, BG, REKin, have changed into AS.

SUBSET D

Pepper and salt effect is highly pronounced in the non-fuzzy image (especially BG and AS present as isolated pixels). This effect has mostly disappeared in the fuzzy3 image. Spectacular transformation of the zone on the East of the image: completely scattered pixels from all sorts of classes into a nearly homogeneous zone of REKin in fuzzy3

SUBSET E

The number of pixels in the landward *Amar* zone that were classified as *Ctag* in the MXS image is reduced in the MXS fuzzy7 image.

SUBSET F

The non-fuzzy classification consists of large clumps of AS and RPlant and in between a very heterogeneous zone of classes BG, SA, REKin, CWMak, *etc.* This zone is changed into a homogeneous zone of AS and RWMak. The *Bgym* zone in the North of the image is classified as BG dominated in the non-fuzzy image mixed with isolated pixels of SA, REKin, RPlant and RWMak. The isolated SA pixels are nearly completely gone in the fuzzy3 image. It becomes a zone dominated by BG, interspaced with Rplant, RWMak and REKin, while it is transformed completely in BG in the fuzzy7 image.

SUBSET G

The *Salb* strip at the NFP is classified best in the fuzzy7 image: most isolated pixels of classes BG, CCM, AS, REKin, RPlant, RWMak and CNMak pixels which were present in other classifications are filtered out (fuzzy5 is also quite good). The *Rmuc* dominated zone North of the seaward *Amar* zone is a mixture of *Bgym* and *Rmuc* which is correctly classified in the MXS image but is completely converted into RWMak in the fuzzy7 image. Fuzzy3 and fuzzy5 represent stages of decreasing presence of *Bgym* in the *Rmuc* dominated zone. The mushroom shaped *Salb* island near Subset G is classified entirely as *Salb* in the MXS fuzzy7 image and not in all other images.

OTHER REMARKS

The *Salb* plantation at the OFP is nowhere classified as SA, instead it is a mixture of ALD, CNFP, SA, CNMak, CCM, CWMak, RWMak and BG. The *Salb* plantation is nearly completely classified as AMD in the fuzzy7 image.

Many pixels at the edge of the water are classified as SA in the MXS image, but are changed into either AS or *Rmuc* in the fuzzy classifications.

IV.5.2 Supervised classification of MPXS

IV.5.2.1 TRAINING SITE SELECTION

The TS for the supervised classification of the MPXS image were roughly equal to the ones used in the supervised classification of the MXS image. Some adjustments were needed because some AOI's contained masked pixels on the MPXS image (due to the finer resolution).

IV.5.2.2 TRAINING SITE STATISTICS

Again 15 signatures were created from the TS. Univariate statistical parameters such as minimum, maximum, mean and standard deviation were measured for each signature in each image layer and the covariance matrix for each signature was calculated. Results of these statistical parameter calculations are given in the appendix. The same TS were used to develop signatures for MPXS, MPXS+VAR7 and MPXS+VAR21. Signature means and standard deviations in each band are plotted in Figure 45-Figure 50.

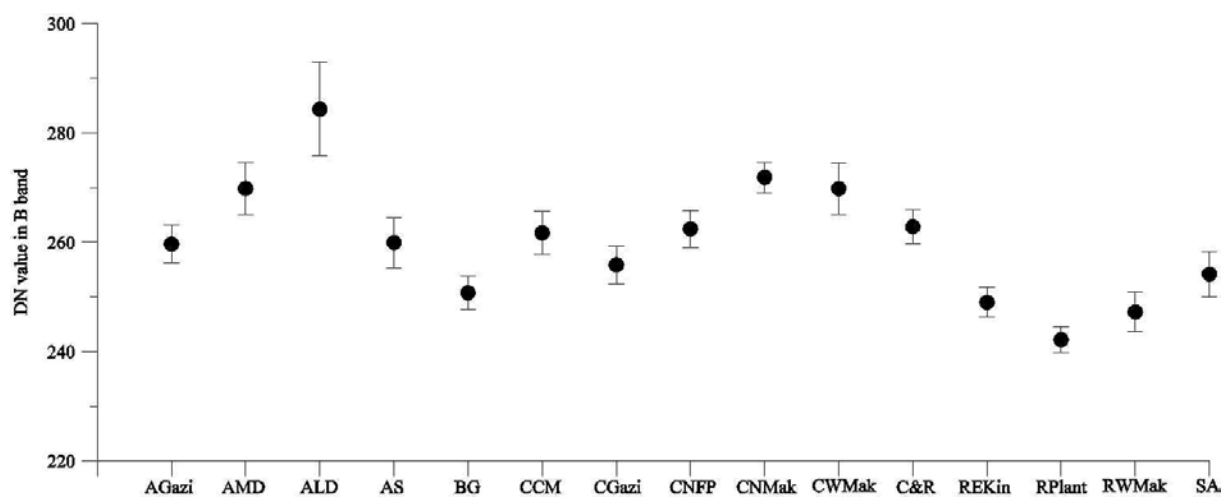


Figure 45. MPXS(+VAR7/21) signature DN means and standard deviations in the B band

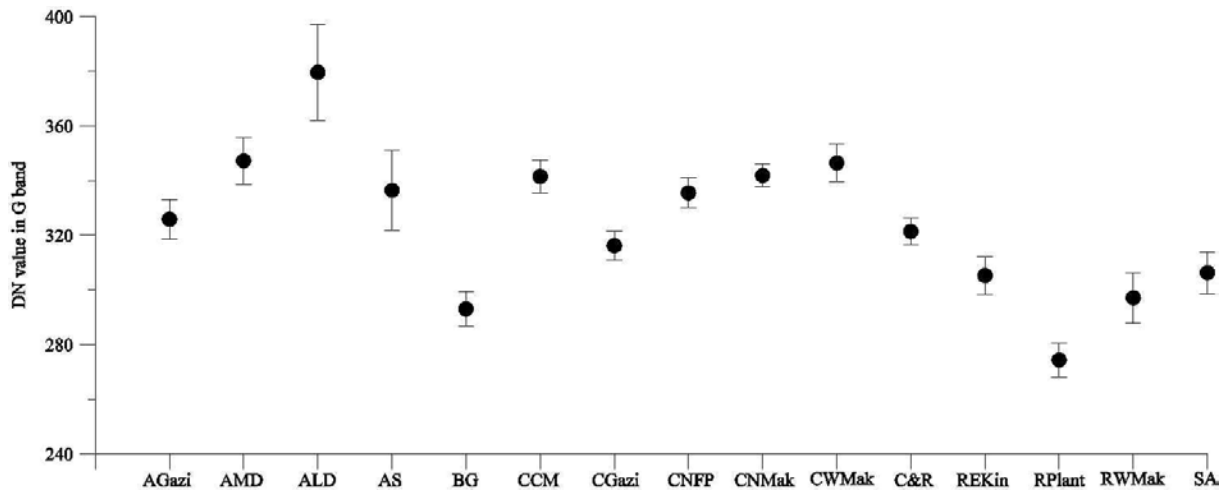


Figure 46. MPXS(+VAR7/21) signature DN means and standard deviations in the G band

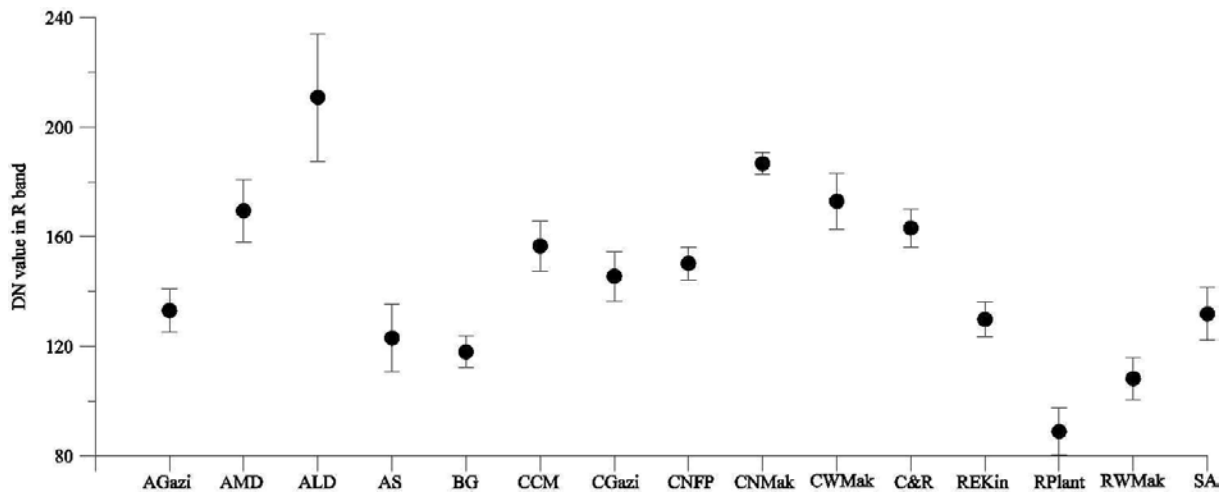


Figure 47. MPXS(+VAR7/21) signature DN means and standard deviations in the R band

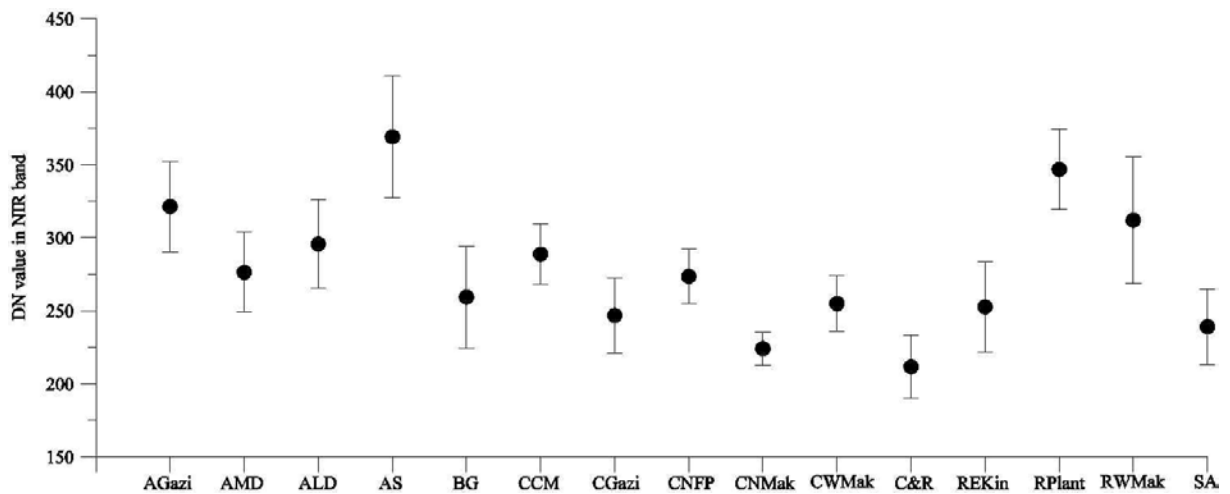


Figure 48. MPXS(+VAR7/21) signature DN means and standard deviations in the NIR band

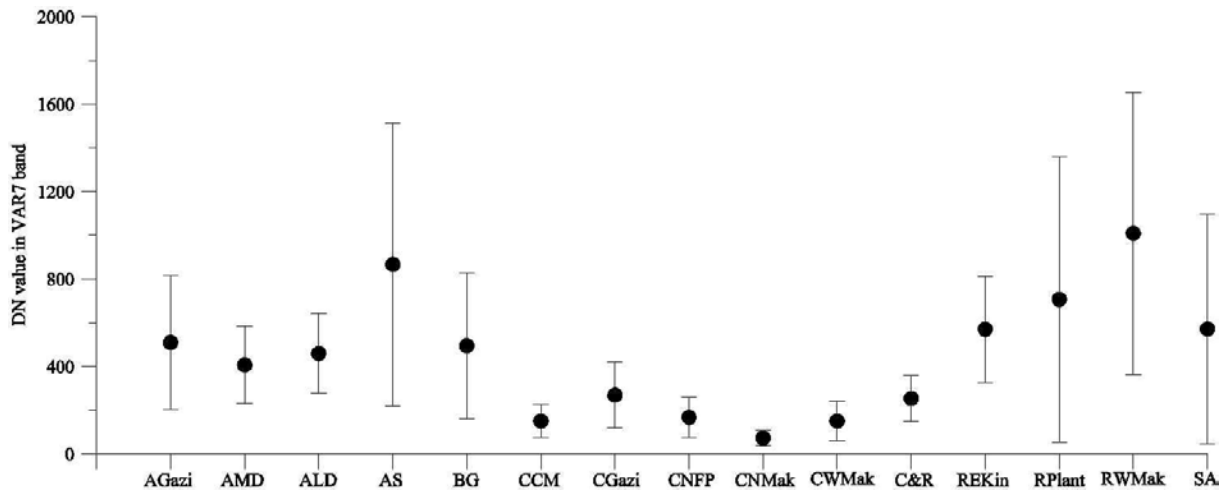


Figure 49. MPXS(+VAR7/21) signature DN means and standard deviations in the VAR7 band

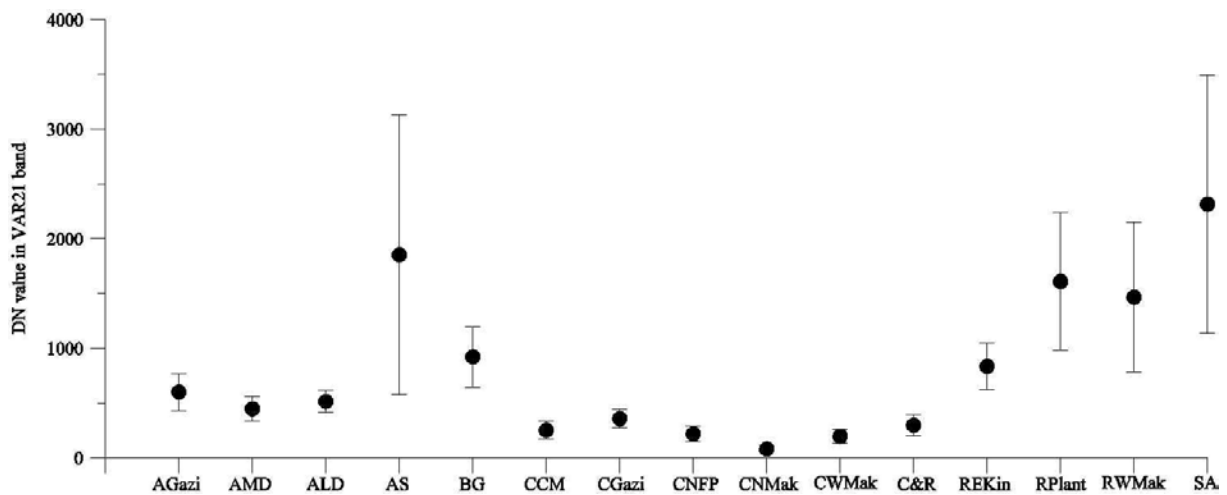


Figure 50. MPXS(+VAR7/21) signature DN means and standard deviations in the VAR21 band

IV.5.2.3 EVALUATION OF THE DEGREE OF BETWEEN-CLASS SEPARABILITY

Contingency matrices were calculated for all 15 signatures. Results for training pixel data extracted from the MPXS, MPXS+VAR7 and MPXS+VAR21 image are shown in Table 29, Table 30 and Table 31, respectively. The overall accuracy for training pixel classification in the MPXS image is 81%, 85% for the MPXS+VAR7 image and 90% for the MPXS+VAR21 image.

Table 29. Contingency matrix for training pixel data from MPXS using the ML decision rule, entries in pixel counts. User's, producer's and overall accuracy are shown

		Reference data														RT ^d	UA ^e	
		AGazi	AMD	ALD	AS	BG	CGazi	CCM	CNFP	CNMak	CWMak	C&R	REKin	RPlant	RWMak			SA
Classified data	AGazi	10430	10		1373	36	45	4	177		0	0	148	0	85	54	12362	0.84
	AMD		2556	1282	0	0	153		225	0	847	0	0		0	0	5118	0.50
	ALD		0	272	10560	2	0	0	0	0	77	0	0	0	0	0	10911	0.97
	AS		345	10	0	16404	0	1	0	2		0	18		164		16944	0.97
	BG		44	0	0	13	6107	0	0	0	0	0	0	527	0	401	7591	0.80
	CGazi		140	432	58	37	0	1449	4		0	375	0	39	0	0	3219	0.45

CCM	38	28	0	10	0	1381	56	0	20	316	0	1	564	3465	0.40	
CNFP	276	590	36	0	0	397	36	3756	0	16	102	0	0	32	5568	0.67
CNMak	0	0	18	0	0	0	0	0	7942	106	32	0	0	0	8098	0.98
CWMak	0	1507	342	0	0	219	0	59	91	3933	21	5	0	0	6191	0.64
C&R	0	1	0	0	0	385	0	0	32	4114	0	0	0	0	4702	0.87
REkin	80	0	0	10	271	261	5	0	0	0	9116	174	788	10708	0.85	
RPlant	0	0	0	1	0	0	0	0	0	0	2856	210	0	3104	0.92	
RWMak	59	0	492	296	0	0	0	0	0	0	445	76	12	7241	0.81	
SA	167	14	0	5	0	217	7	0	0	19	0	16	2865	4537	0.63	

CT^a 11629 5420 12297 18419 6711 2270 2293 4972 8097 5681 4518 12672 2935 6912 4933

PA^b 0.90 0.47 0.86 0.89 0.91 0.64 0.60 0.76 0.98 0.69 0.91 0.72 0.97 0.85 0.58

OA^c 0.81

^aColumn Total. ^bProducer's Accuracy. ^cOverall Accuracy. ^dRow Total. ^eUser's Accuracy

Table 30. Contingency matrix for training pixel data from MPXS+VAR7 using the ML decision rule, entries in pixel counts. User's, producer's and overall accuracy are shown

		Reference data																
		AGazi	AMD	ALD	AS	BG	CGazi	CCM	CNFP	CNMak	CWMak	C&R	REkin	RPlant	RWMak	SA	RT ^d	UA ^e
Classified data	AGazi	10733	22	1	1181	29	18	16	68	0	0	0	34	0	93	12255	0.88	
	AMD	100	3932	1434	0	0	70	6	148	0	295	14	0	0	0	10	6009	0.65
	ALD	0	287	10766	5	0	0	0	0	0	0	0	0	0	0	0	11119	0.97
	AS	338	0	16651	0	0	0	0	0	0	0	0	0	0	164	17177	0.97	
	BG	46	0	6171	0	7	0	0	83	0	349	0	0	0	0	7337	0.84	
	CGazi	100	17	5	0	1576	767	428	0	0	0	0	0	0	0	3066	0.51	
	CCM	29	0	1	3	63	0	18	229	0	776	0	0	0	0	2757	0.58	
	CNFP	53	314	2	0	36	3833	268	12	0	0	0	0	0	13	4923	0.78	
	CNMak	0	0	0	0	0	0	0	7905	57	32	227	0	0	0	8221	0.96	
	CWMak	0	642	76	0	0	227	2	85	4526	4	0	0	0	9	5687	0.80	
	C&R	0	3	0	0	0	0	290	0	76	0	4188	0	0	0	4644	0.90	
	REkin	31	0	0	0	262	0	1	0	0	0	0	2402	0	31	711	3655	0.66
	RPlant	0	0	2	0	0	0	0	0	0	0	0	0	2871	198	0	3073	0.93
	RWMak	0	0	544	0	0	0	0	0	0	0	9	70	6022	64	7093	0.85	
SA	153	2	1	246	0	7	0	39	226	54	2638	0	0	0	3489	0.76		

CT^a 11629 5420 12297 18411 7052 2270 2412 4979 8097 5653 4518 2981 2941 6912 4933

PA^b 0.92 0.73 0.88 0.90 0.88 0.69 0.67 0.77 0.98 0.80 0.93 0.81 0.98 0.87 0.53

OA^c 0.85

^aColumn Total. ^bProducer's Accuracy. ^cOverall Accuracy. ^dRow Total. ^eUser's Accuracy

Table 31. Contingency matrix for training pixel data from MPXS+VAR21 using the ML decision rule, entries in pixel counts. User's, producer's and overall accuracy are shown

		Reference data														RT ^d	UA ^e	
		AGazi	AMD	ALD	AS	BG	CGazi	CCM	CNFP	CNMak	CWMak	C&R	REkin	RPlant	RWMak			SA
Classified data	AGazi	11082	47	0	507	22	29	6	101	0	0	30	0	34		11859	0.93	
	AMD	183	4565	1417	0	0	95	9	123	0	8	0	0	0	0	6645	0.69	
	ALD	2	269	10877	0	0	0	0	0	0	22	0	0	0	0	11170	0.97	
	AS		2	0	17262	0	0	0	0	0	0	0	0	202	0	17582	0.98	
	BG	30		0	0	6336	0	7		0	0	0	107		394	147	7023	0.90
	CGazi	37	223		0	0	1560	11	630	0	319	4	0	0	0	0	2785	0.56
	CCM	69		0	0		7	1823		0	10	318	14	0	0	134	2488	0.73
	CNFP	13	42	0	0	0	398	6	3983	0	297		0	0	0	0	4739	0.84
	CNMak	0		0		0	0	0	0		19		0	0	0	0	7976	1.00
	CWMak	0		2		0	180	0	99		4744		0	0	0	0	5331	0.89
	C&R	0		0		0	1	316	0		25		0	0	0	13	4539	0.91
	REkin	41		0		331	0	102	0		0		2718	0	59	351	3617	0.75
	RPlant	0		0		2	0	0	0		0		0	2860	211	0	3075	0.93
	RWMak	10	0	0	566	227	0	0	0	0	0		20	74	5924	4	6825	0.87
	SA	50	0		64	134		13	0	0	0	28	88	5	88		4753	0.90
CT ^a	11629	5420	12297	18411	7052	2270	2293	4972	8097	5681	4518	2981	2941	6912	4933			
PA ^b	0.95	0.84	0.88	0.94	0.90	0.69	0.80	0.80	0.98	0.84	0.92	0.91	0.97	0.86	0.87			
OA ^c	0.90																	

^aColumn Total. ^bProducer's Accuracy. ^cOverall Accuracy. ^dRow Total. ^eUser's Accuracy

Transformed divergence indices were calculated using all bands in the images MPXS, MPXS+VAR7 and MPXS+VAR21. These indices are a measure for separability between any pair of signatures. A separability listing is a report of the computed divergence for every class pair. This listing contains every divergence value for the bands studied for every possible pair of signatures. According to Jensen (1986) separation is poor if the transformed divergence index between two signatures is below 1700. Values lower than 1700 are therefore highlighted in the separability listings in Table 32, Table 33 and Table 34.

All separability indices increased by the addition of the VAR7 layer to MPXS. The same is true for the addition of the VAR21 layer. If we compare the separability between the signatures extracted from the MPXS+VAR7 image and the ones extracted from the MPXS+VAR21 image it is clear that in most cases separability increased, but for 15 of the 105 (=15x14/2) possible pairs of classes the separability decreased. Decreases ranged from 0.08 to 159.89, but were never large enough to decrease the separability from “good” in MXS+VAR7 to a lower level in MXS+VAR21.

Table 32. Transformed divergence separability indices for the signatures extracted from the MPXS image. Values lower than 1700 are shaded, average and minimum separability are shown

	AGazi	AMD	ALD	AS	BG	CGazi	CCM	CNFP	CNMak	CWMak	C&R	REkin	RPlant	RWMak	SA	
AGazi	0.00	1887.65	1999.78	1558.95	1932.09	1706.30	1882.55	1652.74	2000.00	1985.90	1999.58	1815.06	1999.89	1847.78	1820.78	
AMD	1887.65	0.00	1521.38	1983.38	1999.96	912.93	1943.56	1272.96	1998.81	462.10	1979.60	1982.11	2000.00	1999.71	1936.46	
ALD	1999.78	1521.38	0.00	1999.18	2000.00	1979.41	1999.96	1999.34	1999.93	1800.82	1999.98	1999.97	2000.00	2000.00	1999.00	
AS	1558.95	1983.38	1999.18	0.00	1992.29	1942.89	1994.54	1986.75	2000.00	1999.34	2000.00	1959.20	1999.86	1795.16	1993.15	
BG	1932.09	1999.96	2000.00	1992.29	0.00	1999.88	1952.13	1999.28	2000.00	2000.00	1999.93	1461.18	1990.11	1555.83	1353.34	
CGazi	1706.30	912.93	1979.41	1942.89	1999.88	0.00	1925.94	675.61	1999.99		1990.51	1974.45	2000.00	1998.88	1980.48	
CCM	1882.55	1943.56	1999.96	1994.54	1952.13	1925.94	0.00	1793.20	1999.98	1937.25	1295.07	1114.84	1999.99	1975.86	902.58	
CNFP	1652.74		1999.34	1986.75	1999.28	675.61	1793.20	0.00	2000.00	1521.56	1983.03	1930.29	2000.00	1999.06	1906.28	
CNMak	2000.00	1998.81	1999.93	2000.00	2000.00	1999.99	1999.98	2000.00	0.00	1967.97	1956.63	2000.00	2000.00	2000.00	2000.00	
CWMak	1985.90	462.10	1800.82	1999.34	2000.00	1115.83	1937.25		1967.97	0.00	1952.61	1991.02	2000.00	1999.99	1959.37	
C&R	1999.58	1979.60	1999.98	2000.00	1999.93	1990.51	1295.07	1983.03	1956.63	1952.61	0.00	1960.96	2000.00	1999.99	1851.55	
REkin	1815.06	1982.11	1999.97	1959.20	1461.18	1974.45		1930.29	2000.00	1991.02	1960.96	0.00	1993.61	1618.78	806.62	
RPlant	1999.89	2000.00	2000.00	1999.86	1990.11	2000.00	1999.99	2000.00	2000.00	2000.00	2000.00	1993.61	0.00	1757.84	1997.39	
RWMak	1847.78	1999.71	2000.00	1795.16	1555.83	1998.88	1975.86	1999.06	2000.00	1999.99	1999.99	1618.78	1757.84	0.00	1809.13	
SA	1820.78	1936.46	1999.00	1993.15	1353.34	1980.48	902.58	1906.28	2000.00	1959.37	1851.55	806.62	1997.39	1809.13	0.00	
Average separability:															1842.65	
Minimum separability:																462.10

Table 33. Transformed divergence separability indices for the signatures extracted from the MPXS+VAR7 image. Values lower than 1700 are shaded, average and minimum separability are shown

	AGazi	AMD	ALD	AS	BG	CGazi	CCM	CNFP	CNMak	CWMak	C&R	REkin	RPlant	RWMak	SA
AGazi	0.00	1926.77	1999.90	1759.25	1939.53	1986.80	1939.77	1946.22	2000.00	1998.48	1999.92	1836.09	1999.95	1927.85	1850.45
AMD	1926.77	0.00	1544.35	1993.96	1999.98	1685.50	1958.64	1692.48	2000.00	1330.70	1984.06	1990.88	2000.00	1999.97	1965.27
ALD	1999.90	1544.35	0.00	1999.29	2000.00	1999.92	1999.99	1999.86	2000.00	1962.76	2000.00	1999.99	2000.00	2000.00	1999.39
AS	1759.25	1993.96	1999.29	0.00	1995.07	2000.00	1999.34	1999.99	2000.00	2000.00	2000.00	1965.88	1999.88	1811.30	1994.91
BG	1939.53	1999.98	2000.00	1995.07	0.00	1999.99	1963.66	1999.78	2000.00	2000.00	1999.98	1563.47	1994.73	1688.34	1459.42
CGazi	1986.80	1685.50	1999.92	2000.00	1999.99	0.00	1942.38	694.18	2000.00	1132.34	1995.27	1999.93	2000.00	2000.00	1999.82
CCM	1939.77	1958.64	1999.99	1999.34	1963.66	1942.38	0.00	1815.62	2000.00	1945.20	1487.82	1671.68	2000.00	1998.03	1597.37
CNFP	1946.22	1692.48	1999.86	1999.99	1999.78	694.18	1815.62	0.00	2000.00	1523.60	1991.27	1997.80	2000.00	2000.00	1994.41
CNMak	2000.00	2000.00	2000.00	2000.00	2000.00	2000.00	2000.00	2000.00	0.00	1982.08	1990.56	2000.00	2000.00	2000.00	2000.00
CWMak	1998.48	1330.70	1962.76	2000.00	2000.00	1132.34	1945.20	1523.60	1982.08	0.00	1959.54	1999.83	2000.00	2000.00	1998.43
C&R	1999.92	1984.06	2000.00	2000.00	1999.98	1995.27	1487.82	1991.27	1990.56	1959.54	0.00	1991.45	2000.00	2000.00	1982.95
REkin	1836.09	1990.88	1999.99	1965.88	1563.47	1999.93	1671.68	1997.80	2000.00	1999.83	1991.45	0.00	1996.65	1689.64	855.76
RPlant	1999.95	2000.00	2000.00	1999.88	1994.73	2000.00	2000.00	2000.00	2000.00	2000.00	2000.00	1996.65	0.00	1764.40	1998.38
RWMak	1927.85	1999.97	2000.00	1811.30	1688.34	2000.00	1998.03	2000.00	2000.00	2000.00	2000.00	1689.64	1764.40	0.00	1858.76
SA	1850.45	1965.27	1999.39	1994.91	1459.42	1999.82	1597.37	1994.41	2000.00	1998.43	1982.95	855.76	1998.38	1858.76	0.00
Average separability:				1900.08											
Minimum separability:				694.18											

Table 34. Transformed divergence separability indices for the signatures extracted from the MPXS+VAR21 image. Values lower than 1700 are shaded, decreased values of separability compared to separability values of MPXS+VAR7 are given in bold. Average and minimum separability are shown

	AGazi	AMD	ALD	AS	BG	CGazi	CCM	CNFP	CNMak	CWMak	C&R	REkin	RPlant	RWMak	SA
AGazi	0.00	1902.60	1999.82	1999.61	1952.72	1958.50	1932.57	1965.54	2000.00	1999.35	1999.74	1937.88	2000.00	1990.79	1999.98
AMD	1902.60	0.00	1609.90	2000.00	1999.99	1525.61	1950.00	1796.89	2000.00	1623.00	1983.21	1998.95	2000.00	2000.00	2000.00
ALD	1999.82	1609.90	0.00	2000.00	2000.00	1995.61	1999.98	1999.91	2000.00	1989.51	2000.00	2000.00	2000.00	2000.00	2000.00
AS	1999.61	2000.00	2000.00	0.00	1998.93	2000.00	2000.00	2000.00	2000.00	2000.00	2000.00	1984.75	1999.91	1827.55	1994.26
BG	1952.72	1999.99	2000.00	1998.93	0.00	2000.00	1999.14	2000.00	2000.00	2000.00	1999.99	1570.12	1992.75	1724.01	1977.52
CGazi	1958.50	1525.61	1995.61	2000.00	2000.00	0.00	1954.55	761.33	2000.00	1203.18	1994.05	1999.98	2000.00	2000.00	2000.00
CCM	1932.57	1950.00	1999.98	2000.00	1999.14	1954.55	0.00	1922.85	2000.00	1963.52	1364.34	1999.70	2000.00	2000.00	2000.00
CNFP	1965.54	1796.89	1999.91	2000.00	2000.00	761.33	1922.85	0.00	2000.00	1528.81	1992.23	2000.00	2000.00	2000.00	2000.00
CNMak	2000.00	2000.00	2000.00	2000.00	2000.00	2000.00	2000.00	2000.00	0.00	1987.72	1997.34	2000.00	2000.00	2000.00	2000.00
CWMak	1999.35	1623.00	1989.51	2000.00	2000.00	1203.18	1963.52	1528.81	1987.72	0.00	1961.48	2000.00	2000.00	2000.00	2000.00
C&R	1999.74	1983.21	2000.00	2000.00	1999.99	1994.05	1364.34	1992.23	1997.34	1961.48	0.00	1999.34	2000.00	2000.00	2000.00
REkin	1937.88	1998.95	2000.00	1984.75	1570.12	1999.98	1999.70	2000.00	2000.00	2000.00	1999.34	0.00	1995.71	1701.90	1831.16
RPlant	2000.00	2000.00	2000.00	1999.91	1992.75	2000.00	2000.00	2000.00	2000.00	2000.00	2000.00	1995.71	0.00	1769.08	1998.92
RWMak	1990.79	2000.00	2000.00	1827.55	1724.01	2000.00	2000.00	2000.00	2000.00	2000.00	2000.00	1701.90	1769.08	0.00	1874.80
SA	1999.98	2000.00	2000.00	1994.26	1977.52	2000.00	2000.00	2000.00	2000.00	2000.00	2000.00	1831.16	1998.92	1874.80	0.00
Average separability:				1933.17											
Minimum separability:				761.33											

IV.5.2.4 CLASSIFICATION ACCURACY ASSESSMENT

MPXS, MPXS+VAR7 and MPXS+VAR21 were classified with the ML decision rule in the 15 classes described above. Results will not be shown here, because the differences with the fuzzy classifications (given in next section) can hardly be seen.

Table 35 - Table 37 represent the error matrices from the classification of MPXS, MPXS+VAR7 and MPXS+VAR21 obtained when only those transect data that fulfil the requirement that the adult tree layer represents the remotely sensed canopy (see materials and methods) are taken into account as reference data.

Including texture in the classification increased the OA, κ and τ of the classification. The OA, κ and τ are the highest for the MPXS+VAR7 image.

The UA of *Amar* increased from 57.3% in the MPXS classification to 59.7% in the MPXS+VAR7 classification and remained 57.3% in the MPXS+VAR21 classification. The PA of *Amar* increased from 81.3% in the MPXS classification to 90.4% in the MPXS+VAR7 classification and to 91.7% in the MPXS+VAR21 classification.

Not a single *Bgym* PCQM observation was classified correctly in the MPXS classification where both the UA and PA are 0. The UA of *Bgym* was highest (but still very low) in the in the MPXS+VAR7 image (7%), while the PA of *Bgym* was 8.3% in both classifications including texture.

The UA of *Ctag* increased with the inclusion of texture in the classification from 86.4% to 95.4% and even to 100% in the MPXS+VAR21 classification, while the PA of *Ctag* decreased with the inclusion of texture from 66.6% to 66.3% in the MPXS+VAR7 classification and further to 56.3% in the MPXS+VAR21 classification.

The UA of *Rmuc* increased with the inclusion of texture in the classification from 66.1% to 84.6% in the classification of MPXS+VAR7 and to 91.3% in the MPXS+VAR21 classification. The PA of *Rmuc* decreased with the inclusion of texture from 69.0% to 61.0% in the MPXS+VAR7 classification to 64.2% in the MPXS+VAR21 classification.

The UA of *Salb* increased with the inclusion of texture in the classification from 39.6% to 44.5% in the classification of MPXS+VAR7 and to 44.4% in the MPXS+VAR21 classification. The PA of *Salb* increased with the inclusion of texture as well from 13.5% to 70.3% in the MPXS+VAR7 classification and further to 85.4% in the MPXS+VAR21 classification.

Table 35. Error matrix of the supervised ML classification of MPXS taking into consideration only those transect data where the adult tree layer corresponds with the remotely sensed canopy

		Reference data					RT ^d	UA ^e	
		<i>Amar</i>	<i>Bgym</i>	<i>Ctag</i>	<i>Rmuc</i>	<i>Salb</i>			Nil
Classified data	AGazi	47.33	0.00	12.08	22.15	0.00	0.00	81.56	
	AMD	9.50	0.00	5.25	0.00	0.00	0.00	14.75	
	ALD	74.00	0.00	48.00	0.00	0.00	0.00	122.00	
	AS	0.83	0.00	0.00	10.83	0.00	0.00	11.66	
	<i>Amar</i>	131.66	0.00	65.33	32.98	0.00	0.00	229.97	0.573
	BG (<i>Bgym</i>)	0.00	0.00	0.50	9.80	3.50	0.33	14.13	0.000
	CGazi	3.33	0.00	11.25	1.50	0.00	0.00	16.08	
	CCM	0.00	0.00	3.33	0.50	0.00	1.00	4.83	
	CNFP	14.50	0.00	43.58	0.00	0.00	0.00	58.08	
	CNMak	0.00	0.00	73.00	0.00	0.00	1.00	74.00	
	CWMak	0.75	0.00	12.00	0.00	0.00	0.00	12.75	
	C&R	0.00	0.00	0.00	0.00	0.00	0.00	0.00	
	<i>Ctag</i>	18.58	0.00		2.00	0.00	2.00	165.74	
	REkin	0.00	4.00	2.00	75.97	31.00	14.33	127.30	
	RPlant	0.00	0.00	0.00	0.00	0.00	0.00	0.00	
	RWMak	0.00	0.00	2.50	28.81	0.00	0.00	31.31	
	<i>Rmuc</i>	0.00	4.00		104.78	31.00	14.33	158.61	
	SA (<i>Salb</i>)		0.00	1.50	2.32	6.50	5.33	16.40	0.396
	Nil	11.00	0.00	0.00	0.00	7.00	9.00	27.00	0.333
	CT ^a		161.99	4.00	214.99	151.88	48.00	30.99	
PA ^b		0.813	0.000	0.666	0.690	0.135	0.290		
OA^c		0.646	κ		0.519	τ		0.412	

aColumn to tal. bProducer's accuracy. cOverall accuracy. dRow Total. eUser's accuracy.

Table 36. Error matrix of the supervised ML classification of MPXS+VAR7 taking into consideration only those transect data where the adult tree layer corresponds with the remotely sensed canopy

		Reference data						RT ^d	UA ^e
		<i>Amar</i>	<i>Bgym</i>	<i>Ctag</i>	<i>Rmuc</i>	<i>Salb</i>	Nil		
Classified data	AGazi	55.00	0.00	10.50	12.32	0.00	0.00	77.82	
	AMD	16.50	0.00	11.50	0.00	0.00	0.00	28.00	
	ALD	75.00	0.00	43.00	0.00	0.00	0.00	118.00	
	AS	0.00	0.00	0.00	21.55	0.00	0.00	21.55	
	<i>Amar</i>		0.00		33.87	0.00		245.37	
	BG (<i>Bgym</i>)	0.00		0.00	3.15		0.00	4.73	0.070
	CGazi	2.00	0.00	11.00	0.00	0.00	0.00	13.00	
	CCM	0.00	0.00	1.50	1.41	1.00	0.00	3.91	
	CNFP	2.50	0.00	38.50	0.00	0.00	0.00	41.00	
	CNMak	0.00	0.00	64.33	0.00	0.00	0.00	64.33	
	CWMak	0.00	0.00	19.33	0.00	0.00	0.00	19.33	
	C&R	0.00	0.00	7.83	0.00	0.00	0.00	7.83	
	<i>Ctag</i>	4.50	0.00	142.49	1.41	1.00	0.00	149.40	0.954
	REkin	0.00	1.50	0.50	38.13	4.75	2.00	46.88	
	RPlant	0.00	0.00	0.00	0.00	0.00	0.00	0.00	
	RWMak	0.00	1.33	4.00	54.63	0.25	2.50	62.71	
	<i>Rmuc</i>	0.00	2.83	4.50	92.76	5.00	4.50		0.846
	SA (<i>Salb</i>)		0.83		20.78	33.75	17.50	75.86	0.445
Nil	11.00		0.00	0.00	7.00		27.00	0.333	
CT ^a		162.00	3.99	214.99	151.97	48.00	31.00		
PA ^b		0.904	0.083	0.663	0.610	0.703	0.290		
OA^c		0.694	κ		0.593	τ		0.463	

aColumn Total. bProducer's accuracy. cOverall accuracy. dRow Total. eUser's accuracy.

Table 37. Error matrix of the supervised ML classification of MPXS+VAR21 taking into consideration only those transect data where the adult tree layer corresponds with the remotely sensed canopy

		Reference data						RT ^d	UA ^e
		<i>Amar</i>	<i>Bgym</i>	<i>Ctag</i>	<i>Rmuc</i>	<i>Salb</i>	Nil		
Classified data	AGazi	57.50	0.00	16.50	2.66	0.00	0.00	76.66	
	AMD	16.00	0.00	22.00	0.00	0.00	0.00	38.00	
	ALD	66.50	0.00	44.00	0.00	0.00	0.00	110.50	
	AS	8.50	0.00	3.00	22.50	0.00	0.00	34.00	
		148.50	0.00	85.50		0.00	0.00	259.16	
	BG (<i>Bgym</i>)	0.00	0.33	0.00	5.91	0.33	0.00	6.57	0.050
	CGazi	0.00	0.00	6.66	0.00	0.00	0.00	6.66	
	CCM	0.00	0.00	0.66	0.00	0.00	0.00	0.66	
	CNFP	0.00	0.00	25.33	0.00	0.00	0.00	25.33	
	CNMak	0.00	0.00	62.00	0.00	0.00	0.00	62.00	
	CWMak	0.00	0.00	17.33	0.00	0.00	0.00	17.33	
	C&R	0.00	0.00	9.00	0.00	0.00	0.00	9.00	
	<i>Ctag</i>	0.00	0.00	120.98		0.00	0.00	120.98	1.000
	REkin	0.00	3.33	4.00	48.24	0.33	0.00	55.90	
	RPlant	0.00	0.00	0.00	0.00	0.00	0.00	0.00	
	RWMak	0.00	0.33	1.00	49.23	0.33	0.00	50.89	
	<i>Rmuc</i>	0.00	3.66	5.00	97.47		0.00	106.79	0.913
SA (<i>Salb</i>)	2.50	0.00	3.50	23.40	41.00		92.40	0.444	
Nil	11.00	0.00	0.00		6.00		26.00	0.346	
CT ^a		162.00	3.99	214.98	151.94	47.99	31.00		
PA ^b		0.917	0.083	0.563	0.642	0.854	0.290		
OA^c		0.682	κ		0.582	τ		0.462	

aColumn Total. bProducer's accuracy. cOverall accuracy. dRow Total. eUser's accuracy.

IV.5.2.5 FUZZY CLASSIFICATION

Fuzzy classifications using the two best classes of the MPXS, the MPXS+VAR7 and the MPXS+VAR21 images were calculated and fuzzy convolution was performed using a window size of 7x7 pixels. Results are shown in Figure 51-Figure 53.

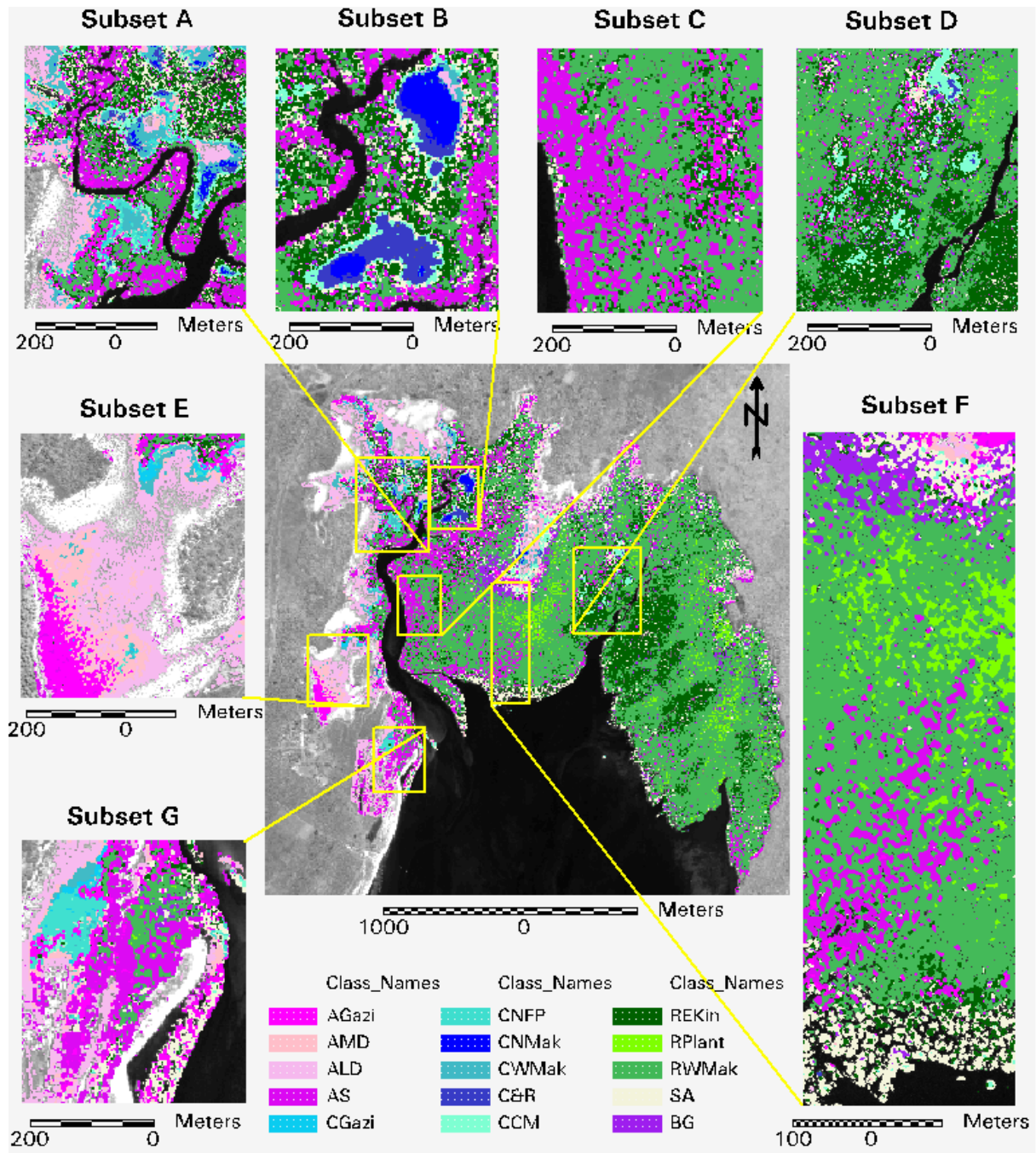


Figure 51. Fuzzy 7x7 ML classification of MPXS image

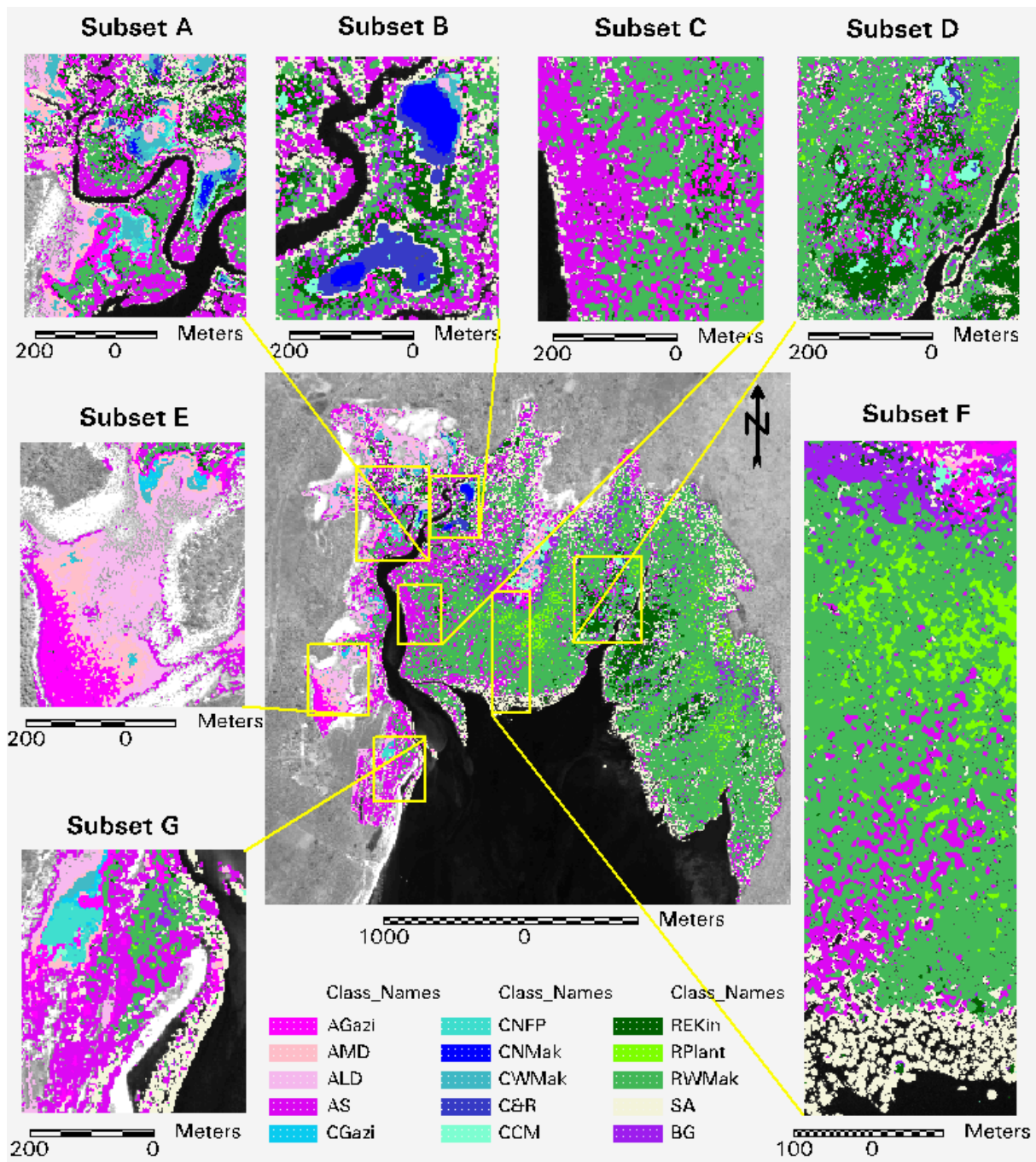


Figure 53. Fuzzy 7x7 ML classification of MPXS+VAR21 image

IV.6 Area covered by each mangrove species

The area covered by each class was calculated for each classification (ML classification and fuzzy classifications of MXS and MPXS image classifications) and was deduced from the histogram values of each class. Area calculations for MXS classifications are given in Table 38, for MXS+NDVI in Table 39, and for MPXS in Table 40. Areas covered by classes representing the same species are added to represent the area covered by that mangrove species and are shown in bold.

Table 38. Area covered by each class expressed as percentage of the total area covered in the supervised classifications of MXS

Class	Area (% total area covered)			
	mxs	fuzzy 3x3	fuzzy 5x5	fuzzy 7x7
AGazi	4.70	5.09	4.88	4.78
AMD	1.55	2.87	3.47	3.90
ALD	6.86	6.68	6.53	6.39
AS	7.11	6.13	5.88	5.75
<i>Amar</i>	20.23	20.78	20.76	20.81
<i>BG (Bgym)</i>	10.03	4.62	3.47	2.96
CGazi	0.94	0.40	0.22	0.16
CCM	4.03	3.02	2.79	2.68
CNFP	1.90	1.10	0.79	0.60
CNMak	0.51	0.33	0.29	0.27
CWMak	2.31	2.01	1.87	1.83
C&R	0.76	0.49	0.36	0.30
<i>Ctag</i>	10.45	7.34	6.33	5.82
REkin	13.28	12.58	11.95	11.55
RPlant	10.85	6.28	5.24	4.80
RWMak	29.01	45.24	49.84	51.90
<i>Rmuc</i>	53.14	64.10	67.03	68.25
<i>SA (Salb)</i>	6.14	3.17	2.42	2.15
TOTAL	100.00	100.00	100.00	100.00

In the supervised classifications of MXS (shown in Table 38) the areas covered by RWMak and AMD increased through fuzzy classification, at the expense of all other classes, which decreased through fuzzy classification. The larger the window size used in the fuzzy convolution, the more the areas decreased or increased. For AGazi an increase in area is observed from ML classification to fuzzy 3x3 classification, followed by a decrease in area with increasing window sizes. The ranking of the areas covered by each species did not change through fuzzy classification: *Rmuc* covered the largest area (53-68%), followed by *Amar* (ca. 20%), *Ctag* (5-10%), *Bgym* (3-10%) and *Salb* (2-6%).

Table 39. Area covered by each class expressed as percentage of the total area covered in the supervised classifications of MXS+NDVI

Class	Area (% total area covered)			
	mxs+ndvi	fuzzy 3x3	fuzzy 5x5	fuzzy 7x7
AGazi	6.77	4.92	4.24	3.93
AMD	1.37	1.22	1.11	1.05
ALD	6.27	6.25	6.21	6.14
AS	5.57	5.28	5.60	5.87
Amar	19.98	17.68	17.16	16.99
BG (Bgym)	10.00	9.52	8.61	8.21
CGazi	0.65	0.40	0.32	0.30
CCM	3.64	3.16	2.97	2.91
CNFP	2.35	2.71	2.65	2.55
CNMak	0.62	0.43	0.41	0.41
CWMak	2.91	2.50	2.43	2.46
C&R	0.85	0.64	0.50	0.45
Ctag	11.02	9.86	9.29	9.07
REkin	12.45	12.30	11.80	11.49
RPlant	9.12	6.14	5.04	4.37
RWMak	31.04	40.49	44.94	47.07
Rmuc	52.61	58.93	61.77	62.93
SA (Salb)	6.39	4.01	3.16	2.80
TOTAL	100.00	100.00	100.00	100.00

In the supervised classifications of MXS+NDVI the area covered by RWMak and CNFP increased through fuzzy classification, at the expense of all other classes, which decreased through fuzzy classification. The larger the window size used in the fuzzy convolution, the more the areas decreased or increased. No trend was observed for class AS. The ranking of the areas covered by each species did not change through fuzzy classification and was the same as in the classifications of mxs: *Rmuc* covered the largest area (52-63%), followed by *Amar* (17-20%), *Ctag* (9-11%), *Bgym* (8-10%) and *Salb* (3-6%).

In the supervised and fuzzy 7x7 classifications of MPXS (shown in Table 40) the area covered by AMD, REKin and RWMak increased through fuzzy classification, at the expense of all other classes, which decreased through fuzzy classification. The ranking of the areas covered by each species did not change through fuzzy classification but was different from the ranking in the classifications of mxs and mxs+ndvi: *Rmuc* covered the largest area (55-60%), followed by *Amar* (20-21%), *Bgym* (8-11%), *Ctag* (7-9%) and *Salb* (ca. 5%).

In the supervised and fuzzy 7x7 classifications of MPXS+VAR7 (shown in Table 40) the area covered by AGazi, AMD, AS, RWMak and SA increased through fuzzy classification, at the expense of all other classes, which decreased through fuzzy classification. The ranking of the areas covered by each species changed through fuzzy classification, but the difference between the last and the last but one ranked species in the MPXS+VAR7 fuzzy7 classification

was only 0.22% and 0.31% in the *mpxs+var7* classification. The ranking in the *mpxs+var7* ML classification was *Rmuc* (covering 59% of the total mangrove forest), followed by *Amar* (23%), *Salb* (8%), *Bgym* (5.55%) and *Ctag* (5.24%). The ranking in the *mpxs+var7* fuzzy7 classification was: *Rmuc* (covering 56% of the total mangrove forest), followed by *Amar* (25%), *Salb* (10%), *Ctag* (4.33%) and *Bgym* (4.11%).

In the supervised and fuzzy 7x7 classifications of *MPXS+VAR21* (shown in Table 40) the area covered by AMD, AS, BG and RWMak increased through fuzzy classification, at the expense of all other classes, which decreased through fuzzy classification. The ranking of the areas covered by each species did not change through fuzzy classification but was different from the ranking in the classifications of *mxs* and *mxs+ndvi*: *Rmuc* covered the largest area (54-55%), followed by *Amar* (21-23%), *Salb* (15-16%), *Bgym* (ca. 5%) and *Ctag* (ca. 3%).

Table 40. Area covered by each class expressed as a percentage of the total area covered in the supervised classifications of MPXS

Class	Area (% total area covered)					
	mpxs	mpxs fuzzy7	mpxs+var7	mpxs+var7 fuzzy7	mpxs+var21	mpxs+var21 fuzzy7
AGazi	6.74	6.41	5.16	6.67	2.28	3.06
AMD	1.44	2.28	1.80	2.11	1.76	2.07
ALD	7.43	6.98	7.03	6.73	4.64	4.27
AS	5.20	4.73	8.80	9.67	11.91	13.17
Amar	20.82	20.40	22.78	25.17	20.60	22.58
BG (Bgym)	10.78	8.25	5.55	4.11	4.84	5.34
CGazi	1.04	0.74	0.30	0.18	0.29	0.22
CCM	2.52	2.46	1.84	1.36	1.14	1.02
CNFP	1.66	1.38	0.72	0.66	0.23	0.23
CNMak	0.54	0.32	0.35	0.26	0.24	0.22
CWMak	1.87	1.82	1.47	1.44	1.06	0.99
C&R	0.99	0.68	0.56	0.42	0.50	0.45
Ctag	8.62	7.39	5.24	4.33	3.47	3.12
REkin	15.71	17.83	12.91	4.96	14.62	5.88
RPlant	4.78	2.48	5.47	2.12	4.91	2.04
RWMak	34.25	39.14	40.22	49.31	35.39	46.01
Rmuc	54.75	59.44	58.60	56.39	54.92	53.93
SA (Salb)	5.04	4.51	7.83	10.00	16.17	15.03
TOTAL	100.00	100.00	100.00	100.00	100.00	100.00

IV.7 Automated delineation of vegetation assemblages

Assemblage maps derived from the fuzzy classification of the MXS and MXS+NDVI image using a 7x7 convolution window after elimination of continuous groups of pixels (belonging to the same image class) covering less than 50 pixels are shown in Figure 54 and Figure 55, respectively. Contour lines derived from these classified images are shown in Figure 56 and Figure 57. These images are also put on transparency so that they can be overlaid on the classifications.

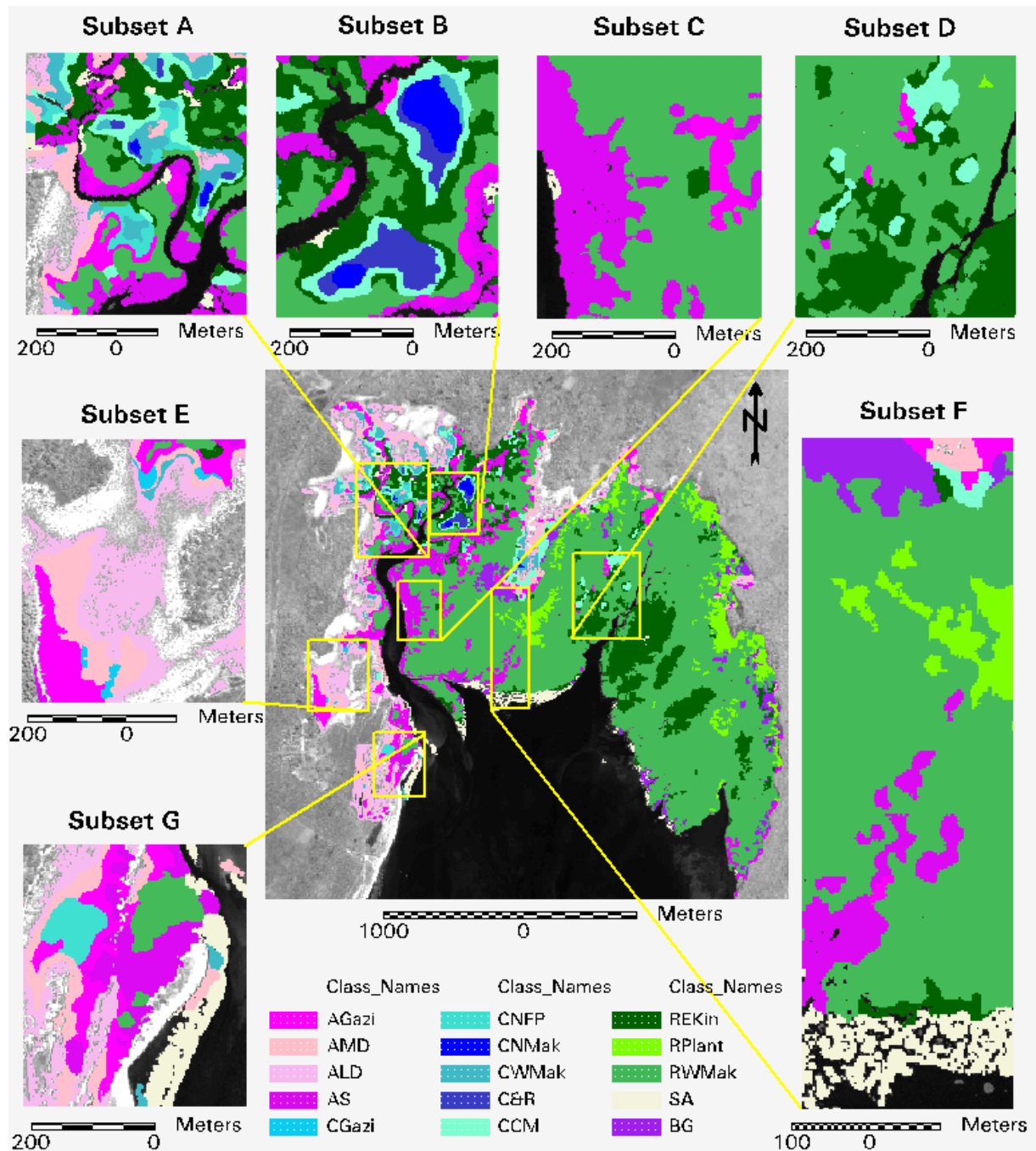


Figure 54. Automated assemblages derived from the fuzzy classification of MXS using a 7x7 pixels convolution window, after elimination of continuous groups of pixels (belonging to the same image class) covering less than 50 pixels

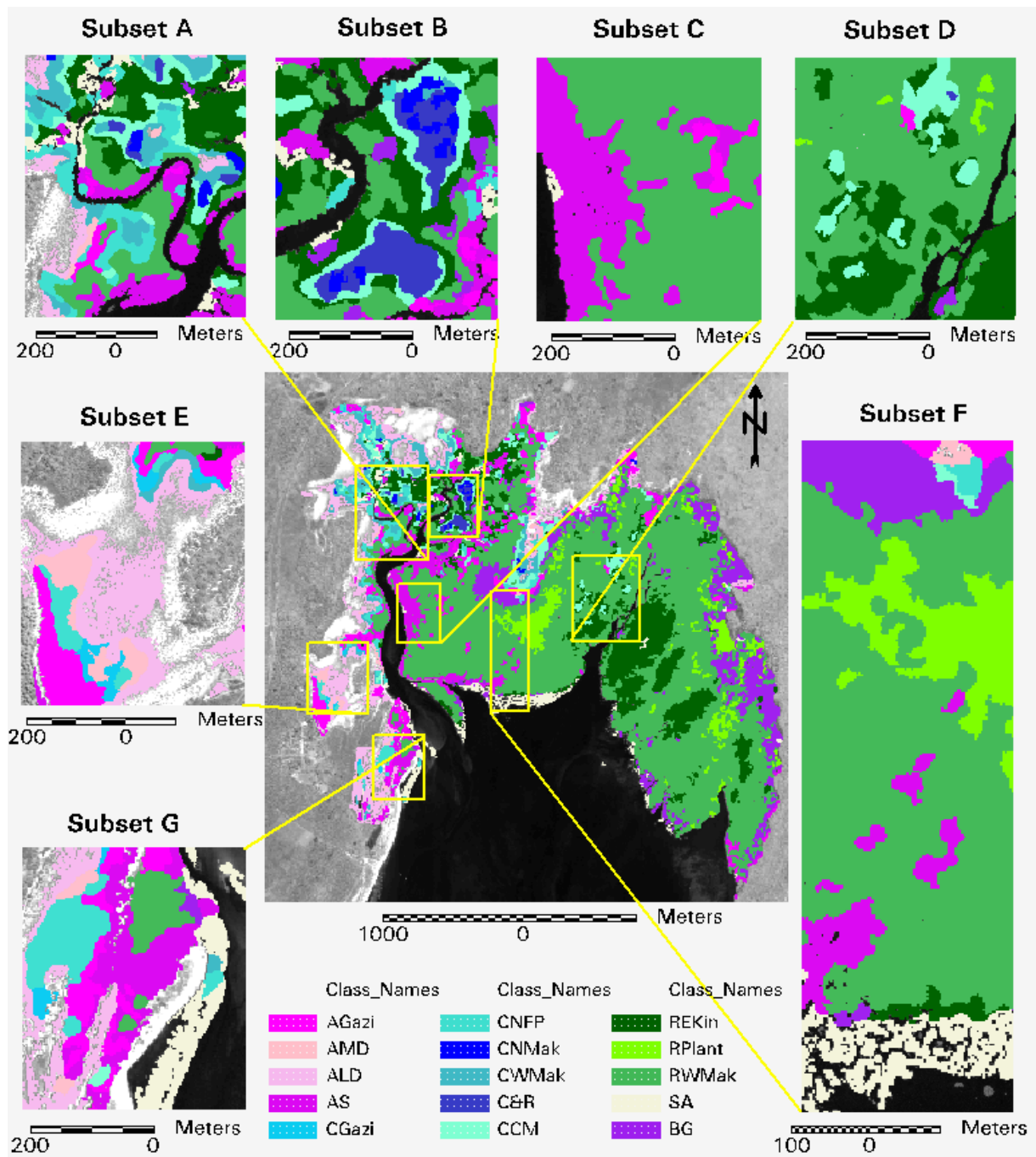


Figure 55. Automated assemblages derived from the fuzzy classification of MXS+NDVI using a 7x7 pixels convolution window, after elimination of continuous groups of pixels (belonging to the same image class) covering less than 50 pixels

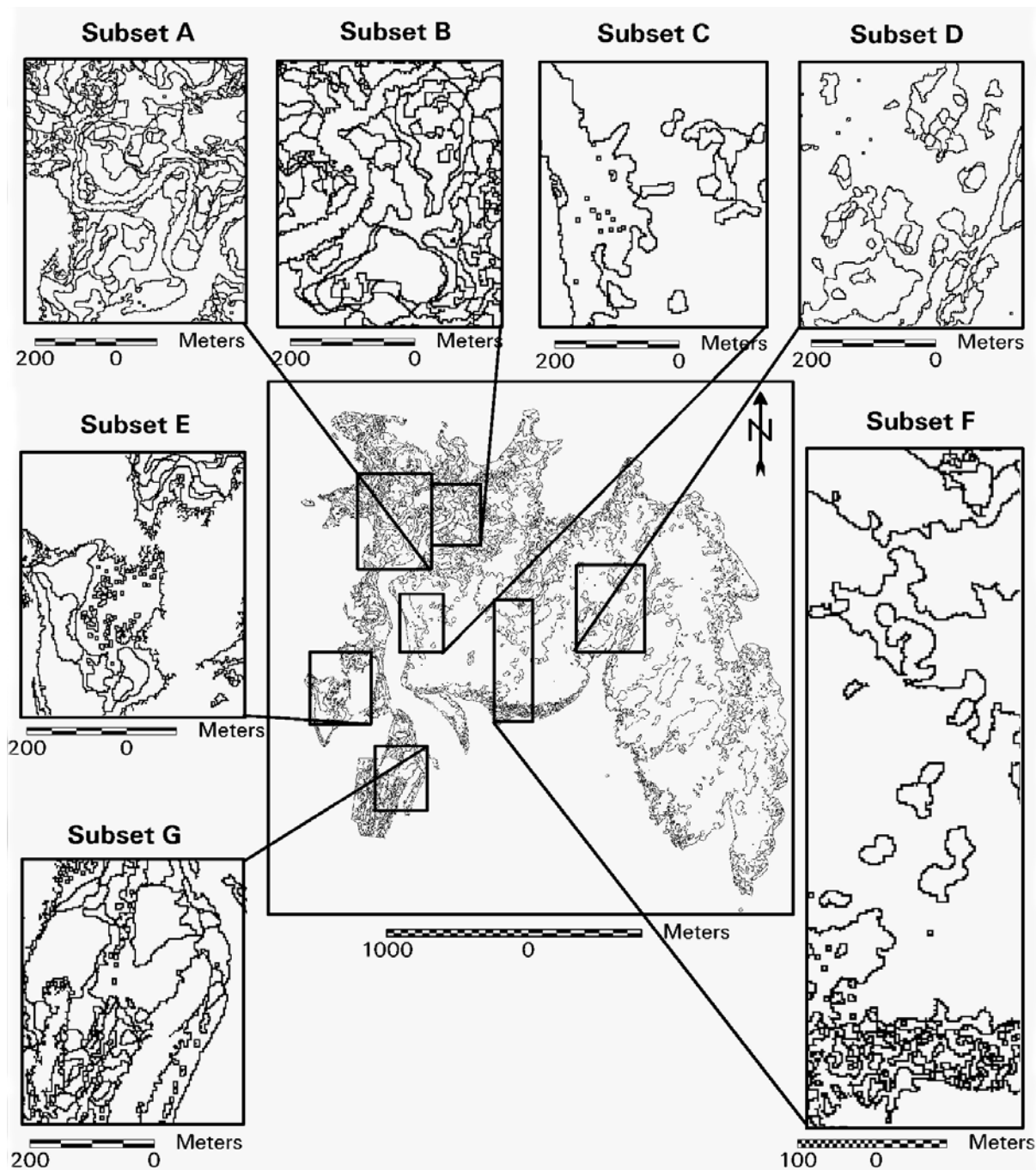


Figure 57. Contour lines derived from the fuzzy classification of MXS+NDVI using a 7x7 pixel convolution window, after elimination of continuous groups of pixels (belonging to the same image class) covering less than 50 pixels

The differences between the fuzzy classification (using a 7x7 pixel convolution window) of MXS and MXS+NDVI after grouping the classes per species are shown in Figure 58. Pixels classified as *Amar* in both classifications are shown in magenta, as *Bgym* in purple, as *Ctag* in blue, as *Rmuc* in green and as *Salb* in beige. Pixels that were classified as *Amar* in the classification of MXS and as *Ctag* in the classification of MXS+NDVI are given in red. Pixels that were classified as *Rmuc* in the classification of MXS and as *Bgym* in the classification of MXS+NDVI are given in orange. All other pixel changes are shown in yellow. An exact quantification (the number of pixels) of this changes is given in Table 41.

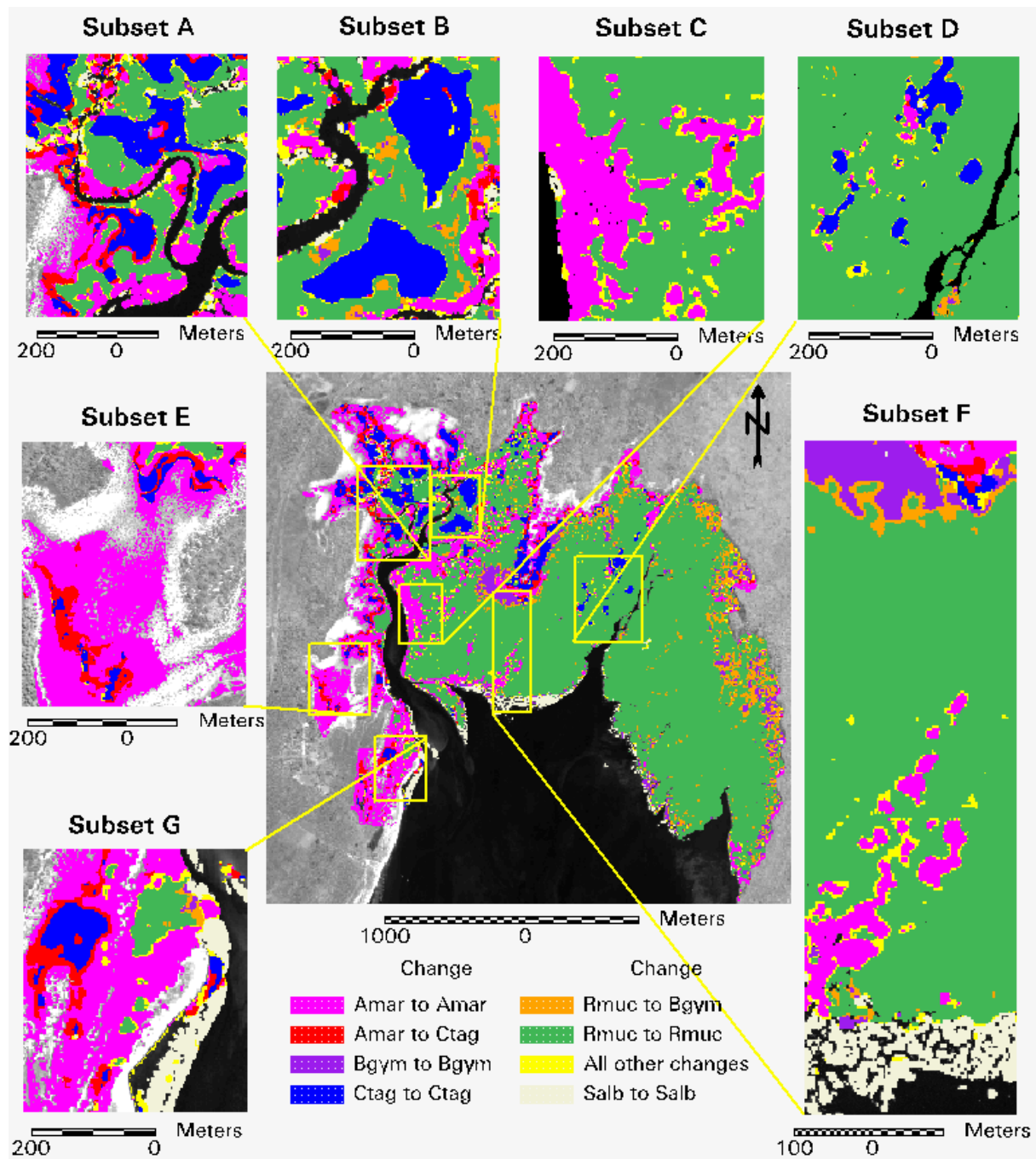


Figure 58. Differences between the fuzzy classification (using a 7x7 pixel convolution window) of MXS and MXS+NDVI after grouping the classes per species. Changes are written as classification of species on the MXS image to classification of species on the MXS+NDVI image

Table 41. Differences in number of pixels and in area (km²) between the species fuzzy classification (using a 7x7 pixel convolution window) of MXS and MXS+NDVI. Changes are written as classification of species on the MXS image “to” classification of species on the MXS+NDVI image. Classifications into the same species in both classifications are in bold

Change	#pixels	Area (km²)	Change	#pixels	Area (km²)
<i>Amar to Amar</i>	117317	0.919765	<i>Bgym to Amar</i>	71	0.000557
<i>Amar to Bgym</i>	334	0.002619	<i>Bgym to Bgym</i>	20428	0.160156
<i>Amar to Ctag</i>	21901	0.171704	<i>Bgym to Ctag</i>	70	0.000549
<i>Amar to Rmuc</i>	6904	0.054127	<i>Bgym to Rmuc</i>	271	0.002125
<i>Amar to Salb</i>	3042	0.023849	<i>Bgym to Salb</i>	412	0.003230
<i>Ctag to Amar</i>	491	0.003849	<i>Rmuc to Amar</i>	4149	0.032528
<i>Ctag to Bgym</i>	154	0.001207	<i>Rmuc to Bgym</i>	37611	0.294870
<i>Ctag to Ctag</i>	39933	0.313075	<i>Rmuc to Ctag</i>	2655	0.020815
<i>Ctag to Rmuc</i>	665	0.005214	<i>Rmuc to Rmuc</i>	443879	3.480011
<i>Ctag to Salb</i>	604	0.004735	<i>Rmuc to Salb</i>	2060	0.016150
<i>Salb to Amar</i>	40	0.000314			
<i>Salb to Bgym</i>	450	0.003528			
<i>Salb to Ctag</i>	605	0.004743			
<i>Salb to Rmuc</i>	383	0.003003			
<i>Salb to Salb</i>	13996	0.109729			

IV.8 Visual delineation of vegetation assemblages

The visual delineations of each naïve interpreter were digitised in a vector layer. These delineations are shown in Figure 59, Figure 60 and Figure 61 and are also printed on transparencies so that they can be overlaid on the fuzzy 7x7 classifications of MXS and MXS+NDVI after elimination of continuous pixel groups smaller than 50 (shown in Figure 54 and Figure 55) and on the mpxs image (Figure 22).

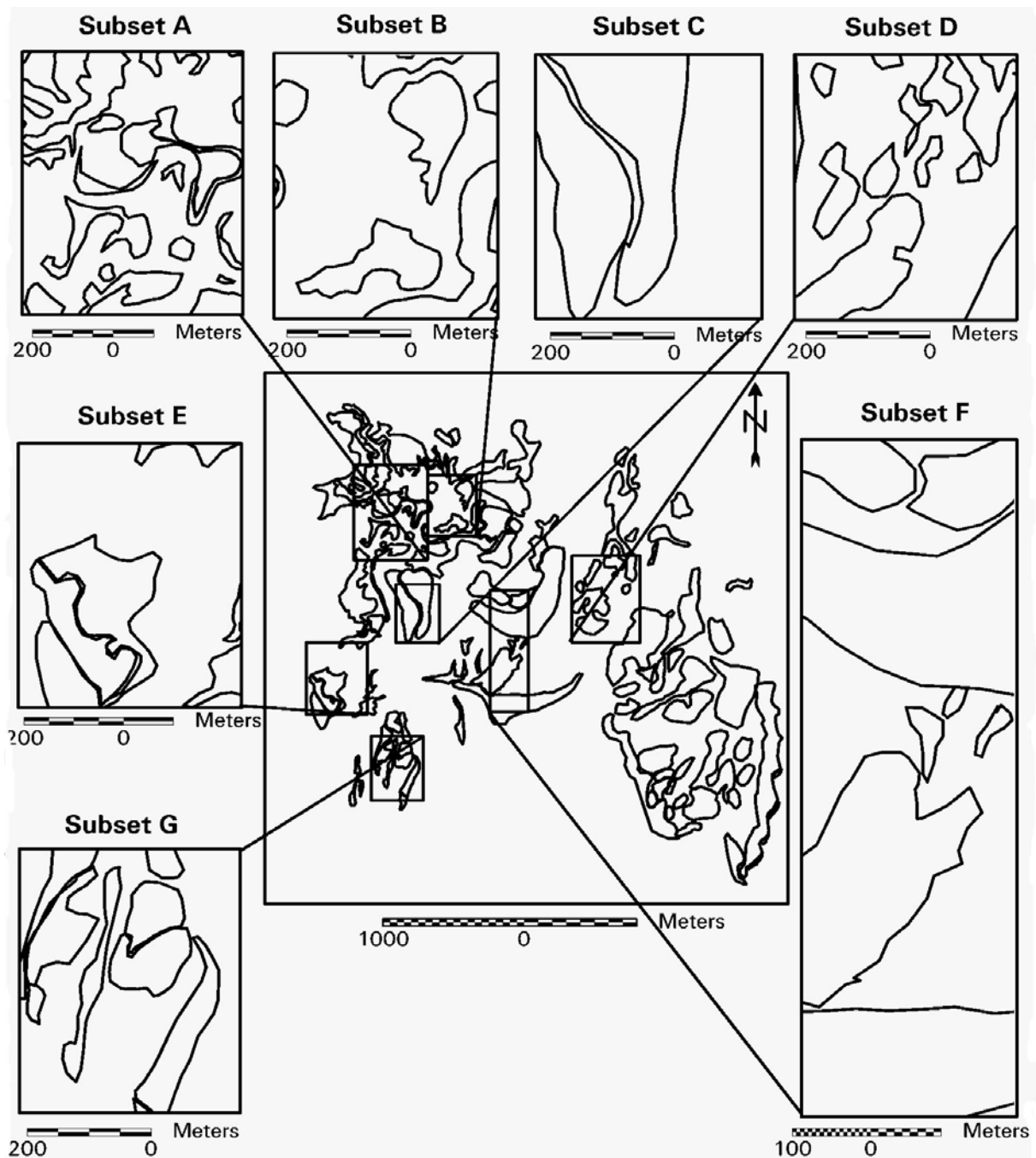


Figure 61. Visual delineation of assemblages by interpreter 3

IV.9 Area covered by mangrove, sand and water

The mangrove forest of Gazi Bay covers an area of 5.746564 km². Less than 0.5 km² (0.352551 km²) is covered by sand.

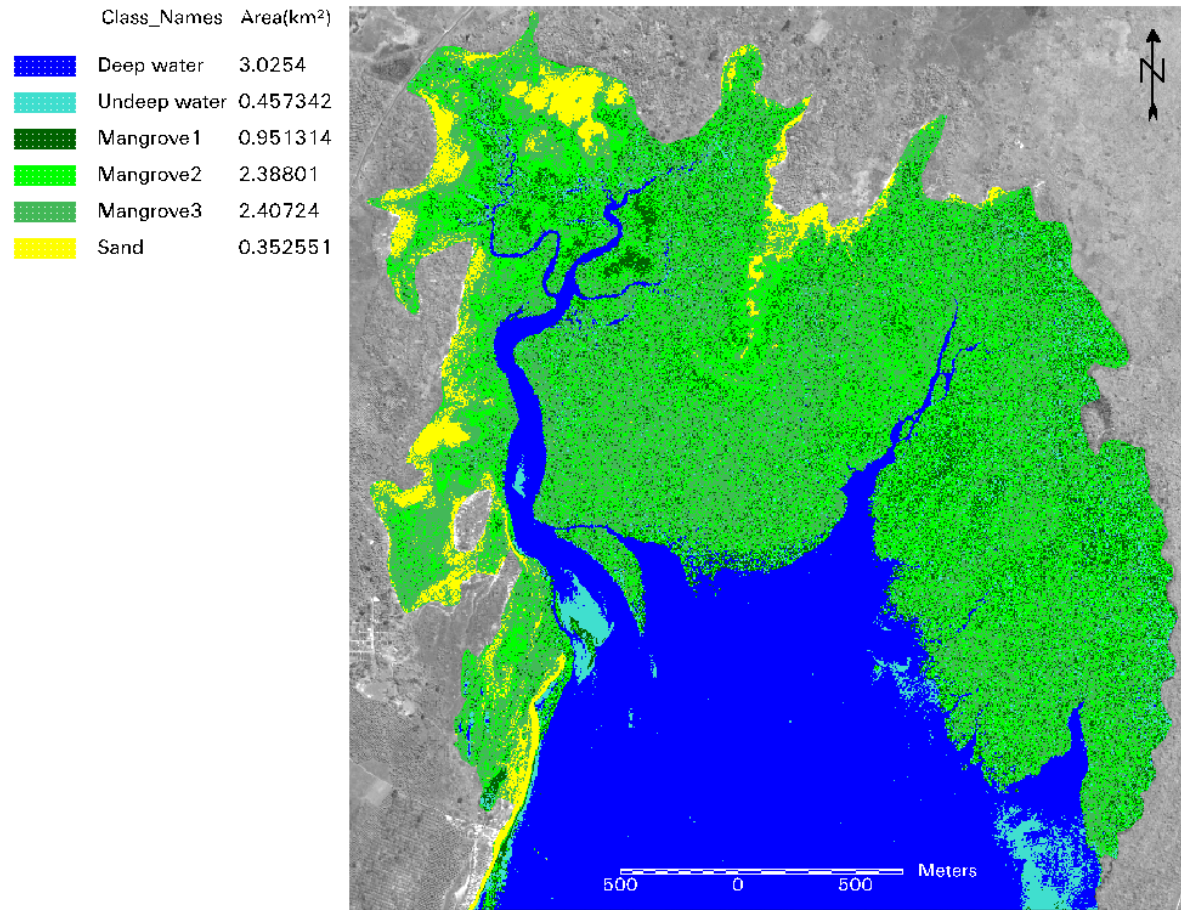


Figure 62. Calculation of area covered by mangrove, water and sand from an unsupervised classification with 6 classes

V Discussion

V.1 Visual interpretability of the satellite image

In order of increasing ease of visual interpretability we list: multispectral (XS), panchromatic (PAN), pansharpened multispectral image (PXS), Natural colour transformation of PXS, false colour composite of PXS, principal components transformation of MPXS (PCA_MPXS)/masked false colour composite (MPXS).

In a first stage the panchromatic high resolution data and the multispectral low resolution data were merged resulting in a multispectral image of high resolution (PXS), enhancing the visual interpretability of the satellite image. The false colour composite, which includes the NIR band, allowed a better distinction between the mangrove species than the natural colour composite of the PXS image.

Ctag and *Amar* are also found in the desert areas of the mangrove where they grow less tall (dwarf structure, shrubs) than at the seaward side of the mangrove due to (salt)stress. Canopy closure is also very low, so that the light penetrates through the leaves easily, resulting in a spectrally mixed signal sensed by the satellite. Those stressed and small trees can be recognized from the PAN image, but not on the XS image and through multiresolution merging, information on these trees is lost as compared to the PAN image.

In a second stage all non-mangrove area, sand and water was masked out of the PXS image resulting in a contrast stretch, drastically improving the visual interpretability of the QuickBird PXS image.

Principal component transformation of MPXS resulted in an increased visual texture and structure in areas of low crown cover and for *Ctag*, but not for *Rmuc* and *Bgym*.

V.2 Comparison between unsupervised classification of MXS and MPXS

Associating spectral clusters with information classes was found to be more difficult in the MPXS image. The in-field spectral variability is much larger for the MPXS image, as compared to the MXS image. One single seaward *Amar*-crown for example corresponds to 10 spectral classes in the MPXS classified image, while only to 7 classes in the MXS classified image.

V.3 Separability between classes in supervised classification

Transformed divergence separability indices were very low (<1700) between classes AMD and CGazi, CWMak and CNFP in all images where the signatures were extracted from*. Incorporation of NDVI values and texture did not help to separate these classes to an acceptable level (except for CNFP in MPXS+VAR21). Low separability between classes representing the same mangrove species does not constitute a problem as we are interested in

* MXS, MXS+NDVI, MPXS, MPXS+VAR7, MPXS+VAR21

classifying species. The poor separability between AMD and CGazi may be attributed to the effect of background reflectance. It might be possible that the crown cover is comparably low in these TS so that light reflected by the top substratum reaches the satellite, resulting in a spectrally mixed signal. The top substratum characteristics are the same in these TS (pers. obs.): sandy. The reflectance of the top substratum can dominate the reflectance of the vegetation and it is no longer possible to classify these pixels as being “mangrove species *x*”.

Low separability for signatures AS and RWMak (as extracted from MXS and MXS+NDVI) might be attributed to the fact that AS has an *Rmuc*-understory. However separability is not problematic when signatures are extracted from the pansharpned images, maybe because the TS were slightly adapted.

The low separability between BG and REKin and RWMak may be caused by the fact that the TS for BG are a set of very small groups (tree crowns) of pixels, because they were extracted from an area of *Bgym* interspaced with *Rmuc*. It was not always easy to separate tree crowns, especially not on the coarser resolution images (MXS and MXS+NDVI).

Care should be taken in interpretation of the separability indices as the histograms of the image classes in the image bands were probably not normally distributed (ERDAS Field Guide, 2002) (histograms were only checked for unimodality).

V.4 Effect of increasing window sizes in fuzzy classifications

Fuzzy convolution reduces the pepper and salt effect present in the MXS and MXS+NDVI classified images. The bigger the window size used in fuzzy convolution the more homogeneous the classification. On the other hand the floristic details in mixed mangrove stands are lost through fuzzy classification with a big window size (e.g. 7x7 pixels).

Fuzzy classification with a window size of 3x3 pixels seems to yield the most realistic results: the pepper and salt effect that is observed in the ML classifications of MXS and MXS+NDVI is removed and at the same time floristic details are preserved. Fuzzy classification with a window size of 7x7 pixels produced the most homogeneous thematic map but nearly all floristic details in mixed stands is lost (even larger clumps of pixels that could represent a tree crown of a different class than its neighbouring pixels are swallowed up by the neighbouring dominant class). This image is therefore most suited to represent assemblages.

V.5 Effect of the incorporation of NDVI values in supervised classification of multispectral data

Addition of the NDVI layer in the classification of MXS increased the separability between the image classes, but as argued by Green *et al.* (2000) “a high separability of classes is not assumed to be indicative of an accurate habitat map”. Below a comparison is done between MXS and MXS+NDVI fuzzy 3x3 and 7x7 classifications, because differences between the classifications are more easily observed on fuzzy classified images (due to the reduction of the salt and pepper effect). The classifications are evaluated using field knowledge and visual image interpretation.

V.5.1 Comparison between fuzzy classifications of MXS and MXS+NDVI using 3x3 pixels convolution window

SUBSET A

- ♦ *Salb* island is correctly classified in both images
- ♦ Pixels are classified as SA in *Ctag* area in the NDVI classification, which is impossible
- ♦ Seaward *Amar* crowns (along the creek) are incorrectly classified as SA and CGazi in the NDVI image (and partly correctly as a mixture of AGazi, AS and AMD). Seaward *Amar* is best classified on the MXS image as a mixture of AS, AGazi and AMD.

SUBSET B

- ♦ Pixels in *Ctag* area are misclassified as SA in the NDVI classification, this is not the case on the MXS classified image
- ♦ More pixels surrounding the *Ctag* zones are classified as BG in the NDVI classification as compared to the MXS classification (no field data available to check if this is true)
- ♦ Seaward *Amar* is classified as CCM and SA and CNFP in the NDVI image (and partly correctly as a mixture of AGazi and AS) and is again better classified on the MXS classification.

SUBSET C

More SA present in *Amar* seaward zone in NDVI image (most of them are incorrectly classified). This is not the case in the MXS classified image.

SUBSET D

Ctag patches are correctly classified as CCM in both images.

SUBSET E

- ♦ Many more pixels in the middle of the landward *Amar* zone are classified as CNFP and CGazi in the NDVI image (there is no *Ctag* present in this zone in reality)
- ♦ Around the creek in the North of the subset there is a clear zonation of ALD most landward, followed by CWMak, CGazi and then by AGazi and RWMak (this zonation is known to exist; *e.g.* Dahdouh-Guebas *et al.*, 2002)

SUBSET F

- ♦ The monospecific *Salb* zone in the South of the image is nearly completely classified as SA except for some pixels incorrectly classified as BG or REKin and also some CCM
- ♦ The *Bgym* zone in the North of the subset is more extended in the NDVI image (no ground-truth data available to check if this is true)

SUBSET G

- ♦ More pixels are classified as AGazi in the *Ctag* zone in the MXS image (which is incorrect). This is not the case on the NDVI classified image
- ♦ The natural *Salb* fringe in front of NFP is dominantly classified as SA, but substantial parts are incorrectly classified as BG, AS, CNFP and CWMak and also ALD (near the edges)
- ♦ Seaward *Amar* zone is correctly classified in both classifications
- ♦ *Rmuc* dominated zone (interspaced with *Bgym*) in the North of the subset is correctly classified as a mixture of RWMak, RPlant and BG in both classifications

V.5.2 Comparison between fuzzy classifications of MXS and MXS+NDVI using 7x7 pixels convolution window

SUBSET A

- ♦ Seaward *Amar* crowns (along the creek) are incorrectly classified as SA and CGazi in the NDVI image (and partly correctly as a mixture of AGazi, AS and AMD). Seaward *Amar* is best classified on the MXS image as a mixture of AS, AGazi and AMD.
- ♦ The internal *Ctag* zone is also correctly classified as a mixture of CCM (at the edge), CNMak, CWMak, CNFP and C&R. In the middle of the internal *Ctag* zone the *Amar* zones are classified as AMD (North West) and as ALD (South East)
- ♦ There is a clear vegetational zonation from the land to the sea: ALD+AMD most landward, followed by CWMak, CCM, CNFP and CNMak (the latter only in NDVI image), REKin and RWMak, followed by AS, AGazi, AMD and SA (but also wrongly classified CNFP in NDVI image which should be *Amar*)

SUBSET B

- ♦ *Ctag* zones are correctly classified: CNMak in the Northern patch and C&R with 2 smaller patches of CNMak, surrounded by CCM in the Southern patch
- ♦ The *Ctag* zone in the North of the image in the NDVI image is more crumbled and less homogeneous than in the MXS image.
- ♦ More pixels are classified as BG in the NDVI image, which are classified as RWMak in the MXS image (no field knowledge available to check which is the most correct)

SUBSET C

- ♦ The shape and size of the correctly classified seaward *Amar* zone is nearly the same in both classifications
- ♦ Some pixels at the edge of the water are correctly classified as SA in both classifications.

SUBSET D

Ctag patches are correctly classified on both images.

SUBSET E

- ♦ A substantial part in the centre of the landward *Amar* zone is incorrectly classified as CNFP and CGazi in the NDVI image, which is not the case in the MXS image
- ♦ Along the creek in the north of the subset there is a clear zonation from land to sea: ALD, CWMak, CGazi, and CCM, AMD (the latter only in the XS image), AS and RWMak (also some REKin) (This zonation is known to exist; *e.g.* Dahdouh-Guebas *et al.*, 2002)

SUBSET F

- ♦ Most of the *Salb* zone is correctly classified, with the exception of some BG. Classification largely the same in both images
- ♦ RPlant and BG clumps are larger in the NDVI image

SUBSET G

- ♦ Seaward *Amar* zone correctly classified as AS in both images
- ♦ *Salb* strip fronting NFP nearly completely correctly classified. An isolated *Amar* crown in this zone is correctly classified on the MXS image and not on the NDVI image

- ♦ Classifications are less good at the edges of the *Salb* area: classification into CWMak, CNFP and also AMD in the MXS image
- ♦ South of the *Ctag* zone a patch is classified as AGazi and not as CNFP in the MXS image and is correctly classified on the NDVI image

CONCLUSION

It seems that the fuzzy classifications of MXS are more accurate than the ones of MXS+NDVI. This may be because NDVI values are not indicative of a certain mangrove species. This was also found by Jensen *et al.* (1991) who used SPOT XS imagery of a mangrove forest in South-West Florida to derive forest characteristics. They found that correlation between NDVI and species composition was poor, but that NDVI correlated well with percentage canopy closure.

V.6 Effect of the incorporation of texture in supervised classification of pansharpened multispectral image

To assess the effect of incorporation of texture in the classification of MPXS a comparison between fuzzy7 classifications of MPXS, MPXS+VAR7 and MPXS+VAR21 is done and are evaluated using field knowledge and visual image interpretation.

SUBSET A

- ♦ Pixels at the edges of *Amar* crowns are wrongly classified as CWMak in MPXS and as SA in the VAR21 image
- ♦ In the middle of the Northern and Southern *Ctag* area pixels are incorrectly classified as SA in the VAR21 image which is not the case in the other images
- ♦ Along the water, pixels are incorrectly classified as SA on the VAR21 image, which is not or less the case in the other images
- ♦ The SA island is only fully classified as SA in the VAR21 image and only partly in the other images (part is CCM)
- ♦ The central part of seaward *Amar* crowns are correctly classified in all images. Classifications are problematic at the water-edges of the crowns: classified as CWMak in the MPXS image, as RWMak in the VAR7 image and as SA in the VAR21 image
- ♦ *Rmuc* fringe is classified as SA in VAR21 image (water side) and correctly classified in the other images

SUBSET B

- ♦ The *Ctag* areas are both surrounded by a CCM strip in the MPXS image, by a mixture of CCM and SA (incorrect) in the VAR7 image and dominantly by SA (incorrect) in the VAR21 image (especially the Southern *Ctag* area)

SUBSET C

- ♦ A small seaward fringe is completely classified as SA in the VAR21 image (water side edge of *Amar* crowns), as AS and RWMak in the VAR7 image and as CWMak and CNFP in the MPXS image
- ♦ SA is present more inland in Eastern direction from the seaward *Amar* zone in VAR21 image (which is incorrect). This is less the case in VAR7 and in MPXS image

SUBSET D

- ♦ SA is present in the VAR21 image in a 6m zone fringing the water (which is incorrect). This fringe is a mixture of BG and REKin in the MPXS image and of AS and RWMak in the VAR7 image (which are both possible)
- ♦ Interior of the darker zone in the South-West of the subset is classified partly as SA in the MPXS and VAR7 image which is not the case in the VAR21 image (more correct)

SUBSET E

- ♦ Many pixels in the landward *Amar* zone are classified as CGazi, CNFP and CWMak in the MPXS image. This is less the case in the VAR7 image and this is even less the case in the VAR21 image. It is problematic that on the VAR21 image SA is introduced in the landward *Amar* zone
- ♦ Pixels at the edge of the landward zone are classified as AS in the VAR21 image

SUBSET F

- ♦ *Salb* zone in the south of the subset is classified best in the VAR21 image. On the MPXS image, the *Salb* zone is nearly completely classified as REKin. A big improvement is already observed in the VAR7 image, but still substantial parts are wrongly classified
- ♦ In the North of the subset the landward *Ctag* area is incorrectly classified as SA in the MPXS and VAR7 images and correctly as CCM in the VAR21 image
- ♦ The Southeast of the *Bgym* zone is incorrectly classified as SA in MPXS and VAR7 images and correctly as a mixture of CCM and AGazi in the VAR21 image

SUBSET G

- ♦ *Salb* area at NFP is classified best in the VAR21 image, but still many pixels are classified as AS
- ♦ There is many AS present in the VAR21 image. CNFP is classified correctly in all images
- ♦ Large correspondence between the images for the seaward *Amar* zone

CONCLUSION

- ♦ It can be seen that the classification of MPXS even with the inclusion of texture is worse than the supervised classification of MXS
- ♦ SA is over-represented amounting to 16% of the total mangrove cover, which is unrealistically high
- ♦ AS is also over-represented amounting to 13% of the total mangrove area covered

The classifications of MPXS (even with inclusion of texture) are less accurate than the classifications of MXS. Especially *Salb* is problematic.

Franklin *et al.* (2000) give a checklist of the obvious sources of error or uncertainty in the application of digital image texture to forest inventory classification. The sources relevant to this work are listed below:

- ♦ The choice of the texture measure itself
- ♦ The area or window size for the textural calculation
- ♦ The way in which the texture is used in the analysis (*i.e.* classification, preprocessing, segmentation, combination of these, other)
- ♦ The type and range of inventory classes that are considered

The main source of error is probably due to the way the variance was calculated (from the original PAN image). There is a sharp change in DN values on the transition of vegetation to water or sand, resulting in high variance values for pixels close to water or sand. This on the one hand creates some kind of context in the classification, but on the other hand it results in an over-representation of the *Salb* and seaward *Amar* classes (see area calculations in section IV.6). A possible solution is to mask out water and sand before the variance is calculated and then calculate the variance ignoring the masked pixels.

V.7 Area covered by each mangrove species

All classifications agree on the dominance of *Rmuc* in the mangrove forest of Gazi Bay. *Rmuc* always covered more than 50% (even up to 68%) of the total mangrove area. The second most important species was *Amar*, covering 17-25% of the total mangrove area in all classifications. On the ranking of the other 3 species, there are differences between the classified images. The classifications (also the fuzzy classifications) of MXS and MXS+NDVI agree on the following ranking: *Ctag*, *Bgym* and *Salb*. In the classifications of mxps *Bgym* and *Ctag* switched places. If texture is included in the classification, *Salb* conquers the third place, covering 8-16% of the total mangrove forest and *Ctag* is ousted to the last place (covering less than 6%), except in the fuzzy 7x7 classification of MPXS+VAR7, where *Bgym* is on the last place.

Unfortunately no recent literature was found on the species area coverage of the Gazi mangroves. Thus a comparison between the results obtained here and literature can not be done. However, it seems that the MPXS+texture classifications give an area coverage for *Salb* that is too high and for *Ctag* that is too low.

The area covered by RWMak increased through fuzzy classification in all classified images. The bigger the window size used in fuzzy convolution, the more the area increased. This is because most assemblages in Gazi are *Rmuc* dominated, interspersed with other species. The differently classified pixels corresponding to those “other species” are absorbed by the RWMak class through fuzzy convolution, unless they form a big enough patch. The bigger the window size, the more detail is lost, so the larger the area covered by RWMak.

Many pixels at the transition of water to mangrove forest are classified as SA in the classifications of MXS, but are changed into either AS or *Rmuc*-classes in the fuzzy classifications. This explains why the surface covered by SA is reduced by nearly 50% through fuzzy classification.

V.8 Automated stand delineation versus manual/visual stand delineation

Although visual interpretation suffers from the subjectivity of the interpreters, a high correspondence between the delineated assemblages done by the 3 interpreters was found. Below, a comparison is done between the visually distinguished assemblages and the automated assemblages. The following abbreviations will be used: I1 as interpreter 1, I2 as interpreter 2 and I3 as interpreter 3.

SUBSET A

- ♦ The seaward *Amar* zone boundaries (classified as AS, AMD and AGazi on MXS and as SA and CGazi on NDVI) correspond well to the delineated polygons drawn by all interpreters.
- ♦ The boundaries of the *Ctag* areas in the Northern half of the subset (classified as a combination of CWMak, CNMak, C&R and the Southern *Ctag* area fringed by CCM) correspond well to the polygons drawn by all interpreters. CCM and CNFP are not included in the Northern *Ctag* area. CCM is separated from CNFP by I3 only. The CCM fringing the Southern *Ctag* area is recognized by I1 and I3. AMD patch in the Southern *Ctag* area is delineated only by I1. ALD patch in the northern *Ctag* area is not delineated.
- ♦ In the *Ctag* area in the Southern half of the subset, CWMak is separated from CNFP by I1, but are joined together in one polygon by I3.
- ♦ RWMak is partly separated from AS and CNFP by I1 and I2 (I-shaped polygon in the Southern half of the subset)
- ♦ The CCM patch in the southern half of the subset is recognized by I3 only.
- ♦ At the landward side of the mangrove, AMD and ALD are separated from all other classes by I2.

SUBSET B

- ♦ The classification of the Northern *Ctag* patch consists of CNMak, C&R and CWMak, surrounded by a CCM strip. This strip is partly included in the delineating polygon by I1 and I2 and is completely excluded by I3. The CCM strip itself is partly delineated by I1.
- ♦ The Southern *Ctag* patch (classified as CNMak, C&R, fringed by CCM) is recognized by all interpreters. The CCM fringe is nearly completely included in the polygon by I2 and is excluded by I1 and I3.
- ♦ The boundaries of the seaward *Amar* (classified as AS, AGazi and some SA) correspond well to the polygons drawn by I1 and I3. Only a small patch of AS was delineated by I2.
- ♦ REKin is not separated from RWMak by any interpreter.

SUBSET C

- ♦ The boundaries of the seaward *Amar* (classified as AS) correspond very well to the polygons delineated by I1 and I3
- ♦ More to the east of the subset, AGazi is included in a polygon together with REKin and RWMak by I1 and I3

SUBSET D

- ♦ The most northern and most eastern CCM patches are recognized by all interpreters
- ♦ The most western CCM patch was only recognized by I3. This patch was joined together with another CCM patch nearby (to the Southeast) by I1 and I2.
- ♦ In the upper left corner of the subset, REKin is separated from RWMak by I2
- ♦ In the lower half of the subset, REKin is separated from RWMak by all interpreters. I2 and I3 joined the REKin patch together with another REKin patch nearby (more to the North), while this was not done by I1.

SUBSET E

The landward *Amar* zone is classified from West to East as AGazi, AMD and ALD. These 3 classes are separated from each other only by I3. I1 made no distinction between AMD and ALD, neither did I2.

SUBSET F

- ♦ SA is well recognized by all interpreters
- ♦ The *Amar* strings running north-south are best delineated by I3, and are cut halfway by I1 and I2

SUBSET G

- ♦ The boundaries of the RWMak patch correspond very well to the polygons delineated by all interpreters.
- ♦ The seaward *Amar* zone (classified as AS) is well recognized by I1 and I3. The polygon drawn by I2 does not cover the whole AS patch
- ♦ The *Salb* strip at the NFP was well recognized by I1 and I3, but was not delineated by I2.
- ♦ The landward *Ctag* zone (classified as CNFP) was included in a polygon also containing and AGazi patch (South) and an AMD patch (North) by all interpreters.

OTHER

- ♦ BG patch north of subset F is well delineated by I2 and I3, but is split up in 2 halves by I1.
- ♦ *Rmuc* plantation (classified as RPlant) is well recognized by all interpreters
- ♦ Different assemblages are recognized by all interpreters in the huge homogeneous RWMak zone in the central and East Kinondo mangrove areas.
- ♦ REKin is well separated from RWMak by all interpreters in the East Kinondo mangrove area
- ♦ A broad banana shaped band, intersecting subset F, was drawn by all interpreters (the extent of this band varies though), in which two big patches of RPlant are joined.
- ♦ A long string, running north-south, bordering the mangrove in the Southeast of East Kinondo mangrove area is drawn by all interpreters (although the string extends more north for I2 than for I1 and I3). For I2 and I3, this sting corresponds to the presence of BG (especially in the north).
- ♦ In the East Kinondo mangrove area, RPlant is well separated from REKin by I1, partly by I2 and not by I3 (except for the *Rmuc* plantation).

CONCLUSION

There are two kinds of disagreements between the visual assemblages (assemblages visually delineated by the interpreters) and the automated assemblages (continuous groups of pixels belonging to the same class):

1. More than one automated assemblage is included in a visual assemblage (*e.g.* *Ctag* areas in subset B)
2. More than one visual assemblage is included in an automated assemblage (*e.g.* huge RWMak zone in East Kinondo mangrove area)

Disagreements of the first kind are a consequence of the fact that each pixel in the image represents 2^{44} (4 bands at 11-bit resolution) unique spectral signatures and the incapability of the human eye to distinguish that many levels of tones and hues in an image. Moreover, the false colour composite is displayed on the screen by projecting the near-infrared band through

the red, the green band through the green and the blue band through the blue colour guns of the monitor. Thus the information from the red band (which is available in digital image classification) cannot be used in visual interpretation. Visual interpretation therefore does not come close to utilizing the full information content of an image (Green *et al.*, 2000).

Disagreements of the second kind are caused by the elimination of nearly all detail in the classification firstly by fuzzy convolution with a large window size (7x7 pixels) and secondly by elimination of areas covering less than 50 connected pixels. Consider two *Rmuc* dominated assemblages, the first one interspaced with species *x* and the second one interspaced with species *y*. These assemblages will be considered different in visual interpretation, but through fuzzy and elimination filtering, information on species *x* and *y* will be lost, resulting in one large *Rmuc* automated assemblage.

Classes are not consistently separated by the interpreters. For example, RWMak is separated from REKin in subset D and in East Kinondo mangrove area, but not in subset B. Another example is AGazi and AMD: these classes are separated in subset E, but not in the delineation of seaward *Amar* fringing the Creek in subset A. This is because the human eye integrates context in the delineation, which is something that even the fuzzy classifier cannot accomplish.

In many cases the delineations overlapped (*e.g.* seaward *Amar*, *Salb*, *Ctag* patches, *Rmuc* plantation...) in other cases their views were complementary (*cf.* Subset A).

A higher correspondence between the automated and visual assemblages is probably found when the following classes are merged together:

- ♦ CNMak, CWMak and C&R
- ♦ AS, AGazi and AMD

V.9 Classification accuracy determination

When all PCQM transect data are used, the classification accuracy measures (OA, PA, UA, κ and τ coefficients) are quite low. Several causes for these low accuracies can be:

- ♦ deviation of navigational direction and distance between sampling points on the PCQM transects
- ♦ the positional inaccuracy of the GPS reading at the beginning, in the middle and at the end of a transect
- ♦ the inaccuracy of the image geometric correction
- ♦ errors in digitalisation of the PCQM quadrants
- ♦ the ground-truth method (PCQM) was not suited to describe the remotely sensed canopy

To make the deviations from a straight transect line as small as possible, an additional GPS reading was done in the middle of each transect. In past studies *e.g.* Dahdouh-Guebas *et al.* (2004a, in press), this was only done at the beginning and at the end of a transect. Unfortunately the positional accuracy of the GPS readings is low under dense canopy (see Table 14).

The Total RMS error for the geometric correction was 1.0954 pixels (=3.0671m) on the XS image. This is quite large compared to the size of a PCQM quadrant, which is 5m.

The PCQM was used to ground truth the satellite image under the assumption that the adult tree layer corresponds with the remotely sensed canopy (*cf.* Dahdouh-Guebas *et al.*, 2004a, in press). This assumption was violated in many cases, especially in areas of mixed species composition (*e.g.* adults of the species *Ctag* are overtopped by adults of the species *Amar*). Therefore another classification accuracy assessment was done, only including PCQM data where this assumption was fulfilled. As such, 8 of the 15 transects remained available for the classification accuracy determination: *Amar*, *Amar2*, *Ctag* (until 13th PCQM point), *Ctag2*, *Ctag3*, *Rmuc*, *Rmuc2* and *Salb*. After elimination of unsuitable test data the OA increased from 55.9% to 68%. All UA and PA's increased except the PA of BG, probably because of the limited occurrences of *Bgym* (only 8 out of 612 observations) in the remaining test data. The kappa coefficient increased from 41.7% to 57.3% and the tau coefficient increased from 37.7% to 46.6%, meaning that 46.6% more pixels are classified correctly than would be expected by chance alone*.

In the seaward zone *Ctag* adults tend to be smaller than *Amar*, *Rmuc* and *Bgym* adults (pers. obs.). Therefore when a *Ctag* adult is recorded in a quadrant where adults from other species (*e.g.* *Amar*) are also present, the PCQM data are not fit to be used in classification accuracy determination. In case the classification is correct (being that the area is classified as *Amar*), overlay with the PCQM data will lead to the erroneous conclusion that *Ctag* area is wrongly classified as *Amar*. After elimination of unsuitable test data the PA (which is the proportion of pixels that is correctly recognized by the classifier) of *Ctag* increased from 46.3% to 64.6% in the MXS classification accuracy assessment.

V.10 Comparison between classifications

The kappa coefficient can be used to compare classified images using different techniques (Mather, 1999) where the same number of classes and the same test data are used. If images were compared solely based on the κ value, we would have to conclude that the ML classification of MPXS+VAR7 is the best (with the highest κ value of 59.3%). But if field knowledge and visual image interpretation are used, the fuzzy 3x3 classification of MXS is probably the best and the ML classification of MPXS+VAR7 lags far behind. Mather (1999) warned that κ values are only reliable when the assumption that the data are randomly sampled from a multinomial distribution, with a large sample size is met. Due to the selectivity of the test data in the PCQM transects the test data are not randomly obtained. Also through the elimination of unsuitable test data, only 612 observations remained. 35% of the total number of observations were observation of *Ctag*, 26% of *Amar*, 25% *Rmuc*, 8% *Salb*, 0.1% *Bgym* and 4% Nil. These observations are clearly unrepresentative of the forest composition, which may pose a problem for their use in the classification accuracy determination.

The addition of the NDVI layer in the classification of MXS did not significantly increase the accuracy measures of the classification (OA, κ and τ). In fact, based on a visual comparison between the fuzzy 7x7 classifications of MXS and MXS+NDVI, the addition of the NDVI layer in the classification process actually decreased the accuracy of the thematic map.

* Green *et al.* (2000)

The PA and UA of Nil in the MXS and MXS+NDVI accuracy assessment was very low. The accuracy of the Nil class increased for MPXS, MPXS+VAR7 and MPXS+VAR21, as expected because of the higher resolution of the latter images.

VI Conclusion

VI.1 Research objectives fulfilled

All research objectives of this thesis work stated in the Introductory chapter were successfully achieved.

SPECTRAL AND SPATIAL ENHANCEMENT OF THE SATELLITE IMAGE TO EASE VISUAL INTERPRETABILITY

The most visually interpretable images were the contrast-stretched pansharpened false colour composite and the first three principal components of its principal component transformation. The former allows an easier recognition of *Rmuc* and *Bgym* and the latter of *Ctag* and areas of lower crown cover. Their use is therefore complementary.

VISUAL DELINEATED ASSEMBLAGES VERSUS AUTOMATICALLY DELINEATED ASSEMBLAGES

The delineations of the assemblages by the interpreters on the contrast-stretched pansharpened false colour composite overlapped in many cases, in other cases their views were complementary. Visual separation between two classes by the interpreters was inconsistent and thus we cannot conclude which classes are separated from other classes by the interpreters in the image, because the interpreter includes context in visual delineation, which cannot be done even by fuzzy classification. More than one automated assemblage could be included in a visual assemblage and vice versa.

CLASSIFICATION OF THE SATELLITE IMAGES AT MANGROVE SPECIES LEVEL INCORPORATING NDVI AND TEXTURE MEASURES AND DETERMINE CLASSIFICATION ACCURACIES

Incorporation of texture and NDVI measures in image classification both increased the spectral separability between the image classes, but this is not indicative for an accurate map. On the contrary, the supervised fuzzy classification of the contrast-stretched multispectral image using a 3x3 pixels convolution window appears to be the most accurate one. If the classified images are compared based on their classification accuracies using PCQM field data (even after elimination of unsuitable PCQM data) we would have to conclude that the classification of the pansharpened multispectral image incorporating a variance texture measure calculated in a 7x7 pixels window is the most accurate. However, it is clearly seen that this is not the case.

VI.2 Research questions still remaining – Future work

During the course of this thesis work other research questions arose:

- ♦ Does object-oriented image analysis yield better and more accurate results?
- ♦ Are other vegetation indices more appropriate for use in the classification of mangrove species?

- ♦ Are other texture measures more appropriate for use in the classification of mangrove species?
- ♦ Does the wavelet resolution merge offered by ERDAS Imagine 8.7 keep the detail of the panchromatic image of the shrubby vegetation?
- ♦ How should the degree of agreement between the visually delineated assemblages and the automated delineation be quantified?
- ♦ Which ground control methods (besides the one proposed below) are suited for classification accuracy assessment?
- ♦ How and to which degree do the understorey and the top substratum have an effect on the final vegetation signal sensed by the satellite?
- ♦ Does inclusion of radar imagery improve the classification accuracy (*cfr.* Aschbacher *et al.*, 1995)?

During the field work, more than 100 trees were selected whose crowns were clearly distinguished on the QuickBird panchromatic image and for which the stem diameter was measured. The information on stem diameter can be related to crown area on the satellite image (Read *et al.*, 2003; Clark *et al.*, 2004). Integration of this information with automated tree crown delineation programmes (Brandtberg and Walter, 1998; Warner *et al.*, 2000; Ticehurst *et al.*, 2001; Gougeon and Leckie, 2003; Leckie *et al.*, 2003) may allow the prediction of ecosystem variables such as stand biomass and basal area.

VI.3 Recommendations

My suggestion for the future is to add a canopy layer to the PCQM, describing the remotely sensed canopy which can be used in classification accuracy assessment instead of the adult tree layer (which does not always correspond to the remotely sensed canopy). In such a way, PCQM can still be used to determine structural forest parameters (such as absolute density, basal area, relative density, dominance, frequency, *etc.*) and at the same for classification accuracy.

Standardisation of fieldwork is an important issue in multitemporal analysis for the detection of small scale vegetation cover changes. The classification accuracy determination was a very time consuming process as

- ♦ The 1200 PCQM quadrants had to be copy-pasted and rotated manually
- ♦ The measurement of the adult tree species in each of the 1200 quadrants had to be compared with the classification manually
- ♦ If there was no domination (>50% cover) of a certain class in a quadrant, estimation of the surface covered by each class was done at a glance. This is probably inaccurate and susceptible to subjectivity.

To speed up the process of classification accuracy determination and to make this less susceptible to subjectivity of the operator, automation of this assessment is necessary.

More attention should have been paid to the determination of ground control points (including a measurement of their accuracy) for the eventual geometric correction of the satellite image. The classification accuracy determination using the PCQM is highly dependant on the accuracy with which begin, middle and end points of a transect are measured. Even a small error (a few meters) in the measurement of these positions could mean a total shift in every

direction of the PCQM quadrants. The accuracy of the GPS positions should be as high as possible, therefore other machines than Garmin's GPS III could be used.

Training sites should be identified on the satellite image in advance (selection of representative and homogeneous areas) and on the field itself if found to be necessary. Each training site should be described in terms of:

- ◆ Density of trees
- ◆ Crown cover
- ◆ Basal area
- ◆ Characteristics of the top substratum,

possibly allowing the estimation of the density, basal area and crown cover of the entire mangrove forest.

A more descriptive approach to ground-truthing can also be useful. The mangrove forest can be systematically explored and descriptive observations on assemblages can be recorded. The chance of recording a rare tree species in an assemblage with the PCQM is very small, while this floristically important information could be more easily included in a descriptive approach. Photographic material helps to refresh one's memory on the field conditions and details that were not noted on the field might be revealed from these photographs and can help to solve questions (*e.g.* type of top substratum in a certain assemblage). Sometimes it was possible to get a good view on a part of an assemblage (or even the complete assemblage) from climbing large trees in the neighbourhood (*pers. obs.*). Photographic information can be collected from these positions on parts of the forest, together with a GPS measurement of the location. The direction in which a photograph was taken can be recorded with a compass. With today's technology, it is quite easy and inexpensive to massively collect images of parts of the mangrove forest.

An immediate processing of data on the field would allow to quickly detect and repair ambiguities.

Due to problems with the ERDAS imagine licence (in March-April 2003) and due to the early departure to the field (on the 4th of July, one week after the exams) it was not feasible to do an unsupervised classification and a thorough study of the satellite image. Only the panchromatic images were taken to the field on which the identification of assemblages (visual delineation) is more difficult than on the pansharpended multispectral image. The best would be to take the contrast-stretched image (or the principal component transformation of this image) to the field, on which assemblages are easily recognized.

VII Relevance of this thesis in the framework of development co-operation

As East African human populations have grown over recent decades, increasing pressure has been placed on mangrove resources. The Kenyan coastal people (Swahili community) have strong economic ties with the coastal ecosystem, providing them with a large variety of goods and services, either directly (wood products such as fuel wood, building poles, fishing gear, furniture and non-wood products such as food items, medicines and tannins) or indirectly (protection of the shoreline against erosion, acting as important fishing grounds, waste-water treatment) (Tomlinson, 1986; Ewel, 1998; Dahdouh-Guebas *et al.*, 2000; Jayatissa *et al.*, 2002). A majority of people living along the coast live from fishing or at least consume fish as a primary source of proteins. Since mangroves act as important breeding, spawning, hatching and nursing grounds for many marine animal species, a direct link between the mangrove cover on one hand and both the lagoon and offshore fishery on the other hand has been found (Nagelkerken *et al.*, 2002; Mumby *et al.*, 2004) and several areas have witnessed a decrease in production from fisheries with more intense mangrove destruction (Baran, 1999). For the sake of the livelihoods of the communities depending on mangrove and on fisheries it is therefore essential that the mangrove ecosystem be protected worldwide and that a plan for **sustainable management** is adopted.

Habitat maps derived using remote sensing technologies are widely being used to assess the status of coastal natural resources, as a basis for coastal planning, and for the conservation, management, monitoring and valuation of these resources (Green *et al.*, 2000). Mangrove habitat maps have been used for three general management applications: resource inventory, change detection and the selection and inventory of aquaculture sites.

In this thesis work habitat maps at mangrove species level were derived from very high resolution QuickBird satellite imagery, allowing an assessment of the floristic composition of the mangrove as well as its areal extent, which are both important in the detection of mangrove degradation. The mangroves of Gazi Bay are degraded as a consequence of human-induced stress (Dahdouh-Guebas *et al.*, 2004a, in press). Sequential habitat maps of mangroves can be used to give a qualitative and quantitative evaluation of degradation.

References

- Aschbacher, J., Ofren, R., Delsol, J.P., Suselo, T.B., Vibulsresth, S. and T. Charrupat, 1995. An integrated comparative approach to mangrove vegetation mapping using advanced remote sensing and GIS technologies: preliminary results. *Hydrobiologia* 295: 285-294.
- Ahmad, W. and Neil, D.T., 1994. An evaluation of Landsat Thematic Mapper digital data for discriminating coral reef zonation: Heron Reef (GBR). *International Journal of Remote Sensing* 15: 2583-2597.
- Baatz, M. and Schäpe, A., 2000. Multiresolution Segmentation – an optimization approach for high quality multi-scale image segmentation. In: Strobl, J., Blaschke, T., Griesebner, G. (eds): *Angewandte Geographische Informationsverarbeitung XII*, Wichmann-Verlag, Heidelberg, 12-23.
- Ball, G.H. and Hall, D.J., 1967. A clustering technique for summarising multivariate data. *Behavioral Science* 12: 153-155.
- Baran, E., 1999. A review of quantified relationships between mangroves and coastal resources. *Phuket Marine Biology Centre Research Bulletin* 62: 57-64.
- Barbier, E.B., 2001. Valuing the Environment as Input: Applications to Mangrove-Fishery Linkages. *Ecological Economics* 35: 47-61.
- Barbier, E.B., 2003. Habitat-fishery linkages and mangrove loss in Thailand. *Contemporary Economic Policy* 21(1): 59-77.
- Barbier, E.B. and I. Strand, 1998. Valuing Mangrove-Fishery Linkages: A case study of Campeche, Mexico. *Environmental and Resource Economics* 12: 151-66.
- Biging, G. and Congalton, R.G., 1989. Advances in forest inventory using advanced digital imagery. *Proceedings of Global Natural Research Monitoring and Assessments: Preparing for the 21st century*. Venice, Italy, September 1989, 3: 1241-1249.
- Blaber, S.J.M. and T.G. Blaber, 1980. Factors affecting the distribution of juvenile estuarine and inshore fish. *J Fish Biol* 17: 143-162.
- Burke, L., Y. Kura, K. Kassem, C. Revenga, M. Spalding, D. McAllister, 2001. *Pilot analysis of global ecosystems : coastal ecosystems*. World Resources Institute, Washington, D.C., U.S.A.
- Blaschke, T., S. Lang, E. Lorup, J. Strobl & P. Zeil, 2000. Object-oriented image processing in an integrated GIS/remote sensing environment and perspectives for environmental applications. In : *Environmental Information for Planning, Politics and the Public. Volume II*. A. Cremers & K. Greve (eds), Metropolis-Verlag, Marburg, Germany: 555-570.

- Blaschke, T. & J. Strobl, 2001. What's wrong with pixels ? Some recent developments interfacing remote sensing and GIS. *GIS* 6: 12-17.
- Bosire, J., F. Dahdouh-Guebas, J.G. Kairo & N. Koedam, 2003. Colonisation of non-planted mangrove species into restored mangrove stands in Gazi Bay, Kenya. *Aquatic Botany* 76(4): 267-279.
- Brandtberg, T. & F. Walter, 1998. Automated delineation of individual tree crowns in high spatial resolution aerial images by multiple-scale analysis. *Machine Visions and Applications* 11: 64-73.
- Brokaw, N. & J. Thompson, 2000. The H for DBH. *Forest Ecology and Management* 129: 89-91.
- Byrne, G.F., Crapper, P.F., and Mayo K.K., 1980. Monitoring land-cover change by principal component analysis of multitemporal Landsat data. *Remote sensing of environment* 10: 175-184.
- Chapman, V.J., 1976. *Mangrove vegetation*. J. Cramer, Vaduz, Liechtenstein. (pages 74-105 (African Mangroves), 190-301 (Ecological Factors), 375-376 (Keys based on macroscopic characters), 380-402 (Taxonomic Appendix)).
- Chavez, P.S., Sides, S.C. and J.A. Anderson, 1991. Comparison of three different methods to merge multiresolution and multispectral data: Landsat TM and SPOT Panchromatic. *Photogrammetric Engineering and Remote Sensing* 57:295-303.
- Cintrón, G. & Y. Schaeffer Novelli, 1984. Methods for studying mangrove structure. In : *The mangrove ecosystem : research methods*. Snedaker, S.C. & J.G. Snedaker, eds. UNESCO, Paris, France: 91-113.
- Clark, D.B., Carlomagno, S.C., Alvarado, L.D.A. and J.M. Read, 2004. Quantifying mortality of tropical rain forest trees using high-spatial-resolution satellite data. *Ecology Letters* 7:52-59.
- Congalton, R.G., Oderwald, R. and R., Meade, 1983. Landsat classification accuracy using discrete multivariate analysis statistical techniques. *Photogrammetric Engineering and Remote Sensing* 49:1671-1678.
- Cottam, G. & J.T. Curtis, 1956. The use of distance measures in phytosociological sampling. *Ecology* 37(3): 451-460.
- Curran, P.J., 1985. Principles of remote sensing. Longman Scientific and Technical Group, Essex, England, 282pp.
- Curtis, J.T., 1959. The Vegetation of Wisconsin. An Ordination of Plant Communities. Madison, University of Wisconsin Press. 657 pp.
- Dahdouh-Guebas, F., C. Mathenge, J.G. Kairo & N. Koedam, 2000. Utilization of mangrove wood products around Mida Creek (Kenya) amongst subsistence and commercial users. *Economic Botany* 54(4): 513-527.

Dahdouh-Guebas, F., 2001. *Mangrove vegetation dynamics and regeneration*, Ph.D. dissertation, Vrije Universiteit Brussel, Brussels, Belgium.

Dahdouh-Guebas, F., 2002. The use of remote sensing and GIS in the sustainable management of tropical coastal ecosystems. In : F. Dahdouh-Guebas (ed.), *Remote sensing and GIS in the sustainable management of tropical coastal ecosystems*, *Environment, Development and Sustainability* 4(2): 93-112.

Dahdouh-Guebas, F., M. Verneirt, S. Cannicci, J.G. Kairo, J.F. Tack & N. Koedam, 2002. An exploratory study on grapsid crab zonation in Kenyan mangroves. *Wetlands Ecology and Management* 10(3): 179-187.

Dahdouh-Guebas, F., I. Van Pottelbergh, J.G. Kairo, S. Cannicci & N. Koedam, 2004a. Human-impacted mangroves in Gazi (Kenya): predicting future vegetation based on retrospective remote sensing, social surveys, and distribution of trees. *Marine Ecology Progress Series* 272: 77-92, in press.

Dahdouh-Guebas, F., E. Van Hiel, J.C.-W. Chan, L.P. Jayatissa & N. Koedam, 2004b. Qualitative distinction of congeneric and introgressive mangrove species in mixed patchy forest assemblages using high spatial resolution remotely sensed imagery (IKONOS). *Systematics and Biodiversity* (in press).

Dahdouh-Guebas, F., R. De Bondt, P.D. Abeysinghe, J.G. Kairo, S. Cannicci, L. Triest & N. Koedam, 2004c. Ecologic-comparative study of the disjunct zonation pattern of the grey mangrove *Avicennia marina* (Forsk.) Vierh. in Gazi Bay (Kenya). *Bulletin of Marine Science* (in press).

De Bondt, R., 1995. *Het disjuncte patroon van Avicennia marina (Forsk.) Vierh. Langs de oostkust van Afrika (Kenya, Gazi Bay). Een ecologisch vergelijkende studie* [The disjunct pattern of *Avicennia marina* (Forsk.) Vierh. along the East coast of Africa (Gazi Bay, Kenya)]. Biology Thesis, Vrije Universiteit Brussel, Brussels, Belgium. 132 pp.

Defever, H., 2004. Voorspellingen van de gevolgen van zeeniveaustijging op het mangrove-ecosysteem van Gazi (Kenia) [Prediction of the consequences of sea level rise on the mangrove ecosystem of Gazi (Kenya)]. MSc. Biology thesis, Vrije Universiteit Brussel, Brussels, Belgium.

Definiens Imaging eCognition. URL:<http://www.definiens-imaging.com/>. Products , Services, Purchase, Support, Company. Copyright 2000-2004 Definiens Imaging GmbH.

Dekker, R.J., 2003. Texture Analysis and Classification of ERS SAR Images for Map Updating of Urban Areas in The Netherlands. *IEEE Transactions on Geoscience and Remote Sensing* 41(9): 1950-1958.

de Kok, R., Schneider, T. and Ammer, U., 1999. Object based classification and applications in the Alpine forest environment. In: *Fusion of sensor data, knowledge sources and algorithms*, Proceedings of the Joint ISPRS/EARSel workshop, 3-4 June 1999, Valladolid, Spain. International Archives of Photogrammetry and Remote Sensing 32, Part 7-4-3 W6.

Digital Globe Satellite Imagery. URL: <http://www.digitalglobe.com>. Press Room, Product Information, Industry Applications, About us. Latest Access: 30 May 2004. Copyright Digital Globe Inc. 2004.

Duke, N.C., Pinzon, Z.S., M. and Prada, M.C.T.: 1997, 'Large-scale damage to mangrove forests following two large oil spills in Panama', *Biotropica* **29**(1), 2-14.

Eastern Africa Database and Atlas Project (EADAP), 1994. Database for Marine and Coastal Resources of Kenya . KMFRI, Mombasa, Kenya.

Eastman, J.R., 1999. Idrisi 32 Guide to GIS and Image Processing Volume 1. Clark Labs, Worcester, MA, USA.

ERDAS Imagine, version 8.6. November 12, 2002. Leica Geosystems, GIS & Mapping Division, Atlanta, Georgia, USA.

ERDAS Field Guide, 2002. Leica Geosystems, GIS & Mapping Division, Atlanta, Georgia, USA. Sixth Edition.

Estes, J.E., Hajic, E.J., and Tinney, L.R., 1983. Fundamentals of image analysis: Analysis of visible and thermal infrared data. In: *The manual of remote sensing*, second edition, R.N. Colwell, (ed.), American Society of Photogrammetry.

Ewel, K.C., R.R. Twilley & J.E. Ong, 1998. Different kinds of mangrove forests provide different goods and services. *Global Ecology and Biogeography Letters* **7**: 83-94.

Farnsworth, E.J. and Ellison, A.M.: 1997, 'The global conservation status of mangroves', *Ambio* **26**: 328-334

Franklin, S.E., Hall, R.J., Moskal, L.M., Maudie, A.J. and Lavigne, M.B., 2000. Incorporating texture into classification of forest species composition from airborne multispectral images. *International Journal of Remote Sensing* **21**: 61-79.

Franklin, S.E., Wulder, M.A. and Gerylo, G.R., 2001. Texture analysis of IKONOS panchromatic data for Douglas-fir forest age class separability in British Columbia. *International Journal of Remote Sensing* **22**: 2627-2632.

Frankot, R.T., and Chellappa, R., 1987. Lognormal random-field models and their applications to radar image synthesis. *IEEE Transactions on Geoscience and Remote Sensing*, **25**: 195-207.

Friedman, S.Z., 1980. Mapping Urbanized Area Expansion through Digital Image Processing of Landsat and Conventional Data. Publication 79-113. Pasadena, California: Jet Propulsion Laboratory.

Gougeon, F.A. and D.G. Leckie, 2003. Forest Information Extraction From High resolution images using an individual tree crown approach. Information report BC-X-396. Canadian Forest Service, Pacific Forestry Center, Victoria, British Columbia, Canada.

Green, E. P., Mumby, P. J., Edwards, A. J. & C.D. Clark, 2000. *Remote sensing handbook for tropical coastal management*. Coastal Management Sourcebooks 3, UNESCO, Paris.

Haralick, R.M., K.S., Shanmugam and I., Dinstein, 1973. Textural features for image classification. *IEEE Transactions on Systems, Man and Cybernetics* 3: 610-622.

Hemminga, M.A., F.J. Slim, J. Kazungu, G.M. Ganssen, J. Nieuwenhuize & N.M. Kruyt, 1994. Carbon outwelling from a mangrove forest with adjacent seagrass beds and coral reefs (Gazi Bay, Kenya). *Marine Ecology Progress Series* 106: 291-301.

Heywood, V.H. (ed.), 1995. Global Biodiversity Assessment. United Nations Environment Programme. Cambridge University Press, Cambridge.

Hofmann, P., 2001. Detecting informal settlements from Ikonos image data using methods of object oriented image analysis – an example from Cape Town (South Africa). In : *Remote Sensing of Urban Areas*. C. Jürgens (ed.), Regensburger Geographische Schriften, Heft 35, Regensburg, Germany: 107-118.

Holdridge, L., Grenke, W.C., Hatheway, W.H., Liang, T. and Tosi, J.A., 1971. Forest Environment in Tropical Life Zones. Pergamon Press. New York, pp. 747.

Hughes, G.F., 1968. On the mean accuracy of statistical pattern recognizers, *IEE transaction on information theory* 14: 55-63.

INRIA, The French National Institute for Research in Computer Science and Control. URL: <http://www.inria.fr/index.en.html>. News, Scientific research, Valorisation and transfer, Publications & Documentation, Working and Training at INRIA. Last update: 27/05/2004; Latest access: 30 May 2004.

Jayatissa, L.P., M.C.Guero, S. Hettiarachchi & N. Koedam, 2002. Changes in vegetation cover and socio-economic transitions in a coastal lagoon (Kalametiya, Sri Lanka), as observed by teledetection and ground truthing, can be attributed to an upstream irrigation scheme. In : F. Dahdouh-Guebas (ed.), *Remote sensing and GIS in the sustainable management of tropical coastal ecosystems, Environment, Development and Sustainability* 4(2): 167-183.

Jensen, J.R., 1983. Biophysical Remote Sensing. *Ann. Assoc. Am. Geogr.* 73: 111-132

Jensen, J.R., 1986. Introductory digital image processing: a remote sensing perspective. Prentice Hall, Englewood Cliffs, New Jersey.

Jensen, J.R., Ramset, E., Davis, B.A., and Thoemke, C.W., 1991. The measurement of mangrove characteristics in south-west Florida using SPOT multispectral data. *Geocarto International* 2: 13-21.

Jordan, C.F., 1969. Derivation of leaf area index from quality of light on the forest floor. *Ecology* 50: 663-666.

Jupp, D.L.B., Mayo, K.K., Kuchler, D.A., Heggen, S.J., Kendall, S.W., Radke, B.M. and Ayling, R., 1986. Landsat based interpretation of the Cairns section of the Great Barrier Reef

Marine Park. Natural Resources Series 4 (Canberra: CSIRO Division of Water and Land Resources).

Kairo, J.G., 1995. *Community participatory forestry for rehabilitation of deforested mangrove areas of Gazi Bay (Kenya). A first approach*. Final technical report. University of Nairobi, Department of Botany, Nairobi, Kenya.

Kairo, J.G., F. Dahdouh-Guebas, J. Bosire & N. Koedam, 2001. Restoration and management of mangrove systems – A lesson for and from the East African region. *South African Journal of Botany* 67: 383-389.

Kairo, J.G. and F. Dahdouh-Guebas, in prep. Conservation Status of Mangrove Resources in Kenya.

Kaneko, T., 1978. Colour composite pictures form principal axis components of multispectral scanner data, *IBM journal of Research and development* 22: 386-392

Kitheka, J.U., 1996. Water circulation and coastal trapping of brackish water in a tropical mangrove-dominated bay in Kenya. *Limnology and Oceanography* 4: 169-176.

Kitheka, J.U., 1997. Coastal tidally-driven circulation and the role of water exchange in the linkage between tropical coastal ecosystems. *Estuarine Coastal and Shelf Science* 45: 177-187.

Kitheka, J.U., 1998. Groundwater outflow and its linkage to coastal circulation in a mangrove-fringed creek in Kenya. *Estuarine, Coastal and Shelf Science* 47(1): 63-75.

Kristóf, D., É. Csató & D. Ritter, 2002. Application of high-resolution satellite images in forestry and habitat mapping – evaluation of Ikonos images through a Hungarian case study. In : *Symposium on Geospatial Theory, Processing and Applications*, Ottawa, Canada.

Kuchler, D., Biña, R.T. and Claasen, D.R., 1989. Status of high-technology remote sensing for mapping and monitoring coral reef environments. Proceedings of the 6th International Coral Reef Symposium, Townsville 1: 97-101.

Leckie, D.G., Gougeon, F.A., Walsworth, N. and D. Paradine, 2003. Stand delineation and composition estimation using semi-automated individual tree crown analysis. *Remote Sensing of the Environment* 85: 355-369.

Lillesand, T.M. and Kiefer, R.W. Remote sensing and image interpretation. 1994, John Wiley & Sons, Inc. New York. Third Edition.

Luczkovich, J.J., Wagner, T.W., Michalek, J.L. and Stoffe, R.W., 1993. Discrimination of coral reefs, seagrass meadows on sand bottom types from space: a Dominican Republic case study. *Photogrammetric Engineering and Remote Sensing* 59: 385-389.

Ma, Z. and Redmond, R.L., 1995. Tau coefficients for accuracy assessment of classification of remote sensing data. *Photogrammetric Engineering and Remote Sensing* 61: 435-439.

Marguillier, S., G. van der Velde, F. Dehairs, M.A. Hemminga & S. Rajagopal, 1997. Trophic relationships in an interlinked mangrove-seagrass ecosystem as traced by $\delta^{13}\text{C}$ and $\delta^{15}\text{N}$. *Marine Ecology Progress Series* 151: 115-121.

Mather, P.M., 1999. Computer processing of remotely-sensed images: an introduction. John Wiley & Sons, Chichester. Second Edition.

Matthijs, S., 1995. *Relatie tussen de zonatie van de mangroven in Gazi Bay (Kenia) en de redoxtoestand en samenhangende factoren* [Relationship between the zonation of the mangroves of Gazi Bay (Kenya) and the redox state and linked factors]. Biology Thesis, Vrije Universiteit Brussel, Brussels, Belgium.

McDonald, A.J., Gemmell, F.M., and P.E. Lewis, 1998. Investigation of the Utility of Spectral Vegetation Indices for Determining Information on Coniferous Forests. *Remote sensing of the environment* 66: 250-272.

Meinel, G., M. Neubert & J. Reder, 2001. The potential use of very high resolution satellite data for urban areas – first experiences with Ikonos data, their classification and application in urban planning and environmental monitoring. In : *Remote Sensing of Urban Areas*. C. Jürgens (ed.), Regensburger Geographische Schriften, Heft 35, Regensburg, Germany: 196-205.

Mangrove Management Group. URL: <http://www.vub.ac.be/mangrove/>. About us, members, contacts, publications, projects, bibliography, links and photos. Created: 1 February 1999 by David P. Gillikin. Latest update: 1 March 2001 by Anouk Verheyden. Latest Access: 30 May 2004.

Montserud, R.A. and R., Leamans, 1992. Comparing global vegetation maps with the kappa statistic. *Ecological modelling* 62: 275-293.

Morad, M., Chalmers, A.I., and O'Regan, P.R., 1996. The role of root-mean-square error in the geo-transformation of images in GIS. *International Journal of Geographical Information Systems* 10: 347-353.

Mumby, P.J., Edwards, A.J., Arias-Gonzales, J.E., Lindeman, K.C., Blackwell, P.G., Gall, A., Gorczynska, M.I., Harborne, H.R., Pescod, C.L., Renken, H., Wabnitz, C. and G., Llewellyn, 2004. Mangroves enhance the biomass of coral reef fish communities in the Caribbean. *Nature* 427: 533-536, Letters to Nature.

Munro, J.L., 1996. The scope of tropical reef fisheries and their management. In: Polunin N.V.C., Roberts, C.M. (eds) *Reef fisheries*. Chapman & Hall, London, 1-14.

Nagelkerken, I., Roberts, C.M., van der Velde, G., Dorenbosch, M., van Riel, M.C., Cocheret de la Morinière, E., Nienhuis, P.H., 2002. How important are mangroves and seagrass beds for coral-reef fish? The nursery hypothesis tested on an island scale. *Marine Ecology Progress Series* 244:299-305.

Odum, W.E., and E.J., Heald, 1972. Trophic analyses of an estuarine mangrove community. *Bulletin of Marine Science* 22: 671-738.

- Ogden, J.C. and J.C. Zieman, 1977. Ecological aspects of coral reef - seagrass bed contacts in the Caribbean. *Proceedings of the Third International Coral Reef Symposium* 1: 377-382.
- Ogden, J.C., 1987. Cooperative coastal ecology at Caribbean marine laboratories. *Oceanus* 30: 9-15.
- Ogden, J.C., 1988. The influence on adjacent systems on the structure and function of coral reefs. *Proceeding, Sixth International Coral Reef Symposium*, Australia, 1: 123-129.
- Parrish, J.D., 1989. Fish communities of interacting shallow-water habitats in tropical oceanic regions. *Marine Ecology Progress Series* 58: 143-160.
- Pycke, P., 2003. *Teledetectie en grondcontrole van de distributie en samenstelling van mangrovesoorten in Chilaw Lagoon met zeer hoge resolutie satellietbeelden* [Remote sensing and ground-truthing of mangrove species distribution and composition in Chilaw Lagoon with very high resolution satellite imagery] Lic./MSc. Biologie Thesis, Vrije Universiteit Brussel, Brussels, Belgium. 113 pp.
- Rawlins, S.P., 1957. The East-African mangrove trade. Unpublished manuscript #51 of the National Museum of Kenya, Nairobi, Kenya.
- Read, J.M., Clark, D.B., Venticinque, E.M. and M.P. Moreira, 2003. Application of merged 1-m and 4-m resolution satellite data to research and management in tropical forests. *Journal of Applied Ecology* 40: 592-600.
- Reddy, S.R.C., and S.P. Chakravarty, 1999. Forest dependence and income distribution in a subsistence economy: evidence from India. *World Development* 27(7): 1141-1149.
- Robertson, A.I., and S.J.M. Blaber, 1992. Plankton, epibenthos and fish communities. In: Robertson, A.I., Alongi, D.M. (eds) *Tropical mangrove ecosystems*. Coastal and Estuarine Studies 41: 173-224.
- Rouse, J.W., Haas, R.H., Shell, J.A., and D.W., Deering, 1973. Monitoring vegetation systems in the Great Plains with ERTS-1. In: *Third Earth Resources Technology Saterllite Symposium* 1: 309-317.
- Ruitenbeek, H.J., 1994. Modelling Economy-Ecology Linkages in Mangroves: Economic Evidence for Promoting Conservation in Bintuni Bay, Indonesia. *Ecological Economics* 10: 233-47.
- Russ, G.R., 1991. Coral reef fisheries: effects and yields. In: Sale, P.F. (ed.). *The ecology of Fishes on Coral Reefs*. Academic Press, New York.
- Ruwa, R.K., 1993. Mangroves of Kenya. In: Conservation and Sustainable Utilization of Mangrove Forests in Latin America and Africa regions. Part II-Africa. Diop., E.S. (ed.). *Mangrove Ecosystems Technical Reports*. International Society for Mangrove Ecosystems, Okinawa, Japan, pp. 227-243.
- Salvat, B. (ed.), 1987. Human Impacts on Coral Reefs: Facts and Recommendations. Antenne Museum Ecole Pratique des Hautes Etudes, French Polynesia.

- Sathirathai, S. and E.B. Barbier, 2001. Valuing Mangrove Conservation, Southern Thailand. *Contemporary Economic Policy* 19(2): 109-22.
- Schiewe, J., L. Tufte & M. Ehlers, 2001. Potential and problems of multi-scale segmentation methods in remote sensing. *GIS* 6: 34-39.
- Schiewe, J., 2002. Segmentation of high-resolution remotely sensed data – concepts, applications and problems. *Symposium on Geospatial Theory, Processing and Applications*, Ottawa, Canada.
- Semesi, A.K., 1992. Developing management plans for the mangrove reserves of mainland Tanzania. *Hydrobiologia* 247: 1-10.
- Shulman, M.J., 1985. Recruitment of coral reef fishes: effects of distribution of predators and shelter. *Ecology* 66: 1056-1066.
- Snedaker, S.C., 1989. Overview of ecology of mangroves and information needs for Florida bay. *Bulletin of Marine Science* 44 (1): 341-347.
- Spalding, M., F. Blasco & C. Field, 1997. *World Mangrove Atlas*. The International Society for Mangrove Ecosystems, Okinawa, Japan. 178 pp.
- Stafford-Deitsch, J., 1996. *Mangrove : the Forgotten Habitat*. Immel Publishing Limited, London, UK. 277 pp.
- Tack, J.F., and Polk, P., 1999. The influence of tropical catchments upon the coastal zone: modelling the links between groundwater and mangrove losses in Kenya, India and Florida. In: Harper, D., Brown, T. (Eds.), *Sustainable Management in Tropical Catchments*. Wiley, London, UK.
- Taylor, M., Ravilious, C. and E.P. Green, 2003. Mangroves of East Africa. United Nations Environment Programme World Conservation Monitoring Centre (UNEP-WCMC), Cambridge, UK, 24 pp.
- Ticehurst, C., L. Lymburner, A. Held, C. Palylyk, D. Martindale, W. Sarosa, S. Phinn & M. Stanford, 2001. Mapping tree crowns using hyperspectral and high spatial resolution imagery. Presentation at the Third International Conference on Geospatial Information in Agriculture and Forestry, Denver, Colorado, U.S.A.
- Tomlinson, C. B., 1986. *The Botany of Mangroves*. Cambridge Tropical Biology Series, Cambridge University Press, Cambridge, New York, U.S.A.
- Townshend, J., Huang, C. , Kalluri, S., DeFries, R., Liang, S., Yang, K., 2000, beware of per-pixel characterisation of land cover. In: *International Journal of Remote Sensing* 21 (4): 839-843.
- Tso, B. and Mather P.M., 2001. Classification methods of remotely sensed data. Taylor and Francis , London, England and New-York, USA

Twilley, R.R., 1988. Coupling of mangroves to the productivity of estuarine and coastal waters. In : *Lecture Notes on Coastal and Estuarine Studies* 22. B.O. Jansson, ed., Coastal-Offshore Ecosystem Interactions, Springer Verlag, Berlin, Germany: 155-180.

Van Hiel, E., 2002. *Identification of mangrove assemblages using very high resolution IKONOS satellite images*. MSc. Environmental Science and Technology thesis, Vrije Universiteit Brussel, Brussels, Belgium. 99 pp.

Van Tendeloo, A., 2004. Veranderingen in traditionele en commerciële mens-ecosysteemrelaties in de mangrovebaai van Gazi (Kenia): etnobiologie, percepties van de lokale gemeenschap en ecotoeristische activiteiten [Changes in traditional and commercial man-ecosystem relations in the mangrove bay of Gazi (Kenya): ethnobiology, perceptions of the local people and ecotouristic activities]. MSc. Biology thesis, Vrije Universiteit Brussel, Brussels, Belgium. 162 pp.

Véhel, J.L. and P. Mignot, 1994. Multi-fractal Segmentation of Images, *Fractals* 2(3): 371-378.

Verheyden, A., 1997. *Ruimtelijke analyse van flora and fauna in mangrovegebieden van Sri Lanka. Luchtfoto-interpretatie en GIS toepassing in het onderzoek naar mangrovedynamiek*. [Spatial analysis of fauna and flora in Sri Lankan mangrove areas] Biology Thesis, Vrije Universiteit Brussel, Brussels, Belgium. 153 pp.

Verheyden, A., F. Dahdouh-Guebas, K. Thomaes, W. De Genst, S. Hettiarachchi & N. Koedam, 2002. High resolution vegetation data for mangrove research as obtained from aerial photography. In : F. Dahdouh-Guebas (ed.), *Remote sensing and GIS in the sustainable management of tropical coastal ecosystems, Environment, Development and Sustainability* 4(2): 113-133.

Verneirt, M., 1994. *Faunistische factoren in de regeneratie van de Oostafrikaanse mangrove - een case-study in Gazi, Kenya* [Faunistic factors in the regeneration of the East-African mangrove- a case study in Gazi, Kenya]. Biology Thesis, Vrije Universiteit Brussel, Brussels, Belgium. 114 pp.

Warner, T., McGraw, J., Dean, C., and R. Landenberger, 2000. Automatic delineation of individual deciduous trees in high resolution imagery. Presented at the 28th International Symposium on Remote Sensing of Environment, Cape Town, South Africa.

Wolanski, E., Mazda, Y., Furukawa, K., Ridd, P., Kitheka, J., Spagnol, S. and T., Stieglitz, 2001. Water-circulation in mangroves and its implications for Biodiversity. In: Wolanski, E. (ed), *Oceanographic processes of coral reefs: physical and biological links in the Great Barrier Reef* (53-76). London: CRC Press.

Woodcock, C.E., Scott, A.M. and Kumar, L., 2002. Vegetation mapping and monitoring. In: *Environmental modelling with GIS and remote sensing*, Andrew Skidmore (Ed.), 2002, Taylor & Francis, 97-120.

Index

A

Aerial photographs, 1; 10; 16
Aquaculture, 2; 5; 8; 9; 152

C

channel. *See* Band
Classification accuracy
 Definition, 31
Classifier
 Definition, 31
 Hard, 31
 Non-parametric, 31
 Parametric, 31
 Soft, 31
Climate change, 7
Clustering. *See* Unsupervised classification
Confusion matrix
 Definition, 31
Contingency matrix
 Definition, 30
Convolution window
 Definition, 39
Coral reef, 2; 3; 4; 5; 7; 10; 46; 47; 48;
 170; 172; 173; 174; 175
Covariance matrix, 24; 27; 28; 29; 30; 35;
 88; 108
 eigenvectors, 24; 55; 75
Covariance matrix
 eigenvalue, 24; 75

D

Digital image processing, 17; 18; 42
 Definition, 17
Digital number
 Definition, 18
Divergence
 Formula, 30
DN. *See* Digital number

E

Electromagnetic spectrum, 14; 15; 18

Error matrix. *See* Confusion matrix
Error of commission. *See* User's accuracy
Error of omission. *See* Producer's accuracy
Euclidean distance
 Formula, 35

F

Feature space, 18; 19; 26; 27; 29; 34; 35;
 36; 39; 40; 54; 56; 71; 91; 92
 Definition, 19
Feature space ellips, 29; 36; 56; 91; 92
 Definition, 29
Feature vector
 Definition, 19
Fuzzy classification
 Purpose, 39
Fuzzy classification (ERDAS)
 Formula, 39

G

Geographic Information System, i; xvi; 2;
 9; 10; 18; 151; 166; 167; 168; 169; 170;
 172; 174; 175

H

Habitat mapping, 9; 42; 171
Histogram, 26; 29; 38; 56; 58; 59; 60; 122;
 138
 Definition, 29
Hughes effect, 29

I

IKONOS, 10; 11; 14; 17; 18; 41; 168; 175
ISODATA algorithm, 27; 55

K

Kappa coefficient, xvi; 33; 34; 98; 147;
 172
 Definition, 33

M

Mahalanobis distance
Formula, 35

Mangrove, 1; 2; 3; 5; 7; 8; 167; 172; 173;
174
deforestation, 2
destruction, 2
ecosystem, 1; 2; 4; 7; 11; 152; 167; 173
management, iii; 1; 2; 4; 9; 10; 32; 37;
42; 152; 168; 170; 171; 172; 173;
174; 175
remote sensing, 1; 10

Mangrove cutting ban, 8

Mangrove Management Group, 1

Mangrove Management Plan, 9

Maximum likelihood classifier
Description, 36

Minimum distance classifier
Description, 35

ML. *See* Maximum likelihood classifier

Multiresolution merging, 25
Definition, 25

N

NDVI. *See* Normalized Difference
Vegetation Index

Normalized difference vegetation index
Definition, 25

Normalized Difference Vegetation Index,
iii; xvii; 12; 25; 55; 56; 57; 59; 78; 79;
88; 89; 90; 91; 92; 93; 100; 104; 105;
106; 122; 124; 127; 130; 131; 132; 137;
138; 139; 140; 141; 147; 149; 157; 158;
159; 160; 161

O

Oil pollution, 2; 5; 8; 169

Overall accuracy
Definition, 32

P

Parallelepiped classifier
Description, 34

Pattern. *See* Feature vector

PCA. *See* Principal Component Analysis

Photo-interpretation, 16

Pixel, 18

Principal Component Analysis, xvi; 18; 23

Producer's accuracy
Definition, 32

Q

QuickBird, i; iii; 1; 14; 17; 18; 48; 49; 50;
53; 137; 150; 152

R

Radar imagery, 14

Remote sensing, xvi; 9; 14; 167; 168; 170;
171; 172; 173; 175
Definition, 14

River diversion, 7

S

Sea level rise, 8; 11

Seagrass beds, 3; 4; 5; 46; 47; 170; 172

Signature
Definition, 28

Spectral reflectance, 15; 56

Supervised classification
Definition, 27

T

Tau coefficient, xvi; 98; 147
Definition, 34

Training sites
Definition, 27

Transformed divergence
Formula, 30

U

Unsupervised classification
Definition, 26

User's accuracy
Definition, 32

V

Vegetation index, iii; 25; 55

Vegetation maps, 10; 16; 172

Visual image interpretation, iii; 9; 11; 16;
17; 37; 143; 146

